Neutrino Physics from Supernovae

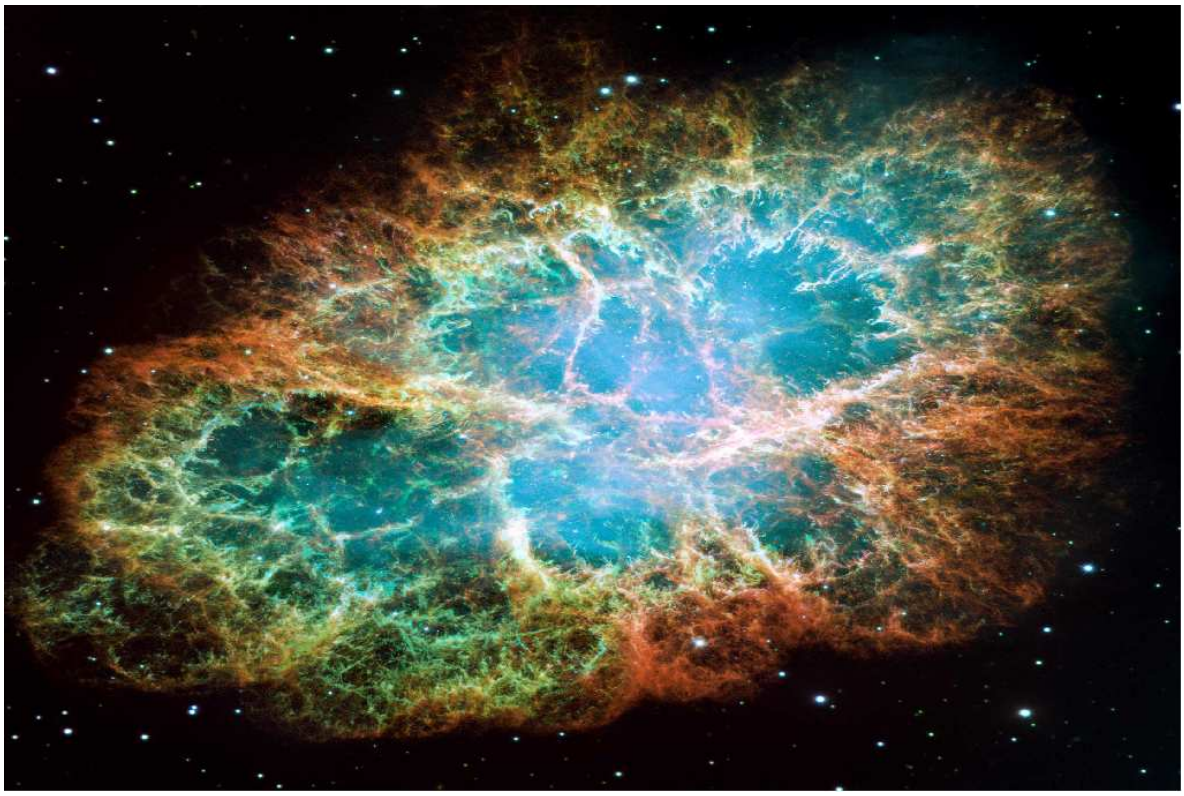

Tina Lund

Dissertation for the degree of Doctor of Philosophy

January 2011

Department of Physics and Astronomy
Aarhus University
Denmark

Neutrino Physics from Supernovae

A Dissertation
Presented to the Faculty of Science
of the University of Aarhus
in Partial Fulfilment of the Requirements for the
PhD Degree

by
Tina Lund
January 2011

Supervisor: Professor Steen Hannestad, IFA, Aarhus University
Co-supervisor: Dr. Georg G. Raffelt, MPI für Physik, München

Abstract

Our understanding of the explosive phase of core-collapse supernovae is still incomplete. The intricate interactions between hydrodynamical mass motions, neutrino heating and cooling, and possible other effects are much debated and the objects of much research. This thesis looks closer at the role of the neutrino in the explosion.

Firstly a novel strong interaction between the neutrino and a low mass pseudo-scalar particle is investigated. The decoupling radii of the annihilation process and the bremsstrahlung process are calculated. Subsequently the neutrino energy spectrum is estimated. With the inclusion of this new interaction the resulting energy spectrum is different from the energy spectrum where only charged current and neutral current interactions are included. The differences are sufficient to distinguish the two spectra, but the predicted spectrum is still within bounds imposed from the neutrino observations of SN1987A.

Secondly, the signature the Standing Accretion Shock Instability will leave on the neutrino emission from a supernova is investigated. This is done by calculating the neutrino signal expected in IceCube from the energy and luminosity results of recent 2D simulations of a 15 $M_\odot$ progenitor, with and without rotation, and an 11.2 $M_\odot$ supernova model. A Fourier transform of the signal reveals characteristic frequencies. The frequency of $\sim$50 Hz for the $\ell = 1$ dipolar mode is evident in the neutrino signal, when the employed progenitor model allows the Standing Accretion Shock Instability to grow strong.

Dansk resumé

Stjerner med store masser ender deres liv som spektakulære fænomener kaldet supernovaer. Vores viden om explosionsfasen i den type der kaldes kerne-kollaps supernovaer er stadig mangelfuld, trods mange års forskning. Det komplicerede samspil mellem neutrinoer, der fjerner energi fra stjernens indre og delvist afsætter den igen længere ude, de hydrodynamiske bevægelser der foregår, og bidrag fra andre potentielle mekanismer er genstand for megen debat. Denne afhandling omhandler hvad vi kan lære om supernovaer ud fra neutrino observationer.

Først undersøges en ny stærk vekselvirkning mellem neutrinoen og en pseudo-scalar partikel med lav masse. Afkoblingsradierne for annihilations-processen og for bremsestrålingsprocessen beregnes. Ud fra dem estimeres energispektret for neutrinoen. Det resulterende spektrum er tilpas anderledes til at vi kan skelne det fra det spetrum, der opnåes, hvis kun de sædvanlige svage vekselvirkninger medtages. Dog er det ikke så anderledes at det er udelukket ud fra neutrinoobservationer fra SN1987A.

Derpå undersøges den effekt som bevægelsen af et stationært tilvækst-chok vil have på neutrinoer udsendt fra en supernova. Dette gøres ved at beregne det forventede neutrino signal i IceCube ud fra energier og luminositeter fra 2D simuleringer af tre supernova modeller. De undersøgte modeller er; en stjerne med en masse på 11.2 $M_\odot$ og en med en masse på 15 $M_\odot$, med og uden rotation. De karakteristiske frekvenser i signalet findes ved en Fourier transformation. En frekvens på $\sim$50 Hz, svarende til den dipolære bevægelse af chokket, er tydelig i neutrinosignalet for de stjerner, hvor bevægelsen får et stort udsving.

Acknowledgements

Thank you to all the people, whom I have met on the journey towards this day. Without you, I would not be where I am today or the person I am. The past four years have been filled with good times as well as bad times, but to qoute one of my favourite authors, Douglas Adams:

> *"I may not have gone where I intended to go, but I think I have ended up where I intended to be."*

Thank you to my supervisor Steen Hannestad for giving me the opportunity to pursue PhD studies.
Thank you to Georg G. Raffelt who gave me plenty of advice during my stay in Munich, and for his repetitive use of "This can't be right" until I got it right.
Thank you to Thomas Janka and Andreas Marek for permission to use their data, plenty of help with handling the data files, and always quick, useful replies to questions.
Thank you to all the CAPPA-people; Jacob, Philip, Katrine, Anna, Jan, Anders, Ole and Thomas for sharing offices, making coffee breaks more fun, general good spirits, not to forget CAPPA nights out.
Thank you to Gülnur and all the other astro-people, for a good working environment and the friendly banter.
Thanks goes to all the people in Munich who made my time there pleasant and memorable: Basu, Mattias, Enrique, Koushik, Irene, Carla, Alessandro and all the PhD students - for Friday Board Game nights and coffee breaks filled with discussions of physics and life.
Thank you to Ane Gadegaard and Thomas Amby Ottosen for plenty of time spent thinking and talking about something else than physics.
Thank you to my wonderful supportive family, especially to my father for making me see things in other perspectives when needed.
Thank you to Philip Jarnhus for helping to keep my head straight over the past 4 years, and for his generous use of red pen while proofreading this thesis.
Thank you to my great boyfriend Troels Bjerre Sørensen for providing the rock where I could find support and shelter, and for keeping my home front stable thereby enabling me to tackle what life would send my way.

Tina Lund
Århus, January 2011

Contents

Abstract **v**

Dansk resumé **vii**

Acknowledgements **ix**

Preface **1**

I Overview – Knowing the past... **3**

1 Stellar life and death **5**
1.1 Supernova types . . . 6
1.2 Stellar life . . . 7
1.3 Collapse and explosion sequence . . . 8
1.3.1 Infall . . . 8
1.3.2 Neutrino capture . . . 9
1.3.3 Bounce and prompt explosion . . . 11
1.3.4 Neutrino break-out . . . 11
1.3.5 Delayed explosion . . . 11
1.3.6 Non-explosion . . . 12
1.4 Reviving the shock . . . 12
1.4.1 Alternate explosion mechanisms . . . 12
1.5 Standing Accretion Shock Instability – SASI . . . 14
1.5.1 Acoustic cycle . . . 14
1.5.2 Advective-acoustic cycle . . . 16
1.5.3 Parameterization with spherical harmonics . . . 16
1.6 Neutrino spheres . . . 17
1.6.1 Reactions . . . 18
1.7 Model Spectra . . . 19
1.7.1 Energy hierarchy . . . 19
1.8 Neutrino oscillations . . . 21

2 Numerical simulations and the IceCube detector **23**
2.1 Numerical simulations of supernova models . . . 23
2.1.1 "Ray-by-ray plus" simulation as employed by the Garching group . . . 24
2.2 Equations of State . . . 25
2.2.1 Lattimer & Swesty EoS . . . 25

2.2.2 Hillebrandt & Wolff EoS . . . 26
2.2.3 EoS of Shen, Toki, Oyamatsu and Sumiyoshi . . . 26
2.2.4 Impact of EoS in simulations . . . 26
2.3 IceCube hard facts . . . 27
2.3.1 Aims and appearance . . . 27
2.3.2 Cherenkov Telescope . . . 27
2.3.3 IceCube background noise . . . 29

3 Neutrino physics **31**
3.1 Mixing matrix . . . 31
3.2 Mass hierarchies . . . 32
3.3 Making masses . . . 33
3.3.1 Seesaw mechanism . . . 33
3.4 Neutrino oscillations . . . 35
3.4.1 Vacuum effect . . . 35
3.4.2 Matter effect . . . 36
3.4.3 Collective effect . . . 37
3.4.4 Implications for supernova neutrinos . . . 38

4 Fourier Analysis **41**
4.1 Basic idea . . . 41
4.2 Sampling our signal in the time domain. . . . 42
4.2.1 Proper sampling . . . 42
4.2.2 Aliasing . . . 43
4.3 The Discrete Fourier Transform . . . 45
4.4 The Inverse Discrete Fourier Transform . . . 46
4.5 The exponential as basis function . . . 47

II My work – Adding to present knowledge **49**

Neutrino interactions with a pseudo-scalar **51**

5 A strong pseudo-scalar neutrino interaction **53**
5.1 Motivations . . . 53
5.2 Breaking a symmetry . . . 54
5.3 The singlet Majoron model . . . 55
5.3.1 Specification to our model . . . 56
5.4 Calculating decoupling radii . . . 56
5.4.1 NC and CC radii . . . 59
5.5 Bremsstrahlung calculations . . . 59
5.6 Effects of the $\nu - \phi$ interaction . . . 60
5.7 Summary and conclusions . . . 62

SASI imprints on a neutrino signal observed in IceCube **63**

6 Single ray **65**
6.1 Initial approach . . . 65
6.2 Spectral information on *one* ray . . . 66
6.2.1 Doppler transformations . . . 67
6.2.2 Calculating energy moments and total fluxes . . . 68
6.3 Resampling of event rate . . . 69
6.3.1 Gaussian interpolation and extrapolation . . . 70
6.3.2 Choice of σ . . . 70
6.3.3 Emulating a 1D signal . . . 71

7 Fourier Transformation of the signal **73**
7.1 Basic quantities . . . 73
7.1.1 Nyquist frequency revisited . . . 74
7.2 Window function . . . 74
7.2.1 The Hann window . . . 75
7.3 Definition of Fourier Amplitude . . . 76
7.4 Definition of spectral power . . . 76
7.5 Fourier spectrum of single ray signal . . . 77

8 Noise **79**
8.1 Signal shot noise . . . 79
8.2 Theoretical estimate of shot noise power level for IceCube background . . . 80
8.2.1 Application to our data . . . 81
8.3 Numerical tests of analytic results . . . 82
8.3.1 The Poisson distribution . . . 82
8.3.2 Generating noise with the Marsaglia Polar method . . . 82
8.3.3 Numerical shot noise power level . . . 83
8.3.4 Ensemble average of power . . . 84

9 Data on multiple rays **87**
9.1 Hemispheric averaging . . . 87
9.1.1 Equatorial average . . . 88
9.1.2 Polar averages . . . 89
9.2 Ensemble average of rays . . . 89
9.3 Power level smoothing . . . 90

10 Non-rotating 15 $M_\odot$ model **93**
10.1 Comparison with spherical symmetric case . . . 96
10.2 Directional dependence . . . 97
10.3 Flavor dependence . . . 98
10.4 Equation of State dependence . . . 99
10.5 Thirds method . . . 100
10.5.1 Thirds method: results and discussion . . . 102
10.6 Time evolution of frequencies . . . 102
10.6.1 Interpretation of time evolution figures . . . 104

10.7 Physical interpretation . . . 105
10.7.1 Stiffer EoS revisited . . . 108
10.7.2 Signatures of SASI . . . 108
10.8 Implications of detection . . . 108
10.9 Luminosity versus energy fluctuations . . . 109
10.9.1 Time domain . . . 109
10.9.2 Frequency domain . . . 110
10.9.3 Correlation calculations . . . 111
10.9.4 Summary . . . 111

11 Extended studies **113**
11.1 The 11.2 $\mathbf{M}_\odot$ model . . . 113
11.1.1 Neutrino signals in the time domain . . . 114
11.1.2 Results in the frequency domain . . . 116
11.1.3 Comparison with non-rotating 15 $\mathbf{M}_\odot$ model . . . 120
11.2 The rotating 15 $\mathbf{M}_\odot$ model . . . 120
11.2.1 Time domain neutrino signals . . . 121
11.2.2 Results in the frequency domain . . . 121
11.2.3 Comparison with 11.2 $\mathbf{M}_\odot$ model . . . 124
11.3 Heavier progenitor . . . 125
11.4 Summary . . . 126

III Conclusions – Looking to the future **129**

12 Conclusions **131**

A Matrix element calculation **135**

B Paper: Fast time variations... **139**

The frontpage picture shows the Crab nebula. This is the remnant of a core-collapse supernova in the constellation Taurus 2 kpc away. The supernova explosion occurred in the year 1054 AD. The picture is taken from http://www.nasa.gov/multimedia/imagegallery/image_feature_1604.html.

Preface

Welcome to my thesis, and thank you for taking an interest in my work. Over the past 4 years I have delved into the properties of neutrinos and core-collapse supernovae. My work can be divided into 2 rather different topics, with the only common denominator being neutrinos in core-collapse supernovae.

The first topic I studied was the interaction of a new pseudo-scalar particle and what influence a strong coupling between this "new" particle and the neutrino would have. This project was inspired by previous investigations focused on a regime of weaker interaction strengths. Limitations of this interaction arises from the Big Bang epoch where neutrinos are free streaming, from constraints on allowed alternative energy losses from supernovae, as well as from the need to prevent current day scattering of neutrinos on a relic background of this pseudo-scalar. To comply with these constraints a small mass was assigned to the pseudo-scalar. In this work, I particularly concentrated on the effect on observed energy spectra of neutrinos emitted from a core-collapse supernova, since effectively this interaction provides a back-door for neutrino flavor changes.

The second topic, which I started to work on during my stay in at the MPI für Physik in Munich, was the observational signatures of a hydrodynamical instability in core-collapse supernovae. The only way of "seeing" the hydrodynamical motions that goes on deep inside the star is through the use of neutrinos. The mass motions leave imprints on the luminosity and energy spectra of the emitted neutrinos, making them fluctuate. Fluctuations that could be observed with the detector IceCube. The delayed explosion scenario remains the standard paradigm for the core-collapse supernova mechanism. After core bounce a shock wave forms that stalls in its outward motion at a typical radius of 100–200 km. Matter keeps falling onto the shock front forming a standing accretion shock. Several hundred ms can pass before the shock is re-launched presumably after sufficient neutrino energy deposition in the region behind the shock. Two- and three-dimensional hydrodynamic simulations reveal convective instabilities that quickly develop into large-scale convective overturns. A strong dipole oscillation of the neutron star against the "cavity" formed by the standing shock also develops: the standing accretion shock instability (SASI)

My work centered on a detailed analysis of the output of axially symmetric hydrodynamical simulations which predict relatively large amplitude motions of the SASI. I investigated the corresponding fast time-varying fluctuations of the neutrino emission. The resulting neutrino signal in IceCube, when transformed to frequency space would possess large amplitudes up to frequencies of a few hundred Hz. In collaboration with G. Raffelt, T. Janka and A. Marek, I sought to estimate what information might be extracted about the physics inside core-collapse supernova and the explosion mechanism from the observation of these fast time-variations.

The conclusion was that if these two-dimensional simulations are roughly representative of realistic supernovae, the fast fluctuations of the neutrino signal due to SASI would be easily

observable with IceCube.

The structure of this thesis is as follows:

Part I includes the necessary background knowledge for the work reported in this thesis. Chapter 1 presents the basic understanding of the late stages of stellar evolution according to the standard paradigm. Chapter 2 briefly presents the numerical simulation that provide the background for this work, and discusses the crucial role played by the nuclear equation of state. Essential facts about the IceCube detector are related at the end of the chapter. Chapter 3 introduces basic issues of neutrino physics such as mass generation and neutrino oscillations. Chapter 4 outlines the principles and caveats of applied Fourier analysis.

Part II and III convey the work I have done, and the results that have been achieved during this thesis work. Chapter 5 details the work on the interaction between the neutrino and a pseudo-scalar particle, plus some introduction to the necessary background theories. Chapters 6, 7, 8 and 9 present some of the preliminary work done to facilitate the analysis outlined in subsequent chapters. Chapter 10 contains the work on the detection of neutrinos in IceCube from a 15 $M_\odot$ star. Chapter 11 covers the work on the signal from a 11.2 $M_\odot$ star and a rotating 15 $M_\odot$ star.

In part IV conclusions and a look into the future conclude this thesis.

Part I

Overview – Knowing the past to understand the present

"Are we human because we look at the stars? Or do we look at the stars because we are human?"

— narrator, from the movie "Stardust"

1

Stellar life and death

On February 23rd 1987 a spectacular event happened, see fig. 1.1. A star in the Large Magellanic Cloud exploded as SN1987A (roughly 50 kpc[1] away), and here on Earth we detected neutrinos emitted during this explosion. These roughly 20 neutrino events were detected by the Irvine-Michigan-Brookhaven, the Kamiokande II and Baksan detectors (see fig. 1.2). From these few events astrophysicists got confirmation of their overall understanding of the explosion mechanism of massive stars. An explosion such as this is termed a supernova and marks

[1] 1 kpc is 3.085×10^{19} m.

Figure 1.1: *Left:* The area with Sanduleak -69 202 before it exploded. *Middle:* same area shortly after explosion. *Right:* SN1987A 18 years after. Figures are from the Anglo-Australian Observatory (left) and the Hubble Space Telescope (right).

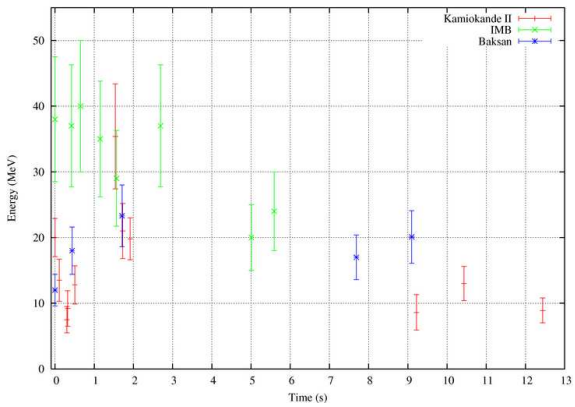

Figure 1.2: Detections of the neutrino events from SN1987A, in the detectors at IMB, Kamiokande II and Baksan.

the end of a star's life. Today more than 20 years after this monumental event, we are still working to understand the details of the core-collapse supernova explosion mechanism. The work of understanding the supernova mechanism, however, was started much before the event of SN1987A, namely already in 1934 when W. Baade and F. Zwicky suggested that *"[...] the phenomenon of a super-nova represents the transition of an ordinary star into a body of considerably smaller mass"* [BZ34], effectively proposing the prompt explosion mechanism. The art of understanding core-collapse supernovae have developed over time and has turned out to be closely tied to the understanding of an elusive particle — the neutrino. The work on understanding the neutrino started when it was first proposed in 1930 by W. Pauli to solve the mystery of the energy distribution in beta-decay. Through the past 80 years we have learned increasingly more about the neutrino, but as we learn more we also discover unexpected new sides of the neutrino. One significant event was the discovery of neutrino oscillations in the detection of neutrinos coming from the sun, which was seen in the Homestake mine in the late 1960's by R. Davis and J. N. Bahcall. This discovery of neutrino oscillations between flavors lead to an extension of the Standard Model of particle physics. In the new model, neutrinos had to have a mass, to facilitate the flavor change.

1.1 Supernova types

The supernova explosion 1987A in the Large Magellanic Cloud belongs to a class called the core-collapse supernovae (ccSNe). There exits several different types of supernovae denoted from an observational viewpoint with Type Ia, Ib, Ic and Type II, based on the absence (Type I) or presence (Type II) of hydrogen lines in the optical spectrum. The theoretical classification on the other hand is based on the two different explosion mechanisms. The first one, which is associated with the Type Ia, is a thermonuclear supernova, where a carbon-oxygen white dwarf accretes a sufficient amount of matter from its binary companion to push it to the Chandrasekhar limit of $1.4M_{\odot}$[2]. The star collapses and a runaway fusion reaction follows

[2]One solar mass is $1\,M_{\odot} = 1.989 \times 10^{33}\,g$.

Table 1 Evolution of a 15-solar-mass star.

Stage	Timescale	Fuel or product	Ash or product	Temperature (10^9 K)	Density (gm cm^{-3})	Luminosity (solar units)	Neutrino losses (solar units)
Hydrogen	11 Myr	H	He	0.035	5.8	28,000	1,800
Helium	2.0 Myr	He	C, O	0.18	1,390	44,000	1,900
Carbon	2000 yr	C	Ne, Mg	0.81	2.8×10^5	72,000	3.7×10^5
Neon	0.7 yr	Ne	O, Mg	1.6	1.2×10^7	75,000	1.4×10^8
Oxygen	2.6 yr	O, Mg	Si, S, Ar, Ca	1.9	8.8×10^6	75,000	9.1×10^8
Silicon	18 d	Si, S, Ar, Ca	Fe, Ni, Cr, Ti, ...	3.3	4.8×10^7	75,000	1.3×10^{11}
Iron core collapse*	~1 s	Fe, Ni, Cr, Ti, ...	Neutron star	>7.1	$>7.3\times10^9$	75,000	$>3.6\times10^{15}$

* The pre-supernova star is defined by the time at which the contraction speed anywhere in the iron core reaches 1,000 km s^{-1}.

Figure 1.3: Stellar evolution phases for a 15 $M_\odot$ star. From [WJ05].

releasing enough energy to unbind the star and blow it apart in a supernova explosion. The second class, covering Type Ib,c and Type II, is collectively called core-collapse supernovae. Here a star undergoes a gravitational collapse once the fuel in its core has been exhausted. In this thesis I will focus on the core-collapse type.

1.2 Stellar life

Stars come in a variety of masses ranging from $M \sim 0.1\,M_\odot$ to $M \sim 100$–$150\,M_\odot$. Only the more massive ones, $M \gtrsim 8\,M_\odot$, end their lives as core-collapse supernovae resulting in either a neutron star or a black hole ($M \gtrsim 20\,M_\odot$) depending on their mass. It is believed that stars more massive than $\sim 50\,M_\odot$ end their lives in a direct black hole formation without a preceding supernova phase. Not one single mechanism is believed to be the cause of the final explosion in the still vast range of masses for core-collapse supernovae.

As a star ages, it progresses from the initial hydrogen burning and on to burning increasingly heavier elements. When it runs out of a given fuel it contracts. Each contraction leads to an increase in temperature and the burning of a new fuel can commence. The onset of a new burning state halts (temporarily) the slow gravitational collapse, and stable burning proceeds for a time until this fuel has been used up and the process repeats itself. A table showing the duration of the different burning phases can be seen in fig. 1.3. The repeated sequence continues successively through the chain of H, He, C, Ne, O until it reaches burning of silicium. Above silicium it will no longer be possible to generate energy by assembling lighter nuclei into heavier ones. Only fission processes will produce energy for nuclei heavier than iron. How far in this fusion chain a star reaches depends on its mass. At the end of the burning sequence, the star will have an onion layer structure with shells burning different fuels throughout the star, see fig. 1.4. The innermost shell, burning silicium, will continue to dump the fusion products, iron-group nuclei such as Fe, Mg and Ni, onto the so-called iron core, until the core reaches the Chandrasekhar mass of $1.4\,M_\odot$. When this happens the electron degeneracy pressure (due to the Pauli exclusion principle of fermions) can no-longer sustain the core against its own inward gravitational pull, and the core becomes unstable. A change in the adiabatic index, $\gamma = (\partial \ln P/\partial \ln \rho)_s$, will change the relationship between the pressure, P, and the density, ρ. As γ falls below 1.2 the star becomes unstable, and starts to collapse.

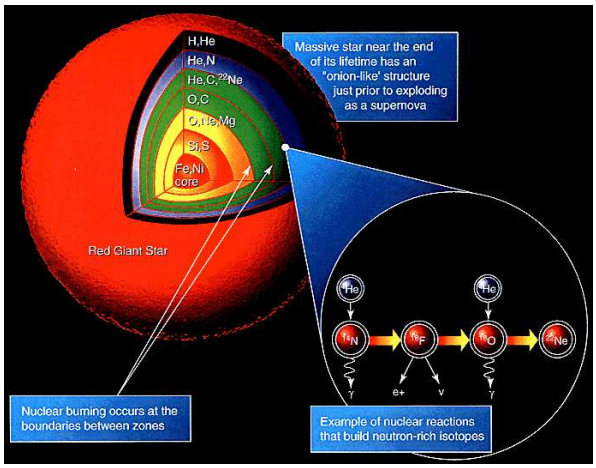

Figure 1.4: Shell burning structure of massive star.

Throughout the evolution of the star, energy is lost with escaping neutrinos. The neutrino luminosity increases from $\sim 0.03\%$ of the total luminosity in the helium burning phase to a million times the optical luminosity in the silicium burning stage [FY03]. Thus in the later stages of the stellar evolution by far the largest energy losses are due to neutrinos. A majority of the neutrinos are created when degenerate electrons meet with free positrons and pair annihilate. The neutrinos escape the star removing energy, but also thereby effectively reducing the electron degeneracy pressure [WJ05, FY03].

A rough divide at $11M_\odot$, groups the stars into two natural categories: Stars below this limit end with a core consisting primarily of oxygen, neon and magnesium (O-Ne-Mg cores), and due to their less massive envelopes, and thereby steeper density gradients, they can explode by the help of a neutrino driven wind. The low explosion energy of the Crab supernova (depicted on the front page) is consistent with a O-Ne-Mg supernova. The more massive stars, that continue the burning of elements until they have an iron core, have to be exploded by a different mechanism.

1.3 Collapse and explosion sequence

The evolution of stars can be found in many introductory astrophysics books,[3] and for a more specific treatment of the energy losses due to neutrinos at late times, the reader is referred to [FY03]. Below we will follow the development of the star from its initial instability to the cast off of the outer layers and the core cooling into a neutron star[4].

1.3.1 Infall

Once the collapse has been initiated electron capture (EC), β-decay and photo-disintegration of iron group elements contribute to increasing energy losses. Photo-disintegration of iron

[3]"Introduction to Modern Astrophysics" by Carroll and Ostlie [CO96] can be recommended.
[4]This section and the following ones are based on [JLM+07, FY03, Raf96].

proceeds as

$$\gamma + {}^{56}Fe \rightarrow 13\,{}^{4}He + 4n - 124,4\,\mathrm{MeV}\,,$$

where more energy can be lost by splitting the produced helium nuclei into nucleons

$${}^{4}He \rightarrow 2p + 2n - 28,3\,\mathrm{MeV}\,.$$

The resulting proliferation of free protons enables capturing of more electrons since the cross section for EC on protons

$$e^- + p \rightarrow n + \nu_e \tag{1.1}$$

is much larger than the cross section for EC on nuclei. This leads to a reduction of the number of electrons per nucleon (Y_e) and thus reduces the electron pressure. The many neutrinos produced through EC remove more energy from the star [FY03, Raf96], and the combination of all the above processes leads to the acceleration of the collapse.

The different stages in the progressing explosion, from the initialization of the collapse to the neutrino-driven cooling of the proto-neutron star (PNS) can be seen in fig. 1.5. Picture a) shows the situation immediately after the infall has begun, and we see that neutrinos leave the iron core unimpeded.

1.3.2 Neutrino capture

When the density in the stellar interior reach $\rho = 10^{12}\,\mathrm{g/cm^3}$, at roughly $r \lesssim 100$ km, neutrinos get trapped, fig. 1.5b. Their diffusion timescale t_{dif} is now longer than the dynamical collapse timescale, t_{dyn}. The diffusion timescale depends primarily on the coherent scattering on heavy nuclei [JLM+07, Raf96]. One can make the following "back of the envelope" calculation to gain some feeling for the timescales. The diffusion timescale is given by

$$t_{\mathrm{dif}} \sim \frac{R^2}{\lambda c} \tag{1.2}$$

where R is the radius of the inner core ($R \sim$20 km), and the mean free path λ is given by

$$\lambda^{-1} = n\,\sigma \tag{1.3}$$

The number density of nuclei is $n \simeq 1.8 \times 10^{38}\mathrm{cm}^{-3}$ and the reaction cross section σ can be approximated by the cross section for neutral current interactions with nucleons:

$$\sigma_{N\nu} \sim 1.7 \times 10^{-42}\,\mathrm{cm}^2 \left(\frac{E_\nu}{10\,\mathrm{MeV}}\right)^2 \tag{1.4}$$

This leads to a diffusion timescale of about

$$t_{\mathrm{dif}} \sim 1\,\mathrm{s} \quad \text{for 30 MeV neutrinos,}$$

and should be compared with a dynamical timescale for $\rho = 10^{12}\,\mathrm{g/cm^3}$ of [FY03];

$$t_{\mathrm{collapse}} \sim 25 \left(\frac{\rho}{10^{11}\,\mathrm{g/cm^3}}\right)^{-0.7} \mathrm{ms} \sim 5\,\mathrm{ms}$$

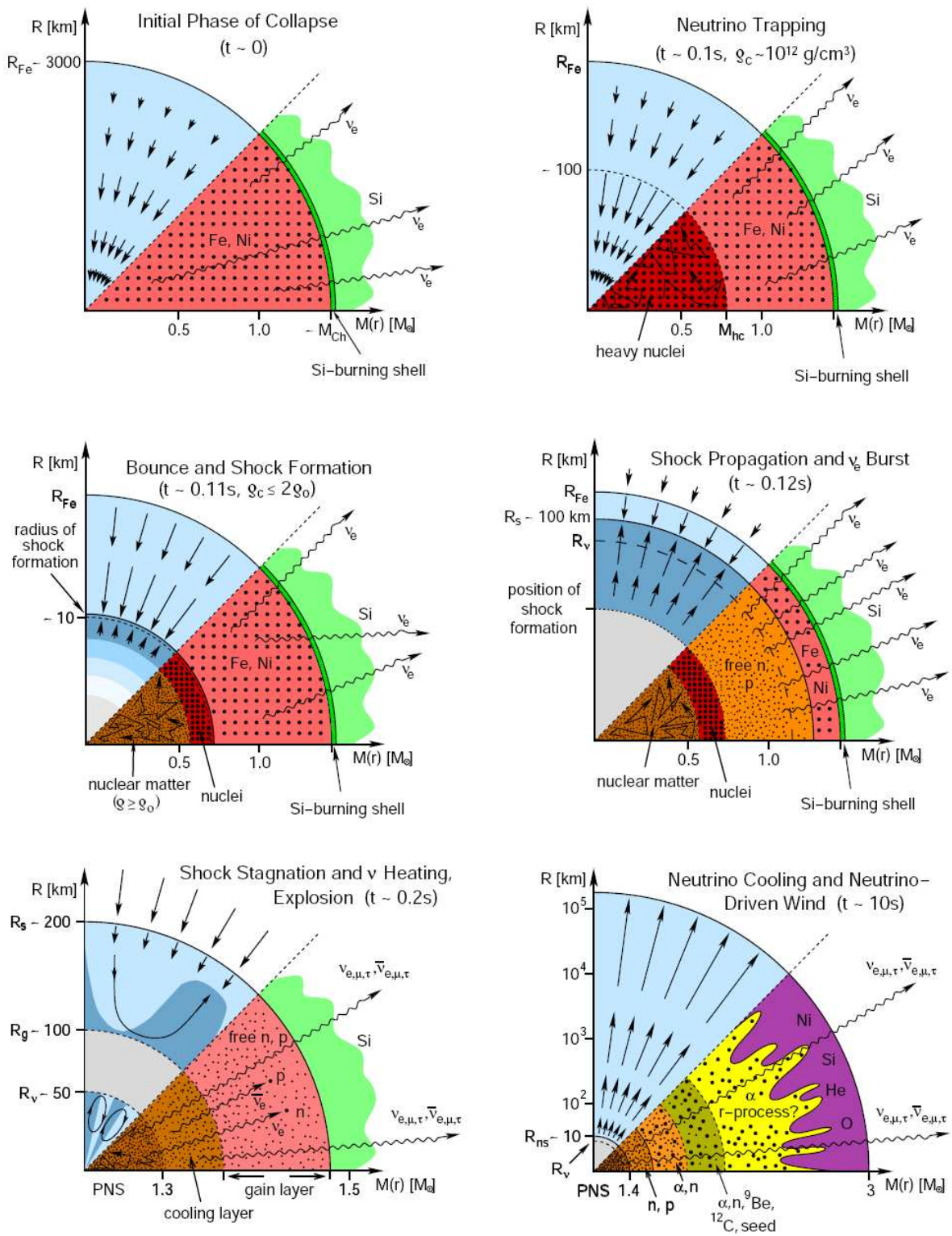

Figure 1.5: Evolutionary phases. The upper part of each figure shows the hydro-dynamical conditions, arrows indicating velocity vectors. Lower parts show nuclear and particle states, along with strong and weak nuclear interaction processes. Horizontal axis designates the mass; M_{Ch} is the Chandrasekhar mass and M_{hc} the mass of the homologous core. Vertical axis signifies radii; R_{Fe} radius of the iron core, R_s shock radius, R_g gain radius, R_{NS} neutron star radius and R_ν neutrino sphere radius. R_g is defined to be the point where the neutrino heating and cooling are equal in size. Picture a) is in the top left corner, b) top right and so forth. The figure is from [JLM+07].

The two timescales thus differ by 3 orders of magnitude, and the infall happens a lot faster than neutrinos can diffuse out. Neutrinos therefore will remain trapped in the inner core during the progressing collapse. After the neutrinos have been trapped, the inner core collapses homologously[5]. The result is that the infall velocity is proportional to the radius: $v \propto r$, and in this case $v/r \in [400; 700]$ s^{-1} [Raf96]. The decoupling of the inner core from the outer core happens at the radius where the infall velocity equals the sound speed: $v \sim v_{\text{sound}}$. This decoupling point is called "the sonic point". The outer part of the core now collapses supersonically while in the inner core the collapse velocity remains subsonic. Information of the collapse can only travel with the speed of sound which means that the outer layers of the star end up "floating" above the collapsing core.

1.3.3 Bounce and prompt explosion

As the density in the inner core reaches and surpasses nuclear densities, $\rho > \rho_{\text{nucl}} = 10^{14}\,\text{g/cm}^3$, the strong nuclear force becomes repulsive. The inner core "stiffens" and when the infalling material of the outer core hits the hard inner core it bounces back [ABKW89, Raf96]. This creates a pressure wave that moves into the outer parts of the core, see fig. 1.5c. Previously it was thought that the pressure wave would proceed all the way out through the star eventually "blowing" off the outer layers of the star. This "prompt explosion scenario" is no longer considered plausible. The energy contained in the shock wave is simply not enough to blow the outer parts off when the shock wave reaches the surface of the star. The energy is lost as the shock wave moves out through the star, with a major part of the energy going into dissociating nuclei to nucleons.

1.3.4 Neutrino break-out

On its way out through the star the shock wave encounters the neutrino sphere. The neutrino sphere is the demarcation of where the neutrinos are trapped: Here they stop moving by diffusion and instead stream freely. As the shock wave passes through the neutrino sphere, the dissociation of nuclei makes it a lot easier for neutrinos to escape since they are no longer trapped by coherent scattering on nuclei. Furthermore the dissociation of nuclei produce many more protons for EC (eq. 1.1). The increased number of electron captures creates a vast amount of electron neutrinos. These ν_e's leave the star bringing along the energy they have received. The sudden release of electron neutrinos is called "the neutrino burst". This burst results in a large energy loss from the shock wave. Due to the various energy losses the shock wave stops just outside the neutrino sphere and turns into an accretion shock, as material continues to fall onto it, fig. 1.5d.

1.3.5 Delayed explosion

Inside the radius where the shock originated, the beginning of a neutron star is appearing. Inside this proto-neutron star (PNS) neutrinos are still trapped since $\lambda_{mfp} < R_{NS}$, but they diffuse out to the neutrino sphere in seconds, as we saw earlier. Through the diffusion the degenerate energy distribution of the neutrinos change to a thermal distribution due to collisions with nuclei.

[5] A homologous collapse means a change in radius can happen without a change in total energy, but it requires $\gamma = 4/3$ [CW66]

Some of the electron neutrinos escaping from the ν-sphere can deposit part of their energy through the charged-current (CC) interactions

$$\bar{\nu}_e + p \rightarrow n + e^+ \tag{1.5}$$

$$\nu_e + n \rightarrow p + e^- \tag{1.6}$$

in the area between the neutrino sphere and the shock front thus reviving the shock. The revival of the shock depends crucially on the balance between the neutrino-cooling and -warming in the area below the shock front. The radius where the neutrino heating equals the neutrino cooling is called the gain radius, R_g, see fig. 1.5e. The heating through the deposition of the neutrino energy makes the stellar material expand and a so-called "hot bubble" is created, fig. 1.5 e). In the hot bubble the density is relatively low while the temperature is high: $\rho \sim 10^6 - 10^8\,\mathrm{g/cm^3}$ and $T \sim 1$ MeV, corresponding to $\sim 10^{10}$ K. For sufficient heating to occur, the electron neutrinos and anti-neutrinos have to deposit between 10 and 20% of their energy in the hot bubble area. If the heating is sufficient, then contrary to the 20 ms for the prompt explosion this explosion sequence takes ∼10 s, and has very appropriately received the name "delayed explosion" [ABKW89, Raf96].

1.3.6 Non-explosion

In current numerical supernova models it appears that the neutrino heating mentioned above, is not enough on its own to make all model stars explode. Only stars of mass $M \sim 8 - 10 M_\odot$ explode. Including convection in the hot bubble pushes the limit for explosion up to $M \sim 11 M_\odot$. Explosion of even higher mass stars are not consistent, not even with a suggested shock instability [JLM+07, FY03]. The understanding of the explosion mechanism is thus clearly not complete.

1.4 Reviving the shock

The revival of the outward movement of the shock wave is among the most debated topics, and holds a great deal of attention in current supernova theory. One might dare say it is the most important issue currently in ccSN theory. The idea of neutrino heating to restart the shock, described above, has turned out not to be sufficiently effective on its own, and several new mechanisms, as well as extensions to the neutrino heating scenario, have been proposed to revive the shock movement. Some of them work on short timescales, others take longer times before they grow powerful enough to make the star explode. Here we will list briefly the most promising of the different proposed solutions, before we turn our attention to a more detailed presentation of the mechanism that serves as the background for the signatures studied in this thesis.

1.4.1 Alternate explosion mechanisms

The prompt explosion mechanism (working on short time scales) where the initial shock wave moves all the way out through the outer layers resulting in the finally observed explosion has, as mentioned above, lost its credibility and we will therefore not discuss it further.

1.4.1.1 Hydrodynamic effects

The neutrino heating mechanism mentioned in section 1.3.5 has been shown incapable of instigating explosions by its own accord in 2-dimensional simulations, except for the very lightest stars of $\sim 8\,M_\odot$ because of the steep density gradient in their outer layers. This has fortunately not been the end of the rather promising neutrino mechanism, that contains a potentially large amount of energy, as recent simulations suggest it can be enhanced by non-radial **hydrodynamic instabilities** in the hot bubble area [Mar07, MJ09].

However, Nordhaus et al. [NBAB10] imply that the inclusion of hydrodynamical instabilities is unnecessary, and ventures that when simulations go to 3D instead of 2D the neutrino heating may be strong enough to explode the star without the added help of hydrodynamic instabilities. They find in going from 1D to 2D simulations for a $15\,M_\odot$ model a reduction of ~ 30 % of the critical neutrino luminosity necessary for explosion, and in going from 2D to 3D a further reduction of $\sim 15 - 25$ % was found. They therefore conclude that with their simplified treatment of neutrino transport simply going to three dimensions may enable the neutrino mechanism to work alone.

The hydrodynamical instabilities proposed to aid the neutrino mechanism can be large convective overturns in the hot bubble area or an instability of the accretion shock radius (the Standing Accretion Shock Instability (SASI), see section 1.5), or a combination of both. The effect of these hydrodynamical instabilities is that infalling matter will spend longer time in the heating layer between the gain radius and the shock front, thereby exposing it for longer to the neutrino heating and thus enabling a stronger energy transfer. For stars more massive than $\sim 11\,M_\odot$ the addition of these large scale hydrodynamical instabilities seem to be a crucial for a neutrino driven explosion. And the combination of neutrino heating and hydrodynamics seems to give positive explosion results for stars of mass up to $\sim 15\,M_\odot$. For yet higher mass stars the effectiveness of this mechanism is still indetermined.

1.4.1.2 Magneto-rotational models

For a rotating star it has recently been proposed that a combination of rotation and magnetic effects may affect, and help, in the explosion phase of a ccSN [ODMA09]. Any initial rotation will be amplified during collapse and differential rotation will emerge. If the initial rotation is sufficiently fast it can help the explosion, since the rotational energy can be tapped (relatively more easily than the neutrino energy can be utilized) through viscosity of the stellar matter or through magnetic fields, and be transferred into thermal explosion energy. Furthermore magnetic fields can effectively transfer angular momentum, which may alter the structure and rotation of the PNS. A few conditions need to be fulfilled for the **magneto-rotational instability** to have a potential role in ccSNs: the initial rotation of the progenitor has to be fast ($P \sim 2$–$3\,\mathrm{s}$ [BDL+07]), the initial magnetic field has to be strong ($B \gtrsim 10^{12}\,G$), and, which is the case in most ccSN, the rotational profile has to have a negative radial gradient [ODMA09]. If these conditions are fulfilled, Obergaulinger et al. see a change in the collapse dynamics and bipolar outflows from the PNS, however the effect on the explosion is still not completely determined. The resulting neutron stars will have very large magnetic fields, $B \sim 10^{15}\,G$ and can rotate very rapidly ($P \sim 1\,\mathrm{ms}$).

1.4.1.3 g-mode excitations

An explosion mechanism that works on rather long time scales is the **g-mode oscillations** of the nascent neutron star. As accreted matter flows in and hits the PNS, core g-mode oscillations with large amplitudes are excited [BLD$^+$06, BLD$^+$07]. The "ringing" of the neutron star then set up acoustic (pressure) waves that travel outwards and steepens into shocks, thereby efficiently depositing their acoustic energy, and some of their momentum, in the outer core regions, eventually setting off the explosion of the supernova. Infalling matter will continuously pound the NS star, which in turn continues to produce acoustic power. The energy transformation from gravitational energy, to acoustic energy, to thermal shock energy can therefore continue until an explosion sets in, which can take up to a second or even longer.

In their simulations Burrows et al. see an advective-acoustic oscillation below the stagnated shock, but the oscillations saturate without generating enough power to instigate the explosion. Also the SASI is observed, but again with insufficient power to result in an explosion. The emitted acoustic power from the unstable gravity modes of the NS will however have an a-spherical angular distribution [BLD$^+$06], matching well with the observed anisotropic explosions.

1.5 Standing Accretion Shock Instability – SASI

When the shock front is halted, as explained in section 1.3.3, the continually infalling matter accretes onto the stationary shock front creating what is called a "standing accretion shock" (SAS) [BM06]. In the theory of the Standing Accretion Shock Instability (SASI)[6] an instability arises in the hot bubble below the shock. Between the gain radius and the shock front thermal convection will develop due to the negative entropy gradient in the area. How exactly the instability of the standing accretion shock gets generated and powered is a matter of some debate. Currently the favored models are the "purely acoustic cycle" [BMD, BM06] or the "advective-acoustic cycle" [FGSJ07, SJFK07], both mechanisms having their strong advocates. From a numerical simulation view point it is, however, difficult to make an exact discrimination between the two driving effects [Mar07].

1.5.1 Acoustic cycle

The "acoustic cycle" advocated by Blondin et al. [BMD, BM06] is based on pressure waves rising up from the surface of the neutron star. The pressure, or acoustic, waves will be generate from infalling matter hitting the surface of the neutron star and the rising acoustic waves will then perturb the shock front. Once the pressure wave has hit the shock front it will be reflected and move towards the other side of the cavity comprised by the area between the shock front and the PNS. On the other side the acoustic wave will perturb the shock front here and once more be reflected, see fig. 1.6. The result is a growing standing pressure wave.

As the shock front is perturbed outwards the ram pressure from the infalling material will be slightly smaller, this in turn means that the pressure just below the shock front will be smaller, but further in the post-shock pressure will be higher than it would have been for an unperturbed shock front. The increase in pressure deeper in then, in turn, leads to further

[6] Usually SASI is used as an abbreviation for Standing Accretion Shock Instability, but in the paper of Blondin & Mezzacappa [BM06] the abbreviation is for Spherical Accretion Shock Instability.

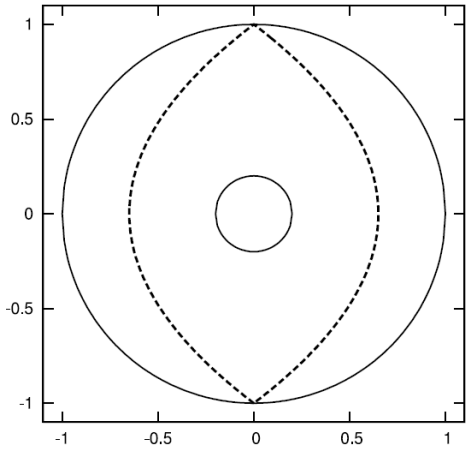

Figure 1.6: Example of round-trip path (dashed line) for an acoustic wave. The outer circle is the shock front, the inner circle the surface of the PNS [BM06].

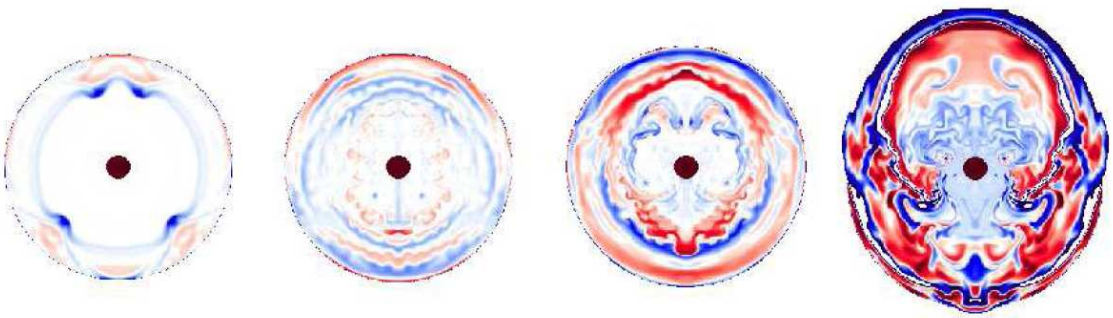

Figure 1.7: The instability of the spherical standing accretion shock shown through the changes in entropy (red is higher entropy, blue is lower entropy than the equilibrium value). A steady accretion would have constant entropy in the post-shock region [BMD].

pressure perturbations that presses the shock further out, creating a positive feedback cycle [BM06]. The perturbed shock front will cause the infalling matter to hit it at an oblique angle, which results in the shock deflecting the radially infalling matter, creating highly non radial flows behind the shock front. The final result of it all is a dipolar-like oscillation of the shock front, as shown in fig. 1.7, although power is also observed in the quadrupolar mode.

In Blondin & Mezzacappa [BM06] they conclude that the frequencies of the acoustic modes, i.e. the time scales it takes for pressure waves to traverse the post-shock cavity, corresponds well with the frequencies of the SASI modes. They furthermore point out that the advective-acoustic cycle work on too long timescales to be comparable to the SASI frequencies.

1.5.2 Advective-acoustic cycle

Turning now our attention to the "advective-acoustic cycle". T. Foglizzo [Fog08] finds the purely acoustic cycle advocate by Blondin et al. to be stable in his flow model, and instead he finds the instability mechanism to be amplified by the advective-acoustic cycle. The advective-acoustic cycle is based on an assumption that the pressure waves rising from the PNS surface perturbs the shock front (as in the acoustic model) but as a result vorticity perturbations are generated. These vorticity perturbations are, together with entropy fluctuations, then advected down below the gain radius to the region where infalling matter is decelerated and compressed, where they couple to the rising acoustic waves enhancing them and thereby establishing an amplifying feedback cycle [SJFK07, Fog08]. As with the purely acoustic model, once the shock front is perturbed the infalling matter hits the shock front at an oblique angle, and gets diverted from its radial path, giving transverse velocities that in this case enhance the vorticity perturbations. The longest timescale in this model is the advection timescale, and the combined time for advection plus acoustic travel is what is supposed to match the SASI frequencies. This correspondence is found in Scheck et al. [SJFK07], and they therefore dismiss the purely acoustic model as being responsible for the SASI.

In numerical models the SASI is usually initiated either by putting asymmetrical overdense rings (density enhanced by 20% [BMD]) in the infalling material or by randomly generated velocity or density fluctuations of the order $\sim 1\%$. [BMD, BM06, Mar07].

1.5.3 Parameterization with spherical harmonics

In order to better describe and parameterize the shock instabilities, not least get a better visualization of them, it is common to expand the shock radius $r_s(\theta, t)$ in terms of spherical harmonics $Y_{l,m}(\theta, \phi)$ [Mar07]

$$r_s(\theta, t) = \sum_{l=0}^{\infty} a_{l,0}(t) Y_{l,0}(\theta) \tag{1.7}$$

Here the dependence of the azimuthal angle ϕ in $Y_{l,m}(\theta, \phi)$ has been removed in the axially symmetric 2D models ($m = 0$). This parameterization leads to commonly talking of $\ell = 1$ or 2 modes in connection with the SASI, where the different modes corresponds to given motions of the shock front: The $\ell = 0$ mode is the average radius of the shock front, i.e. purely radial motions. It is in most cases found to be relatively stable between the time of shock stagnation and the explosion taking off. The dipolar $\ell = 1$ mode is the up-down "sloshing" mode, and the $\ell = 2$ mode is the quadrupolar "butterfly-like" mode. Another way of describing the $\ell = 2$ mode

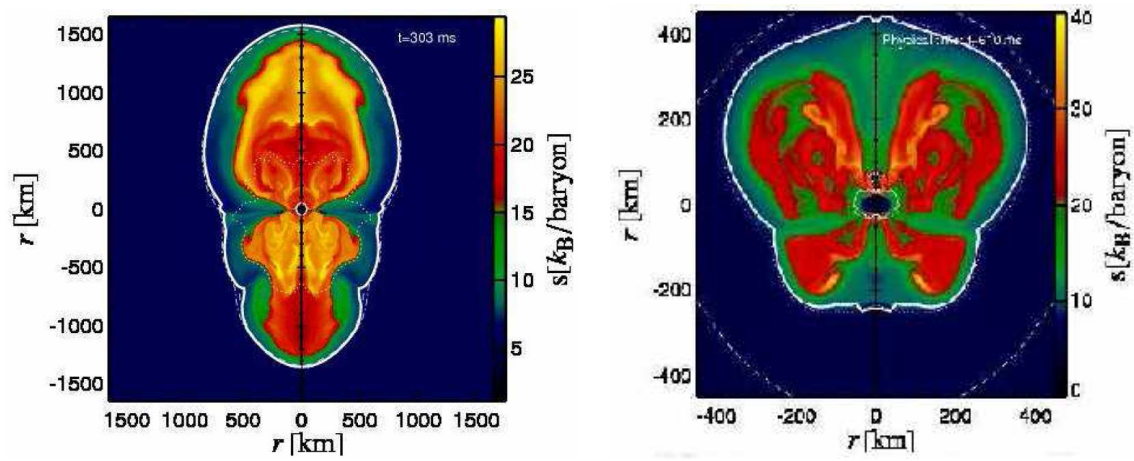

Figure 1.8: Examples of SASI modes, from [MJ09]. The fat solid white line represents the shock radius, and the dark circles at the center are the neutron stars. Colours represent entropy. *Left:* $\ell = 1$ dipolar "sloshing" mode (non rotating 11.2 $M_\odot$ model). *Right:* $\ell = 2$ quadrupolar "butterfly-like" mode (rotating 15 $M_\odot$ model).

is using the image of a pear; the shock changes between having the "bulky" end towards one polar direction and then inverting the shape having the "bulky" end in the opposite direction. These two last modes appear to grow into the non linear regime before the explosion. We show 2 representative snapshots of the dipolar $\ell = 1$ and the quadrupolar $\ell = 2$ oscillation modes in fig. 1.8. Apart from showing some of the SASI modes, fig. 1.8 also gives nice impressions of some of the general features that develop in full simulations, including neutrino heating, nuclear burning and convection. We see a clear feature being the accretion funnels along the equator, that leads the matter inwards before it is being forced outward again along the polar direction by the SASI.

Naturally the turbulent motions between the surface of the forming neutron star and the shock front will have a profound impact on the emission of neutrinos from the neutrino sphere located below the PNS surface. In the following section we will therefore look closer at the properties of the neutrino sphere and the emitted neutrino spectra.

1.6 Neutrino spheres

The neutrino sphere mentioned in previous sections should not be interpreted as *one* thin spherical shell. It is actually several different areas of the star - several neutrino spheres. Owing to the different interactions neutrinos participate in there will be different neutrino spheres corresponding to the different flavors. Additionally, each of the neutrino spheres will be extended because the interaction cross sections depend on the neutrino energy squared, c.f. section 1.3.2. For neutrinos of the same flavor those with low energy will consequently decouple before those of high energy, and the radius of their neutrino sphere will be smaller.

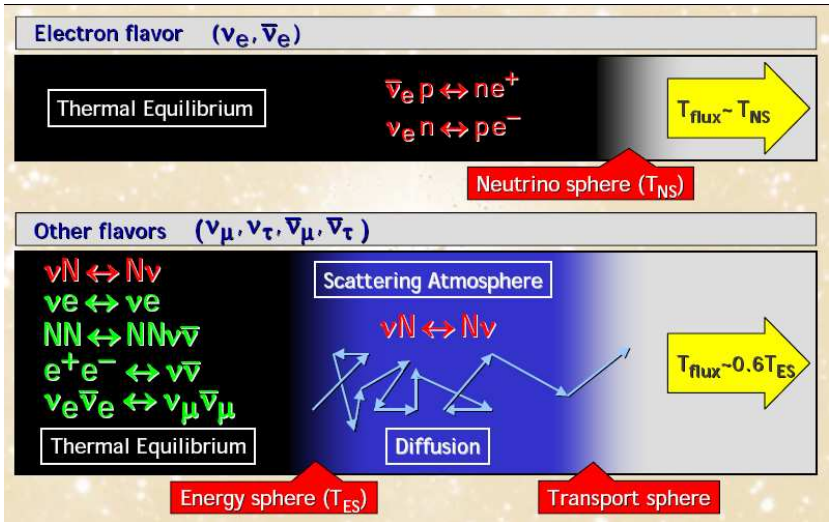

Figure 1.9: Definitions of the neutrino spheres with the relevant interactions: at the top the electron flavor and below the μ and τ flavors. The figure is from [Raf07].

1.6.1 Reactions

One defines the different neutrino spheres with basis in the interactions the different neutrino species participate in. All neutrino flavors have neutral-current (NC) interactions;

- nucleon bremsstrahlung: $N + N \leftrightarrow N + N + \nu + \bar{\nu}$
- pair-production: $e^- + e^+ \leftrightarrow \nu + \bar{\nu}$ or $\nu_e + \bar{\nu}_e \leftrightarrow \nu_\mu + \bar{\nu}_\mu$
- scattering: $\nu + e \leftrightarrow \nu + e$ or $\nu + N \leftrightarrow \nu + N$

In addition to the NC-processes ν_e and $\bar{\nu}_e$ also participate in the CC-processes given in eq. 1.5 and 1.6. Since CC-interactions are about 4 times stronger than NC-interactions, this means we only need to consider CC-processes for ν_e and $\bar{\nu}_e$ and can ignore their NC-processes. The CC-processes will keep ν_e and $\bar{\nu}_e$ in thermal equilibrium with the medium out to a larger radius than the NC-processes for the non-electron flavor neutrinos. Therefore it is sufficient to define one neutrino sphere for ν_e, and one for $\bar{\nu}_e$. These two will not coincide since in the beginning there are more neutrons than protons, and ν_e thus remain in equilibrium longer than $\bar{\nu}_e$. The CC-reactions for ν_τ and ν_μ, corresponding to eq. 1.5 and 1.6, does not take place because the corresponding leptons are heavier than e, and the neutrino energies available are too small ($E_\nu \simeq$ 10–30 MeV). Since non-electron flavor neutrinos only have NC-interactions and thus behave very similarly, we will in the remainder of this thesis let ν_x designate ν_μ, ν_τ, $\bar{\nu}_\mu$ and $\bar{\nu}_\tau$ jointly.

The processes of nucleon bremsstrahlung and pair-production changes the number of ν_x's and their energy distribution, which is why the decoupling radius of these processes are taken to define the "energy-sphere" of the ν_x's, see fig. 1.9. After these processes have decoupled the ν_x's are not free, however, to leave the supernovae yet. The neutrinos (and anti-neutrinos) still have a relatively large cross section for scattering on nucleons. Therefore, a transport

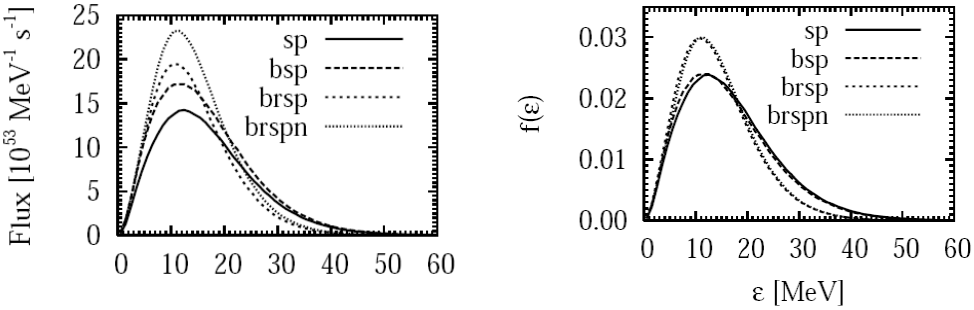

Figure 1.10: *Left:* Differential particle fluxes. *Right:* Normalized flux spectra of neutrinos. The figure is from [KRJ03].

sphere is defined (very similar to a scattering atmosphere for photons). The neutrinos diffuse through the transport sphere and are finally free to stream through the rest of the star. The diffusion through the transport sphere happens through scatterings which are often assumed to be iso-energetic, i.e. without energy transfer. The resulting energy spectrum for the ν_x's, once they start streaming from the transport sphere, will therefore resemble a thermal spectrum. However, due to the energy dependence of the different cross sections, the spectrum will be "pinched" compared to a normal thermal spectrum: there will be fewer neutrinos with high as well as low energy [KRJ03, Raf01].

1.7 Model Spectra

The modelling of neutrino energy spectra can be done using Monte Carlo simulations. The various reactions one chooses to include in the numerical models naturally change the resultant spectra. In their paper [KRJ03] M. Keil et al. show the results of a number of simulations where different interaction processes have been included alternately. In fig. 1.10 one can see four curves displaying the effect of different reactions. From the picture on the left we see that if one includes bremsstrahlung (b) and $\nu_e\bar{\nu}_e$-annihilation (n), as well as scattering on electrons (s) and e^+e^- annihilation (p), then the number of neutrinos increase as expected. If also nucleon recoil (r) is included, i.e. allowing energy transfer in the νN-scatterings, then the spectrum becomes even more pinched than the "original" spectrum. In the picture on the right where the curves have been normalized to the same particle flux this "pinching" effect is more pronounced. The spectra in fig. 1.10 are time integrated spectra where we see the number flux as a function of the neutrino energy. Another way to display the results of numerical calculations is a time dependent flux spectrum: here the energy of the neutrinos is plotted as a function of time.

1.7.1 Energy hierarchy

An example of a spectrum that is not time integrated is the result from the Livermore research group [TKDW98] in fig. 1.11. The lower part of the figure displays how the average energy of the different neutrino flavors develops during the explosion. We see that apparently there is an overall hierarchy of the energies: $\langle E_{\nu_e}\rangle < \langle E_{\bar{\nu}_e}\rangle < \langle E_{\nu_x}\rangle$, apart from the average energy

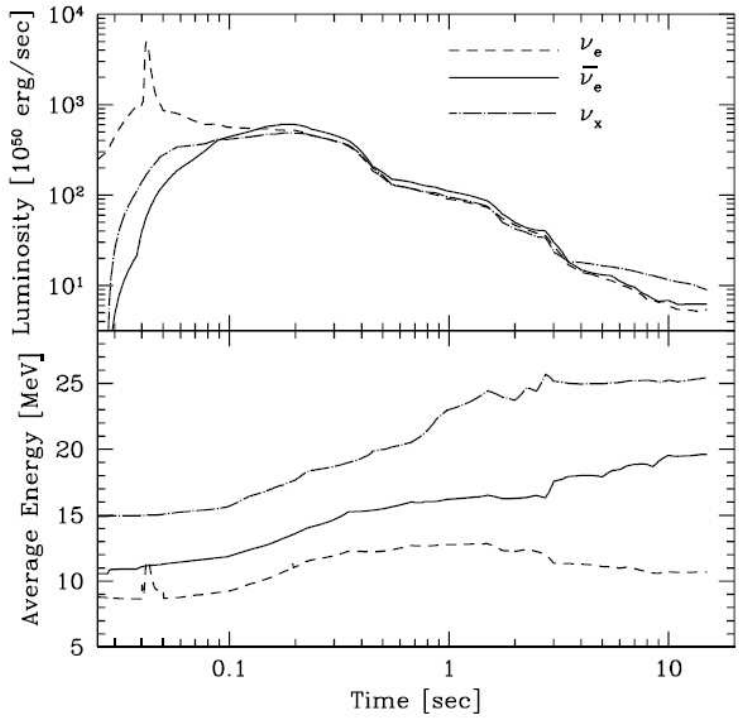

Figure 1.11: Time development of the luminosity and average energy of the neutrinos. The accretion phase lasts about 0,5 s while the cooling phase extends from 0,5 s to 10 s after the explosion. The neutrino burst is easily identified as the peak in ν_e. (In our terminology ν_x is ν_μ.) The figure is from [TKDW98].

of ν_e being relatively high during the neutrino burst. The energy hierarchy is a consistent characteristic in numerical models of the ν-spectra. Previously we have touched upon the reason for this hierarchy; namely that ν_x's only have NC-interactions that has lower cross sections than the CC-interactions. Hence these neutrinos decouple earlier, i.e. at smaller radii where the temperature is higher. The higher average energy of $\bar{\nu}_e$ compared to ν_e is due to the fact that in the beginning there are more neutrons than protons. The capture of $\bar{\nu}_e$ on p therefore decouples before the capture of ν_e on n. Naturally the average energies varies depending on the exact numerical model, but most of the simulations give energies in the following ranges ([FY03]):

$$\langle E_{\nu_e} \rangle \sim 10 - 15\,\text{MeV} \quad \langle E_{\bar{\nu}_e} \rangle \sim 12 - 18\,\text{MeV} \quad \langle E_{\nu_\mu} \rangle \sim 20 - 25\,\text{MeV}$$

In the upper part of fig. 1.11 we see the neutrino luminosity. As is apparent, the luminosity of the different flavors is roughly the same, although ν_e has an extra contribution from the neutrino break-out. The neutrino burst is roughly 25 ms after the explosion, and an energy of $E \sim 10^{51}\,\text{erg} = 1\,\text{Bethe}$ [B] is released. The total liberated gravitational energy in a ccSN is of the order of a few hundred Bethe ($E_{\text{grav}} \sim 3 \times 10^{53}\,\text{erg}$), and less than 1% percent of this goes into the kinetic energy of the rapidly out-flowing matter ($E_{\text{kin}} \sim 1\text{–}2 \times 10^{51}\,\text{erg}$ [WJ05]). The vast majority of the gravitational energy is released as neutrinos.

The optical emission, despite being less than one percent of the totally released energy, has a peak luminosity of $L \sim 3\text{–}5 \times 10^{51}$ erg/s (the luminosity of the Sun is $L_\odot = 3.8 \times 10^{33}$ erg/s). A supernova at its brightest will therefore quite often outshine its host galaxy.

1.8 Neutrino oscillations

One may think that once the neutrinos have been released from the neutrino sphere then we would observe them with the energy spectrum they have at the neutrino sphere. This is not the case. The reason is that neutrinos can undergo oscillations due to the fact that their mass and flavor eigenstates are different [DS00]. As they propagate through the outer layers of the star and if they pass through the Earth before we observe them these oscillations will be enhanced [DKR03b]. The physics involved in neutrino oscillations will be discussed in section 3.4.

"A computer will do what you tell it to do, but that may be much different from what you had in mind"

— Joseph Weizenbaum

2

Numerical simulations and the IceCube detector

Aspects of a star's life and death was given in the previous chapter. The theoretical consensus on supernova explosions was presented, and there was alluded to a very important tool used in our efforts to understand these violent star deaths; the numerical simulations. This chapter will summarize briefly the numerical supernova code we employed, and emphasize the importance of the choice of nuclear equation of state. Finally, IceCube, our detector of choice for observing the neutrino signals with imprints of the SASI, will be introduced.

2.1 Numerical simulations of supernova models

Several different approaches are used in the numerical simulations of SN explosions. In the early stages only 1-dimensional (1D) spherically symmetric models were available, but later 2-dimensional (2D) axisymmetric models have been added, and recently even 3-dimensional models have appeared. We mention a few representative codes and refer the interested reader to the corresponding papers and the references therein. An example of a 1D code is the Agile-Bolztran code employed by the Basel group [FWM$^+$09], for 2D codes we can mention the PROMETHEUS-VERTEX code used by the Garching group [MJM08] or the VULCAN/2D by Burrows and collaborators [BLD$^+$07], and for 3D codes CASTRO by Nordhaus, Burrows, Almgren and Bell can be mentioned [NBAB10], not to forget the CHIMERA code (1D, 2D and 3D) by Bruenn, Mezzacappa, Hix, Blondin and collaborators [BMH$^+$10]. They each have their strengths and weaknesses, but for the purpose of this thesis we will not go into a detailed description of the differences. The differences among other things pertain to the way inclusion of relativistic effects has been done, the grid lay-out, the inclusion of interactions, both for neutrinos but also for nuclei, the spectral resolution of neutrino energies, the choice of the nuclear equation of state and much more. We will for all practical purposes view the

underlying numerical simulation as a "black box" that provides us with information on the neutrino luminosities and energies, and how these depend on direction and time.

2.1.1 "Ray-by-ray plus" simulation as employed by the Garching group

For completeness, however, we include below the description of the numerical simulation providing the data for our analysis, as it was outlined in our paper Lund et al. [LML+10], and refer the interested reader to the paper by Buras et al. [BRJK06] or the PhD thesis by Andreas Marek, and references therein, for a more detailed explanation.

We use a numerical simulation to compare the expected signal fluctuations with the sensitivity of IceCube. The two-dimensional (axially symmetric) simulations which this discussion is based on were performed with the Prometheus-Vertex Code [RJ02, BRJK06] and the simulations were already discussed in detail in Ref. [MJM08]. We therefore repeat only a few essential aspects of both the numerical treatment and the simulation runs and refer to Refs. [MJM08, MJ09] for more complete information.

The hydrodynamic part of the code is based on a conservative and explicit Eulerian implementation of a Godunov-type scheme with higher-order spatial and temporal accuracy. It solves the non-relativistic conservation equations for the stellar fluid, whose self-gravity is described by an "effective relativistic potential" [MDJ+06]. It provides a sufficiently accurate approximation of general relativistic corrections [MJD10].

The neutrino transport solver, which is coupled to the hydrodynamics module via lepton number, energy and momentum source terms, is computed with a "ray-by-ray plus" scheme [BRJK06]. It accounts for the full neutrino-energy dependence in the transport but assumes the neutrino flux at every point to be radial (i.e. the neutrino phase space distribution function is assumed to be axially symmetric around the radial direction), which is numerically less demanding and more efficient than a full multi-dimensional version of the transport.

The simulations used here are based on the progenitor model s15s7b2 from Woosley and Weaver [WW95], and is representative for the collapse of stars with progenitor masses around $15\,M_\odot$. The dense proto-neutron star matter is described by the equation of state (EoS) of Lattimer and Swesty [LS91], which leads to a radius of 12 km for a cold neutron star with a gravitational mass of $1.4\,M_\odot$. We also consider briefly an example with the EoS of Hillebrandt and Wolff that is considerably stiffer [HW85]. Unless otherwise noted, our discussion always refers to the Lattimer and Swesty case as a benchmark.

The two-dimensional model was computed under the assumption of axial symmetry and covers the region between north and south pole with 192 equally spaced angular grid points. The model was evolved in total for about 600 ms from the onset of the collapse to a time of about 450 ms after the formation of the SN shock front and shows in the post-bounce evolution a strong SASI sloshing activity of the SN shock front.

The oscillations of the SN shock front due to SASI activity and convective overturn cause luminosity fluctuations by modulating the mass accretion on the proto-neutron star: a strong shock retraction leads to a transient increase of the gas flow towards the neutron star and to the compression and enhanced cooling of the matter (i.e. enhanced neutrino emission) near the neutron star surface [MJM08]. On the other hand, a shock expansion has the opposite effect because it causes a deceleration of the infall or even outward acceleration of material that is accreted through the shock front. Thus shock expansion stretches the time this matter

stays in the gain layer and less cooling by neutrino emission occurs.

From the 192 angular rays of the models, we used in the post processing the luminosity for all species ν_e, $\bar{\nu}_e$ and ν_x and the corresponding $\langle E \rangle_{\rm rms}$ on every second angular bin and extracted the information in steps of about 0.5 ms that were subsequently resampled in exact 1 ms steps.

2.2 Equations of State

From the above account of physics entering the numerical simulation we see that at least one very important issue is the choice of an appropriate nuclear equation of state.

An equation of state (EoS) relates the density (ρ), temperature (T) (or entropy S) and composition (here one usually uses the electron fraction, Y_e (number of electrons or protons per baryon)) inside the star to the pressure of the plasma, and the free energy of the system.[1] To make realistic numerical simulations of the processes going on during the collapse and explosion of a supernova, we therefore need realistic equations of state for the nuclear matter in the star. These EoSs should cover the wide density and temperature ranges, as well as the changing electron fractions present during the course of collapse and explosion. There is no single EoS available that cover the entire range of densities from the supra-nuclear densities ($\rho > 2.7 \times 10^{14}$g/cm^3) inside the stellar core and down to the low densities (a few 100 g/cm^3) in the outer parts of the stellar envelope. Therefore the density range is usually split in two: a "high" and a "low" region, with corresponding EoSs.

In the low density region, the EoS employed by A. Marek [Mar07] assumes thermodynamical equilibrium of electrons, positrons, photons, free protons and neutrons, alpha-particles and 14 species of heavier nuclei. The leptons are described as Fermi gasses with arbitrary degeneracy and an arbitrary degree of relativity, and the baryonic parts are described as classical non-relativistic Boltzmann gasses, and Coulomb lattice effects are included. For temperatures above 0.5 MeV ($T = 5.8 \times 10^5$ K) it is assumed that particles are in nuclear statistical equilibrium (NSE), i.e. that strong and electromagnetic interactions have equilibrated, while nuclear burning is taken into consideration for temperatures below.

In the high density region the EoSs most commonly employed are the Lattimer & Swesty EoS (from now on LS EoS) [LS91], the Shen et al EoS (Shen EoS) [STOS98], and the EoS of Hillebrandt & Wolff (HW EoS) [HW85]. We give a brief summary below of these 3 EoS, and their specializations as employed by Marek et al. Common features for all 3 high density EoSs are (cf. [Mar07]): they all assume matter to be homogeneous above nuclear densities (i.e. no phase transition or hadronic degrees of freedom (kaons, pions and so on)), and that the baryons are floating in a gas of positrons and electrons, that are in equilibrium with photons via pair creation processes. They all assume NSE, and for the inhomogeneous baryonic matter they include free protons, free neutrons, alpha-particles but only one representative heavier nuclei. In the homogeneous part, only the nucleons are included.

2.2.1 Lattimer & Swesty EoS

The EoS of Lattimer & Swesty (LS) [LS91] is more or less the "standard" EoS employed in supernova modelling. It is based on a compressible liquid drop model of nuclei, and a

[1] The archetypical case of an EoS is the ideal gas law: pV = NkT.

Skyrme- force between the nucleons is assumed. Leptons are treated as ideal Fermi gasses, and photons as an ideal Bose gas, and everything is done in a non-relativistic framework. The incompressibility modulus of the bulk nuclear matter and the symmetry energy, that enters into the equation for the free energy per baryon of the bulk nuclear matter, is assumed to be 180 MeV and 29.3 MeV respectively by Marek et al. [Mar07, MJM08]. The transition from the low density EoS described above and to the higher density EoS when using the LS EoS happens at $\rho = 6 \times 10^7$ g/cm^3 during the collapse phase, but during the post bounce phase the LS EoS was only applied above $\rho = 10^{11}$ g/cm^3 for technical reasons [Mar07].

To put the effect of the LS EoS in more tangible terms, the numerical simulation of a 15 $M_\odot$ progenitor with the LS EoS results in a neutron star with a radius of roughly 12 km, and with a mass of 1.4 $M_\odot$ [MJM08]. Although the LS EoS has been the "standard" model in simulations, it is nolonger compatible with observed neutron star masses. The observed masses are higher than what can be obtained with the LS EoS.

2.2.2 Hillebrandt & Wolff EoS

Like the LS EoS, the HW EoS [HW85] employs a Skyrme-force for nucleon interactions, but it is calculated with a full Hartree-Fock approach. The transition from the low density EoS described above and to the higher density EoS when using the HW EoS happens at $\rho = 1.5\times10^9$ g/cm^3 [Mar07], and the values of the incompressibility modulus is 263MeV and the symmetry energy is 32.9 MeV [MJM08].

The neutron star resulting from a simulation which employs the HW EoS will have a slightly larger radius than the one produced with the LS EoS, namely 14 km [MJM08], due to the larger incompressibility modulus, but the same mass.

2.2.3 EoS of Shen, Toki, Oyamatsu and Sumiyoshi

The EoS of Shen et al. (Shen) [STOS98] uses a relativistic mean field theory instead of the Hartree-Fock method, and employs full Fermi-Thomas calculations for the inhomogeneous parts of the nuclear matter. The incompressibility modulus is 281 MeV, the symmetry energy 36.9 MeV [MJM08], and the transition from the low density EoS described above and to higher density EoS happens at $\rho = 3 \times 10^8$ g/cm^3 [Mar07] for the Shen EoS. The Shen EoS is stiffer than the LS EoS, but softer than the HW EoS.

2.2.4 Impact of EoS in simulations

A few general comments can be made on the impact of the choice of EoS on 2D simulations. The impact of an EoS reflects itself in many ways, the compactness of the PNS being one example, as a softer EoS leads to a more compact core. This in turn directly impacts also the position of the shock front, and the energies and luminosities of neutrinos. A softer EoS will result in higher neutrino luminosities and energies because a more compact core will allow for more gravitational binding energy to be turned into neutrino emission. This means that we will have a stronger cooling due to neutrinos, but also that we have the opportunity for a stronger neutrino heating in the gain layer. The neutrino heating for the LS EoS can therefore be 50% larger than for the HW EoS [Mar07]. The choice of EoS can also lead to completely different growth rates of convective instabilities inside the PNS, which again will influence the neutrino emission. We therefore see that the effect the EoS has on the development of the

supernova explosion will to a degree be reflected in the observable neutrino quantities, thus giving us a unique opportunity to learn about the obscured inner parts of a supernova through neutrino observations.

2.3 IceCube hard facts

The theoretical and numerical work done on supernovae and the involved neutrino physics is overwhelming, but it is hampered by one major fact: the lack of observational evidence. Part of the work in this thesis is an effort to illustrate a feasible way for us to actually test these numerical models by "looking" inside the supernova through the use of neutrinos.

To do this, we propose to use the neutrino Cherenkov telescope IceCube. It has been completed this Arctic summer (December 18th 2010) at the South Pole, and will have the largest event rate for a galactic SN among detectors currently in operation (or soon to be operational). Therefore it will be the best suited candidate to detect the fast time variations of the neutrino signal induced by the Standing Accretion Shock Instability.

2.3.1 Aims and appearance

The IceCube telescope is designed to observe point sources of high energy neutrinos such as active galactic nuclei and gamma ray bursts. Correspondingly the energy of target neutrinos would usually be in the energy range 1 TeV to 1 PeV (10^{12-15} eV), although the recent addition of the DeepCore array would allow optimal detection down to 10 GeV (10^9 eV), increasing the observational investigation of atmospheric neutrinos. The study of these phenomena will be done using 4800 digital optical modules (DOM) (main detector), which effectively instruments a kilometer cubed of the clear and almost dust free south polar ice. The DOMs are distributed in a hexagonal pattern with a spacing of 125 m between individual strings, and 17 m between each DOM on the strings. The uppermost DOMs are positioned 1450 m below the surface and the lower layer reached down to a depth of 2450 m to utilize the most optimal volumes of the ice, see the left figure of fig. 2.1. The sub-array DeepCore adds another 360 DOMs in the lower central part of IceCube. We will not take these additional DOMs into account in our calculation as DeepCore was a fairly recent addition and the efficiencies of the photo-multipliers used here are different from the ones used in the surrounding main IceCube detector. Our calculations are only a feasibility study, so although including the DeepCore array could be beneficial, we do not find it crucial for our results.

2.3.2 Cherenkov Telescope

The IceCube detector is a Cherenkov telescope meaning that it has been constructed to observe the blue Cherenkov light emitted from positrons being produced by the inverse beta reaction when anti-electron neutrinos interact with free protons in the ice

$$\bar{\nu}_e + p \rightarrow n + e^+ \tag{2.1}$$

The emission of Cherenkov light occurs when a particle moves faster than light-speed in the medium. The rapidly moving particle, in this case the positron, emits photons and subsequently slows down. As the positron moves, a cone of blue light will thus follow at its tail, see the right figure of fig. 2.1.

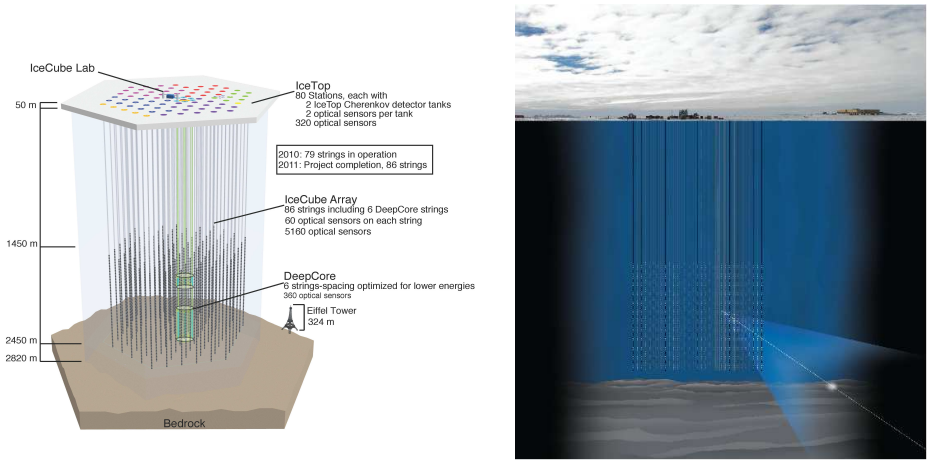

Figure 2.1: *Left:* Schematic layout of IceCube. *Right:* Illustration of a high-energy neutrino event in IceCube (light burst in lower right corner) with the subsequent cone-emission of blue Cherenkov light. Figures are from [Col].

To calculate the anti-electron neutrino interaction rate in IceCube, we will use the low-energy approximation (zeroth order in $1/M_{\text{nucleon}}$, [VB, DKR03a]) for the total interaction cross section for the inverse beta decay

$$\sigma = 9.52 \times 10^{-44}\,\text{cm}^2 \left(\frac{E_{\bar{\nu}_e}}{\text{MeV}}\right)^2 \tag{2.2}$$

The simple dependence on $\text{E}^2_{\bar{\nu}_e}$ arises from neglecting the difference between the proton and neutron mass (i.e. setting $E_{\bar{\nu}_e} = E_{e^+}$), as well as neglecting the mass of the electron (and setting $p_{e^+} = E_{e^+}$) [VB], and ignoring weak magnetism and nucleon recoil effects [DKR03a].

As mentioned in the previous section, IceCube is intended for neutrinos with energies between 1 TeV to 1 PeV, and the spacing of DOMs is correspondingly large. In contrast to these high energies, typical SN $\bar{\nu}_e$ energies range from 15-25 MeV depending on the simulation. Therefore the interaction rate will be smaller due to the energy dependence of the interaction cross section. Additionally, the resulting positron will be less energetic and its Cherenkov cone therefore less luminous. Furthermore the emission time of the cone will be much shorter as the positron slows down more quickly. The result of the shorter emission time and lower luminosity is that only one photon will be registered in a single DOM from a given neutrino. Thus each photon detection can be directly correlated with the arrival of a neutrino (or a background). We will therefore use the term an "event" for a photon detection to indicate the interaction, and detection, of *one* neutrino.

The fact that only one DOM gets hit, and only by one photon means that we cannot reconstruct the track of the incoming neutrino with IceCube. Consequently we can not reconstruct the energy or the direction of the incoming neutrino, as would have been the case for a dedicated low energy water Cherenkov detector. On the other hand IceCube will not saturate from the immense burst of neutrinos, which would be the case with e.g. the water Cherenkov detector Super-Kamiokande. Over the 10 second duration of a supernova, IceCube is expected to register of the order 10^6 events, all collected in 1.6384 ms time bins. This is

a factor of 100 more than would be expected in Super-Kamiokande (fiducial volume 22.5 kt). So despite Super-Kamiokande being essentially background free, IceCube would be superior due to its larger event rate, albeit lacking energy resolution. The event rate in IceCube would be comparable the event rate expected from future Megaton Water Cherenkov detectors. A megaton water Cherenkov detector would also provide detailed energy information on each event, and as such be far superior to IceCube, more so since we will show later that fluctuations in the energy will not be insignificant (see section 10.9). In this thesis we will not discuss the additional benefits expected from a future megaton water Cherenkov detector.

2.3.3 IceCube background noise

Using a schematic model of the IceCube detector and the latest efficiencies [DKR03a, KGftIC09, HR09], we estimate from eq. 9.1 up to ∼1000 events per ms in IceCube during a burst of supernova neutrinos for a SN at a fiducial distance of 10 kpc. As the time it takes a neutrino to transverse the entire IceCube (1 km) will be a few microseconds, the effect of the supernova neutrino's passing will be registered simultaneously all over IceCube. In other words, the background noise will correlatedly rise above the usual level. The height of the rise varies depending on the input model for the supernova (see chapters 10 and 11).

The amount of events expected due to a supernova is comparable to the intrinsic background noise in IceCube, which is roughly

$$\Gamma_{\text{bckgr noise}} = 1340\,\text{ms}^{-1} \tag{2.3}$$

This background is the dark current for each DOM 280 s^{-1} times the total number of 4800 DOMs in the main detector. Here the dark current is mainly due to light from decays of ^{40}K and radioactive decay chains in the glass of the DOMs [KGftIC09].

"I have done a terrible thing. I have postulated a particle that cannot be detected."

— W. Pauli, after his postulation of the existence of the neutrino

3 Neutrino physics

The previous chapters provided the necessary background of a star's evolution through to collapse and explosion. They further demonstrated the vital interplay between the neutrino emission and the star's demise.

To proceed, we need to turn our attention more exclusively on the neutral little rascal, and see how the neutrino is described from a particle physics viewpoint. This chapter will briefly cover some of the fundamental particle physics aspects of the neutrinos. These aspects are useful for the understanding of the neutrino interactions.

3.1 Mixing matrix

The electrically neutral neutrino comes in three different flavors corresponding to the three charged leptons; electron ν_e, muon ν_μ and tau ν_τ. These flavor eigenstates are the ones which participate in the weak interactions in the Particle Physics Standard Model (PPSM). However, for neutrinos flavor eigenstates are not identical to mass eigenstates, as opposed to many other particles. The three neutrino flavor eigenstates, ν_e, ν_μ, and ν_τ, each consists of a unique mixture of the three mass eigenstates; ν_1, ν_2, and ν_3. The mass eigenstates are the eigenstates of the free Hamiltonian in vacuum. Greek indices will denote flavor states, and roman letters mass eigenstates.

The way we display the mixing between the mass and the flavor states is with a mixing matrix $\mathcal{U}$

$$\vec{\nu}_{weak} = \mathcal{U}\ \vec{\nu}_{mass} \quad \text{, or equivalently}$$

$$\begin{pmatrix} \nu_e \\ \nu_\mu \\ \nu_\tau \end{pmatrix} = \begin{pmatrix} \mathcal{U}_{1,e} & \mathcal{U}_{2,e} & \mathcal{U}_{3,e} \\ \mathcal{U}_{1,\mu} & \mathcal{U}_{2,\mu} & \mathcal{U}_{3,\mu} \\ \mathcal{U}_{1,\tau} & \mathcal{U}_{2,\tau} & \mathcal{U}_{3,\tau} \end{pmatrix} \begin{pmatrix} \nu_1 \\ \nu_2 \\ \nu_3 \end{pmatrix}$$

This mixing matrix can be split into a product of three matrices, each one containing only one of the mixing angles, θ_{ij}, describing the degree of mixing between certain states:

$$\mathcal{U} = \begin{pmatrix} c_{12} & s_{12} & 0 \\ -s_{12} & c_{12} & 0 \\ 0 & 0 & 1 \end{pmatrix} \begin{pmatrix} 1 & 0 & 0 \\ 0 & c_{23} & s_{23} \\ 0 & -s_{23} & c_{23} \end{pmatrix} \begin{pmatrix} c_{13} & 0 & s_{13}e^{-i\delta} \\ 0 & 1 & 0 \\ -s_{13}e^{i\delta} & 0 & c_{13} \end{pmatrix} \quad , \tag{3.1}$$

$$c_{ij} = \cos\theta_{ij} \quad , \quad s_{ij} = \sin\theta_{ij} \quad \text{and} \quad 0 \leq \theta_{ij} \leq \pi/2$$

The mixing angles θ_{12} and θ_{23} are well determined from observations of neutrino oscillations in the atmosphere and neutrinos from the sun. The mixing angle θ_{13} is on the other hand still unknown. Table 3.1 lists the currently favored values of the mixing angles. The CP (charge and parity) violating phase δ is not relevant for our further purposes.

3.2 Mass hierarchies

Another unknown set of parameters is the absolute masses of the neutrinos. We know from oscillation experiments that neutrinos have non-zero mass, but not the exact value. However, from cosmology the limit on the overall neutrino mass scale is 0.2 eV [HMRW10]. Each of the mass eigenstates ν_i has a corresponding definite mass m_i. We know the difference of m_1^2 and m_2^2, which we call $\Delta m^2_\odot$, from solar and Kamland data, and we know the absolute value of the difference between m_2^2 and m_3^2, Δm^2_{atm}, from atmospheric, Minos and K2K data [eaPDG08]. The best values for the mass splittings are given in table 3.1.

$$\Delta m^2_{32} \equiv m_3^2 - m_2^2 = \Delta m^2_{\text{atm}} \tag{3.2}$$

$$\Delta m^2_{21} \equiv m_2^2 - m_1^2 = \Delta m^2_\odot \tag{3.3}$$

$$|\Delta m^2_{32}| \approx |\Delta m^2_{31}| \gg |\Delta m^2_{21}| \tag{3.4}$$

From experiments with tritium decays we know that [Kin07]

$$m_{\nu_e} \equiv \sqrt{\sum_i |\mathcal{U}_{i,e}|^2 m_i^2} < 2.2\ eV\ ,$$

and even though the experimental limits on ν_μ and ν_τ are not quite as strong it is presumed that also these two should be below 2.5 eV. Furthermore, taking the lightest neutrino mass to be zero leads, with the known mass splittings, to at least one neutrino with a mass of $\approx 0.04\,\text{eV}$ (section 5.3 in [FY03]).

Because we only know the absolute value of Δm^2_{atm}, we have two possible hierarchies for our masses; the normal and the inverted hierarchy. In the normal hierarchy ν_3 is the heaviest, while in the inverted hierarchy ν_3 is the lightest and ν_2 is the heaviest state.

Table 3.1: The best values as of January 2010, from [eaPDG10].

Parameter	best value	uncertainty
$\Delta m^2_{\odot}$ $[10^{-5}\ eV^2]$	7.59	$\pm$ 0.2
$\lvert\Delta m^2_{\rm atm}\rvert$ $[10^{-3}\ eV^2]$	2.43	$\pm$ 0.13
$\sin^2 2\Theta_{12}$	0.87	$\pm$0.03
$\sin^2 2\Theta_{23}$	$>$0.92	
$\sin^2 2\Theta_{13}$	$<$0.15	90% CL

3.3 Making masses

The neutrino mass could be proposed to come about in the same way as leptons acquire mass in the PPSM: give them a Yukawa coupling to the all-pervading Higgs field Φ. When the $\mathrm{SU}(2)_L\otimes\mathrm{U}(1)_Y$ symmetry is spontaneously broken, the Higgs field acquires a vacuum expectation value, vev, and thus gives mass to e.g. the electron [KP93]. However, this requires the lepton to have a right-handed partner, which is a singlet under $\mathrm{SU}(2)_\mathrm{L}\otimes\mathrm{U}(1)_Y$, providing terms which are invariant under $\mathrm{SU}(2)_\mathrm{L}\otimes\mathrm{U}(1)_Y$ e.g.;

$$\mathcal{L}_{Yuk,e} = -G_e\bar{e}_L\Phi e_R + \mathrm{h.c.} \tag{3.5}$$

Here G_e is a coupling constant, and $\bar{e}_L$ and e_R are lepton fields. In the PPSM there is no right-handed neutrino and so the neutrino is massless. However, we know from experiments that $m_\nu \neq 0$. So far in experiments no right-handed neutrino has been needed to explain data, and generally it is enough to presume the existence of a left-handed neutrino and a right-handed anti-neutrino. Thus, to use the above Dirac mechanism for mass generation, we would need to postulate two new fields, two new particles; the right-handed neutrino and the left-handed anti-neutrino. We could then make a Dirac mass term with a coupling constant to be determined by experiment to suit the observed smallness of the neutrino mass;

$$\mathcal{L}_{Yuk,\nu} = -G_\nu\bar{\nu}_L\Phi^c\nu_R + \mathrm{h.c.} \tag{3.6}$$

Another way to give neutrinos mass would be to assume neutrinos to be Majorana particles. Then the neutrino would be its own antiparticle[1] and we would not need to postulate new neutrino fields. The right-handed partner of the neutrino would simply be the "anti"-neutrino. If the neutrino is a Majorana particle, the mixing matrix $\mathcal{U}$ in section 3.1 would have to be multiplied by a matrix containing the Majoron phases [Kin07, eaPDG08];

$$\mathcal{U}_{Maj} = \mathrm{diag}[\exp(i\alpha_1/2), \exp(i\alpha_2/2), 1].$$

Let us take a closer look at a way of generating the small neutrino masses.

3.3.1 Seesaw mechanism

For simplicity let us start by looking at only one generation of neutrinos. When we introduce the extra fields of a right-handed neutrino and a left-handed anti-neutrino, the following two

[1] This is only allowed since the neutrino carries no electromagnetic charge.

Majorana and one Dirac mass terms are in principle available;[2]

$$\mathcal{L} = -m_D \overline{\nu_L} \nu_R + \text{h.c.} \qquad \text{Dirac} \tag{3.7}$$

$$\mathcal{L} = -\frac{1}{2} m_{LL} \overline{\nu_L} \nu_L^c + \text{h.c.} \qquad \text{Majorana “left”} \tag{3.8}$$

$$\mathcal{L} = -\frac{1}{2} M_{RR} \overline{\nu_R} \nu_R^c + \text{h.c.} \qquad \text{Majorana “right”} \tag{3.9}$$

The superscript c denotes the combined operation of a charge conjugation C (changing a particle to its antiparticle or vice versa) and a parity transformation P (inverting the spatial coordinate system, i.e. effectively changing the spin direction of the particle). Thus a left-handed neutrino will turn into a right-handed “anti”-neutrino.

The Dirac term is effectively the interaction of a right- and left-handed neutrino, and thus conserves lepton number. The Majorana terms on the other hand couples a left-handed neutrino ν_L with its right-handed “anti”-neutrino ν_L^c (Majorana “left”), or a right-handed neutrino ν_R with its CP conjugate, the left-handed “anti”-neutrino ν_R^c (Majorana “right”) thus violating lepton number by two units in either interaction. So besides extending the PPSM model with a right-handed neutrino and a left-handed anti-neutrino, we would also need to introduce an extra Higgs field since the ordinary PPSM doublet cannot change a left-handed neutrino into a right-handed anti-neutrino.

The left-handed neutrino ν_L interacts with the W and Z bosons through the weak interaction, so if it had a large mass resulting from the Majorana “left” interaction it would have been observed. The mass m_{LL} must therefore necessarily be small. The right-handed neutrino is a singlet under SU(2)⊗U(1) and therefore does not interact through the weak interaction, which leaves the opportunity of a very large mass M_{RR}.

Now define

$$\nu \equiv \begin{pmatrix} \nu_L^c \\ \nu_R \end{pmatrix} \qquad \bar{\nu} \equiv \begin{pmatrix} \overline{\nu_L} & \overline{\nu_R^c} \end{pmatrix} \tag{3.10}$$

Then we can rewrite the combined mass terms as

$$\mathcal{L} = -\frac{1}{2} \overline{\nu^c} \mathcal{M} \nu + \text{h.c.} \tag{3.11}$$

where

$$\mathcal{M} = \begin{pmatrix} m_{LL} & m_D \\ m_D & M_{RR} \end{pmatrix} \tag{3.12}$$

Now assume the mass m_{LL} to be very small, and for simplicity take it to be zero, and the mass M_{RR} to be much larger than m_D (and the electroweak scale at 250 GeV). Then we can write the mass matrix $\mathcal{M}_0$ as follows and find the eigenvalues of it:

$$\mathcal{M}_0 = \begin{pmatrix} 0 & m_D \\ m_D^T & M_{RR} \end{pmatrix} \tag{3.13}$$

$$\begin{aligned} m_{1,2} &= \frac{1}{2}\left(M_{RR} \pm \sqrt{M_{RR}^2 + 4m_D^2} \right) \rightarrow \\ m_1 &\simeq M_{RR} \quad \text{and} \quad m_2 \simeq -\frac{m_D^2}{M_{RR}} \end{aligned} \tag{3.14}$$

[2]This section is based on [Kin07, KP93].

The eigenstates of the diagonal matrix, consisting of the eigenvalues of $\mathcal{M}_0$, will be the actual physical neutrinos.[3] We see that one of the physical neutrinos will be very heavy (m_1) and the other very light (m_2). We also note that for a fixed m_D, m_1 and m_2 are inversely proportional. This is why it is called the seesaw mechanism. The low mass neutrino is usually interpreted as the "normal" SM neutrino.

In nature we know there is at least three families of neutrinos and the entries in eq. 3.13 will then each be 3x3 matrices thus giving a 6x6 matrix in total. In general, both mass terms will be complex valued, and the Majorana mass matrix must furthermore be symmetric.

3.4 Neutrino oscillations

The fact that neutrinos acquire mass in the modified standard model of particle physics have a serious implication for our discussion of supernova neutrinos. Since neutrinos are massive they can oscillate between the three flavor states. This was already alluded to in the introduction to this thesis, and an extremely simplified way of understanding them will be provided below. We refer the interested reader to [FY03, Raf96, DS00, FLMM07] and references therein for the full detailed understanding.

3.4.1 Vacuum effect

In 1957 B. Pontecorvo proposed the vacuum oscillations. This type of oscillation was later confirmed by the measurements of neutrinos from the Sun in the Homestake mine in the late 1960s. These **vacuum oscillations** are caused by the slightly different propagation speeds of the mass states comprising the neutrinos as they move through space. As the mass states move, they change phase relative to one another and with a changed mass content the flavor state will no longer be the same.

We write the evolution of the neutrino mass eigenstates ν_i with the use of plane waves

$$\nu_i(t) = e^{-i(E_i\, t - \vec{p_i}\vec{x})}\, \nu_i(0) \tag{3.15}$$

and assume that the neutrinos are ultra-relativistic, so that $|\vec{p_i}| \gg m_i$ and $E_i = p_i$. We then let E denote the neutrino energy and use natural units with $c = 1$, such that the time t equals the distance travelled L and the above equation reduces to

$$\nu_i(L) = e^{-i m_i^2 L/2E}\, \nu_i(0) \tag{3.16}$$

Then we can write the evolution equation for a given neutrino flavor state ν_α as:

$$i\frac{\mathrm{d}}{\mathrm{dt}}\nu_\alpha(t) \simeq H_{vac}\, \nu_\alpha \tag{3.17}$$

where we identify the effective Hamiltonian in vacuum with

$$H_{vac} = \frac{M^2}{2E} \tag{3.18}$$

[3] The negative eigenvalue m_2 is not a problem as we can always redefine the corresponding neutrino eigenstate to absorb the minus.

The matrix M^2 is given by

$$M^2 = \mathcal{U} m^2_{diagonal} \mathcal{U}^\dagger \tag{3.19}$$

where $\mathcal{U}$ is given in eq. 3.1, and

$$m^2_{diagonal} = \begin{pmatrix} m_1^2 & 0 & 0 \\ 0 & m_2^2 & 0 \\ 0 & 0 & m_3^2 \end{pmatrix}$$

Now with the evolution equation given above, the probability that one observes a neutrino as one flavor ν_β that was originally another flavor ν_α is

$$P_{\nu_\alpha \to \nu_\beta} = \nu_\beta^\dagger \nu_\alpha = \left| \sum_i \mathcal{U}^*_{\alpha\, i} \mathcal{U}_{\beta\, i}\, e^{-i m_i^2 L/2E} \right|^2 \tag{3.20}$$

If we restrict ourselves to consider only two-flavor mixing, which is a good approximation since the 3 flavor mixing can be parameterized as two 2 flavor mixings since θ_{13} is small and $\Delta m^2_{12} \ll \Delta m^2_{13}$, then the probabilities for observing a ν_e as a ν_e, respectively as a ν_μ, are [FY03, p.328]

$$P_{\nu_e \to \nu_e} = 1 - \sin^2(2\theta)\, \sin^2\left(\frac{\Delta m^2_{21}}{4E} t\right) \tag{3.21}$$

$$P_{\nu_e \to \nu_\mu} = \sin^2(2\theta)\, \sin^2\left(\frac{\Delta m^2_{21}}{4E} t\right) \tag{3.22}$$

We thus clearly see that as time passes by (i.e. as the neutrino travels along) the probability of a flavor change will oscillate.

3.4.2 Matter effect

Since the proposal of the vacuum oscillation saw the light of day further two types of neutrino oscillations have been discovered. First in line was the **matter induced oscillations** proposed in 1985 by Mikheyev and Smirnov, and separately by Wolfenstein in 1978[4]. The latest type of oscillations, the collective flavor oscillations, is the topic of section 3.4.3. The matter induced oscillations are based on the fact that when neutrinos propagate through matter, the background of (positrons) electrons provide an extra charged current contribution to the diagonal part of the potential for the (anti) electron flavor neutrinos

$$V = \sqrt{2} \mathrm{G_F} n_e \begin{pmatrix} 1 & 0 & 0 \\ 0 & 0 & 0 \\ 0 & 0 & 0 \end{pmatrix}$$

Here the electron density is denoted with n_e and defined as $n_e \equiv n_{e^-} - n_{e^+}$, and $\mathrm{G_F}$ is the Fermi constant. The resulting Hamiltonian in the evolution equation 3.17 thus changes to

$$H_{matter} = H_{vac} + V \qquad , \tag{3.23}$$

and the probabilities for a given neutrino flavor to survive changes as well.

[4] Apart from matter effect this oscillation effect is also known as the MSW-effect.

3.4.2.1 Matter effect in supernovae

When neutrinos pass through very dense matter, such as the supernova environment, the matter effect have resonance points, where the oscillation probability gets enhanced. These resonance points are denoted with H and L and correspond to the mass differences Δm^2_{atm} and $\Delta m^2_{\odot}$ respectively. The resonances take place at densities $\rho_L = 10 - 30 g/cm^3$ and $\rho_H \sim 10^3 - 10^4 g/cm^3$ in the stellar envelope [DS00]. This means that the flavor change will not affect the energy deposition in the hot bubble layer, but that we should take care when we interpret the signals here on Earth. Neutrinos formed in the inner regions of the supernova will thus meet both resonance points on their way out through the outer layers of the supernova, and have a calculable probability to change into another flavor. To take account of these matter induced oscillations in a simple way, we will follow Dighe & Smirnov [DS00] and write the flux we receive here on Earth as

$$\begin{pmatrix} F_{\nu_e} \\ F_{\bar{\nu}_e} \\ 4F_x \end{pmatrix} = \begin{pmatrix} p & 0 & 1-p \\ 0 & \bar{p} & 1-\bar{p} \\ 1-p & 1-\bar{p} & 2+p+\bar{p} \end{pmatrix} \begin{pmatrix} F^0_{\nu_e} \\ F^0_{\bar{\nu}_e} \\ F^0_x \end{pmatrix} \tag{3.24}$$

where quantities F^0 are the original fluxes, $F_x = F_{\nu_\mu} + F_{\nu_\tau} + F_{\bar{\nu}_\mu} + F_{\bar{\nu}_\tau}$, p (neutrinos) and $\bar{p}$ (anti-neutrinos) are the individual survival probabilities, and the expression is valid for both the normal and the inverted mass hierarchy. The survival probablities are given by

$$p = |U_{e1}|^2 P_H\, P_L + |U_{e2}|^2 (P_H - P_H\, P_L) + |U_{e3}|^2 (1 - P_H) \tag{3.25}$$

$$\bar{p} = |U_{e1}|^2 (1 - \bar{P}_L) + |U_{e2}|^2 \bar{P}_L \tag{3.26}$$

The probabilities P_L and P_H are the flip probabilities P_{flip} that a neutrino will change from one flavor to another at the L resonance layer and the H resonance layer respectively. Under the condition of adiabaticity in the crossing of the layers, they are given by

$$P_{\text{flip}} = \exp\left(-\frac{\pi}{2}\gamma\right) \tag{3.27}$$

$$\gamma \equiv \frac{\Delta m^2}{2E} \frac{\sin^2 2\theta_{ij}}{\cos 2\theta_{ij}} \frac{1}{(1/n_e)(dn_e/dr)} \tag{3.28}$$

where θ_{ij} is the mixing angle corresponding to the mass difference Δm^2 in consideration.

3.4.3 Collective effect

Only quite recently has it been discovered that in addition to the vacuum and matter oscillations, a third kind of oscillation can change the flavor of the neutrinos. Similarly to how background matter provides an extra potential for the electron flavor neutrinos in the case of the matter oscillations (and thus increased oscillation probabilities), the neutrinos can provide a "background" for themselves [RS07]. This new oscillation phenomenon affects all three kinds of neutrinos, but only when the density is very high, as in e.g. in the supernova environment. The oscillations caused by this self-interaction are named **collective flavor oscillations** or collective flavor change. The collective flavor oscillations depend on the species and the momentum of neutrino in consideration, as well as the individual momentum of *all* the background neutrinos and anti-neutrinos.

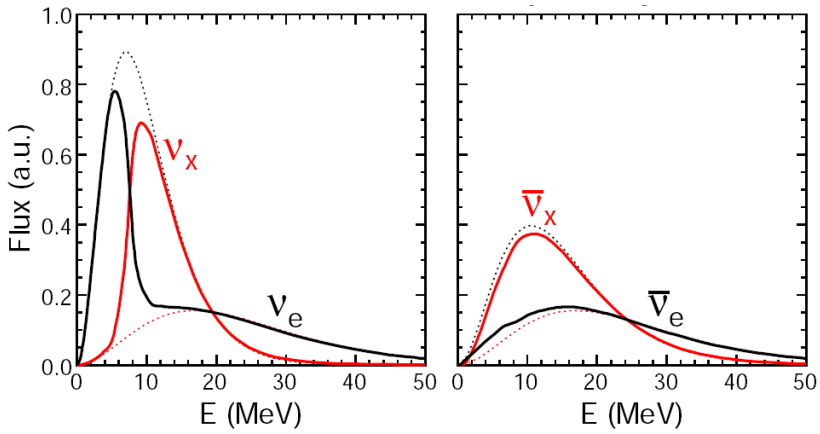

Figure 3.1: The neutrino flux spectrum for the inverted hierarchy showing the effect of collective flavor transformation. Dotted lines are the original spectra, full lines the swapped spectra. *Left:* swap in the neutrino channel. *Right:* swap in the anti-neutrino channel. The figure is from [FLMM07].

Following our notation above one would need to include the following extra term in the Hamiltonian (rewritten from [HRSW06])

$$H_{coll} = \sqrt{2}\mathrm{G_F} \int \frac{\mathrm{d}^3\boldsymbol{q}}{(2\pi)^3} (\varrho_{\boldsymbol{p}} - \bar{\varrho}_{\boldsymbol{q}}) \, (1 - \cos\theta_{\boldsymbol{p},\boldsymbol{q}}) \tag{3.29}$$

where the angle is between the momenta of the two neutrinos in question, and the integral is over the momenta of *all* the background neutrinos and anti neutrinos. The quantities ϱ and $\bar{\varrho}$ are the number densities of neutrinos and anti-neutrinos. The equation for the anti-neutrinos is similar, which results in the nonlinear coupling of the neutrino and the anti-neutrino.

The addition of a self-interaction term means that the equation of motion is not linear anymore, and calculating the probabilities for a flavor change becomes much more difficult. Several papers outline how this collective flavor oscillation can be compared with a pendulum in a magnetic field to simplify the understanding of the effect, see e.g. [HRSW06].

We will not go into details of the complicated calculations and dependencies of the collective flavor oscillations here. Instead, to give an impression of the effect of the swap of neutrino flavor, we show in fig. 3.1 how the energy dependent flux spectrum changes under the assumption of two-flavor collective effects in the inverted hierarchy. The figure show the spectral flux dependence of neutrinos without a swap (dotted lines) and the spectra after a full flavor swap (full lines).

3.4.4 Implications for supernova neutrinos

The major concern for us in connection with supernova neutrinos, is that flavor oscillations may change neutrinos originally born as $\bar{\nu}_e$ in the supernova interior into another flavor, thus not allowing us to detect them with Cherenkov telescopes. Furthermore non-electron flavor neutrinos may be transformed into $\bar{\nu}_e$'s altering the energy spectrum we observe, and muddling

our interpretation. We therefore need to be aware of the effects of neutrino oscillations when we interpret neutrino flux spectra observed here on Earth.

However, this alteration of the energy spectrum might possible not be as pronounced as believed hitherto, since recent simulations show that the differences in mean energies between the $\bar{\nu}_e$ and the $\bar{\nu}_x$ neutrinos might only amount to $\sim 20\%$ [HMJ$^+$, KRJ03].

"In mathematics you don't understand things. You just get used to them."

— Johann von Neumann

4
Fourier Analysis

This chapter will outline the principles and pitfalls of the Fourier transform, as it is employed in digital signal processing. We will show how to extract the frequencies of the underlying signal from a set of measurements taken over time. These frequencies can then be used to reconstruct a signal that mimics the underlying signal, as it appears from the measurements. The reconstruction is done by the use of well-known basis functions. In the process we will point out the caveats that require special attention, lest the final result should be misinterpreted.

4.1 Basic idea

The basic idea of Fourier analysis is that you can reconstruct any function periodic in time from a number of sine and cosine waves if you know the frequency content of the original function.

As an example let us take a saw tooth waveform like the red curve given in fig.4.1. This waveform can be reproduced by adding up sine and cosine waves with different amplitudes and different frequencies. As one includes more and more sinusoids the replication will become more and more accurate. Using an infinite number of sinusoids will provide an exact copy of any periodic function. In fig. 4.1 we see that using only 1 sine wave (panel a) is a bad approximation to the sawtooth wave. But already when we use 3 sines (panel b) the approximation is much better. As we increase the number of sines we get an increasingly better approximation to the original waveform.

Using the Fourier transform on a function we will get a set of frequencies back, and the amplitude corresponding to each frequency. These two sets of numbers will allow us to reconstruct the original function. This is done using the basis functions of the Fourier transform: the sines and cosines. However, before we move on to the mathematical details of Fourier

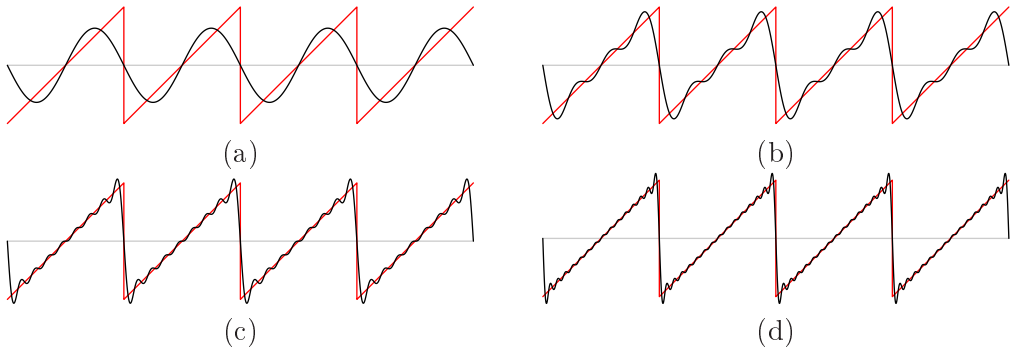

Figure 4.1: Sawtooth signal (red) approximated by a series of sines (black). In (a) only 1 sine is used, in (b) 3 sines, in (c) 8 sines and in (d) 15 sines.

analysis, we need to get a few more issues out of the way.

4.2 Sampling our signal in the time domain.

When we deal with real life signals, we are not continuously taking measurements, but rather sampling the underlying signal at different points in time. Imagine that the red sawtooth signal in fig. 4.1 represents the voltage in some system, then each time we take a measurement we get a value for the voltage at that instant. Here we only consider samples that are evenly spaced in time, but the analysis can be generalized to variable intervals. Taking N measurements over a given time stretch, τ, we want to reconstruct the signal that these measurements represent. In order to do this, we need to identify from the measurements the frequency content in the original signal, such that we can replicate the signal. Using our old example: We want to reconstruct how the voltage changes in our system.

4.2.1 Proper sampling

For us to uniquely identify a frequency in a signal we must sample, i.e. take a measurement, the signal at least at twice the frequency of interest. In other words, if we have a sinus function as the full line shown in fig. 4.2 then we need to sample it two times in one period. If we sample less than two times in a period the resulting measurements will look like they were taken from a sinus function with a larger period. This is clear in fig. 4.2 where the full line sinusoid is sampled only 1.05 times in a period, and the sample points (squares) clearly mimic a sinusoid of a lower frequency. The original frequency was 0.95 times the sampling rate, but from the measurements it *looks like* the frequency is 0.05 times the sampling rate.

4.2.1.1 Nyquist frequency

To avoid this effect, we should sample our signal with a frequency at least twice the highest frequency we want to look for. Or to put it the other way around, if we sample a signal at a given rate, then the highest frequency we can uniquely identify from these measurements will be

$$f_{\max} = \frac{1}{2} f_s \tag{4.1}$$

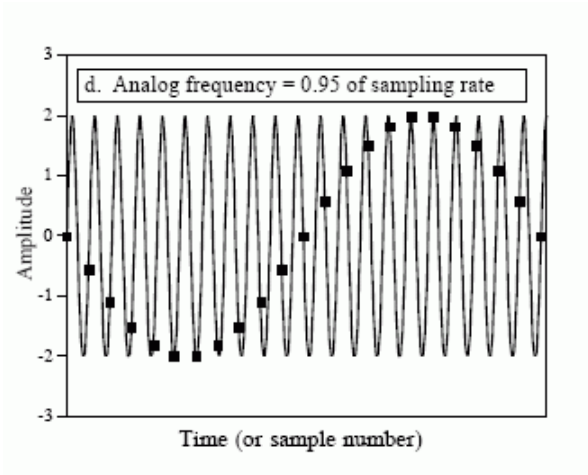

Figure 4.2: Sinusoid sampled only 1.05 times in a period. The squares illustrate the sample points. Instead of the original frequency of 0.95, the samples will appear to be from a sinusoid with a frequency of 0.05 times the sampling frequency. The figure is from [Smi97].

where f_s is the sample frequency. This maximum frequency that can uniquely be identified from a set of samples of a signal is called the **Nyquist frequency**, f_{Nyq}. Defining it with basis in the elapsed time between two consecutive samples, Δ, we get

$$f_{\text{Nyq}} = \frac{1}{2\,\Delta} \tag{4.2}$$

Now if all frequencies in the signal are below the Nyquist frequency, we have properly sampled the signal. If this is not the case, we experience the phenomenon of aliasing.

4.2.2 Aliasing

The fact that one sinusoid can appear as another when we sample it is called **aliasing**. We will illustrate the effect of aliasing using the time domain signal shown in the top left panel of fig. 4.3. The top right panel of the same figure shows the amplitudes for the frequencies actually contained in the signal. In the middle panels the time signal is sampled with a rate that is 3 times the highest frequency present in the signal. The amplitude spectrum on the right, now correctly represents the amplitudes of the frequency content between 0 and the Nyquist frequency. However, a set of copies, and inverted copies, have appeared centered on integer multiples of the sampling frequency. The inverted copies (lower sidebands) appear because aliasing also can introduce a phase shift. Compare how the aliased wave in fig. 4.2 is a negative sine and the original is a positive sine.

The lower panels show what happens if we instead sample the signal only three times in 2 periods. The proper amplitude distribution and the copies are now no longer well separated, but instead overlap each-other, illustrating exactly the problem of aliasing. The overlapping spectra means that power belonging to a frequency in the lower end of a copy will add to the power for a frequency in the higher end of the original or another copy. The effect of aliasing is thus, that since one frequency will "look like" another, we will misjudge the strength of the

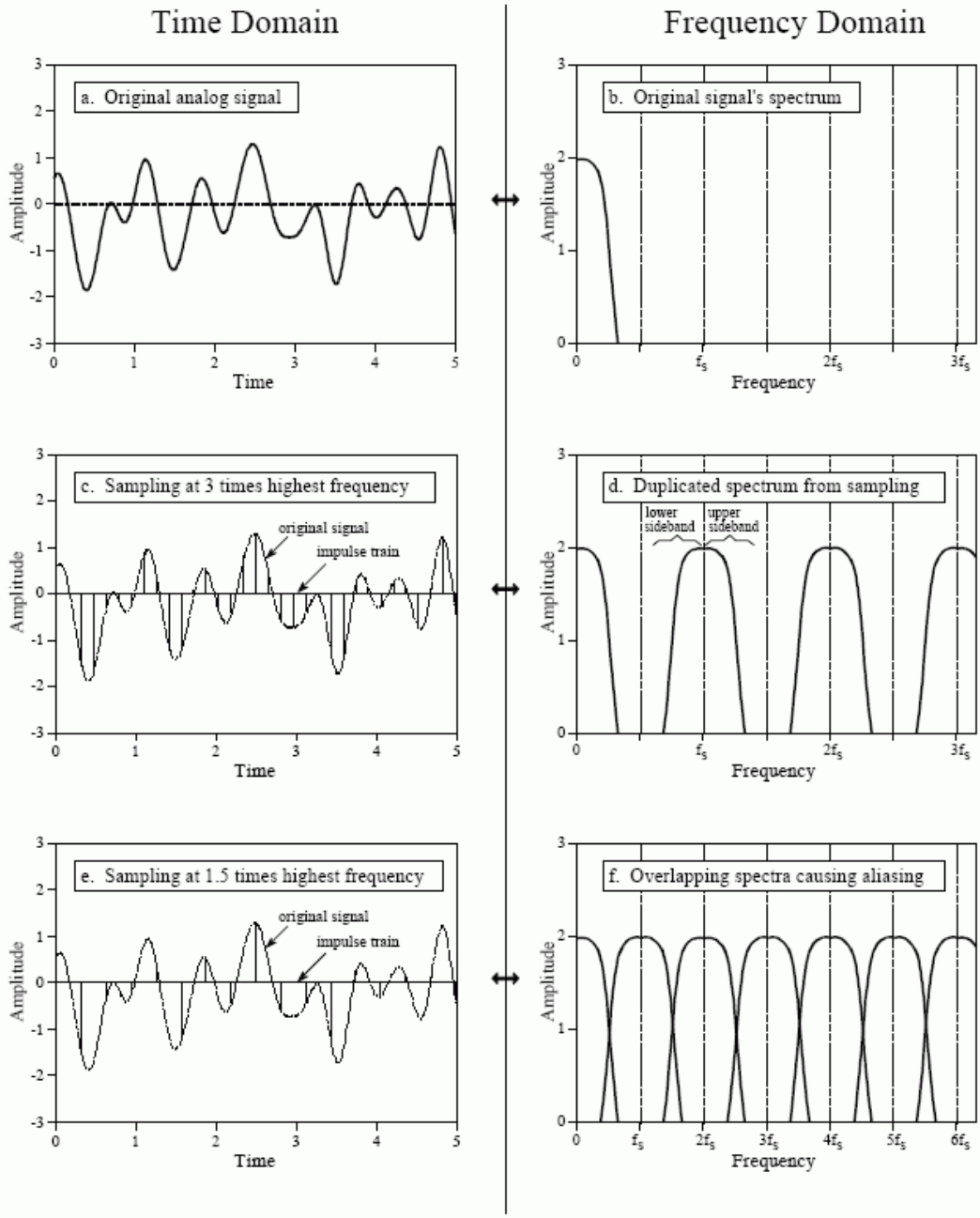

FIGURE 3-5
The sampling theorem in the time and frequency domains. Figures (a) and (b) show an analog signal composed of frequency components between zero and 0.33 of the sampling frequency, f_s. In (c), the analog signal is sampled by converting it to an impulse train. In the frequency domain, (d), this results in the spectrum being duplicated into an infinite number of upper and lower sidebands. Since the original frequencies in (b) exist undistorted in (d), proper sampling has taken place. In comparison, the analog signal in (e) is sampled at 0.66 of the sampling frequency, a value exceeding the Nyquist rate. This results in aliasing, indicated by the sidebands in (f) overlapping.

Figure 4.3: Aliasing. Figure is from [Smi97].

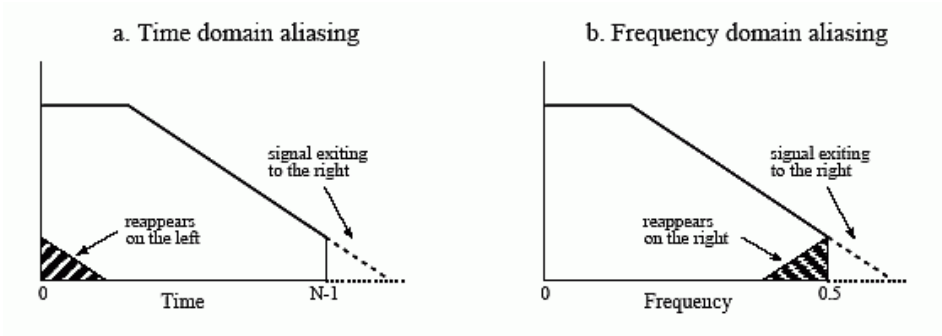

Figure 4.4: Aliasing in the time domain (left) and the frequency domain (right). Note the "folding" around the Nyquist frequency. Figure is from [Smi97].

lower frequency. Therefore if our sampling is not proper, we will add power from an infinite number of higher frequencies to the power of a lower frequency. As an example, the frequency of $0.4f_s$ will receive contributions from the power at $0.4f_s + n\,f_s$, $n = 1, 2, ..$, as well as the power at $n\,f_s - 0.4f_s$, $n = 1, 2, ...$ Here the first part is from the upper sidebands and the latter is from the lower sidebands. Aliasing thus results in loss of information on *both* the higher and the lower frequency. Effectively the attribution of excessive power to a frequency means that when we subsequently try to synthesize a new signal it will not be a precise reconstruction of the original signal.

A simple way to test for aliasing is to look at the amplitude at the Nyquist frequency. If it goes to zero, the sampling is proper. If the amplitude instead seems to rise towards the Nyquist frequency, you have aliased power that is "folded" down from above the Nyquist frequency and added to the power already present, see fig. 4.4.

4.3 The Discrete Fourier Transform

Now that we have made sure, we can uniquely identify all the frequencies present in the original signal, we will move on to how one actually makes the carbon copy signal.

To construct an aperiodic signal, one would need to use an infinite number of sinusoids. This presents a problem since we will only have a finite number of sample points. Therefore we will assume our signal to be periodic instead, where the periodicity comes from assuming that our signal will repeat itself from minus to plus infinity with a period corresponding to the time stretch τ over which we have taken our measurements. The Fourier transform dealing with this type of periodic discrete signals is called the **Discrete Fourier Transform**[1] (DFT).

Using the DFT we will now find the frequency content of an original signal $s(t)$. We sample the signal $s(t)$ N times, where N must be even, giving us the N function values s_j, $j = 0, 1, ..., N-1$. (In our original example the s_j's will be voltages.) Therefore, the number of frequencies we can get information on, with N sample points and the need to have at least 2 samples per period, will be $N/2$. The expressions to calculate the amplitudes for each of

[1] From now on we will always mean the DFT when we say Fourier Transform.

these $N/2$ frequencies are

$$a_k = \sum_{j=0}^{N-1} s_j \, cos(2\pi kj/N) \tag{4.3}$$

$$b_k = -\sum_{j=0}^{N-1} s_j \, sin(2\pi kj/N) \tag{4.4}$$

Where $k = 0, 1, ..., N/2$. Note that $\sin(0) = 0$ and $\sin(\pi j) = 0$, so both b_0 and $b_{N/2}$ will hold no information[2]. The parameter k tells how many full cycles a given sinusoid makes over the N sample points (i.e. over the signal duration τ). Thus the period for k'th sinusoid will be $P_k = \tau/k$, and the frequency will be $f_k = k/\tau$. Hence each a_k and b_k is related to the frequency f_k. From this we learn that the spacing between our frequencies will be

$$\delta f = \frac{1}{\tau} \tag{4.5}$$

Remembering that the time between sample points was Δ, the total time can be written as $\tau = N\Delta$. This means that the frequency spacing can also be written as $\delta f = 1/(N\Delta)$. We now have a frequency domain signal consisting of $N/2+1$ frequencies f_k, each with a corresponding amplitude a_k and b_k.

4.4 The Inverse Discrete Fourier Transform

To reconstruct a copy of the original time domain signal we thus need to use $N/2 + 1$ sine waves and $N/2 + 1$ cosine waves, and add them together. Multiplying each sinusoid by its respective amplitude gives the time signal

$$s_j = \sum_{k=0}^{N/2} \tilde{a}_k cos(2\pi kj/N) + \sum_{k=0}^{N/2} \tilde{b}_k sin(2\pi kj/N) \tag{4.6}$$

where as before $0 \leq j \leq N - 1$, and where the amplitudes of the sines and the cosines are given in terms of the values a_k and b_k

$$\tilde{a}_k = \frac{a_k}{N/2} \tag{4.7}$$

$$\tilde{b}_k = -\frac{b_k}{N/2} \tag{4.8}$$

Except in the two cases

$$\tilde{a}_0 = \frac{a_0}{N} \tag{4.9}$$

$$\tilde{a}_{N/2} = \frac{a_{N/2}}{N} \tag{4.10}$$

The denominators come from our choice of normalization.

[2]The negative sign for the b_k values is included to make the real DFT consistent with the complex DFT.

4.5 The exponential as basis function

Using Euler's formula, it is possible to rewrite the Fourier decomposition as

$$s_j = \sum_{k=-N/2}^{N/2} c_k \, e^{i2\pi \, j \, k/N} \quad j = 0, 1, ..., N-1 \tag{4.11}$$

with

$$c_k = \frac{\tilde{a}_k - i \, \tilde{b}_k}{2} \qquad \text{and} \qquad c_{-k} = c_k^* \tag{4.12}$$

Where the asterisk denotes complex conjugation.

Looking at the $f = 0$ component in frequency space, c_0, we see that all the exponentials will be 1 independent of j. Thus c_0 will be equal to the sum over all the signal values. The average value of the signal $s(t)$ will therefore equal c_0/N.

To minimize confusion we will from now on use f solely to denote frequencies, and functions of time will be denoted with g or h. In the frequency domain primarily capital letters will be used. The Fourier transforms of the functions $g(t)$ and $h(t)$ will thus be $G(f)$ and $H(f)$ respectively.

Part II

My work
– Adding to present knowledge

Neutrino interactions with a pseudo-scalar

5

A strong pseudo-scalar neutrino interaction

The first project I undertook during my PhD studies was an investigation of a strong interaction between the neutrino and a pseudo-scalar particle, the Majoron. I calculated the decoupling radii of two representative interactions between the neutrino and the Majoron: The annihilation process and the bremsstrahlung process. Subsequently I then investigated the influence of this new interaction on the neutrino energy spectrum. This chapter presents the preliminary and unpublished results of these investigations.

5.1 Motivations

In models of neutrino mass creation, the addition of an extra Higgs field (cf. section 3.3) to solve the puzzle of the small neutrino masses brings about an unfamiliar particle, the Majoron ϕ. As we mentioned, it is not necessary for neutrinos to have a mass in the particle physics standard model (PPSM). However, through various oscillation experiments it has now been established that although very small, the neutrino masses are non-zero. The current consensus is neutrino masses of the order 0.2–2 eV, which is 5–6 orders of magnitude smaller than the masses of the other particles in the PPSM (e.g. $m_e = 511$ keV). This hierarchy problem has puzzled physicists for a long time. Often suggestions have been to solve it by using very small coupling constants, without any specific physical motivation, but another possibility is to propose a new field for neutrinos to interact with. Letting this new field gain a vacuum expectation value (vev) due to a symmetry breaking, could lead - perhaps more naturally - to the small neutrino masses. This leads to the emergence of the Majoron, and below we will take a closer look at how it comes into existence. Having brought this new particle into the world, we want to see what the possible effects of neutrinos interacting with the Majoron in the hot and dense interior of a supernova could be. Could this new interaction be helpful in solving the problem

of non-exploding stars?

Even though little is known about the Majoron, we have at few constraints on it. One of these constraints comes from the only supernova so far, which we have actually observed neutrinos from: SN1987A. Due to the fact that the time duration of the neutrino spectrum from SN1987A should not be shortened by more than a factor of two, it is possible to constrain the energy loss that can be tolerated through other mechanisms than photon and neutrino emission. In [CS90] they made a very detailed assessment requiring the Majoron luminosity not to exceed $L_\phi = 3 \times 10^{53}$ erg/s. This made them exclude coupling constants in the range of $5 \times 10^{-7} \lesssim g \lesssim 6 \times 10^{-5}$ (for a B-L breaking scale of 20 GeV.) Here g is the largest of the $\nu - \phi$ couplings. These bounds are consistent with the bounds found in [KTV00].

5.2 Breaking a symmetry

Before we continue the discussion of the neutrino-Majoron interactions in supernovae, let us review how a Goldstone boson arises from a spontaneous broken symmetry.[1] We will look at a generic example with a complex doublet scalar field Φ. Starting from the Lagrangian[2]

$$\mathcal{L} = \frac{1}{2}(\partial_\mu \Phi)^\dagger (\partial^\mu \Phi) - V(|\Phi|) \tag{5.1}$$

$$\text{where} \qquad \Phi = \begin{pmatrix} \Phi_1 \\ \Phi_2 \end{pmatrix} \qquad \text{and} \qquad V(|\Phi|) = -\frac{\mu^2}{2}\Phi^\dagger\Phi + \frac{\lambda^2}{4}\left(\Phi^\dagger\Phi\right)^2 \quad , \tag{5.2}$$

when $\mu^2 > 0$, we find the minimum of the potential to be

$$0 = \frac{\partial V(|\Phi|)}{\partial \Phi} \Rightarrow 0 = -\mu^2 + \lambda^2|\Phi|^2 \quad , \quad \text{assuming } |\Phi| \neq 0\,. \tag{5.3}$$

This gives

$$|\Phi|^2 = \frac{\mu^2}{\lambda^2} \Leftrightarrow |\Phi_1|^2 + |\Phi_2|^2 = \frac{\mu^2}{\lambda^2} \tag{5.4}$$

Thus the potential takes on its minimum value for several combinations of the two fields. In fig. 5.1 we see explicitly that the potential given in eq. 5.2 has a continuous set of symmetric ground states along the bottom.

Choosing one specific ground state

$$\Phi_{1,min} = 0 \qquad \Phi_{2,min} = \frac{\mu}{\lambda} \tag{5.5}$$

we can then reparametrize the field Φ in terms of this ground state value, $\langle \Phi_2 \rangle = \mu/\lambda = v$, and two new real scalar fields $\chi(x)$ and $\phi(x)$:

$$\Phi = (v + \chi) \exp i\frac{\phi}{v} \simeq (v + \chi + i\phi)\,. \tag{5.6}$$

The second expression is obtained by expanding the exponential. Since $v >> \phi$ this is a good approximation, and we only retain terms that are first order in the fields. From the first expression we clearly see the rotational symmetry.

[1] The treatment of spontaneous symmetry breaking can be found in numerous books, e.g. [PS95].

[2] Please note that the last constant in the potential, $\lambda^2/4$, is not defined consistently in the literature.

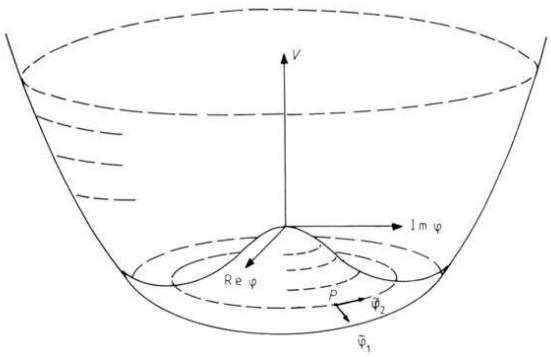

Figure 5.1: Mexican hat potential.

If we plug this new expression for Φ into the Lagrangian in eq. 5.1, we get

$$\begin{aligned}\mathcal{L}_{re} = \frac{1}{2}(\partial\chi)^2 + \frac{1}{2}(\partial\phi)^2 - \mu^2\chi^2 - \frac{\lambda^2}{4}(\chi^4 + \phi^4) \\ -\lambda\mu(\chi^3 + \chi\phi^2 + \frac{1}{2v}\chi^2\phi^2) + \frac{\mu^4}{\lambda^2}\end{aligned} \tag{5.7}$$

We see from this new form that one of the two new fields, χ, acquires a mass through the term $-\mu^2\chi^2$, whereas the field ϕ is massless. This is a general property of spontaneous symmetry breaking. According to Goldstone's theorem: When a continuous global symmetry is spontaneously broken, there will always appear a massless scalar particle - the Goldstone boson.

5.3 The singlet Majoron model

The extra field needed to give Majorana mass terms for neutrinos, and which acquires a vev under the breaking of global lepton number conservation, is what gives us the Majoron. Several models have been proposed to get the Majoron: extra singlet, doublet and even triplet fields. Now it is clear that doublet and triplet Majoron models are excluded. This is because neutrinos interact with Z_0 and if triplet and doublet models existed they would manifest themselves as extra effective neutrinos in Z_0-decays. Experiments show that the decay width of Z_0 is consistent with only 3 effective neutrinos. This leaves us only the possibility of a singlet Majoron model.

The first singlet model was presented by Chikashige, Mohapatra and Peccei in 1980 [CMP81]. It presumes lepton number to be a spontaneously broken global symmetry, such that a massless Goldstone boson appears, as we saw in section 5.2, in this case the Majoron. It also presumes that the Majoron has negligible interactions with ordinary matter, except for neutrinos. By introducing an extra singlet Higgs field (that violates L with two units), and following a treatment very similar to the one given in section 3.3.1 they arrive at two massive physical self-conjugate Majorana fields.

The interaction term in the Lagrangian between the Majoron and the physical neutrino states ν_1 and ν_2 (the eigenstates of the diagonal mass matrix from section 3.3.1) is then given

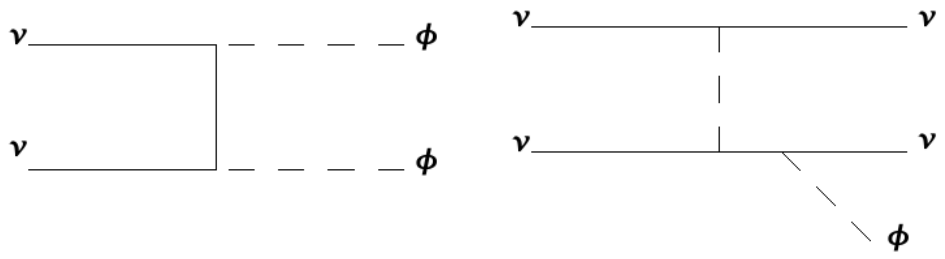

a) annihilation b) bremsstrahlung

Figure 5.2: Feynman diagram of the annihilation of an anti-neutrino and a neutrino into two Majorons (right), and of the bremsstrahlung process (left).

by:

$$\mathcal{L}_{\phi,\nu} = g^2\phi\left[\bar{\nu}_1\gamma_5\nu_1 - \frac{m_D}{M_{RR}}(\bar{\nu}_1\gamma_5\nu_2 + \bar{\nu}_2\gamma_5\nu_1) + \left(\frac{m_D}{M_{RR}}\right)^2\bar{\nu}_2\gamma_5\nu_2\right] \tag{5.8}$$

5.3.1 Specification to our model

Previously, $\nu - \phi$ interactions have been investigated (as mentioned in the introduction to this chapter), but almost always with very small coupling strengths such that the Majoron would leave the supernova without interacting, and always under the assumption of a massless Majoron.

Our investigation of the singlet Majoron model will instead be with strong couplings, so that there may be (several) interactions before the ϕ's and ν's leave the supernova, and we assume the Majoron to have a mass of the order a few keV. One can provide mass to the Majoron by breaking the symmetry of the ground-state continuum. In one dimension, one can imagine tilting the one dimensional version of the potential in eq. 5.2, thus breaking the symmetry of the two ground-states. In more dimensions it is more complicated, and one unfortunately can not just imagine tilting the "Mexican hat". With a Majoron mass of a few keV, neutrinos would not be able to decay into Majorons on their way from the supernova to Earth and the neutrino flux would thus not be diminished. Furthermore with a strong coupling to neutrinos a massive Majoron created in the early universe would decay rapidly, thus leaving no relic population of Majorons. With no background Majorons, neutrinos would not get scattered out of their way en route from a supernova to Earth. So giving the Majoron a relatively small mass makes it escape bounds on the coupling strength given in previous papers, e.g. [HR05, KTV00]. Inside the supernova, however, the neutrino energy is sufficiently high that the mass of the Majoron will not be a problem.

5.4 Calculating decoupling radii

To make more detailed statements of the influence Majoron interactions would have in a supernova, we will in this section calculate the radius where interactions between Majorons and neutrinos effectively cease. We will assume that the Majoron is a pseudo-scalar particle to avoid any unwanted long range forces. Moreover, even though the following is based on

the assumption of neutrinos being Majorana particles, it is likely that it would be possible to make a similar pseudo-scalar coupling as in eq. 5.8 if neutrinos are Dirac particles.

We will start by calculating the decoupling radius for annihilations of neutrinos into Majorons, see fig. 5.2a. To simplify calculations we will use a pseudo-scalar coupling instead of a derivative coupling, this is not entirely equivalent but it is good enough to obtain a conservative bound. We are using an expression for the cross section from the article [DPRV97], which is appropriate since they are using pseudo-scalar couplings between the Majorons and neutrinos. For annihilations to Majorons the cross section is given by

$$\sigma_J(\eta) = \frac{g^4}{128\pi}\frac{1-\eta}{m_\nu^2\eta}\left[\ln\left(\frac{1+\sqrt{\eta}}{1-\sqrt{\eta}}\right) - 2\sqrt{\eta}\right] \tag{5.9}$$

where

$$\eta \equiv 1 - \frac{4m_\nu^2}{s} \tag{5.10}$$

and s is the center of momentum energy squared. Inserting this in the formula for the velocity averaged cross section

$$\langle\sigma_i v\rangle = \frac{4x}{K_2^2(x)}\int_0^1 d\eta\ \frac{\eta}{(1-\eta)^{7/2}}\ \sigma_i(\eta)K_1\left(\frac{2x}{\sqrt{1-\eta}}\right) \quad , \tag{5.11}$$

where $x = m_\nu/T$, and K_1 and K_2 are Bessel-functions of the first and second order, gives us

$$\begin{aligned}\langle\sigma v\rangle = \frac{4x}{K_2^2(x)}\frac{g^4}{128\pi\ m_\nu^2}\int_0^1 d\eta\ \frac{1}{(1-\eta)^{5/2}}\left[\ln\left(\frac{1+\sqrt{\eta}}{1-\sqrt{\eta}}\right) - 2\sqrt{\eta}\right] \\ \times\ K_1\left(\frac{2x}{\sqrt{1-\eta}}\right)\end{aligned} \tag{5.12}$$

Computing the integral numerically in Mathematica, while taking m to be 0.2 eV (a currently acceptable value from cosmology considerations, [Kin07]) and $T = 20$ MeV (a typical energy in the supernova) and thus $x = m_\nu/T = 10^{-8}$, gives us

$$\langle\sigma v\rangle = \frac{g^4\,\hbar^2}{32\pi m_\nu^2\,c}\frac{10^{-8}}{K_2^2(10^{-8})}\cdot 2.08322\times 10^{25} = \frac{g^4\,\hbar^2}{m_\nu^2\,c}\ 5.208\times 10^{-18} \tag{5.13}$$

Here the value of the neutrino mass must be inserted in MeV/c^2. In the last equality 32π has been approximated by 100. The evaluation of the Bessel-function $K_2^2(10^{-8})$ gives a value of $K_2^2(10^{-8}) \sim 4\times 10^{32}$.

Next, to calculate the average of the mean free path $\langle\lambda\rangle$ with respect to this reaction we will use a Maxwell-Boltzmann distribution for the neutrino distribution function; $f_\nu(\omega) = \exp(-\omega/kT)$. We also adopt an expression for the neutrino number density from the article [HRSW06]:

$$n_\nu = \frac{L_0}{\langle E_\nu\rangle\,4\pi r^2} = 1.04\times 10^{32} cm^{-3}\left(\frac{r}{10\ \text{km}}\right)^{-2} \tag{5.14}$$

Then we find

$$\Gamma_{\nu\nu\to\phi\phi} = n_\nu\,\langle\sigma v\rangle \tag{5.15}$$

$$\lambda = \frac{c}{\Gamma}$$

$$\langle\lambda\rangle = \frac{\int \frac{c}{\Gamma} f_\nu\, \omega^2\, d\omega}{\int f_\nu\, \omega^2\, d\omega} = \frac{\int \frac{c}{n_\nu \langle\sigma v\rangle} f_\nu\, \omega^2\, d\omega}{\int f_\nu\, \omega^2\, d\omega} = \frac{T}{N} \tag{5.16}$$

In these expressions ω is the energy of the neutrino.

$$\begin{aligned} N = \int f_\nu\, \omega^2\, d\omega &= \int_0^\infty \omega^2\, e^{-\omega/kT}\, d\omega \\ &= \left[-kT\, e^{-\omega/kT}\left(2(kT)^2 + 2kT\omega + \omega^2\right)\right]_0^\infty = 2(kT)^3 \end{aligned} \tag{5.17}$$

$$\begin{aligned} T = \int \frac{c}{\Gamma} f_\nu\, \omega^2\, d\omega = \int_0^\infty \frac{c\, f_\nu\, \omega^2}{n_\nu\, \langle\sigma v\rangle}\, d\omega &= \frac{c}{n_\nu\, \langle\sigma v\rangle} \int_0^\infty f_\nu\, \omega^2\, d\omega \\ &= \frac{c}{n_\nu\, \langle\sigma v\rangle}\, 2(kT)^3 \end{aligned} \tag{5.18}$$

$$\langle\lambda\rangle = \frac{\frac{c}{n_\nu \langle\sigma v\rangle}\, 2(kT)^3}{2(kT)^3} = \frac{c}{n_\nu\, \langle\sigma v\rangle} = \frac{c}{1.04 \times 10^{32} cm^{-3} \left(\frac{r}{10\ \mathrm{km}}\right)^{-2} \frac{g^4\, \hbar^2}{m_\nu^2\, c}\ 5.208 \times 10^{-18}}$$

$$\langle\lambda\rangle = \frac{m_\nu^2/c^2}{g^4\, \hbar^2\, 5.416 \times 10^{14} \mathrm{cm}^{-3}} \left(\frac{r}{10\,\mathrm{km}}\right)^2 \qquad , m_\nu \text{ to be inserted in MeV} \tag{5.19}$$

We define the point where this reaction falls out of equilibrium to be when $\langle\lambda\rangle$ equals the radius of the neutron star R_{NS}. This leads to the following expression for the decoupling radius

$$R_{NS} = \frac{m_\nu^2/c^2}{g^4\, \hbar^2\, 5.416 \times 10^{14} \mathrm{cm}^{-3}} \left(\frac{r}{10^6\ \mathrm{cm}}\right)^2 \rightarrow r^2 = \frac{g^4\, \hbar^2\, R_{NS}}{m_\nu^2/c^2} 5.416 \times 10^{26} \mathrm{cm}^{-1}$$

The neutron star radius we take to be 10 km.

$$r = g^2\, \frac{\hbar\, c}{m_\nu} 2.327 \times 10^{16} = \frac{g^2}{m_\nu}\, 4.594 \times 10^3 \mathrm{m\,MeV} \qquad , \text{with } m_\nu \text{ in MeV.} \tag{5.20}$$

Inserting the neutrino mass of 0.2 eV leaves us with a dependency only on the coupling strength g. We know that it has to be larger than $\sim 10^{-5}$ from observations of neutrinos from the supernova SN1987A, and we will assume $g = 10^{-3}$. The decoupling radius is then

$$r_{\mathrm{dec}} = \frac{(10^{-3})^2}{0.2 \times 10^{-6}\,\mathrm{MeV}}\, 4.594 \times 10^3 \mathrm{m\,MeV} = 22970\,\mathrm{m} = 22.97\,\mathrm{km} \tag{5.21}$$

Using this value for the decoupling radius together with the equation for the temperature from [Raf01], we find a temperature of

$$T(r) = T_0 \left(\frac{10\,\mathrm{km}}{r}\right)^{2,5} \qquad , \quad T_0 = 31.66\mathrm{MeV} \tag{5.22}$$

$$T(r_{\mathrm{dec}}) = 31.66\,\mathrm{MeV} \left(\frac{10\,\mathrm{km}}{23\,\mathrm{km}}\right)^{2.5} = 3.946\,\mathrm{MeV} \quad , \tag{5.23}$$

which is equivalent to 4.58×10^{10} Kelvin.

5.4.1 NC and CC radii

We would like to compare our decoupling radius to the decoupling radii for the neutral and charged current interactions. Below we sketch the two calculations. They are quite similar to the previous one. The energy in the supernova environment is high enough that we can assume the medium not to be degenerate, thus no Pauli-blocking factors are needed. Assuming further that the interaction medium only consist of neutrons that are non-relativistic, and that we can ignore the mass of the electron and the mass difference between the proton and the neutron compared to the neutrino energy, we can use the mean free paths λ given in [Bru85]. In our case they reduce to:

$$\frac{1}{\lambda_{CC}} = \frac{G^2}{\pi} n_n (g_V^2 + 3g_A^2)\omega^2 \tag{5.24}$$

$$\frac{1}{\lambda_{NC}} = \frac{G^2}{\pi c(\hbar c)^3} n_n (h_V^2 + 3h_A^2)\omega^2 \tag{5.25}$$

Here n_n is the neutron density, G the Fermi constant, ω the neutrino energy, and $g_V = 1$, $g_A = 1.23$ and $h_V = -1/2$, $h_A = -g_A/2$ are charged and neutral nucleon current form factors. This leads to radii $r_{CC} \simeq 23.2$ km and $r_{NC} \simeq 21.0$ km, and temperatures of $T_{CC} \simeq 3.85$ MeV and $T_{NC} \simeq 4.93$ MeV.

We thus see that with our value of the coupling strength $g = 10^{-3}$ for the Majoron-neutrino interaction, the decoupling radius will lie approximately in the same range as the ones for the NC- and CC-interactions.

5.5 Bremsstrahlung calculations

To ensure that the impact of other interactions between Majorons and neutrinos are negligible, we have calculated the cross section corresponding to bremsstrahlung emission of a Majoron, see fig. 5.2b. Starting from the general expression for the matrix element of the process

$$F = \bar{u}(p')\, g\gamma_5\, u(p) \frac{\mathscr{C}}{(p-p')^2 - m_\phi^2} \bar{u}(k') g\, \gamma_5 \frac{i(\not{l} + m_\nu)}{l^2 - m_\nu^2} g\, \gamma_5 u(k)\phi(q) \tag{5.26}$$

where $\mathscr{C}$ is a (complex) constant of order unity which we will ignore, we find (see appendix A)

$$\begin{aligned}\frac{1}{4}\sum |F|^2 = {} & \frac{16g^6}{[(p-p')^2 - m_\phi^2]^2 (l^2 - m^2)^2} \\ & \times \Big[m^4(p'\cdot p - m^2) + 2(k'\cdot l)(k\cdot l)(p'\cdot p - m^2) + 2m^2(p'\cdot p - m^2)(k'\cdot l) \\ & + 2m^2(p'\cdot p - m^2)(k\cdot l) + m^2(p'\cdot p - m^2)(k'\cdot k) \\ & + m^2(p'\cdot p - m^2)(l\cdot l) - (p'\cdot p - m^2)(k'\cdot k)(l\cdot l) \Big]\end{aligned}$$

Since both neutrinos and Majorons are relativistic inside the supernova, we are working in the extremely relativist limit and can neglect terms proportional to m^2 or higher, resulting in

$$\frac{1}{4}\sum |F|^2 = \frac{4g^6}{(p\cdot p')l^4} \left[2(k'\cdot l)(k\cdot l) - (k'\cdot k)(l\cdot l) \right] \tag{5.27}$$

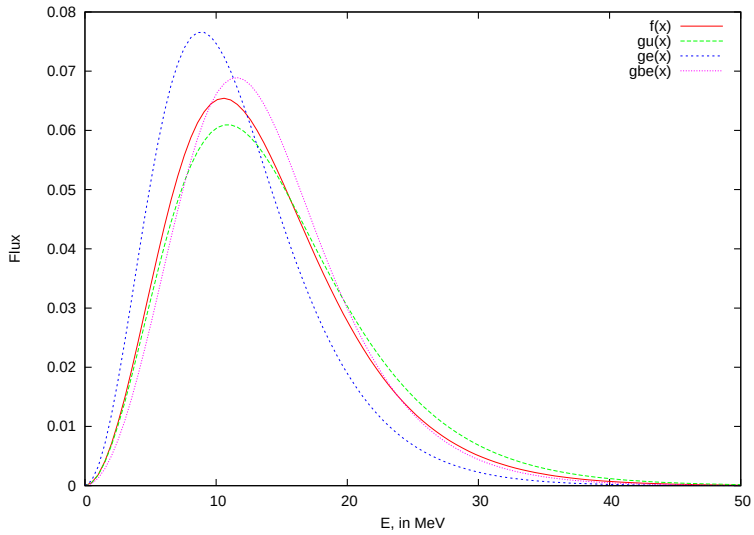

Figure 5.3: Particle fluxes, all normalized to unity. The red line is our result and the remaining three are from [KRJ03]; green: ν_μ, blue: ν_e and purple: $\bar{\nu}_e$.

Now the matrix element can be inserted in the general formula for the differential cross section $d\sigma$

$$d\sigma = \frac{|F|^2}{4[(p\cdot k)^2 - m_\nu^4]^{1/2}}(2\pi)^4\delta^4(p' + k' + q - k - p)\frac{d^3k'}{(2\pi)^3 2E_{k'}}\frac{d^3p'}{(2\pi)^3 2E_{p'}}\frac{d^3q}{(2\pi)^3 2E_q} \tag{5.28}$$

$$\begin{aligned}\sigma = \iiint \frac{16g^6\left[(k'\cdot l)(k\cdot l) - (k'\cdot k)(l\cdot l)\right]}{l^4\,(p\cdot p')}\frac{1}{4[(p\cdot k)^2 - m_\nu^4]^{1/2}} \\ \times (2\pi)^4\delta^4(p' + k' + q - p - k)\frac{d^3k'}{(2\pi)^3 2E_{k'}}\frac{d^3p'}{(2\pi)^3 2E_{p'}}\frac{d^3q}{(2\pi)^3 2E_q}\end{aligned} \tag{5.29}$$

It is not simple to calculate this cross section in the relativistic limit, and since we are not interested in the exact numerical value, we will contend ourselves with noting that the kernel of the integral is not zero. The final result will give us some numerical value times g^6. This is also clear from dimensional analysis, which gives $\sigma \propto g^6/T^2$. In the calculation of the decoupling radius we would then get $r \propto g^3$ thus giving an extra factor of 10^{-3} compared with the decoupling radius calculated in section 5.4 for the annihilation of neutrinos into Majorons. We therefore conclude that it is reasonable to disregard this reaction in our considerations.

5.6 Effects of the $\nu - \phi$ interaction

Now we will turn to the implications of these strong interactions between neutrinos and Majorons. One very obvious result, when we assume the interaction strength to be equal for all flavors, is that this interaction provides a sort of "back-door" for neutrino flavor changes. Through this strong interaction we could effectively have flavor oscillations among the neutrinos via $\nu_x\bar{\nu}_x \to \phi\phi \to \nu_e\bar{\nu}_e$. This would allow non-electron flavor neutrinos to turn into

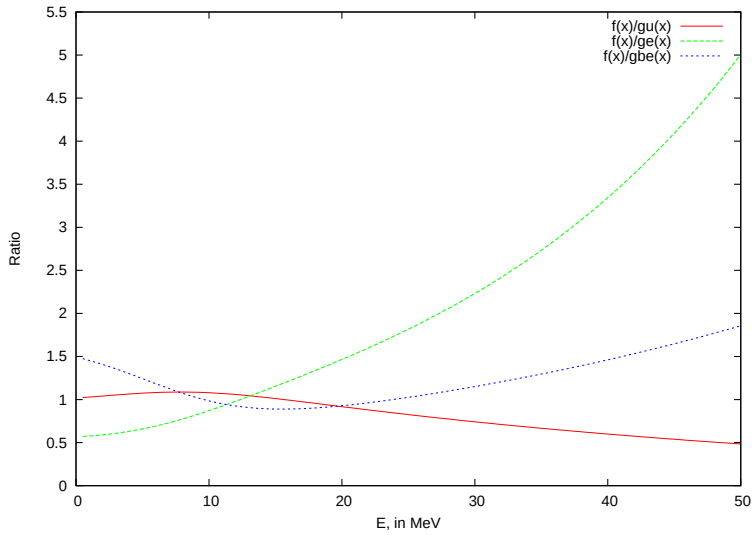

Figure 5.4: Ratio of particle fluxes; our calculation compared with the results of [KRJ03]. The colors show our results divided by the result of [KRJ03] for respectively; red: ν_μ, green: ν_e and blue: $\bar{\nu}_e$.

electron flavor neutrinos, but carrying with them their original higher energy, cf. section 1.7. The electron neutrinos have CC-interactions with the medium allowing them more efficiently to deposit some of their energy as discussed in section 1.6. Thus via this interaction we could transfer some of the energy residing in the non-electron flavor neutrinos to the stellar material behind the shock-front, thereby possibly helping the revival of the stalled shock.

This effect would also be apparent in the neutrino flux and energy spectra. In the upper part of fig. 1.11 we see the time-dependent evolution of the neutrino flux according to the Livermore model and in the lower part the average energy evolution. If neutrinos have strong interactions with Majorons these curves would change: The peak in the ν_e-flux due to the neutrino burst would diminish and partially reappear in the two non-electron flavors. The average energy of the flavors would become similar and follow the same time development. In a future observation of a galactic supernova this could thus be a tell tale signature of this model.

In section 1.7 we saw that one could equally well display ones results as a time-integrated spectrum. To compare our results with numerical models, we have plotted a Fermi-Dirac distribution

$$f(E) = \frac{E^2}{1 + \exp(\frac{E}{T} - \eta)} \tag{5.30}$$

with our values, and the same function using the values obtained in [KRJ03]. We have compared with their values from the "Accretion-Phase Model 1", see table 5.1.

Using the following correspondence between temperature and average neutrino energy (eq. 6 in [KRJ03]); $\langle E \rangle \simeq 3.15\,T$, the energy of neutrinos released at the neutrino-Majoron decoupling radius, at a temperature of 3.946 MeV, is 12.43 MeV in our model. To find the degeneracy parameter η (which is related to the chemical potential) we demanded that

Flavor	E (MeV)	T (MeV)	η
ν_μ	14.3	4.3	1.2
$\bar{\nu}_e$	14.0	3.6	2.7
ν_e	11.8	3.4	1.4

Table 5.1: Values from [KRJ03], "Accretion-Phase Model 1".

our model should produce the same total particle number as was produced in the model of [KRJ03]. This leads to a value of $\eta = 1.6$ for our model. The plot can be seen in fig. 5.3, and in fig. 5.4 we show the ratio of our spectra to the three spectra obtained with data from [KRJ03]. It is clear from fig. 5.3 that our graph is sufficiently similar to the other graphs that it is not ruled out by present observations (i.e. SN1987A) but also sufficiently different that, with good statistics and good energy resolution in an observation of a new supernova, it should be possible to distinguish it from the other spectra. And from fig. 5.4 we see that up to an energy of ~ 30 MeV our results do not differ by more than a factor of 2 from the results of [KRJ03]. If one were to assume a slightly higher coupling strength in the calculation of the decoupling radius (see section 5.4), say $g = 2 \times 10^{-3}$ one would get a decoupling radius of ~ 92 km. This would keep the neutrinos interacting with the Majorons long after the NC- and CC-interactions have decoupled. Majorons and neutrinos would move like a fluid, with a bulk velocity of $c/\sqrt{3}$, until also their interaction ceased. The arrival-time on Earth of some of the neutrinos would therefore be delayed, which could give a very interesting bound on the coupling strength.

5.7 Summary and conclusions

We considered a new strong interaction for the neutrino with the pseudo-scalar Goldstone boson the Majoron, that arise from the spontaneous breaking of lepton number. We have calculated the radius and temperature at the decoupling of the neutrino-Majoron interaction, and conclude that interactions with 3 vertices (e.g. bremsstrahlung processes) can safely be ignored, due to the extra factor of the coupling strength compared to e.g. annihilation processes. We find that the neutrino spectrum is changed sufficiently to be distinguished from spectra of NC- and CC-interactions but not enough to be excluded based on current observational data. Observations with better statistics could confirm or reject this interaction model between neutrinos and Majorons. A future Milky Way supernova may provide the needed neutrino counts in currently operating neutrino detectors.

The investigation of a strong interaction between the neutrino and the Majoron is obviously incomplete in that a proper estimate of the energy transfer should be done. The impact of the redistribution of neutrino energy between the different flavors might also affect the electron fraction and the subsequent nucleosynthesis. Recent papers, e.g. Hüdepohl et al. [HMJ$^+$], however, argue that the mean energies of $\bar{\nu}_e$ and ν_x are so similar that a flavor swap is irrelevant in connection with the nucleosynthesis. This point illustrates quite well that no follow-up work has been done on these calculations in the past two years. Therefore conclusions that may have been disproved in the meantime has not been updated.

Standing Accretion Shock Instability – Imprints on a neutrino signal observed in IceCube

6
Single ray

Numerical simulations show that hydrodynamic instabilities will probably be a crucial ingredient in aiding the neutrino heating mechanism explode stars with masses above $M \sim 11\,M_\odot$. It is natural, then, to look for ways to observe these instabilities. The only way this is possible is to observe the effect they have on the energies and luminosities of neutrinos emitted during the explosion phase. The aim of this and subsequent chapters is therefore to determine the appearance of a supernova neutrino signal as it would be observed by IceCube. It is further esitmated whether the fast time variations that the motions of the Standing Accretion Shock Instability imprints on the signal could be detected with IceCube's sensitivity. To make our considerations as tangible as possible we decided to investigate the results of simulations by Marek and Janka. This was an opportunity for me to improve my skills in data handling and interpretation, as well as C-programming. Something of a change from my previous mainly analytical theoretic work.

6.1 Initial approach

Our initial approach was to examine the detailed spectral energies and number fluxes of neutrinos for *one* single ray. From the detailed energy information we would then calculate the quantities needed in order to calculate the event rate in IceCube, as given by the equation by Dighe et al. [DKR03a]

$$R_{\bar{\nu}_e} = 62\ \mathrm{s}^{-1}\, N_{DOM}\, \frac{L_{\bar{\nu}_e}}{10^{52}\ \mathrm{erg\ s}^{-1}} \left(\frac{10\ \mathrm{kpc}}{D}\right)^2 f_{\mathrm{flux}} f_{\mathrm{detec}} \tag{6.1}$$

Here N_{DOM} is the number of optical modules in IceCube which is 4800 for the primary detector[1]. $L_{\bar{\nu}_e}$ is the anti-electron neutrino luminosity. D is the distance to the supernova, unless noted otherwise we will use a fiducial distance of 10 kpc, and the two fudge factors are defined as:

$$f_{\text{flux}} = \frac{15\text{MeV}}{\langle E_{\bar{\nu}_e} \rangle} \frac{8 \left\langle E^3_{\bar{\nu}_e} \right\rangle}{15\,(15\text{MeV})^3} \tag{6.2}$$

$$f_{\text{detec}} = f_{Ch} \frac{R_{abs}}{100\text{m}} \frac{Q}{0.20} \frac{A_{cat}}{250\text{cm}^2} \frac{\Omega_{acc}}{2\pi} \tag{6.3}$$

The fudge factor f_{detec} incorporates the uncertainties in the theoretical cross section, σ, of $\bar{\nu}_e$ on protons, and various approximations in the estimation of detector efficiencies in IceCube. We will for simplicity assume that f_{detec} equals one.

The idea was to eventually extend this approach and use the detailed information of every ray of the simulation to calculate the event rate, thereby allowing us to look at hemispheric differences and averages. Unfortunately this approach turned out to be infeasible due to the prohibitingly large amount of data needed. Instead we turned to the less data heavy approach of getting only the average energy and the luminosity for each time and flavor on each ray, and then for a number of rays corresponding to an entire hemisphere. We will discuss the results of this multi-ray approach in the following chapters. Below, however, I will still outline the initial work we did as it also illustrates some of the techniques we used in our subsequent work on the multi-ray version. It also gives a good understanding of the process of turning simulation results into observable quantities.

To use equation 6.1 we have to calculate the energy moments and the luminosities for the anti-electron neutrinos. This naturally requires an understanding of the data files, and as the data was given for an observer co-moving with the infalling matter, a Doppler transformation to the reference frame for an observer here on Earth had to be done.

6.2 Spectral information on *one* ray

In the "ray-by-ray plus" method employed by the Garching group, a hemisphere is mapped out by a number of rays, each spanning a predefined number of degrees. The data for the single ray version was for a ray at 5° from the north pole. It covered the time span of 10.5446–416.601 ms, and provided for each time step the full spectral energy information, the differential neutrino flux and the fluid velocity at a distance of 400 km (necessary for the Doppler transformation). The employed EoS was that of Lattimer & Swesty, and all information was given for the three neutrino species, ν_e, $\bar{\nu}_e$ and ν_x. The neutrino energy range covered 0–380 MeV and was divided into 17 energy bins, see table 6.1, where the bin width increases logarithmically as we go up in energy.

The time-dependent differential neutrino flux is in this case defined as the number of neutrinos per second per MeV, and we will denote this quantity with $dS(t)$. It is of course equivalent to the number flux of neutrinos per energy bin, $dN(t)/dE_{\text{bin}}$, where the number flux $dN(t)$ is equal to the differential luminosity divided by the center energy of the bin: $dN(t) = dL(t)/E_{\text{center}}$. This latter formulation was the quantity actually given in the data files, i.e. $dS(t) = dL(t)/(E_{\text{center}}\, dE_{\text{bin}})$ with units [1/(s·MeV)], which will be important to keep

[1] The 360 optical modules of the detector Deep Core is not included in this number.

Bin number	E_{center} [MeV]	dE_{bin} [MeV]
0	2.000000E+00	4.000000E+00
1	4.658506E+00	1.317013E+00
2	6.192335E+00	1.759647E+00
3	8.231181E+00	2.327056E+00
4	1.094132E+01	3.093244E+00
5	1.454379E+01	4.111704E+00
6	1.933238E+01	5.465482E+00
7	2.569763E+01	7.265014E+00
8	3.415866E+01	9.657048E+00
9	4.540551E+01	1.283671E+01
10	6.035542E+01	1.706329E+01
11	8.022763E+01	2.268136E+01
12	1.066428E+02	3.014914E+01
13	1.417553E+02	4.007593E+01
14	1.884287E+02	5.327102E+01
15	2.504695E+02	7.081068E+01
16	3.329374E+02	9.412521E+01

Table 6.1: Tabel of the energy bins. The center energy of each bin along with the bin width is listed. The width of an energy bin is defined as $E_{\text{right}} - E_{\text{left}}$.

in mind to understand the expressions for the energy moments and total luminosities given in section 6.2.2.

As an example we show in fig. 6.1 how the differential number flux of neutrinos is distributed across energy bins at the time $t_{\text{pb}} = 10.5446\,\text{ms}$. The logarithmic spacing of energy bins is evident in the left panel. Less obvious is the pinching of the energy spectra, that we mentioned in chapter 5 was commonly seen in SN neutrino energy spectra. Calculating the pinching parameter of these data, however, show that they are also pinched as expected.

6.2.1 Doppler transformations

The energies and differential number fluxes coming from the numerical simulations are all in the comoving observer frame at a radius of 400 km, i.e. for someone following the infalling gas. The benefit of giving all the information as seen by a comoving observer is that the energy bins remain constant in size. However, this means that we need to take into account the Doppler change induced by changing observer frame from the comoving one to the static Earth. The Doppler change in the energy is given by

$$E_{\text{obs}} = \gamma(1 - v/c)E_{\text{emit}} = E_{\text{emit}}\sqrt{\frac{1 - v/c}{1 + v/c}} \tag{6.4}$$

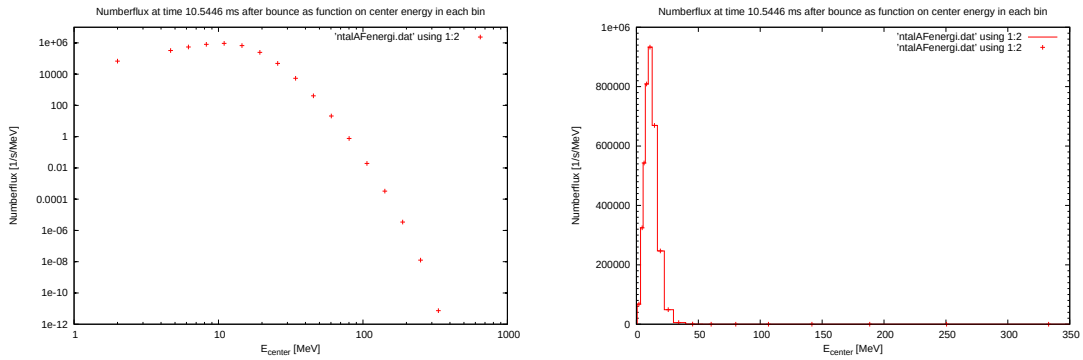

Figure 6.1: The number of neutrinos in a given energy bin at the time $t = 10.5446\,\text{ms}$. *Left:* Logarithmic scales. *Right:* Linear scale.

The velocity entering the Doppler formula should be larger than zero: $v > 0$, since the infalling gas is moving away from the static observer on Earth. And γ is the usual Lorentz factor

$$\gamma \equiv \frac{1}{\sqrt{1 - \frac{v^2}{c^2}}} \quad . \tag{6.5}$$

We define for the Doppler factor

$$\eta \equiv \sqrt{\frac{1 - v/c}{1 + v/c}} \tag{6.6}$$

Furthermore, one will need to take into account the corresponding time transformation that will happen

$$t_{\text{obs}} = t_{\text{emit}} \sqrt{\frac{1 + v/c}{1 - v/c}} = \frac{t_{\text{emit}}}{\eta} \tag{6.7}$$

Thus each time an energy quantity enters in the calculation of the energy moments below, a factor of η is associated with it, while time dependence provides a factor of η^{-1}. In the case of the differential neutrino flux dS (that we recall had units of 1/(s·MeV)), the two Doppler factors thus cancel out.

6.2.2 Calculating energy moments and total fluxes

After the appropriate Doppler transformation has been done, we proceed to calculate the energy moments, total luminosity and the total number flux for each time step from the differential number fluxes and the spectral information. We calculate the total luminosity, total flux and average energies for each of the three flavors: ν_e, $\bar{\nu}_e$ and ν_x. The higher order energy moments are only calculated for the $\bar{\nu}_e$, as only these are relevant for the IceCube event rate. In the following I have suppressed the information of the summations for simplicity. All summations run over the 17 energy bins, thus an index runs from 0 to 16.
The total number flux of neutrinos, $N(t)$, from all energy bins at a specific time is

$$N(t) = \sum_j dS_j(t)\, dE_j\, \eta \tag{6.8}$$

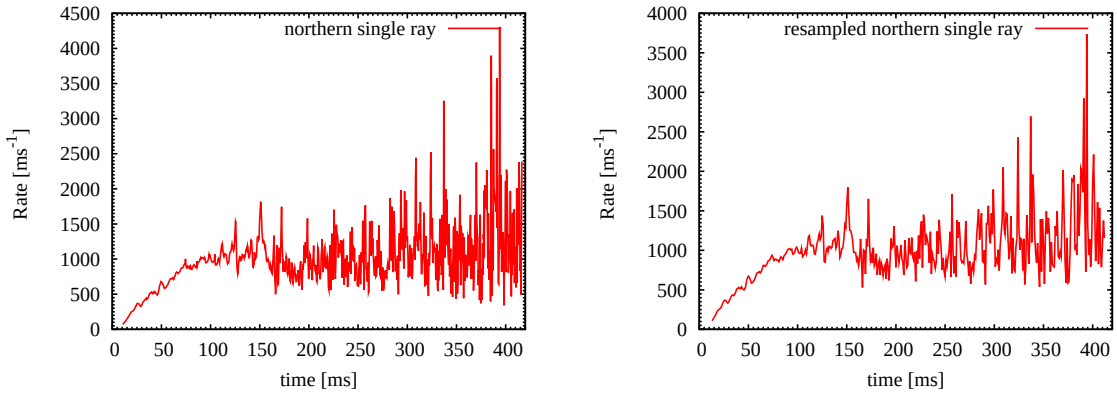

Figure 6.2: The event rate in IceCube calculated for the single northern ray. *Left:* From the original data. *Right:* Resampled at 1 ms intervals.

And the total luminosity at a given time is

$$L(t) = \sum_j dS_j(t)\, dE_j\, E_{\text{center,j}}\, \eta^2\, 1.60217646 \times 10^{-6}\text{erg/MeV} \tag{6.9}$$

where the factor of $1.60217646 \times 10^{-6}$ erg/MeV is merely a conversion factor.
From these two quantities the average energy, in MeV, is easily found:

$$\langle E \rangle = \frac{L(t)}{N(t)\ 1.60217646 \times 10^{-6}\text{erg/MeV}} = \frac{\sum_j dS_j(t)\, dE_j\, E_{\text{center,j}}\, \eta^2}{\sum_i dS_i(t)\, dE_i\, \eta} \tag{6.10}$$

In a similar manner the nth moment of the energy is found as

$$\langle E^n \rangle = \frac{\sum_j dS_j(t)\, E^n_{\text{center,j}}\, dE_j\, \eta^{n+1}}{\sum_i dS_i(t)\, dE_i\, \eta} \tag{6.11}$$

In later sections of this thesis we will be using the root mean squared energy, E_{rms}, that we define as

$$E^2_{\text{rms}} = \frac{\langle E^3 \rangle}{\langle E \rangle} \tag{6.12}$$

Where the averages are taken over the neutrino distribution function. This is an rms energy with respect to the energy spectrum, and not the flux spectrum. And as such it is slightly different from the more commonly used definition of the rms energy: $E_{\text{rms}} = \sqrt{\langle E^2 \rangle}$. However our definition matches the quantity that enters into the calculation of the IceCube event rate through the flux fudge-factor f_{flux} (eq. 6.2), and will therefore be used.

From the calculated luminosities and energy moments we can now calculate the event rate in IceCube, eq. 6.1, for our single ray. The resulting rate can be seen in fig. 6.2.

6.3 Resampling of event rate

The simulation data was given at uneven time intervals but with roughly a 0.5 ms spacing. IceCube on the other hand samples data in 1.6384 ms bins. We therefore found it convenient

to resample the event rate at the intermediate value of 1 ms. This will also facilitate an easier Fourier transform since the data points are now equally spaced in time. The bin width, or the absence of binning, will only affect the sensitivity to frequencies that we will anyway see are too high to be detected.

6.3.1 Gaussian interpolation and extrapolation

We decided to use a simple running Gaussian to resample our signal. The interpolation (and to a limited degree extrapolation for later data sets) between the original data points to find the function values for the new times was done in the following way.

We first define the new times t'

$$t'_k = t_{\text{init}} + \frac{k}{1000} \quad , \quad \text{where} \quad 0 \leq k < M \tag{6.13}$$

The offset t_{init} allows us to start at a time different from 0. The index k runs from 0 to M, the number of new data points we want. In the case of the single ray the resampled time stretch runs from 13 ms to 413 ms, so $M = 400$ and $t_{\text{init}} = 0.013\,\text{s}$.

The function value corresponding to this new time t'_k is then calculated by weighing all the original function values according to their distance from the point we are currently examining. Thus neighboring points will have a large influence on the new function value, but as one moves further away the function values will get less and less influence. The Gaussian weight w_i thus assigned to each original data point, at a time t_i, is given by

$$w_i = \frac{1}{\sqrt{\pi 2\sigma^2}} \cdot \exp\left(-\frac{[t'_k - t_i]^2}{2\sigma^2}\right) \tag{6.14}$$

And the resampled values for the event rate $R(t'_k)$ then become

$$R(t'_k) = \frac{\sum_{i=1}^{N} R(t_i) \cdot w_i}{\sum_{j=1}^{N} w_j} \tag{6.15}$$

Where N is the number of original data points.

Through this resampling we obtain values for the event rate in IceCube that has an evenly and **exact 1 ms spacing**. We will furthermore always choose M such that we get an **even number** of new data points $R(t'_k)$. We emphasize these two issues because in the Fourier transform they will become important.

We acknowledge that the smoothing was done in a simplistic way without any special consideration for the ends of the data sequence, where the Gaussian would "run out of" data on one side of the data point in question. It will have minimal effect though for our subsequent Fourier transform since we will in any case multiply our signal with a window function to suppress edge effects.

6.3.2 Choice of σ

Finding the appropriate value for σ, the standard deviation of the Gaussian, can be a difficult task. Choosing a value too large will smooth away all the details (fig. 6.3a), while a value too small will make the fitted function look "jagged" and square close to the data points (fig. 6.3c).

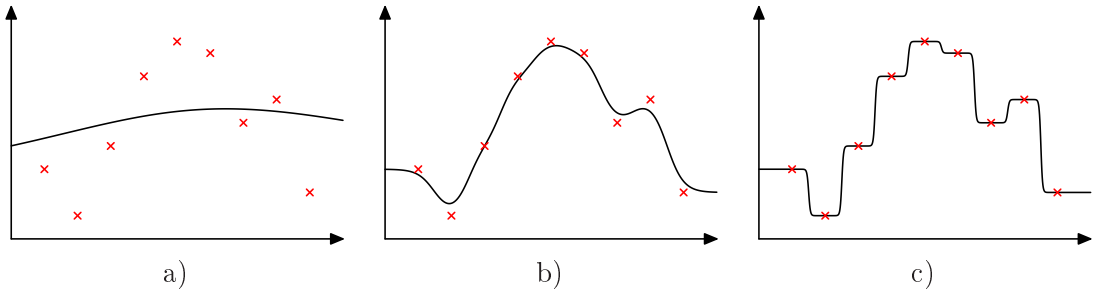

Figure 6.3: These three figures show the same data smoothed with a running Gaussian. The value of sigma decreases from left to right.

From a visual inspection and manual test of various sigmas, we ended up with $\sigma = 0.2236\,\mathrm{ms}$ (corresponding to $2\sigma^2 = 1 \times 10^{-7}\,\mathrm{ms}^2$) for the resampling of our data. We show in the left panel of fig. 6.4 the luminosity for all flavors after resampling, and the resampled $\mathrm{E_{rms}}$ for all 3 flavors can be seen in the right panel of fig. 6.4. The event rate for the $\bar{\nu}_e$ can be seen in its resampled version in the right panel of fig. 6.2. We see that the magnitude of the excursions have diminished slightly compared to the unsampled signal, as expected. Furthermore the most rapid fluctuations, primarily due to numerical noise, are gone. The main fluctuations, however, remain.

Using purely the information from a single ray to estimate the event rate in IceCube is actually a poor approximation of the full signal. We will later show (chapter 10) that there is significant variation in the magnitude of luminosity and energy fluctuations from ray to ray. The most extreme difference being between a polar and an equatorial ray.

6.3.3 Emulating a 1D signal

We wanted to be able to compare the resulting signals from the SASI model to a spherically symmetric, i.e. 1D, supernova model. We therefore decided to make a "super-smoothed" version

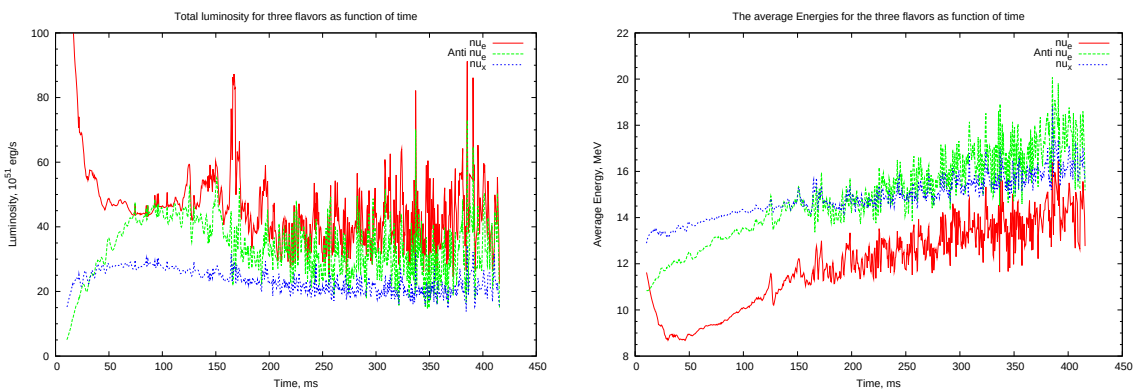

Figure 6.4: *Left:* Luminosity for all 3 neutrino flavors for the single ray at 5° from the north pole. *Right:* The average energies for all flavors. Red curves are for ν_e, green ones for $\bar{\nu}_e$ and blue for ν_x.

of our data. By taking an overly large value for σ all the fast time variations of the signal were removed, but the overall secular variation remained. This super-smoothed signal was our imitation of a signal from a spherically symmetric SN explosion. For the super-smoothed version we used $\sigma = 22.36\,\mathrm{ms}$ ($2\sigma^2 = 1 \times 10^{-3}\,\mathrm{ms}^2$), again found by visual inspection. The approximated 1D signals were primarily used in connection with the luminosities and rms energies to show the excursions due to the fast fluctuations. As the super-smoothing was done in the process of resampling the signals, all plots for the luminosities and energies consequently show 1 ms resampled versions.

In various instances for plotting purposes we also occasionally used a slightly smaller σ, $\sigma = 7.07\mathrm{ms}$ ($2\sigma^2 = 1 \times 10^{-4}\,\mathrm{ms}^2$). The reason is that it follows the original signal slightly more closely, as can be seen in e.g. fig. 10.2. Thus it highlights the excursions better, whereas the 1D emulated signal needed to be as featureless as possible beyond the slow secular variation: the familiar rise and fall off.

7

Fourier Transformation of the signal

In the previous chapter, we saw that fast time variations were present in the neutrino signal observed in IceCube. To better investigate these temporal variations of the event rate, we use a well established tool: the Fourier Transformation. In chapter 4 we outlined the basic principle of the Fourier transform. In this chapter we will specify the general considerations to our case, and state which definitions we use. We have only the need to Fourier transform a relatively small amount of data, and for transparency as well as the educational benefit, I wrote a C program from scratch to implement the Fourier transform instead of using a more general program, as e.g. the Fast Fourier Transform.

7.1 Basic quantities

Referring back to the notation from chapter 4 we make the following identifications for our resampled neutrino signal from section 6.3:

$$N_{\text{bins}} = 400 \tag{7.1}$$

$$\Delta = 1\,\text{ms} \tag{7.2}$$

$$T_{\text{tot}} = N_{bins}\,\Delta = 400\,\text{ms} \tag{7.3}$$

In later chapters the time duration T_{tot} will change but the principle remains the same. In our case the number of samples N will equal the number of bins N_{bins}. The time corresponding to each sample is identical to the resampled times

$$t_k = t_{\text{init}} + k\,\Delta \qquad , k = 0, 1, ..., N-1 \tag{7.4}$$

Here we have rewritten the expression in terms of Δ, the time between each sample, and we still have $t_{\text{init}} = 13\,\text{ms}$. As discussed in chapter 4 it is furthermore assumed that the signal

is periodic with the period T_{tot}. This is not strictly true in our case, but it is a technicality to make the discrete Fourier transform work. As a result of this assumption, we have the $g(t_{k=0}) = g(t_{k=N})$.

We stress that to minimize confusion we will from now on use f solely to denote frequencies, and functions of time will be denoted with g or h. In the frequency domain primarily capital letters will be used. The Fourier transforms of the functions $g(t)$ and $h(t)$ will thus be $G(f)$ and $H(f)$ respectively.

7.1.1 Nyquist frequency revisited

With our sample rate of 1 ms the highest frequency we can uniquely identify, cf. eq. 4.2, is

$$f_{\text{Nyq}} = \frac{1}{2\Delta} = \frac{1}{2 \times 1\,\text{ms}} = 500\,\text{Hz} \tag{7.5}$$

It is only possible to determine a finite discrete set of frequencies from a finite discrete set of data. For our discrete data set, we will therefore seek information on equally spaced frequencies between $f = 0$ and f_{Nyq} with a frequency spacing, δf, given by

$$\delta f = \frac{1}{T_{\text{tot}}} \tag{7.6}$$

The relevant frequencies are then: $f_m = m\,\delta f$, with $m = 0, \ldots, N_{f_{\text{max}}}$ where $N_{f_{\text{max}}} = f_{\text{Nyq}}/\delta f$. The natural frequency spacing for our model is thus 2.5 Hz, when our resampled time duration is 400 ms. Since $\delta f = 1/T_{\text{tot}}$ we have $N_{f_{\text{max}}} = N_{\text{bins}}/2$ and 201 frequencies in total.

7.2 Window function

When dealing with a finite segment of discrete data, edge effects can arise in the Fourier transform. These can be countered by the use of a window function. Several different types of window functions exits: the top-hat, Parzen, Hann and Welch window are the most common [PFTV86]. Each one has its strengths and weaknesses, especially when it comes to the rise and fall time of the window, and the amount of leaking it allows. Leaking is when power from one frequency bin "spills" into neighboring frequency bins, and the window function helps suppress leaking into bins far away. For the top-hat window the leaking is relatively large out to distant frequency bins, which made it undesirable for our purposes. Naturally we should have examined and evaluated thoroughly which other window would be best suited for our needs. However since our experience in signal processing was small, and since we did not need an *exact* power spectra we took to heart the statement of the book Numerical Recipes [PFTV86, p.425]: "However, at the level of this book, there is effectively *no difference* between any of these (or similar) window functions." Since we had initially tried with a Gaussian function for the window, which turned out to be a poor idea since it only goes to zero at infinity, we decided to take the window function with the highest similarity to the Gaussian: the Hann window.

7.2.1 The Hann window

The Hann window is defined by

$$w_j = \frac{1}{2}\left(1 - \cos\left[\frac{2\pi\, j}{N-1}\right]\right) \tag{7.7}$$

The index j runs from 0 to $N-1$, where the N intervals should cover the time span in question, i.e. equal N_{bins}. We clearly see that by construction this window goes to zero at the ends of the time interval, as opposed to the Gaussian. We normalize the window function independently, setting

$$W = \sum_{j=0}^{N-1} w_j \tag{7.8}$$

Furthermore since the sum over a cosine can be given in closed form

$$\sum_{n=0}^{N} \cos(nx) = \frac{\cos(\frac{1}{2}Nx)\sin(\frac{1}{2}(N+1)x)}{\sin(\frac{1}{2}x)} \tag{7.9}$$

we expect W to equal

$$W = \sum_{j=0}^{N-1} \frac{1}{2}\left(1 - \cos\left[\frac{2\pi\, j}{N-1}\right]\right) \tag{7.10}$$

$$= \frac{1}{2}\left(N - \frac{\cos(\pi)\sin(\pi\frac{N}{N-1})}{\sin(\frac{\pi}{N-1})}\right) \tag{7.11}$$

$$= \frac{1}{2}\,(N-1) \tag{7.12}$$

Thus the normalized weight are given by[1]

$$w'_j = \frac{w_j}{W} = \frac{1 - \cos\left[\frac{2\pi\, j}{N-1}\right]}{N-1} \tag{7.13}$$

Where

$$\sum_{j=0}^{N-1} w'_j = 1 \tag{7.14}$$

However due to numerical machine precision issues in the actual Fourier transform code we did not use this analytic version of the summed weights but instead calculate the weights for each run, as given by eq. 7.8. It should be quite clear that with this definition and normalization of the window function, the weights will only depend on the total time duration of our data set and the bin width (since this will dictate the number of weights w_j). Therefore one could equally well use a different window function instead of eq. 7.7 without it having any impact on the underlying programming calculations. By construction our FT-program is therefore capable of using either a top-hat window, a top-hat on half the signal width, a Gaussian or a Hann window, and could easily be altered to deal with other window functions.

[1] This little calculation also shows that the apparently different definitions of the Hann window given here and in our paper, is non-existent, when the window weight is normalized.

7.3 Definition of Fourier Amplitude

Coming now to the definition of the Fourier Amplitude, $H(f_g)$, for a given frequency f_g, we choose not to use the sinusoids as basis functions, as was primarily used in chapter 4. We will instead use the equivalent exponential basis functions: $e^{i\,2\pi\,z}$, as this simplifies the writing of the Fourier transform code. For a signal $h(t)$ sampled at N times, t_k, our definition of the Fourier amplitude $H(f_g)$ is therefore

$$H(f_g) = \Delta \sum_{k=0}^{N-1} h(t_k) \frac{N \cdot w_k}{W}\, \mathrm{e}^{(2\pi \mathrm{i}\, t_k\, g/T_{tot})} \tag{7.15}$$

Where t_k was defined in eq. 7.4, and where the factor $N \cdot w_k/W$ is from the normalized window function. As was discussed in section 4.2.2, the power for the frequencies between f_{Nyq} and $2f_{\mathrm{Nyq}}$ will be a mirror image of the power for the frequencies between 0 and f_{Nyq} (mirrored around the Nyquist frequency). Due to this mirroring we can effectively move the power that belongs to the "negative" frequencies up to be allocated above the Nyquist frequency. The frequencies f_g are given by g/T_{tot} as remarked above, but g now runs from 0 to $N_{bins} - 1$, i.e. to 399. This will all become clearer in the following section on the definition of the power spectrum, 7.4. In our case Δ is in ms and the rate (denoted by $h(t_k)$) is in events/ms, meaning that the resulting Fourier amplitude $H(f_g)$ will be unit-less.

7.4 Definition of spectral power

From our definition of the Fourier amplitude (eq. 7.15) the square of the Fourier amplitude is

$$A(f) = |H(f)|^2 = H^*(f)H(f) \tag{7.16}$$

where the asterisk denotes complex conjugation. This leads to our definition of the spectral power

$$\begin{aligned} P(0) &= \frac{|H(0)|^2}{N_{\mathrm{bins}}^2} \quad for\, f = 0 \\ P(f_{\mathrm{Nyq}}) &= \frac{|H(f_{\mathrm{Nyq}})|^2}{N_{\mathrm{bins}}^2} \\ P(f_k) &= \frac{|H(f_k)|^2 + |H(-f_k)|^2}{N_{\mathrm{bins}}^2} = 2\,\frac{|H(f_k)|^2}{N_{\mathrm{bins}}^2} \quad for\, k = 1, .., N_{f_{\max}} \end{aligned} \tag{7.17}$$

The second equality in the definition of $P(f_k)$ applies when the transformed function is real (because $|H(-f)|^2 = |H(f)|^2$), as in the case of the event rate in IceCube. Since the exponential $e^{i2\pi t_k f_g}$ in eq. 7.15 is 2π-periodic we can also write this as: $H(-f_k) = H(f_{N-k})$. This shows the concept of "moving power" from the negative frequencies to frequencies above the Nyquist frequency discussed in section 7.3 above. With our definition of power, the power $P(0)$ for the $f = 0$ component (also known as the DC component) will then equal the square of the number of events *per* bin, $(N_{\mathrm{events}}/N_{\mathrm{bins}})^2$. If we change the total time duration, but keep the bin size the same, we will therefore not find a change in the DC component of the power.

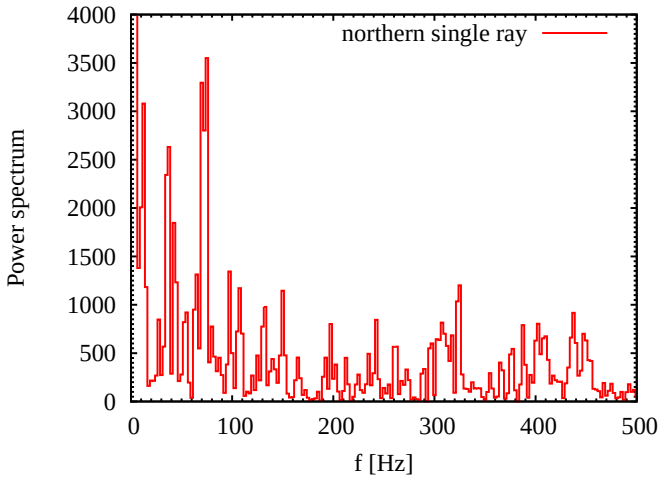

Figure 7.1: Power spectrum for a single northernly ray.

I would like to emphasize that this definition is just one of many ways to define spectral power, but this is how *we* define it. The chosen definition of the spectral power naturally will not influence the comparison between the power spectra we generate, but should be kept in mind when comparing to results from other authors.

7.5 Fourier spectrum of single ray signal

With all the relevant definitions in place, and having tested our final Fourier transform code by applying Parseval's identity to check that the results in the frequency domain were consistent with the time domain signal, we are ready to show the results of our Fourier transform applied to the single ray signal. In fig. 7.1 we show the power spectrum of the neutrino event rate in IceCube, based on data from a single northernly ray.

8 Noise

In our search for significant structure in the fluctuating event rate signal in IceCube, we need to make sure that we will not confuse the intrinsic shot noise of the signal with the actual SASI induced fluctuations. Furthermore we need to make sure the shot noise of the background dark current in IceCube will not cause us trouble either. To determine the impact of shot noise from the IceCube background, we will calculate the average power level due to the background noise. Since the background noise is inherently random, we expect the power contribution to be a flat level independent of frequency, and characteristic of white noise. In order to do this, we will first make a theoretical estimate of the average power level that will be contributed by the shot noise of the background noise in IceCube over the time-duration of our measurement. Thereafter we will make 100 Monte Carlo realizations of the background noise and test the analytic equations.

8.1 Signal shot noise

The average counting rate we register will be influenced by the fact that we only have one realization of the signal, and that each event is intrinsically a random process. Thus if we on average measure 400 counts per second, we will in some seconds only measure 383 counts or 398 counts, and in other seconds maybe measure 412 counts. This fluctuation of the *observed* count rate compared to the average rate is called shot noise. The shot noise of a signal is equal to the square root of the total number of events in a given time.

$$N_{\text{shot}} = \sqrt{N_{\text{total}}} \tag{8.1}$$

The shot noise is also occasionally called Poissonian noise.

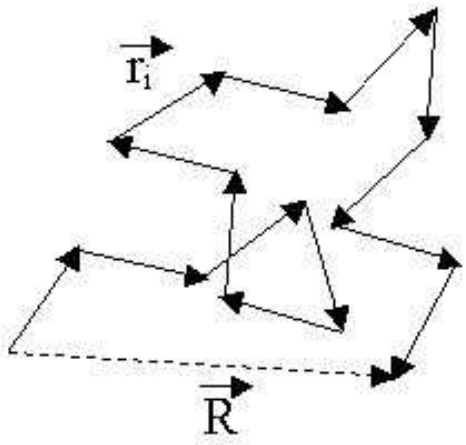

Figure 8.1: Random walk with 14 steps.

For our actual SASI signal, which has an even rate of ∼900 ms^{-1}, the shot noise is 30 events. This corresponds to ∼3% of the signal and is thus much smaller than the SASI induced fluctuations of ∼36%, for the non-rotating 15 $M_\odot$ model with the LS EoS. We are therefore not at risk of confusing these these random shot noise fluctuations about the mean of our signal with the actual fluctuations caused by the SASI and convective overturns. It can furthermore be shown that a Fourier amplitude of 1% of the average signal can be seen with our method. The amplitudes we actually find are much larger than this.

8.2 Theoretical estimate of shot noise power level for IceCube background

To make an analytic estimate of the average power level contributed by the shot noise of the background in IceCube, we first take a look at the Fourier transform of a signal consisting of one individual "blip" arriving at N different but sequentially ordered times t_j. Turning to our definition of the Fourier transform (eq. 7.15) written in a more general form

$$G(f) = \sum_{j=0}^{N-1} g(t_j)\, e^{i2\pi f\, t_j} \tag{8.2}$$

and denoting as before the square of the Fourier amplitude with A; $A(f) = |G(f)|^2$, we easily see that naturally $G(0) = N$. So the Fourier amplitude for $f = 0$ equals the total number of events, and $A(0) = N^2$. This equation can also be viewed in terms of a random walk in the complex plane, see fig. 8.1, where each step $e^{i2\pi f\, t_j}$ has a length of 1. The Fourier amplitude squared $A(f)$, is then the square of the final distance. And from statistical mechanics we know that the square of the final distance of a random walk is normally distributed, i.e. it is less likely we will get very far from the origin because then all the steps should be in more or less the same direction, and that is unlikely if any direction has equal probability for a given

step. From the random walk analogy we thus know, that the probability for a given A, will be given by $p(A) = N^{-1}e^{-A/N}$, and the average expected value will be $\langle A \rangle = N$, independent of frequency. Dividing the average value $\langle A \rangle$ for $f \neq 0$ with the square of the Fourier amplitude for $f = 0$, we get

$$\frac{\langle A_{f\neq 0} \rangle}{A_{f=0}} = \frac{N}{N^2} = \frac{1}{N} \tag{8.3}$$

The leads us to the expectation, that for the shot noise the average Fourier amplitude squared divided by the DC value should equal $1/N$, where N is the total number of events.

Extending this random walk image to the case where a window function is applied, the step size will no longer be constant. The Fourier amplitude is now given by

$$G(f) = \sum_{j=0}^{N-1} w_j \, g(t_j) \, e^{i2\pi f \, t_j} \tag{8.4}$$

where the weight w_j comes from the Hann window, as described in section 7.2, and where the average weight is unity. Since the step size is no longer unity, the steps must be combined in quadrature, and the average value of A will then be $\langle A \rangle = N \langle w^2 \rangle$. For the specific use of the Hann window, we have

$$\langle w^2 \rangle = \frac{3}{2} \tag{8.5}$$

When a window function is included equation 8.3 is modified to

$$\frac{\langle A_{f\neq 0} \rangle}{A_{f=0}} = \frac{\langle w^2 \rangle \, N}{N^2} = \frac{3/2}{N} \tag{8.6}$$

Showing that with a window function the power level of the shot noise will increase. In the specific case of the Hann window it will increase by a factor 3/2.

8.2.1 Application to our data

From the above considerations we can now calculate the average power for the shot noise in IceCube, over a time stretch of τ ms and with the use of a Hann window. Using eq. 8.6 and the fact that power in our definition is related to the square of the Fourier amplitude with a factor of $2/N_{\text{bins}}^2$ (eq. 7.17) for frequencies not equal to 0 or f_{Nyq}, we find

$$\langle A_{f_k} \rangle = \frac{3/2 \; A_{f=0}}{N_{\text{bckgr}}} \quad \Rightarrow$$

$$P_{\text{shot, avg, } f\neq 0} = \frac{2}{N_{\text{bins}}^2} \frac{3/2 \; A_{f=0}}{N_{\text{bckgr}}} = \frac{2}{N_{\text{bins}}^2} \frac{3/2 \, N_{\text{bckgr}}^2}{N_{\text{bckgr}}} \quad \Rightarrow$$

$$P_{\text{shot, avg, } f\neq 0} = \frac{3 N_{\text{bckgr}}}{N_{\text{bins}}^2} \tag{8.7}$$

The number of background events is given by $N_{\text{bckgr}} = \tau \cdot \Gamma_{\text{noise}}$, where $\Gamma_{\text{noise}} = 1344\,\text{ms}^{-1}$. Inserting in the general equation 8.7 the $\tau = 400$ ms time duration for our 15 $M_\odot$ model, and

$N_{\text{bins}} = 400$, we find the average shot noise power level to be

$$P^{15M_\odot}_{\text{shot,avg}} = \frac{3N_{\text{bckgr}}}{N^2_{\text{bins}}} = \frac{3 \times 5.4 \times 10^5}{400^2} = 10.08 \tag{8.8}$$

8.3 Numerical tests of analytic results

In order to test the analytic results, eqs. 8.3, 8.6 and 8.8, given in the above section we made 100 Monte Carlo realizations of the background noise, and took the Fourier transform of them. The realizations of random noise, that will have a Poissonian distribution, was produced via the Marsaglia Polar method as outlined below.

8.3.1 The Poisson distribution

The IceCube background noise is a set of events that happen independently of each other. And to describe such independent events one most often uses the Poisson distribution. It gives the probability that a specific number of events will happen within a given time period, when these events happen at a known average rate, and when the events are happening independently of the time passed since the previous event. The Poissonian is given by

$$P_\lambda(k) = \frac{\lambda^k\, e^{-\lambda}}{k!} \tag{8.9}$$

Where P is the probability that you will get k events if the mean of the distribution (the averaged expected number of events) is λ, with of course $\lambda > 0$. And naturally k has to be a non-negative integer. The variance of the Poisson distribution is $\sigma^2 = \lambda$. Let us take a quick illustrative example: a car dealer normally sells 5 cars a day. What is the probability that he will sell exactly 7 cars? Now $\lambda = 5$ and $k = 7$, and the probability is $P_5(7) = 10.4\%$.

If the mean λ is sufficiently large (say $\lambda > 1000$) then the Poisson distribution is excellently approximated by the normal distribution (using $\sqrt{\lambda}$ as the standard deviation σ). The corresponding normal distribution (or Gaussian) will be

$$g(t) = \frac{1}{\sqrt{\pi 2\sigma^2}} \exp\left[-\frac{(t-\mu)^2}{2\sigma^2}\right] \tag{8.10}$$

Since we need a Poissonian distribution of background noise in IceCube that will have a mean of 1344 events per ms, we will be justified in using a normal distribution to generate the realizations of the fluctuating noise.

8.3.2 Generating noise with the Marsaglia Polar method

To generate the required noise realizations we will implement the Marsaglia Polar method. Each time the Marsaglia Polar method is employed it generates a pair of independent random numbers. This is done by choosing numbers (x, y) in the ranges; $-1 < x < 1$ and $-1 < y < 1$ until the condition

$$\rho = x^2 + y^2 < 1 \tag{8.11}$$

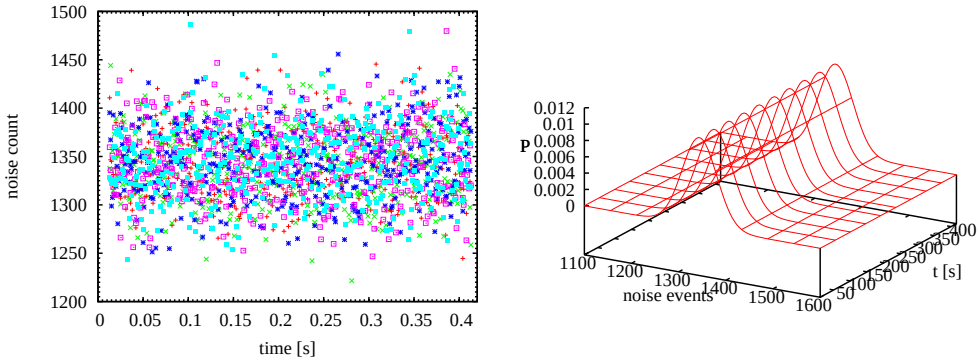

Figure 8.2: *Left:* 5 different realizations of background noise drawn from a normal distribution, made with the Marsaglia Polar method. *Right:* Illustration of how the probability distribution for the number of noise points look at each instance of time.

is satisfied. Then the initial numbers will be normalized according to

$$x' = x \cdot \sqrt{\frac{-2 \ln \rho}{\rho}} \tag{8.12}$$

(similarly for y) and provided as output. All the outputted numbers (x', y') from the Marsaglia Polar method will lie between -∞ and ∞ [1] distributed according to a normal distribution, thus fulfilling our need. We then scaled up this normalized output to be centered on $\lambda = 1344$ instead of 0, and to have a standard deviation of $\sigma = \sqrt{\lambda} = \sqrt{1344} \sim 37$. A noise point or noise value, s, for the background is then given by:

$$s = \lambda + \sqrt{\lambda}\, x' \tag{8.13}$$

In this way we generated 400 noise values, s, and assigned each one to a specific time corresponding to the times in our data. The noise values thus corresponds to the number of background counts each millisecond, for each of the 400 milliseconds that our data cover. In total we made 100 realizations of these 400 ms long runs, effectively mimicking 100 different representative ways the noise could behave in IceCube while we gather our data. An example of 5 different noise realizations generated in this way is provided in fig. 8.2 (left), and in the right part of this figure we show for each instance in time, the Gaussian probability distribution for the noise count.

8.3.3 Numerical shot noise power level

With these 100 realizations we then tested the equations given in section 8.2, by making one Fourier transform without the use of a window function (equivalent to using a top-hat window) and then subsequently making another Fourier transform of all 100 realizations, this time with a Hann window. We show in fig. 8.3 the power for a given frequency averaged over all of the 100 noise realizations, divided by the DC component. Effectively this is the inverse of the two

[1] In theory at least, in reality the computer has a finite precision and cannot go to $\pm\infty$.

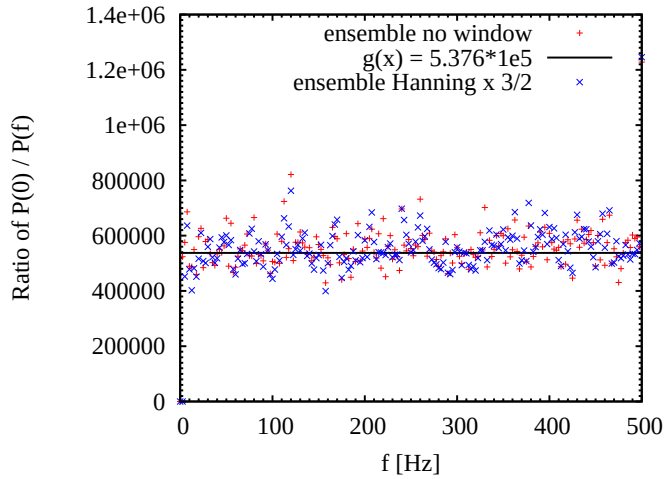

Figure 8.3: Numerical tests illustrating eq. 8.3 (red) and 8.6 (blue).

equations 8.3 and 8.6. The black line is at the $N_{\text{bckgr}} = 5.376 \times 10^5$ level, and the red markers show the power version of the inverted eq. 8.3 (remember our factor $2/N_{\text{bins}}$ for the power for $f \neq 0$ and $f \neq f_{\text{Nyq}}$). The blue markers are equivalently the power analogue of the inverse eq. 8.6. We see that even with this relative low number of realizations the ensemble averages divided by the DC component conforms quite nicely to the theory.

8.3.4 Ensemble average of power

To verify eq. 8.8, which gave the estimate of the overall power level of the noise for our specific model, we made an ensemble average of the noise power spectra. We added the power for each frequency from each realization and divided by the number of realizations. We show an example of the Fourier transform of 3 realizations in fig. 8.4 (red, green, blue lines) alongside the ensemble average of the Fourier transform of all the 100 realizations (black line). We see that as expected from eq. 8.8 the level of the shot noise power is at ~ 10 in our units, and roughly independent of frequency as expected for white noise. The ensemble averaged value for the power given by eq. 8.8, and corroborated by fig. 8.4, is what will appear as our "background" line in the power spectra to be shown in the following chapters.

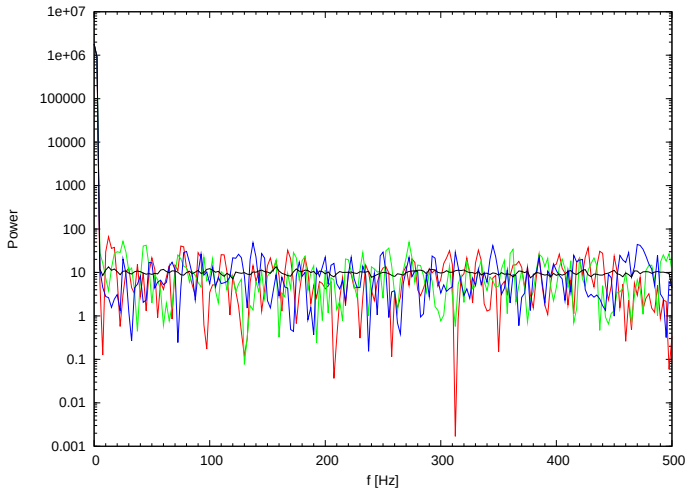

Figure 8.4: Power spectra of 3 of the noise realizations from fig. 8.2 (blue, red and green lines) and the power spectrum of the ensemble average (black line).

9
Data on multiple rays

The work on the single ray data allowed us to optimize our FT routine and get a good understanding of the data as well as the effect of shot noise. However, as stated in the beginning of chapter 6, the idea was to eventually extend the analysis and look at all the rays comprising a hemisphere. As was also stated there, the amount of data corresponding to the full spectral energy information on every ray made that approach infeasible, particularly as long as our main purpose was only to demonstrate that the fast time-variations of the neutrino signal could be seen in IceCube data. We therefore decided on a different approach where we only use the rms energy and luminosity on each ray.

We rewrite the expression in eq. 6.1 for the event rate accordingly, such that it only depends on anti-electron neutrino luminosity and rms energy, and the distance to the supernova. In this revised formulation, the 4800 DOMs of IceCube are explicitly included and updated values for IceCube's detection efficiencies [KGftIC09] gives a value of 0.72 for the detector fudge factor [HR09]. The resulting equation for the event rate is thus

$$R_{\bar{\nu}_e} = 114 \text{ ms}^{-1} \frac{L_{\bar{\nu}_e}}{10^{52} \text{ erg s}^{-1}} \left(\frac{10 \text{ kpc}}{D}\right)^2 \left(\frac{E_{\text{rms}}}{15 \text{ MeV}}\right)^2 . \tag{9.1}$$

Where E_{rms} is given by the definition in eq. 6.12. We will again consider a supernova at the fiducial distance of 10 kpc.

9.1 Hemispheric averaging

The true observed signal would be the integrated neutrino emission over the hemisphere facing the observer. With access to the detailed angular spectral energies and differential number fluxes, we could have reconstructed the expected signal. However, having opted for the less

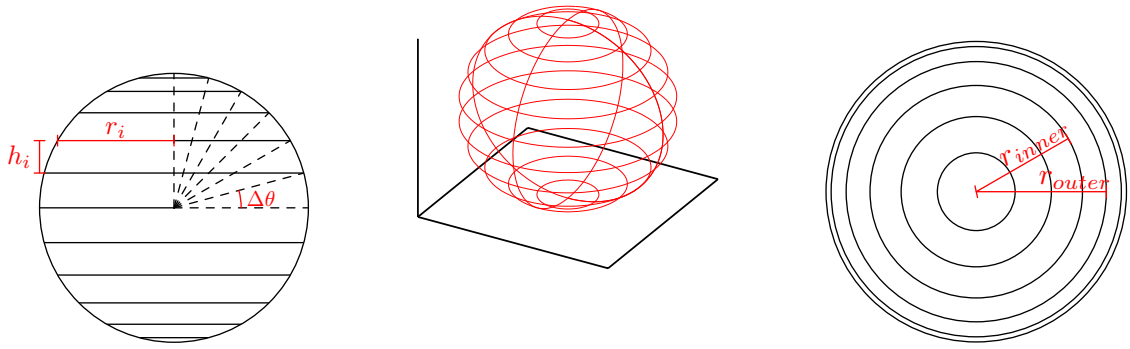

equatorial view 3D view polar view

Figure 9.1: Illustration of the weights used in our hemispheric averages. *Middle:* a sphere in 3D. *Left:* The 2D projection of the sphere when viewed towards the equator. *Right:* The 2D projection of the sphere when viewed towards a pole. In the black figures the angle between each line or circle is 15°.

data heavy approach we will use a simplification. We will assume that each surface element radiates isotropically with an energy spectrum corresponding to the local conditions, and then we will make a hemispheric average over all surface elements. This approximation to the true signal is resonable since 2D simulations as well as the "ray-by-ray plus" transport scheme are only approximative themselves. We weigh the emission from each ray by the projected area a surface of revolution of the ray covers on a disk, relative to the area of the full disk. We set the radius of our disk to 1, giving a total area of π. So all surface elements, dA, should be divided by π. The sum of all weights will then be one, ensuring a correct normalization.

As the extreme cases we will investigate the hemispheric averages corresponding to a viewing direction either towards the equator of our SN or towards one of the poles. These choices corresponds to the directions where we expect the weakest, respectively strongest, signal fluctuations according to the numerical simulations of the SASI.

Below we give the equations used in calculating the hemispheric averages with the luminosity as an example. The luminosity we get on each ray is the 4π equivalent, thus to get the emission corresponding to just a little part of the sphere we need to divide by 4π. The number of rays for the 15 $M_\odot$ model in consideration is 96. Each ray therefore covers an angle, $\Delta\theta = 1.875°$.

9.1.1 Equatorial average

A full 2π revolution of 12 rays covering a hemisphere is illustrated in the middle figure of fig. 9.1. A view towards the equator will give a projected picture corresponding to the left figure of fig. 9.1. The area dA_i corresponding to each ray will appear as a strip across the disk. The luminosity corresponding to a given surface segment dA_i will be $L_i = \frac{L_{i,4\pi}}{4\pi}$. The weight due to the fractional area will be $w_i = dA_i/A$ where dA_i is given by $dA_i = 2\,r_i\,h = 2\sin\theta_i(\cos\theta_i - \cos\theta_{i+1})$, (illustrated in fig. 9.1), where θ is the polar angle measured from the

north. Finally we have $w_i = \frac{2}{\pi}\sin\theta_i(\cos\theta_i - \cos\theta_{i+1})$, and the total equatorial hemispheric averaged luminosity will be:

$$L_{\text{equ}} = \sum_{i=0}^{N_{rays}-1} \frac{1}{2\pi^2} L_{i,4\pi} \sin\theta_i \left(\cos\theta_i - \cos\theta_{i+1}\right) \quad \text{, with } N_{rays} = 96 \tag{9.2}$$

Replacing the explicit use of the luminosity with a generic function $g_n(t)$ that is a function of time t, and ray number n, leads to the expression

$$g_{\text{equ}}(t) = \sum_{n=0}^{N_{rays}-1} g_n(t)\,\frac{2}{\pi}\sin(n\Delta\theta)\,\left(\cos(n\Delta\theta) - \cos((n+1)\Delta\theta)\right) \quad \text{, with } N_{rays} = 96 \tag{9.3}$$

The ray number n is related to the angle since each ray has a width of $\Delta\theta = 1.875°$.

9.1.2 Polar averages

For the polar averages each ray will correspond, not to a strip across a disk as with the equatorial case, but to an annulus, see the right panel of fig. 9.1. The corresponding weights will be different, and the summation will no longer run over all the rays, but rather only those corresponding to the northern (southern) hemisphere, $0 \leq n \leq 48$ ($48 \leq n \leq 96$). Here it is important to stress that $n = 48$ corresponds to 90°, i.e. the equator. Remembering that $R = 1$ for our sphere so the total visible disk has the area $A = \pi$, each annulus will have an area of $dA_i = \pi(r^2_{outer} - r^2_{inner})$. For the northern part this equals

$$dA_{i,north} = \pi(sin^2(\theta_{i+1}) - sin^2(\theta_i))$$

Whereas since θ is measured from the north pole the southern version becomes

$$dA_{i,south} = \pi(sin^2(\theta_i) - sin^2(\theta_{i+1}))$$

With our dummy function $g_n(t)$ the northern polar hemispheric average becomes

$$g_{\text{north}}(t) = \sum_{n=0}^{48} g_n(t)\,\left(\sin^2((n+1)\Delta\theta) - \sin^2(n\Delta\theta)\right) \tag{9.4}$$

and the southern hemispheric average is

$$g_{\text{south}}(t) = \sum_{n=48}^{N_{rays}-1} g_n(t)\,\left(\sin^2(n\Delta\theta) - \sin^2((n+1)\Delta\theta)\right) \tag{9.5}$$

Clearly the sum of the weights equal one.

9.2 Ensemble average of rays

Calculating the northern hemispheric average of the IceCube event rate from the prescription given above and then calculating the power spectrum of the hemispheric averaged signal leads to the red curve in fig. 9.2. The power spectrum for the southern hemispheric average is very

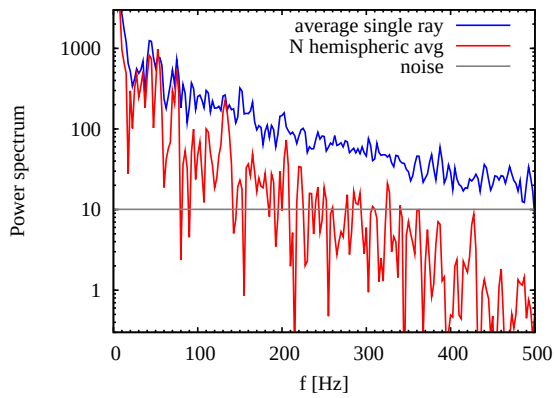

Figure 9.2: Power spectrum of the IceCube event rate for our model (EoS of Lattimer & Swesty) in 2.5 Hz increments. Blue line: Average single-ray power spectrum. Red line: northern hemispheric average. Horizontal line: Shot noise from IceCube dark current.

similar. The blue line in the figure is the power spectrum for an ensemble averaged single ray. The ensemble single ray was computed by taking the simple average over the power spectra of all 96 rays with equal weights. This average represents viewing each ray as responsible for the full 4π emission and thus the observed detector signal, without consideration of corresponding surface areas. The single ray power spectrum we computed in chapter 7 is an example of such a 4π ray power spectrum. The power spectra for a true single ray shows the same trend as the ensemble averaged ray, although much noisier and of course with directional differences.

Comparing the two curves we see that the power for the average single ray stays above the power level of IceCube background noise up to the Nyquist frequency. For the northern hemispheric average the spectral power declines much more rapidly. This is expected because high frequency variations are due to the incoherent "boiling" of the matter on small scales. The lower frequencies are instead due to large scale convective overturn and the SASI and as such strongly correlated. With the hemispheric average we therefore effectively average out the uncorrelated small scale motions of the matter, whereas the correlated motions on larger scales are not suppressed.

9.3 Power level smoothing

We choose to do a smoothing of the power spectra in the frequency domain since the power spectra shown in fig. 9.2 are quite noisy and the general trend is slightly obscured. We are mainly interested in the overall features of the signal, and the rapid fluctuations obscure these features. Furthermore we already know from section 7.2, that to a certain degree one frequency bin will "leak" power into neighboring bins. Therefore the power level smoothing will enhance the features we are looking for at the cost of detailed resolution which is unimportant for us in this study.

For the smoother curve in frequency space we still want to keep the frequency points that we initially had. Frequencies should thus start at $f = 0$ and increase in increments of $\delta f = 2.5$ Hz. To attain this we do a smoothing with at running Gaussian, similar to the one described in

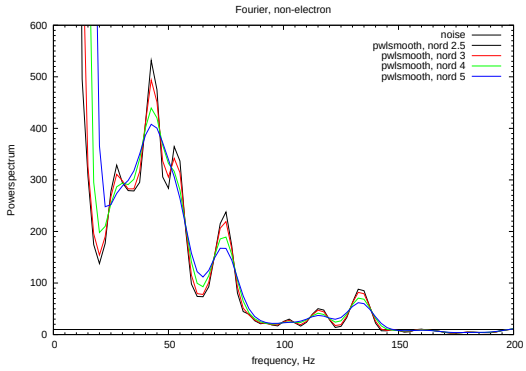

Figure 9.3: The north polar hemispheric averaged power spectra smoothed with a running Gaussian. The different curves corresponds to different values of sigma. This is for the LS EoS and non-electron flavor.

section 6.3 for the resampling of the calculated event rates. The new "power-level-smoothed" power for a frequency f_g is therefore

$$P_{new}(f_g) = \frac{\sum_{i=0}^{N_{f_{\max}}} w_i \cdot P_{old}(f_i)}{\sum_{j=0}^{N_{f_{\max}}} w_j} \tag{9.6}$$

where

$$w_i = \frac{1}{\sqrt{\pi 2\sigma^2}} \cdot \exp\left(-\frac{(f_g - f_i)^2}{2\sigma^2}\right) \tag{9.7}$$

Here $N_{f_{\max}} = 200$ so $f_g = g\,\delta f$ ranges from 0 to $f_{\mathrm{Nyq}} = 500\,Hz$[1].

Again one could probably have chosen some mathematical definition of a good σ, but I tried with 5 different sigmas and looked at the resulting curves. From a purely subjective point of view I then choose the σ, I found best. "Best" meaning that the chosen smoothing length would eliminate the fast fluctuations from frequency bin to frequency bin, but keeping the general undulations of the overall signal. I tested sigmas of 2.5, 3, 4 and 5 Hz, as can be seen in fig. 9.3, and decided that 2.5 and 3 Hz left too much of the jaggedness of the function. Both a sigma of 4 and 5 Hz could be used, and a $\sigma = 4$ Hz was chosen as it preserved more of the overall trend.

In fig. 9.4 we show the power level smoothed versions of the average single ray and northern hemispheric averages from fig. 9.2, along with the equatorial average (black curve). The power for the equatorial average is much lower than the other two curves. In this model the large scale SASI motions were primarily along the polar axis (symmetry axis) which can account for the much larger polar than equatorial power. Furthermore luminosity and temperature variations in the north and south would be anti-correlated. Therefore they would cancel partially in the equatorial average. The 2D axisymmetric nature of this model forces the dipolar motions to be along the polar axis, whereas in a realistic 3D simulation no such confinement of the

[1] We only let g run to $N_{f_{\max}}$ since, as previously explained in section 4.2.1.1 the power spectrum between 500 Hz and 1000 Hz is just a mirror reflection of the power spectrum between 0 Hz and 500 Hz.

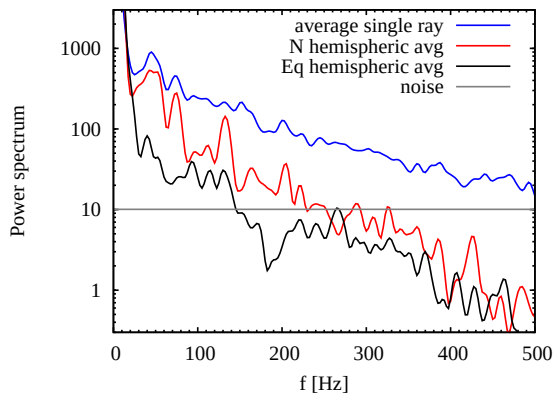

Figure 9.4: Same as Fig. 9.2 with smoothing by a moving average with a Gaussian window function of width $\sigma = 4$ Hz. Average power of all 96 single rays (blue), northern hemispheric average (red), and equatorial hemispheric average (black), from top to bottom.

dipolar motions is present. It is therefore quite unlikely that such a dramatic difference due to viewing direction would be manifest in 3D simulations.

We notice that the hemispheric averages go towards zero as they approach the Nyquist frequency, thus implying we have a proper sampling of the signal. The average ray, however, does not go to zero implying a degree of aliasing. This makes sense since we will expect power on higher frequencies corresponding to mass motions on small scales. For the hemispheric average we have averaged out these small scale motions effectively minimizing the power on these scales.

10

Non-rotating 15 $M_\odot$ model

The previous chapters have outlined the tools we have used. Let us now turn to results we have obtained from employing the described methods. This chapter will cover the results of our analysis applied to a 15 $M_\odot$ model without rotation and with two equations of state. A majority of what follows in this chapter has been published in Physical Review D in the paper "Fast time-variations of supernova neutrino fluxes and their detectability" [LML+10]. The paper has been written in collaboration with A. Marek, T. Janka, G. Raffelt and C. Lunardi. The paper is appended in appendix B.

We investigated the expected time varying signal due to supernova neutrinos that would be observed in the IceCube Cherenkov detector. We base our calculations on simulation results for the 15 $M_\odot$ model from Marek et al. [MJM08] with 2 equations of state: namely the softer Lattimer & Swesty and the stiffer Hillebrandt & Wolff EoS. The former run covers a time stretch of 10.2–417 ms post bounce and the latter a time duration of 4.16–396.4 ms, both with the information given with roughly 0.5 ms intervals. The model is calculated on 192 rays, and we use in our calculations every second ray, resulting in 96 rays in total.

We illustrate the anti-electron neutrino energies and luminosities resulting from this simulation in fig. 10.1 for both EoSs. To show the angular dependencies of the quantities (and through them the angular dependence of the event rate) we have collected the information from the individual rays into 5 different wedges, each spanning 19 rays (20 for the northern one) corresponding to a zenith angle range of 36°, and giving the corresponding simple average of the value in question. The 5 wedges are: a northern one, an equatorial one, a southern one, and one wedge inbetween each of the polar ones and the equatorial one. Clearly there are strong directional differences, with the excursions in the luminosity and energy being largest for the polar directions, well in correspondence with the primarily polar excursions of the shock front evidenced in the numerical simulations. We emphasize that this figure is solely for illustration purposes and does not reflect any observed quantities.

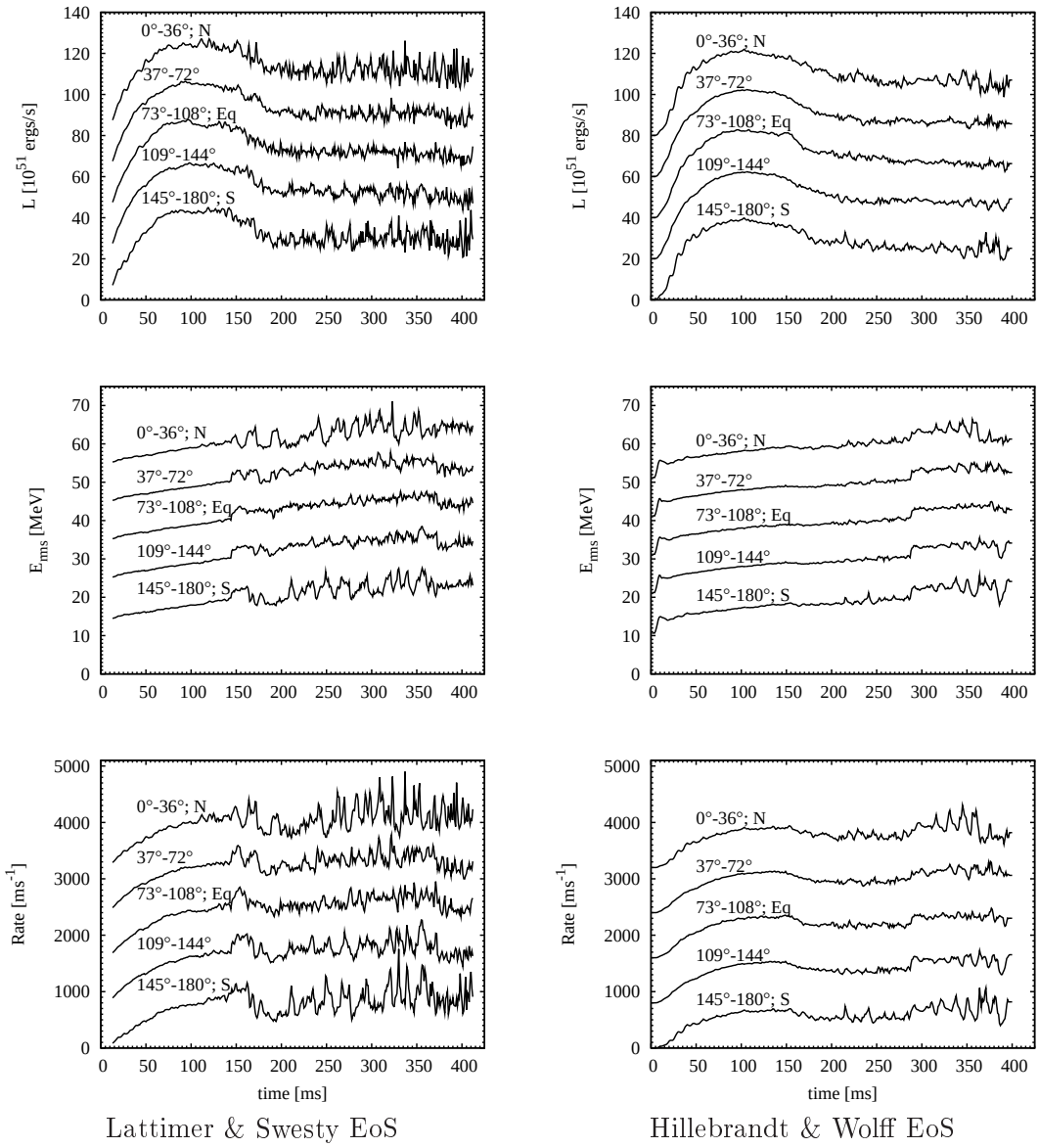

Figure 10.1: *Left:* Luminosity, rms energy and IceCube event rate based on the $\bar{\nu}_e$ fluxes of our model with Lattimer & Swesty EoS. The 96 angular rays have been combined into five averages ranging from north (top curve) to south (bottom curve), where in each panel the curves are offset relative to each other by 20, 10 and 800 units of the vertical axes, respectively. *Right:* Same as left column but for a run with the EoS of Hillebrandt & Wolff.

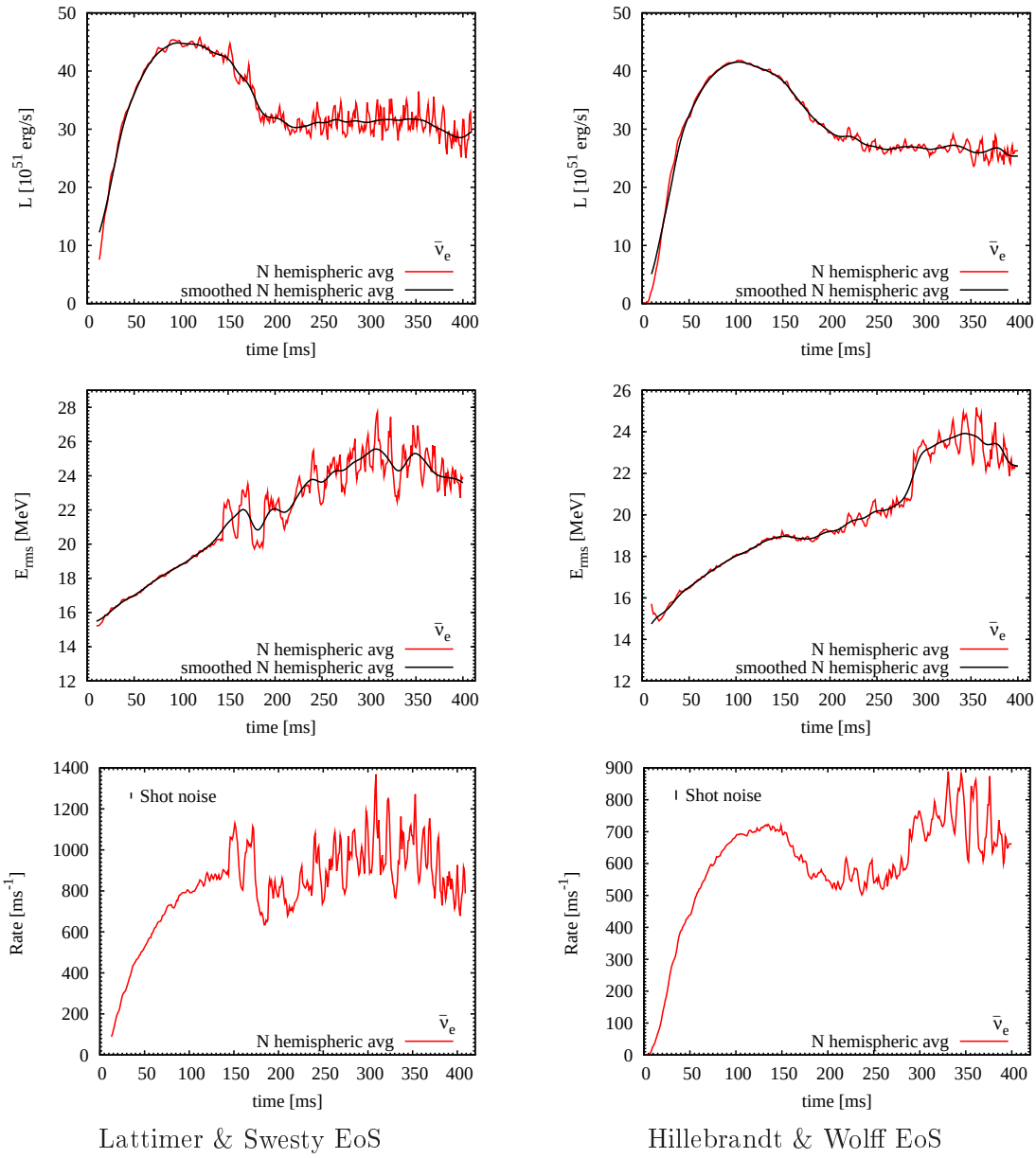

Figure 10.2: *Top:* $\bar{\nu}_e$ luminosity of our baseline SN model sampled at 1 ms intervals. Red line: North hemispheric average. Black line: Moving average with a Gaussian window function ($\sigma = 7$ ms). *Middle:* $\bar{\nu}_e$ rms energy. Red and black lines as the panel above. *Bottom:* Detection rate in IceCube. Also shown is the $1\,\sigma$ range caused by shot noise, assuming a bin width of 1 ms. *Left:* For the EoS of Lattimer & Swesty. *Right:* For the EoS of Hillebrandt & Wolff.

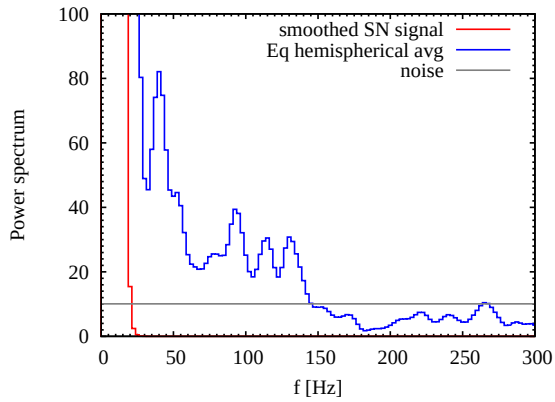

Figure 10.3: Comparison between fluctuating and smooth signal for the model with Lattimer & Swesty EoS. Blue: Power spectrum of equatorial hemispheric average signal. Red: Same for smoothed SN signal.

In order to produce observational spectra we have made hemispheric averages as outlined in section 9.1, and in fig. 10.2 we show the northern hemispheric averages for the energies, luminosities and the calculated event rate expected in IceCube, for both EoSs (The Lattimer & Swesty EoS on the left and the Hillebrandt & Wolff EoS on the right). In the energy and luminosity panels we also show the approximated signal for a spherical symmetric supernova (black lines). We see that for the LS EoS the SASI induced fluctuations sets in after roughly 150 ms, and somewhat later at $\sim$ 300 ms for the HW EoS.

Having made ourselves familiar with the appearance of the signal in the time domain, we made a Fourier transformation of the event rate, as outlined in chapter 7. As previously explained we did this to better investigate the fast time variations that are imprinted on the neutrino signal by the SASI. In the following sections we will present the results of the Fourier transformation of the Lattimer & Swesty model, and discuss their interpretation. We will return to the results of the EoS of Hillebrandt & Wolff in section 10.4.

10.1 Comparison with spherical symmetric case

One of the very first issues that comes to mind, and a very important one, is how well we can distinguish the signal from a spherically symmetric model from a convecting one (e.g. a SASI supernova). To investigate this issue we have created an imitation of a spherically symmetric signal by making an overly smooth resampled version of our signal, as outlined in section 6.3.3. We showed examples of the correspondingly smoothed luminosities and energies in fig. 10.2 (black lines). The signal power for the 1D emulated event rate in the equatorial direction is compared with the equatorial hemispheric averaged signal in fig. 10.3. (Not much difference can be seen between the 3 hemispheric averages for the overly smoothed version, which is as expected since the overly smooth version represents a *spherically symmetric* signal.) We see that the smooth signal plummets below the IceCube background noise level at around 20 Hz. So for the case of the LS EoS, we can be quite confident that the power spectrum above $\sim$20 Hz is a direct reflection of the fast time variations of the neutrino source.

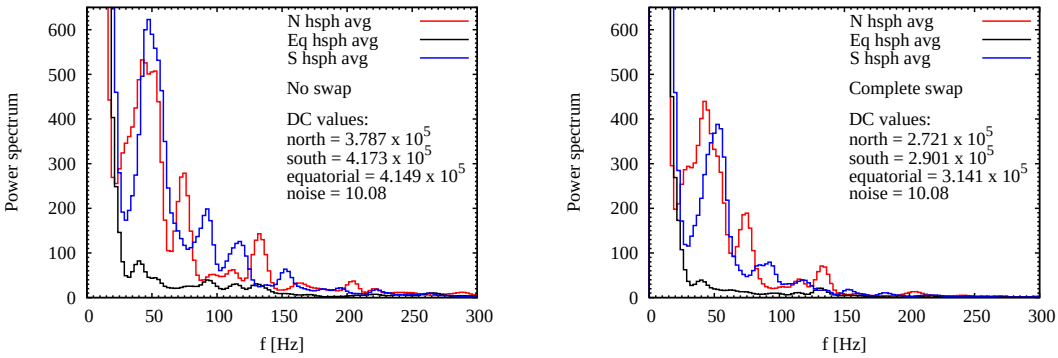

Figure 10.4: Smoothed power spectrum of the event rate for the northern (red), equatorial (black) and southern (blue) hemispheric averages (EoS of Lattimer & Swesty). The shot noise level of the background is at 10.08. *Left:* No flavor oscillations. *Right:* Complete swap $\bar{\nu}_e \leftrightarrow \bar{\nu}_x$. In the panels we also give the DC values, i.e. the power at zero frequency, corresponding to $(N_{\text{events}}/N_{\text{bins}})^2$.

10.2 Directional dependence

For further studies we show in fig. 10.4 the power level smoothed spectra for the northern, southern and equatorial signals (The signals being produced as outlined in section 9.1 and smoothed as outlined in section 9.3). The left panel show the power for the $\bar{\nu}_e$ and the right one shows the power spectrum corresponding to an assumption of a full flavor swap: all neutrinos born originally as $\bar{\nu}_x$ in the interior of the supernova has been converted into $\bar{\nu}_e$ via collective flavor oscillations on their way out of the supernova. The flavor dependent signal will be discussed below in section 10.3.

The first observation we make is that for all 3 hemispheric averages the power is comfortably above the power for the background noise (at 10.08 in these units) out to $\sim$ 150 Hz for the $\bar{\nu}_e$ case. Secondly, the first peak of the northern and the southern signals are roughly coinciding, and although they show different specific patterns at larger frequencies the overall level of the two signals here are comparable. We show the DC values, i.e. the total number of events per bin squared, in the figure.

We conclude that any features observed in the power spectra between 20 Hz and 150 Hz can be associated to the fast time variations of the neutrino signal. The highest peaks around 50 Hz correspond to variations on time scales of 20 ms. A period that is easily recognizable in fig. 5 of reference [MJM08], that is a plot of the dipole motion of the shock-wave surface. We are therefore led to conclude that the peak at 50 Hz can be associated to the dipolar motion of the SASI shock front motions.

In the left panel of fig. 10.4 we observe that the level of the power of the equatorial hemispheric average is a great deal smaller than the polar power levels. This can be understood since the excursions of the SASI motion is primarily along the polar axis, and thus the excursions in the equatorial direction will be minimal. In addition excursions from the northern and the southern directions will have a tendency to add together and cancel each other partially out when looking along the equatorial direction, again leading to a reduced amplitude in the equatorial power spectra.

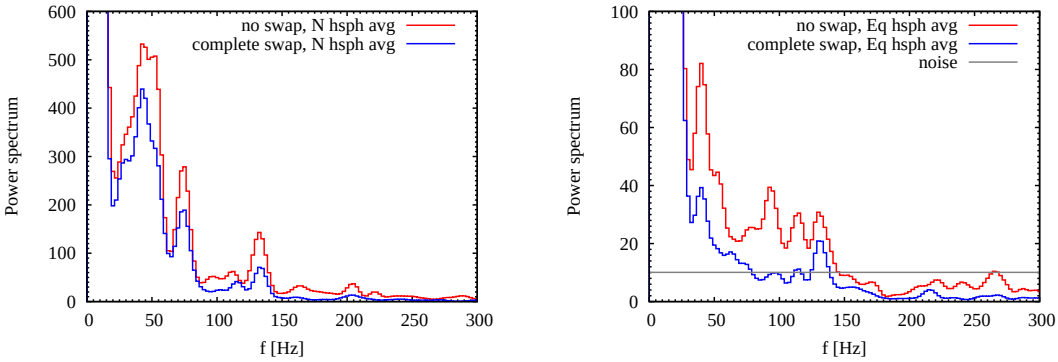

Figure 10.5: Comparing no oscillations (red) with complete flavor swap (blue) for the model with Lattimer & Swesty EoS. *Left:* northern. *Right:* equatorial.

10.3 Flavor dependence

In the right panel of fig. 10.4 we show the power spectra corresponding to a full flavor swap between neutrinos created as $\bar{\nu}_x$ and during their travel converted into the $\bar{\nu}_e$'s we observe in IceCube. (I.e. we exchange all instances of $L_{\bar{\nu}_e}$ and $E_{\mathrm{rms},\bar{\nu}_e}$ in the rate calculation eq. 9.1 with the corresponding quantities for $\bar{\nu}_x$). We notice that the overall levels of the absolute power spectra are lower than the corresponding spectra for the $\bar{\nu}_e$, but the general features remain similar to the $\bar{\nu}_e$ spectrum. This tells us that full or partial flavor transformations will not affect the observed spectrum substantially. This conclusion is even clearer when we show the same information in fig. 10.5, but this time compare the $\bar{\nu}_e$ signal with the $\bar{\nu}_x$ for the northern average (left) and the equatorial average (right). The northern case (which is very similar to the southern case) particularly support the conclusion that flavor transformations will have relatively little impact on the interpretations of the fast signal variations. The lowered overall amplitude is caused by the lower $\bar{\nu}_x$ luminosity compared to the $\bar{\nu}_e$ luminosity during the accretion phase. Although the absolute amplitude of the $\bar{\nu}_x$ spectrum is lower than the $\bar{\nu}_e$ spectrum, the relative fluctuations are comparable. We give the DC values for the $\bar{\nu}_x$ in the right panel of fig. 10.4 as well as we gave the DC values for the $\bar{\nu}_e$ in the left panel. We see that the DC values are lower for the $\bar{\nu}_x$. We therefore show in figs. 10.6 and 10.7 the power spectra divided by their respective DC values. Each flavor is shown on its own in fig. 10.6, and in fig. 10.7 we show the flavors together for a given viewing direction to facilitate an easier comparison. On the left of fig. 10.7 we show the case for the northern hemispheric average and on the right we show the southern hemispheric signals. It is immediately clear that for the northern case the *relative* fluctuations of the power for the $\bar{\nu}_x$ neutrino is equally large as for the $\bar{\nu}_e$ flavor. In a single instance even larger. For the southern hemispheric average we see that the relative power corresponding to the dipolar oscillation ($f \sim 50$ Hz) is equally big for both flavors. For the higher frequency peaks (the ones most likely to correspond to convective overturn) the power for the $\bar{\nu}_x$ flavor is, however, somewhat smaller than the $\bar{\nu}_e$ flavor.

We remind the reader that this way of performing a full flavor swap is meant for illustration purposes only, since the true signal will almost certainly be somewhere inbetween these two signals. A fully detailed treatment of flavor conversions would require the use of a specific choice for the mass hierarchy and mixing angles, as well as detailed use of angular dependencies

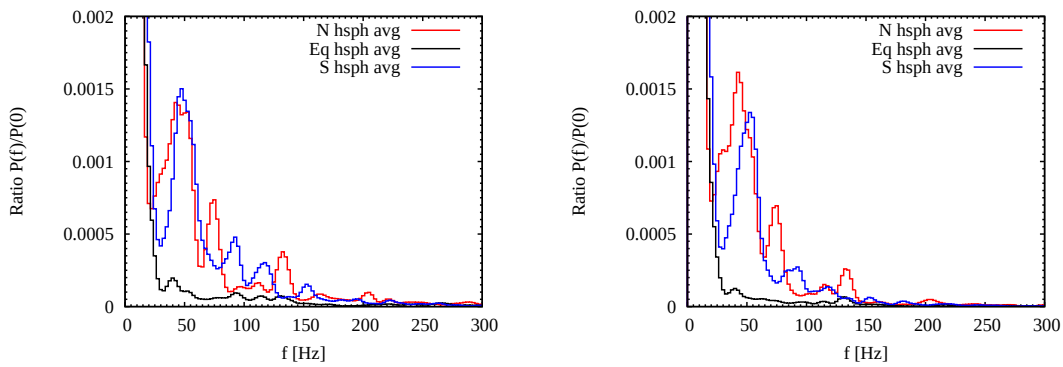

Figure 10.6: Relative power, $P(f \neq 0)$ divided by DC power (LS EoS). *Left:* $\bar{\nu}_e$. *Right:* ν_x.

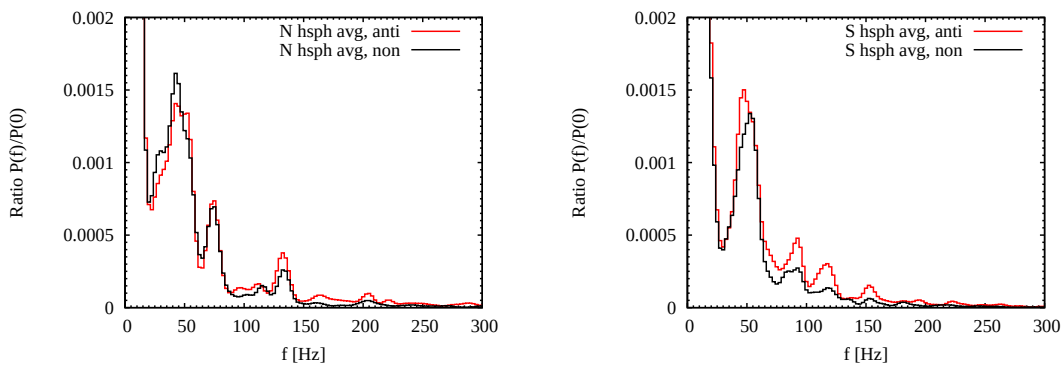

Figure 10.7: Relative power, $P(f \neq 0)$ divided by DC power (LS EoS): $\bar{\nu}_e$ (red lines) and ν_x (black lines). *Left:* North hemispheric average. *Right:* South hemispheric average.

of energies for the different species. We defer such a treatment to a future project and use the present calculation to illustrate a principle only.

10.4 Equation of State dependence

A significant aspect in numerical simulations of supernova is the choice of equation of state. Naturally a need to investigate how our results depend on the employed EoS therefore arises. For this purpose we consider the run of a 15 $M_\odot$ from reference [MJM08] with the EoS of Hillebrandt & Wolff [HW85], similar to the run with the EoS of Lattimer & Swesty discussed above.

We show the graphs for the luminosity, rms energy and event rate for the northern hemispheric average for the Hillebrandt & Wolff EoS in the right panels of fig. 10.2 in analogy to the ones shown on the left for the Lattimer & Swesty EoS. Likewise we show in the right panels of fig. 10.1 the analogous 5 wedge quantities for the Hillebrandt & Wolff EoS. We see that the rate for the HW EoS is roughly at 700 events per ms compared to the larger event rate of roughly 900 events per ms for the LS EoS. The smaller event rate for the HW EoS is simply a reflection of the lower luminosity and rms energy compared to the LS EoS.

Another feature that warrants our attention is the fact that proper fluctuations do not

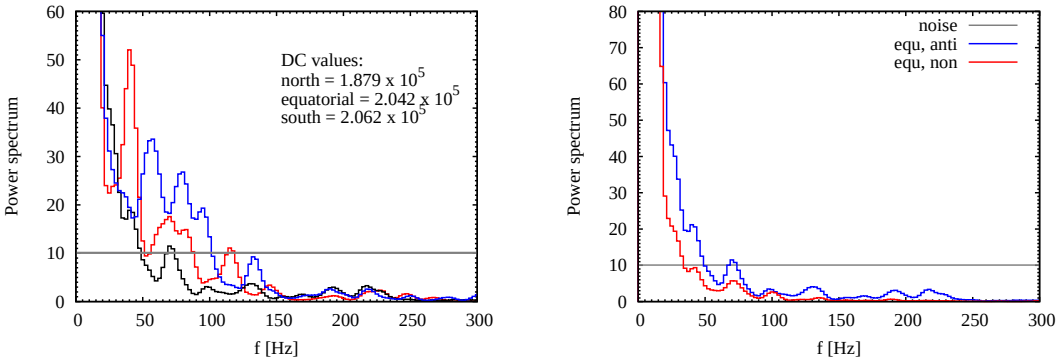

Figure 10.8: *Left:* Smoothed power spectrum of the event rate for the northern (red), equatorial (black) and southern (blue) hemispheric averages (EoS of Hillebrandt & Wolff). The DC values are also given. Analogous of left panel of fig. 10.4. *Right:* Comparing no oscillations (blue) with complete flavor swap (red) for the equatorial average of the Hillebrandt & Wolff EoS. Analogous to the right panel of fig. 10.5.

seem to set in until about 300 ms after bounce for the HW EoS, as is also noted in reference [MJM08]. We will return to this observation in section 10.5.

The resulting power spectra for the three $\bar{\nu}_e$ hemispheric averages for the HW EoS can be seen in the left panel of fig. 10.8. Comparing these 3 power spectra with the ones belonging to the LS EoS in fig. 10.4, we see that the power is dramatically lower. The equatorial average rapidly falls below the noise level (at ~ 50 Hz), and the northern and southern spectra lack the similarity visible in the case of the LS EoS. Turning to the $\bar{\nu}_x$ flavor, we find that the power here is even lower. On the right of fig. 10.8 we see the power spectra for the equatorial hemispheric average for the non-swapped (blue line) as well as the swapped flavor version (red line), in full analogy to the right panel of fig. 10.5 for the LS EoS. Discouragingly the power spectra drops below the noise level between $f \sim 30 - 50$ Hz for both curves.

10.5 Thirds method

To remedy this situation, let us now return to the feature we pointed out previously: from the lower panels of fig. 10.2 it is quite clear that the SASI fluctuations in the model with the HW EoS only begin in earnest at around 270 ms, whereas in the model with the LS EoS, the fluctuations begin around 150 ms post bounce.

From this observation one could become inspired to compare a Fourier transform of the late parts of the signal for each model, instead of making Fourier transforms of the full time duration. This is what we have done in what we call our "thirds method". We have quite simply cut the time duration into 3 equally long time segments of 126 ms. Each one starting at $t = 22$ ms, $t = 148$ ms, and $t = 274$ ms respectively, such that the end of the last time segment will coincide with the end of the full signal time.

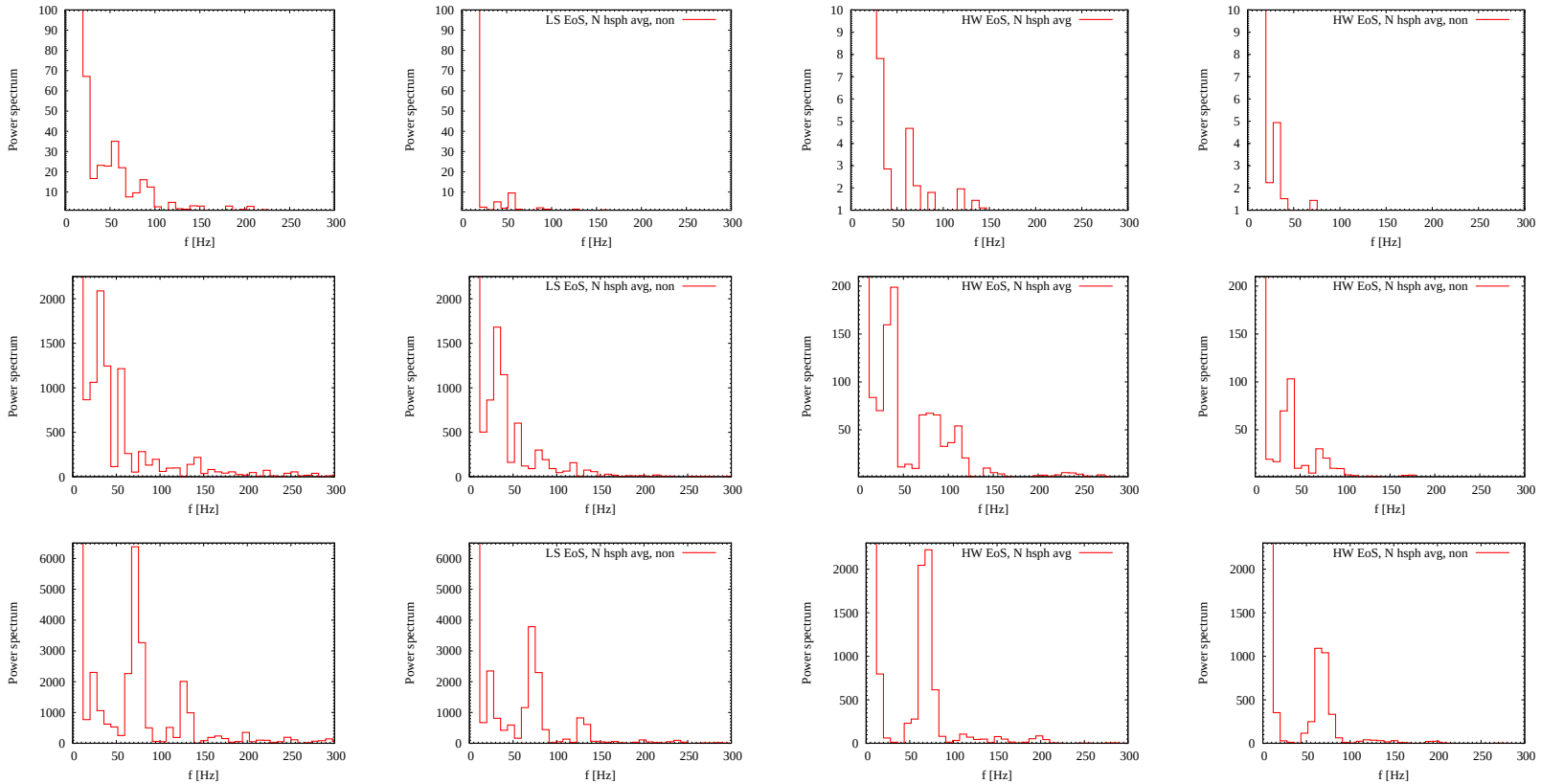

LS EoS $\bar{\nu}_e$ LS EoS $\bar{\nu}_x$ HW EoS $\bar{\nu}_e$ HW EoS $\bar{\nu}_x$

Figure 10.9: *Top row:* Power spectrum from segment starting at 22 ms. *Middle row:* Spectrum from 126 ms segment. *Bottom row:* Spectrum from 274 ms segment. Note the different values on the y-axis in the 3 rows, as well as between the figures for the LS and the HW EoS. All 12 figures show spectra for the north hemispheric averaged rate. *Left two columns:* LS EoS; $\bar{\nu}_e$ and $\bar{\nu}_x$ respectively. *Right two columns:* HW EoS; $\bar{\nu}_e$ and $\bar{\nu}_x$ respectively.

We then did a Fourier transform, similar to the one described in chapter 7, with a Hann window multiplied on each of the shorter time segments. The shorter time segment naturally changes the frequency resolution we can obtain, as explained in section 7.1.1. The frequency resolution now will be $\delta f = 1/126\text{ms} \sim 8$ Hz. This in turn means that a smoothing at the power level with a smoothing length of $\sigma = 4$ Hz, as done hitherto (section 9.3), will no longer make sense. In our thirds method we will therefore refrain from the power level smoothing.

10.5.1 Thirds method: results and discussion

We show the results of our thirds method in fig. 10.9. As mentioned above, we are primarily interested in the latter of the three time segments, but for completeness we show all three. In the same spirit we show the power spectra for both EoSs, and for the non-swapped as well as the fully swapped case. One should keep in mind that the level of the noise will increase roughly with a factor of three in the thirds method. (Since N_{bins} will be reduced by a factor of $400/126 = 3.2$, then P_{shot} will be multiplied by a factor 3.2, cf. eq. 8.8.) However this will lead to a noise level at roughly 32.26, and so the signal will be much more dominant than was the case in the full version. The signal-to-noise ratio will be significantly better.

When looking at the panels corresponding to the $\bar{\nu}_e$ signals in the time segment 274–400 ms (lower row, 1st and 3rd column) we see that both models show a strong power peak around a frequency of 70 Hz, corresponding to a time scale of 14 ms. A feature which is also visible to the naked eye in the time evolution of the rate in the lower right panel of fig. 10.2. The power of the $f \sim$70 Hz peak is larger for the LS case than for the HW case, but unlike the "pessimistic looking" power spectrum for the full time duration for the HW case (fig. 10.8), this representation shows that the fast variations of the signal would be visible for the stiffer EoS with similar significance as for the softer EoS. It is also noteworthy that the 70 Hz peak for the late segment for the LS EoS (lower panel 1st column) is much larger than the corresponding 70 Hz peak in fig. 10.4 (left panel, red line). The difference between the two graphs is only the analyzed time segment. Here (fig. 10.9) it is the final 126 ms of the run, and in fig. 10.4 the full 400 ms. Had the signal been roughly stationary, the power of the peak would have been the same. In this case, however, we have a strong peak at 70 Hz with a much larger signal-to-noise ratio than in fig. 10.4, where in turn we have a much stronger peak at 50 Hz.

The fact that the power at certain frequencies increases in the shorter segment treatment compared to the full spectra actually increases the possibility of detecting the signal. Put in other words, the Fourier spectrum varies significantly as a function of time.

From the 12 figures we see that the detailed development in the frequency content is different in the two flavor cases (1st column vs. 2nd column, and 3rd column vs. 4th column), but has an overall resemblance. Thus once more we get reaffirmed that a potential flavor swap will not seriously affect our capability of detecting fast time variations of the neutrino signal in IceCube.

10.6 Time evolution of frequencies

Partly prompted by the difference over time in the frequency content of the signal displayed in fig. 10.9, we decided to take a closer look at the time evolution of the frequencies. Another motivating factor was that Marek and Janka had done a "running window" Fourier transform on their data in their paper [MJM08]. They made a running window of length 128 ms, and

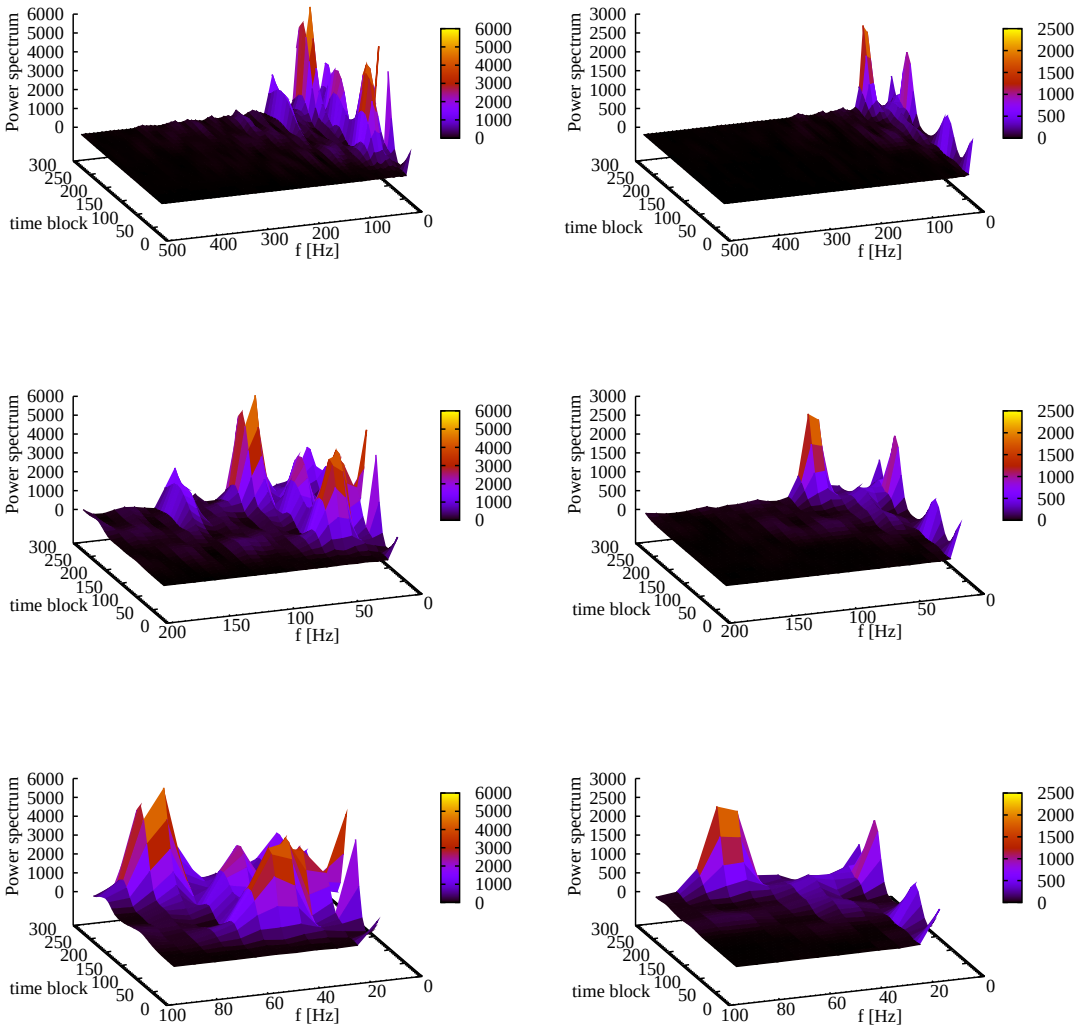

Figure 10.10: Three dimensional plot of the time block evolution of the different frequencies up to 500 Hz (top row), 200 Hz (middle row) and 100 Hz (bottom row). Lattimer & Swesty EoS on the left, Hillebrandt & Wolff on the right. All panels are for the northern hemispheric average.

shifted the window with a 10 ms offset starting from 100 ms post bounce (getting 17 spectra in all). Subsequently they added up all the power of the different frequencies and averaged the power. Figure 8 in their paper [MJM08] show the result. We feel this method is not fully correct as the "running" window is usually done to illuminate and clarify the temporal evolution of frequencies. Thus we decided to do this investigation of the temporal evolution of the frequencies a bit more thoroughly.

Drawing on inspiration from the thirds program, and the running window by Marek and Janka, we chopped the 400 ms resampled signal for each of the 3 hemispheric averages into segments of length 126 ms, starting from $t = 14$ ms and then advancing 10 ms for each consecutive segment. This gives us 26 sets of length 126 ms, that were all Fourier transformed (as previously described). In the following figures the designation "time block" is indicating the starting time (e.g. $t = 104$ ms) for a given time block. The frequency spacing is 8 Hz as in the thirds method, allowing us to probe 64 (126/2+1) different frequencies with this approach, and since the sampling rate is still 1 ms the Nyquist frequency remains at 500 Hz.

10.6.1 Interpretation of time evolution figures

However, as can be seen from the resulting figure 10.10, showing the northern hemispheric average only, nothing much interesting happens for the frequencies above ∼100 Hz. Apart from this conclusion, we make the following observations: As already predicted from the thirds treatment, we see in the lower left panel (LS EoS) that in early time blocks ($\sim 50-150$ ms) the power for the frequency $f \sim 50$ Hz grows dominant, whereas for later times ($\sim 200-300$ ms) it declines again and the power for the $f \sim 70-90$ Hz grows strong. For the HW case (lower right panel) no such growth of the $f \sim 50$ Hz power is seen, but the late time growth of power for the higher frequency is clear. Extracting the frequencies closest to $f \sim 50$ Hz and $f \sim 70$ Hz and showing their time evolution alone in fig. 10.11 for the LS EoS (left) and HW EoS (right) tells us the same tale. For the LS EoS we see that the power for late times for $f \sim 70$ Hz climbs to ~ 7000 in our units where the $f \sim 50$ Hz frequency only reach $2000-4000$ although it does so twice. In comparison the power for the $f \sim 50$ Hz in the HW EoS does not exceed a mere 250 in absolute units, which is a factor of 10 lower that the power for the $f \sim 70$ Hz that reach 2000 for the HW case, and does so for both the southern and the northern averages. Singling out the frequencies $f \sim 50$ Hz and $f \sim 70$ Hz and focusing our attention on them is not only based on the fact that they have the largest power, but also that (as will be discussed in section 10.7) we believe these frequencies can be connected to the dipole and quadrupole motions of the SASI.

In fig. 10.12 we show the evolution of several frequencies for both EoS. The different evolution perceived from fig. 10.10 is still clear and we get reaffirmed that the general power levels are larger for the LS EoS than for the HW EoS. To show in a different way the points related in the above paragraphs, we show in fig. 10.13 how the power is distributed among the different frequencies for 3 different time blocks (block 0 starting at 14 ms (red line), block 13 starting at 144 ms (blue line) and block 26 starting at 274 ms (black line)). On the left we show the distribution for the LS EoS, and we see again for intermediate times power just below 50 Hz and for late times a strong power signal at 70 Hz. For the HW EoS on the right, only the strong peak at late times for at 70 Hz is present.

The conclusion that can be drawn from both the thirds method and the investigation of the time evolution of the frequencies is that: The analysis of a realistic signal would involve

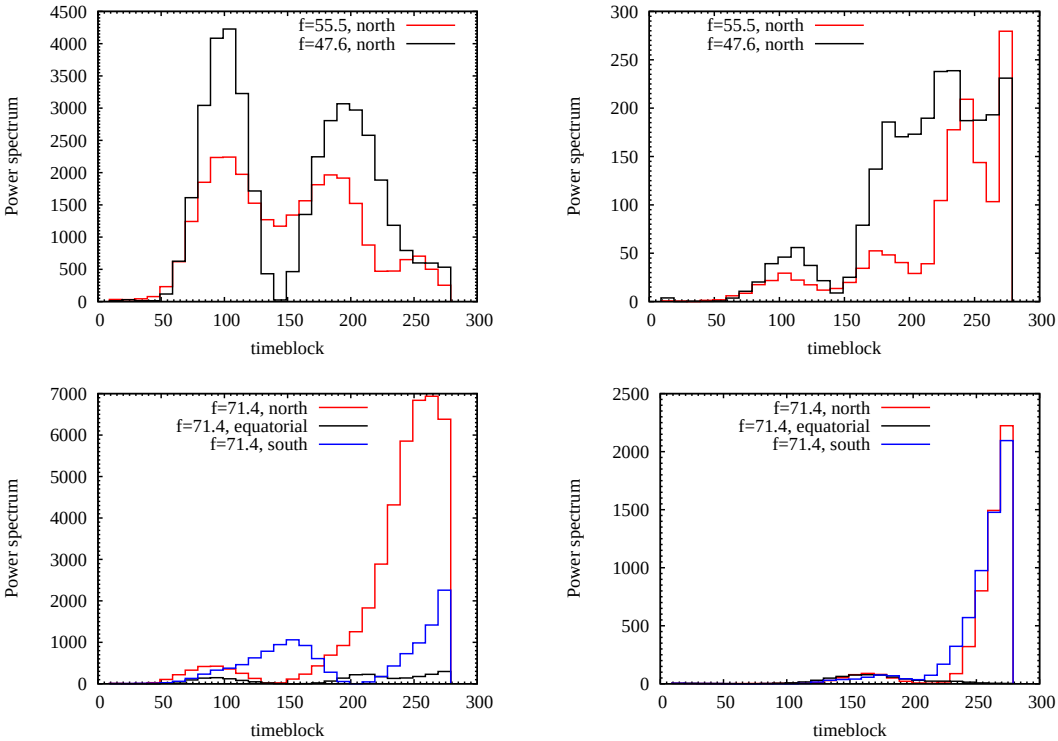

Figure 10.11: Evolution of frequencies as a function of time block. *Top:* the frequencies 48 Hz and 56 Hz. *Bottom:* the frequency 71 Hz. *Left:* LS EoS. *Right:* HW EoS.

studying subsets of the full-length signal where Fourier components can show up with much larger significance in spite of the increased shot noise relevant for a shorter integration time.

10.7 Physical interpretation

Under the assumption that current 2D numerical models are good representations of the ongoing supernova physics, and with the caution that we have here only investigated 1 model with 2 different equations of state, we will try to connect the features in the power spectra with the underlying supernova physics. In a later chapter, we will apply a similar analysis to four other models, and extend our discussion to the similarities and differences we find there (chapter 11).

The peaks in the power spectrum of the neutrino signal reflects the activity in the SN core. SASI activity and convective overturns modulate the stream of infalling mass between the shock front and the surface of the proto-neutron-star (PNS) [MJ09, MJM08]. This results in temporal variations of the accretion rate onto the PNS, which in turn is reflected in temporal variations of the emitted neutrino signal. The accretion down-drafts along the equator can easily be channelled differently towards the northern or southern hemispheres. Therefore one cannot expect exact symmetry for the two hemispheres, and even long-lasting asymmetries of the accretion structures and the strength of the shock expansion can occur. Even the dipolar mode of the SASI may not necessarily have similar strength in the two hemispheres.

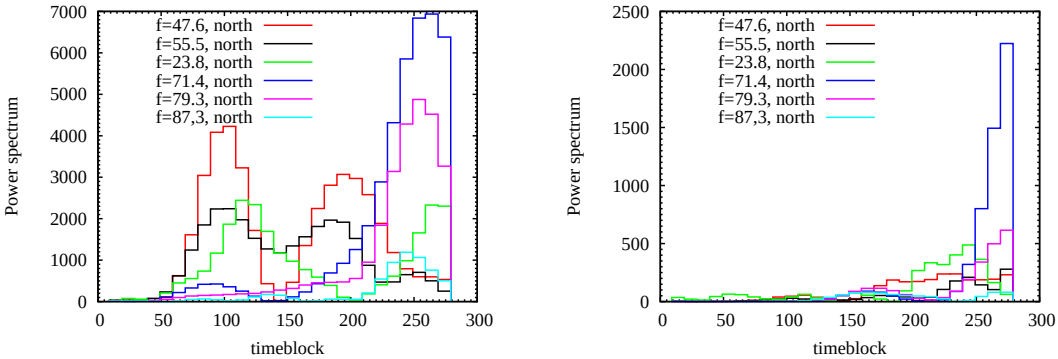

Figure 10.12: Time evolution of many frequencies. *Left:* LS EoS. *Right:* HW EoS.

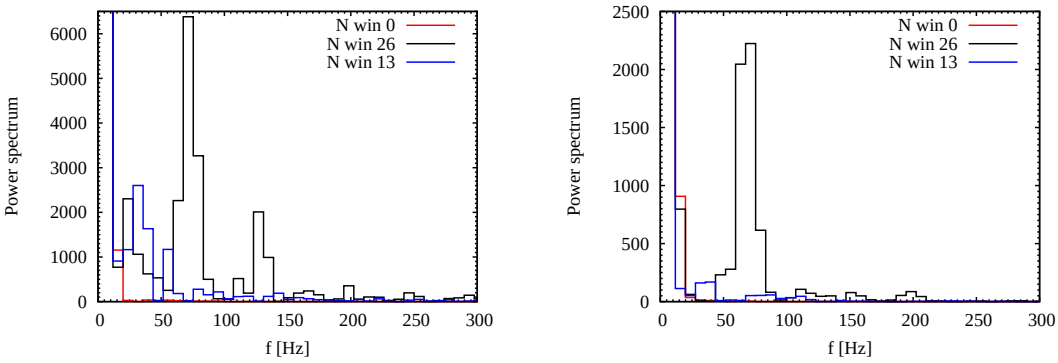

Figure 10.13: Power distribution on the frequencies in 3 time blocks. Block 0 (red) corresponds to a $t_{start} = 14$ ms, block 13 (blue) to $t_{start} = 144$ ms and block 26 (black) to $t_{start} = 274$ ms. *Left:* LS EoS. *Right:* HW EoS.

As a consequence we do not expect the power for the two hemispheres to be identical, a fact abundantly seen in the above figures of the power spectra.

However in the results presented by Marek et al. [MJM08] we find support for a causal connection between the power peaks of the observed fast time variations of the neutrino signal and the underlying physics of the accretion through the shock front, and the deformation of the shock front on a global scale. In fig. 5 (right column) of that paper, they show the Fourier spectra of the time varying amplitudes of the dipole and quadrupole modes of the shock position. In this figure one recognize power peaks corresponding well with the power peaks identified in the neutrino signals at low frequencies.

The 50 Hz peak of the LS EoS we observe in the neutrino signal (e.g. fig. 10.4) corresponds well with the slightly broader feature between 30 and 60 Hz in fig. 5 of [MJM08] (upper panel, black curve). The characteristic feature of a peak around 50 Hz is present in all our three hemispheric averages, even though it is not very distinct in the equatorial case (left panel of fig. 10.4). This 50 Hz peak can then be connected to the $\ell = 1$ dipolar SASI sloshing mode (depicted in the upper panel of fig. 5 of [MJM08]). The SASI sloshing mode leads to semi-periodic variations of the accretion rate onto the PNS for both hemispheres, and thus

also to variations of the associated neutrino emission ([MJM08, p.485]). The north-south differences of the neutrino power peak is attributed to the asymmetry of the SASI variations in the two hemispheres (see fig. 3 in [MJM08]), where the width of the peak is caused by the time evolution of the SASI frequency.

The frequency of the $\ell = 1$ SASI mode develops in time because the mode depends on the sound-travel time and the time scales of mass flow between the shock front and the PNS (see eq. 32 in [OKY05] and eq. 18 in [SJFK07]). Thus it depends on the time varying radius of the shock front, and to a lesser degree the steadily shrinking surface radius of the PNS. In rough terms one can say that when the shock radius is larger, the SASI frequency will be lower, and when the shock radius decreases, the SASI frequency tends to increase. After $t_{\rm pb} \sim 100$ ms the shock radius shows considerable fluctuations (as well as an increase) over time (left panel of fig. 4 in [MJM08]), so it is unsurprising that the SASI peak here becomes quite broad. The time development of the 50 Hz peak for the LS EoS is easily visible, as previously noted, in the lower left panel of fig. 10.10.

The pronounced power peak around $f = 70$ Hz visible in the lower panels of fig. 10.9 (1st and 3rd column) is most reasonably explained by the quadrupolar $\ell = 2$ mode of the SASI. Although in the non-linear regime of both the SASI and convective activity, it is difficult to make a clear distinction between the two hydrodynamical effects. Either instability can trigger the other and they therefore mostly co-exist [SJFK07]. Three facts corroborate the possible association of the 70 Hz power peak with the $\ell = 2$ SASI mode: (1) Analytic analyzes and numerical experiments in the linear regime show that the frequency of the $\ell = 2$ mode is slightly higher than that of the $\ell = 1$ mode. (Consecutive maxima of the amplitudes in fig. 5 in [OKY05] and in fig. 13 in [SJFK07] lie closer for the $\ell = 2$ curve than the maxima for the $\ell = 1$ curve, thus implying a shorter period and higher frequency). The exact frequency ratio, however, depends strongly on the size of the SASI region (see fig. 4 in [BM06]). (2) The appearance of the ~70 Hz peak in the lower left panel of fig. 10.9 ($\bar{\nu}_e$, LS EoS, $t = 274$ ms) and the relative weakness of power at lower frequencies at late times (274–400 ms) in the Lattimer & Swesty EoS model can be explained by the increasing power of the $\ell = 2$ shock oscillation mode. The amplitude of this mode becomes larger than that of the $\ell = 1$ mode at these late times (see the left panels of fig. 5 in [MJM08]). (3) The presence of the peak in the northern power spectrum but relative weakness or absence in the southern hemisphere may correspond to the asymmetry of the quadrupolar shock deformation in the two hemispheres as shown in the panels of fig. 4 in Marek et al. [MJM08].

The peaks at frequencies above 90–100 Hz (fig. 10.4) are most likely associated with localized convective overturns. These mass motions happen on smaller angular scales and on shorter time scales than the large scale dipole and quadrupole modes of the SASI. It is therefore fairly likely that this sort of high frequency structures will exhibit extensive differences between the two polar hemispheres. In the equatorial direction long-lasting but time varying downdrafts arises a late times. It is therefore not surprising that significant differences for high frequencies can be observed in the neutrino power spectra for the 3 hemispheres. We also touched briefly on this subject in connection with figs. 9.2 and 9.4 where we see that the hemispherical averaging eliminates some of the power at high frequencies.

10.7.1 Stiffer EoS revisited

For the stiffer EoS of Hillebrandt & Wolff, we know that the resulting NS will have a larger radius and the shock radius will be slightly smaller compared to the Lattimer & Swesty EoS (see both panels of fig. 4 in [MJM08]). The layer between the surface of the NS and the shock front will consequently be more compact in this SN model. We therefore anticipate that the modes of the global shock movements and the accretion will have smaller amplitudes and higher frequencies than the corresponding ones for the LS EoS model. A possible interpretation of the facts that the peak between 60 and 85 Hz in fig. 10.9 (3rd column, lower panel) is somewhat broad, and that no strong second peak is present at higher frequencies, could be that we see a superposition of the $\ell = 1$ and $\ell = 2$ modes. This interpretation is made even more plausible by the observation in the left panels of fig. 5 in [MJM08] that both modes are present with comparable amplitudes, and from fig. 4 in [BM06] where the characteristic frequencies of the two modes become very similar for compact post-shock layers (i.e. the layer between the surface of the PNS and the shock front).

10.7.2 Signatures of SASI

We conclude that depending on the SASI modes present, different peaks in the neutrino power spectrum will be present. In 2D models the $\ell = 1$ and $\ell = 2$ modes are typically the strongest and the fastest growing ones. At which frequencies the SASI peaks will appear depends sensitively on when in the time evolution we investigate the signal. The strongest SASI activity is expected to occur in a roughly 100 ms window just prior to the explosion taking off. Thus, investigating a shorter time segment just prior to explosion we expect to see a dramatic enhancement of the power compared to the shot noise level (as is also evident when comparing fig. 10.4 (left) and fig. 10.9 (lower left)). This would make a detection of these features more likely.

10.8 Implications of detection

An actual observation with IceCube (or other detectors) of the features in the neutrino power spectrum described in this chapter would lend massive credibility to the existence of large non-radial hydrodynamical instabilities (SASI and convective overturn) around the beginning of the supernova explosion. The magnitude of these instabilities naturally needs to be large enough to produce the observed fluctuations in the neutrino emission.

Through the measurement of fast time variations of the neutrino flux we would get confirmation of the importance of a small piece of the supernova physics puzzle. Currently the relevance of the hydrodynamic instabilities are merely suggested, by numerical models, theoretical considerations, and indirect arguments based on asymmetries of the supernova ejecta at later evolutionary stages.

The prompt explosion (already disfavored by numerical simulations of massive stars) would suffer a fatal blow from the detection of the SASI, along with other explosion mechanisms working on such short time scales that the standing accretion shock instability will not have the time to develop fully. The SASI activity typically reach the non-linear regime after 100–200 ms post bounce (see also fig. 10.2) [OKY05, BM06, SJFK07]. The delayed explosion expected from a neutrino driven mechanism would thus gain further support. A measurement of the SASI

signatures probably would also exclude the magneto-hydrodynamical explosion mechanism that may take place in rapidly rotating stars but leads to explosion in 2D simulations on rather short time scales [BDL+07].

Like the detection of SASI signatures in the neutrino signal would rule out certain explosion mechanisms, so would a lack of detection. The acoustic explosion mechanism [BLD+06, BLD+07] can lead to explosions as late as 1 s (or later) after bounce, leaving plenty of time for SASI to develop. So for the acoustic mechanism we would expect at period of strong SASI activity and convective overturns prior to explosion. A phase with strong hydrodynamical activity is probably important to excite the compact PNS to the required powerful, large-amplitude dipole oscillations that provides the acoustic energy flux for the onset of the explosion.

If we combine the measurement of neutrino fluctuations with the measurement of gravitational waves (as suggested by Ott [Ott08]), we could undoubtedly provide even stronger exclusion arguments. The combined power of neutrino and gravitational wave observations could then bring us one step closer to completing the puzzle of the processes occurring during the explosion of massive stars.

10.9 Luminosity versus energy fluctuations

The primary focus of the previous sections have been on the fluctuations over time of the number of events in IceCube, and what we might learn from these fluctuations. We have not looked in detail at the luminosity or energy fluctuations since IceCube will not have good enough energy resolution to give information on this point. However, with a future megaton water Cherenkov telescope one would not only obtain the same number of events as for IceCube, but also have event-by-event energy information. For a megaton water Cherenkov telescope it would therefore be highly interesting to know more about the spectral energy and luminosity fluctuations.

We want to determine whether the luminosity or the energy fluctuations provide the dominant contribution to the event rate fluctuations. To do this, we investigate the correlation of the energy and the luminosity fluctuations. We anticipate a correlation of the excursions since both the luminosity and energy fluctuates as a result of the mass motions. If, as anticipated, a correlation is observed the fluctuations would interfere constructively and enhance the rate fluctuations. We consider the example of the north hemispheric average of the LS EoS, and limit our considerations to the electron anti-neutrino flavor.

10.9.1 Time domain

We begin with some immediate lessons that can be learnt from a visual inspection of the luminosity and energy plots. The left part of fig. 10.14 show the energy and luminosity of the $\bar{\nu}_e$ with our usual 1 ms resampled data, and a "1D"-like signal obtained with a Gaussian running average with $2\sigma^2 = 1\times10^{-3}\,\mathrm{ms}^2$. The red curves show the luminosity and its smoothed version, the blue ones are for the average energy. The right panel of fig. 10.14 shows a zoom around 240–340 ms. In these plots we observe some degree of correlation. Excursions from the smooth lines are mostly to the same side at the same points in time for both the energy and luminosity fluctuations.

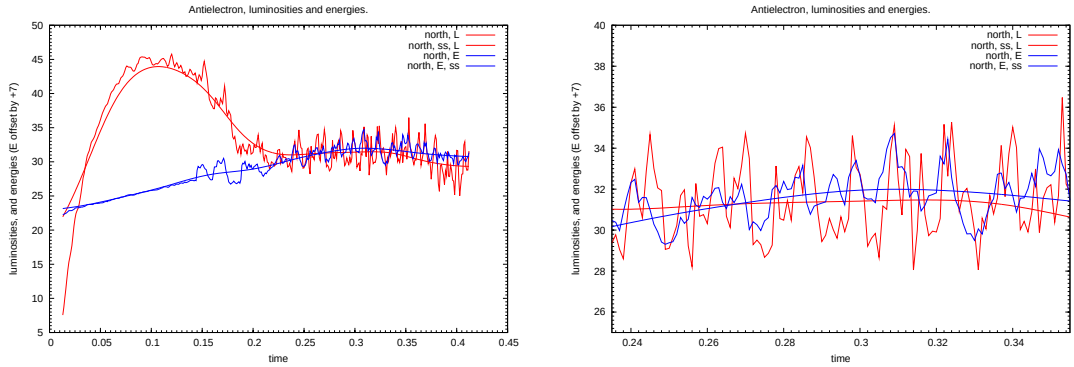

Figure 10.14: Energies and luminosities for $\bar{\nu}_e$. Blue is energy (in MeV), red is luminosity (in 10^{51} erg/s). Also shown are their smoothed versions. The energy has been shifted upwards by +7 units to make the two graphs coincide on the late parts of the curves. *Left:* full time domain. *Right:* close-up.

In order to quantify the correlations we first note that for IceCube it is the $E^2_{\rm rms}$ that enters the event rate in eq. 9.1. Therefore we define the quantity $W(t) = E^2_{rms}(t)$ and study its fluctuations. It is most intuitive to study the relative fluctuations of W and L, so we introduce the dimensionless quantities $\tilde{l}(t)$ and $\widetilde{w}(t)$

$$\tilde{l}(t) = \frac{L(t)}{L_0} \tag{10.1}$$

$$\widetilde{w}(t) = \frac{E^2_{rms}(t)}{E^2_0} \tag{10.2}$$

As the constant reference value L_0 (E^2_0) we decided to take the average value of the luminosity (energy) over the time segment 274–400 ms. A somewhat arbitrary choice inspired by the relatively constant level of both signals in this time range. The results and conclusions we find do not change much if we use the average value from the entire 400 ms.

10.9.2 Frequency domain

To investigate the dimensionless quantities $\widetilde{w}(t)$ and $\tilde{l}(t)$ further, we did the the usual Hann windowed Fourier transform described in chapter 7. Both of the resulting power spectra were smoothed in the frequency domain ($\sigma = 4$ Hz). The power spectra for the relative fluctuations of the luminosity and the energy are displayed in fig. 10.15 (left). The red curve shows the power L corresponding to $\tilde{l}(t)$, the blue curve the power W corresponding to $\widetilde{w}(t)$. Both curves have been multiplied with 10^4 to bring them into the range 0–4. Looking at the two curves it is clear that the power W for the energy squared is much larger than the power for the luminosity L. This confirms the expectation we had from comparing the fluctuations in the two upper left panels of fig. 10.2: The event rate fluctuations are dominated by the energy fluctuations.

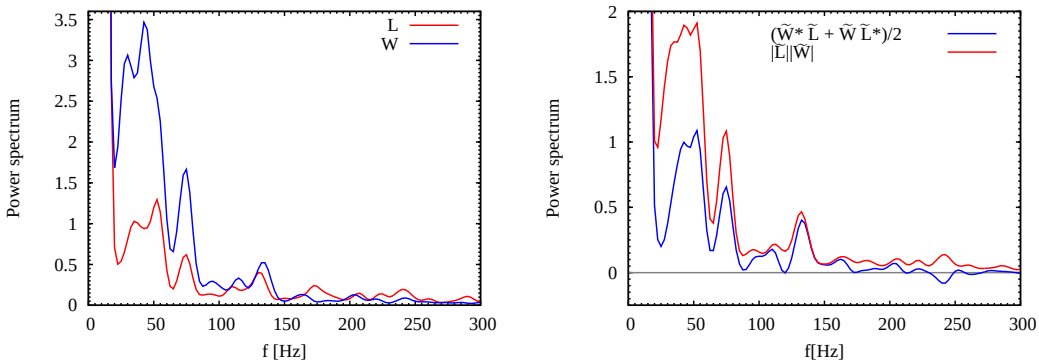

Figure 10.15: Smoothed power spectrum of luminosity (L) and spectral energy ($W = E^2_{\rm rms}$) fluctuations for the model with Lattimer & Swesty EoS. L and W were normalized to their respective average values over the 274–400 ms interval. *Left:* Power spectra of L (red, lower curve) and W (blue, higher curve). *Right:* $|\tilde{L}|\,|\tilde{W}|$ as a red line and correlation function $\frac{1}{2}(\tilde{W}^*\tilde{L} + \tilde{W}\tilde{L}^*)$ as a blue line.

Another interesting point though, is that while the energy contributes the most to the event rate for low frequencies ($f \lesssim 100$ Hz), for higher frequencies the contributions from the energy and the luminosity are more equal.

10.9.3 Correlation calculations

The correlation of $\widetilde{w}(t)$ and $\tilde{l}(t)$ in the frequency domain (with the dependency on frequency suppressed) was obtained as

$$C = \frac{1}{2}\left(\tilde{W}^*\tilde{L} + \tilde{W}\tilde{L}^*\right) \tag{10.3}$$

and was compared with the product of the two moduli

$$M = |\tilde{L}|\,|\tilde{W}| \tag{10.4}$$

Where $\tilde{L}$ and $\tilde{W}$ are the Fourier amplitudes corresponding to $\widetilde{w}(t)$ and $\tilde{l}(t)$ (not the power, thus not containing the factor of $1/N^2_{\rm bins}$). Furthermore we have divided $C(f)$ and $M(f)$ by their DC values, and multiplied them with a factor of 2×10^4 to get them in the range 0–4, and performed the usual frequency level smoothing ($\sigma = 4$ Hz). In fig. 10.15 (right) we show the result of the cross correlation calculation. We see that the graphs for both C (blue line) and M (red line) are positive almost everywhere and similar. This indicates a strong correlation between $\tilde{l}(t)$ and $\widetilde{w}(t)$. Had the C curve been negative it would indicate anti-correlation, and if it had been zero on average, it would imply no correlation between the 2 quantities.

10.9.4 Summary

The results of this section are: the majority of the event fluctuations are contributed by the fluctuations in the energy, and the fluctuations in the luminosity and the energy are correlated. A future megaton water Cherenkov telescope allows resolving energy fluctuations separately. The results therefore implies that more, distinct signatures for the SASI activity might be obtained from future megaton water Cherenkov telescopes.

11

Extended studies: a 11.2 $M_\odot$ model and a rotating model

In this chapter, I give the preliminary results of analyzes similar to the one described in the previous chapter, but this time for a 11.2 $M_\odot$ model and a rotating 15 $M_\odot$ model. The data for these models have been received through personal communication with Andreas Marek and Thomas Janka [JM10]. Our motivation for investigating a lower-mass model, and one where rotation was included, was naturally to search for distinctive features in their power spectra. We wanted to see if there were features repeated over all the different models, and to see if the features attributed to the SASI mode could be identified in other models where SASI is assumed to play a significant role for the explosion. Furthermore we wanted to see how much the rotation of the star would shift the observed frequencies, and whether it would cause a rotational splitting of the observed frequencies.

11.1 The 11.2 $M_\odot$ model

The lighter supernova model was an 11.2 $M_\odot$ model based on a progenitor from Woosley et al. [WHW02][1]. Three different equations of state were employed: the softer Lattimer & Swesty, the harder Hillebrandt & Wolff, and the Shen EoS which falls in between. The time duration of the runs for the three EoS varied from $\sim$ 370 ms to almost 900 ms (see table 11.1). The model was computed with 64 rays spanning a entire hemisphere, thus each ray had a width of 2.8125°. Initially, the run with the HW EoS was only calculated on a 90° wedge, assuming symmetry around the equator, and then re-mapped to the full 180° after

[1] As a curious aside we can mention that the progenitor which exploded to become the Crab nebula (depicted on the front page) is believed to have had a mass between 8 and 11 $M_\odot$ [WHW02, p.1037].

Equation of State	Lattimer & Swesty	Hillebrandt & Wolff	Shen
Time start [ms]	23.52	25.11	24.58
Time end [ms]	394.9	513.5	919.4
Resampled time stretch [ms]	370	488	894
Resampled time start [ms]	24	25	25
δf [Hz]	2.7	2.1	1.1
Shot noise power level	10.9	8.3	4.5

Table 11.1: Parameters for the 3 EoS employed in the 11.2 $M_\odot$ model.

125 ms. This means that only symmetrical modes of the SASI could develop before this time [MJM08]. The frequencies of the SASI modes primarily depends on the sound crossing times in the cavity between the shock and PNS surface. Therefore they are expected to be similar to the frequencies for the 15 $M_\odot$ model for the same EoS [JM10], as the distances between shock and PNS will be comparable. Of the three EoSs only the Shen and the LS EoS are on their way to explode at the end of the runs. The HW EoS on the other hand do not have indications of the explosion having taken off at the end of the run time.

Due to the new number of rays and different time spans, a few alterations to the treatment outlined in chapter 9 has been made. For instance, the reduction of the number of rays to 64, means that the N_{rays} in the calculation of the polar hemispheric averages (section 9.1) will be 32 instead of 48. The difference in time duration will also be reflected in the calculated power level for the background shot noise, cf. eq. 8.7. The number of background events scale linearly with time, $N_{\text{bckgr}} = T_{\text{tot}}\,\Gamma_{\text{noise}}$, and we can therefore easily recalculate the new shot noise levels. For the Shen EoS with $T_{\text{tot}} = 894\,\text{ms}$, and thus 894 bins, we find

$$P_{\text{shot,Shen}} = \frac{3N_{\text{bckgr}}}{N_{\text{bins}}^2} = \frac{3\ \times 894\,\text{ms} \times 1344\,\text{ms}^{-1}}{894^2} = 4.5 \tag{11.1}$$

The values of the adjusted power levels for the other two EoS are given in table 11.1. We maintained a 1 ms sampling in the resampling of the rates, thus the Nyquist frequency remains at 500 Hz. The frequency spacing however is different for each EoS, as it depends on the total time (section 4.2.1.1), and it is given for each EoS in table 11.1. For the power level smoothing (section 9.3) we decided to keep the $\sigma = 4$ Hz smoothing length, although one could argue for using a smaller smoothing length in the case of the Shen EoS, due to its small frequency splitting. We choose to keep the same smoothing length for all three EoSs.

11.1.1 Neutrino signals in the time domain

In fig. 11.1 we show, in analogy to fig. 10.2, the north hemispheric averaged luminosity, rms energy and event rates for $\bar{\nu}_e$ for each EoS, along with the approximated 1D signals for the luminosity and energies. The first overall observation is that the rates for all three EoSs have approximately half the magnitude of the rate for the 15 $M_\odot$ non-rotating (NR) model. This is merely reflecting the fact that all of the luminosities and the energies are smaller in the lighter model.

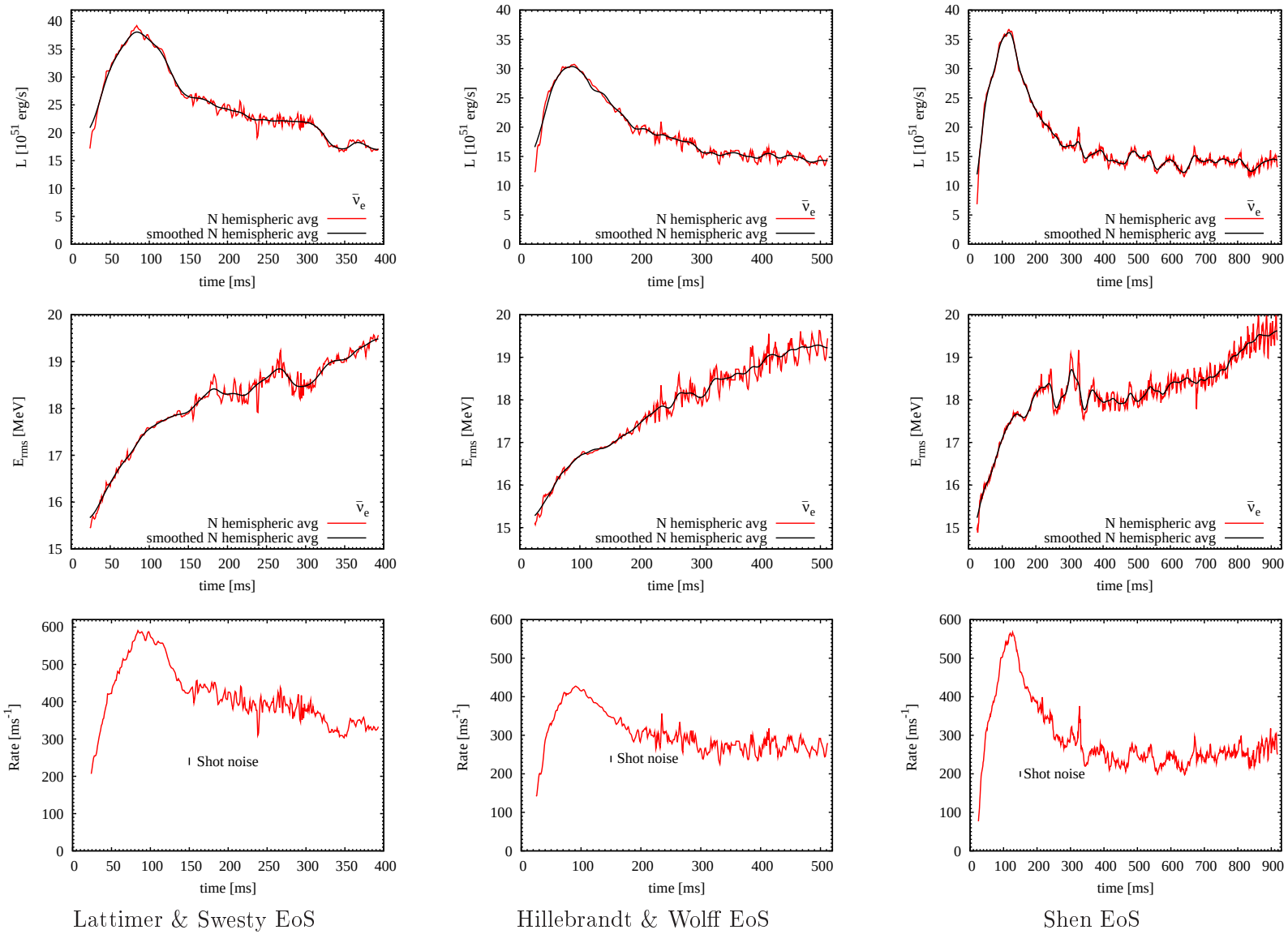

Figure 11.1: *Left to right:* The EoS of LS, HW and Shen respectively. *Top to bottom:* $\bar{\nu}_e$ luminosity, rms energy and event rate for the north hemispheric average (red lines). Black lines are smoothed versions, imitating 1D signals. The figure is analogous to fig. 10.2.

11.1.1.1 Lattimer & Swesty EoS

Looking at the energy and luminosity for the LS EoS we see that the fluctuations are not regular. Comparing the magnitude of the fluctuations with the LS case for the $15M_\odot$ (NR) model we also see that they are smaller. This difference is explained by the SASI being relatively weak in this model. As we discussed in section 1.5 the SASI takes a while to develop (∼200 ms, depending on the specifics of the simulation) and in the LS EoS 11.2 $M_\odot$ model, the shock revival is relatively fast. The shock takes off between 200 and 300 ms post bounce [JM10]. The fairly quick revival is also the cause of the drop in luminosity observed at ∼300 ms, even though some accretion onto the PNS continues after this time.

11.1.1.2 Hillebrandt & Wolff EoS

For the unexploding HW EoS model the fluctuations of the luminosity are around 20% and roughly 5–6% for the energy. These are slightly smaller than the ∼30% and ∼10% for the luminosity and energy in the 15 $M_\odot$ case. Although the fluctuations for the HW EoS appear slightly more regular than for the LS EoS, they too look less regular than for the 15 $M_\odot$ model. However, a direct comparison is hampered by the shorter time duration of the heavier model. As the explosion has not taken off by the end of the run for the lighter model, the SASI has had time to develop to some degree which can account for the larger fluctuations seen at late times $\gtrsim$ 250 ms.

11.1.1.3 Shen EoS

The luminosity fluctuations of ∼ 25–30% for the Shen EoS, and 4–5% in the energy are comparable with the ones observed for the HW EoS. The explosion sets in at ∼250 ms post bounce [JM10]. However, the continued accretion onto the PNS after the shock has taken off is larger than in the case with the LS EoS. This is why no drop in luminosity is visible in the Shen case. We note that the initial "bump" (corresponding to the secular variation) in the luminosity is more narrow for the Shen case compared to the other two EoSs, also when the longer time span has been taken into account, but have no explanation for it at present. The advection that triggers the SASI is not as strong in the Shen EoS case as for the other EoSs. The SASI therefore sets in somewhat later, and is thus relatively weak [JM10].

11.1.2 Results in the frequency domain

We show in fig. 11.2 a comparison between the Fourier transform of the ensemble ray and a hemispherical average, similar to fig. 9.2. From top to bottom it is the LS EoS, the HW EoS and the Shen EoS respectively. Evident in all three cases is the more rapid fall off in power for the hemispheric averages compared to the ensemble average, due to the effective removal of small scale uncorrelated turbulent hydrodynamic motions. Unfortunately the fall off in power for all cases is so rapid for the hemispheric averages that they drop below the background noise level almost instantaneously.

One remedy would be to assume a closer supernova. The event rate scales with the distance as $1/D^2$, cf. eq. 9.1. When we make the power spectrum, we get an extra power of 2, thus giving us an overall scaling of the power spectrum with distance as $1/D^4$. The background noise level, however, only scales with time. Therefore, assuming a closer supernova would

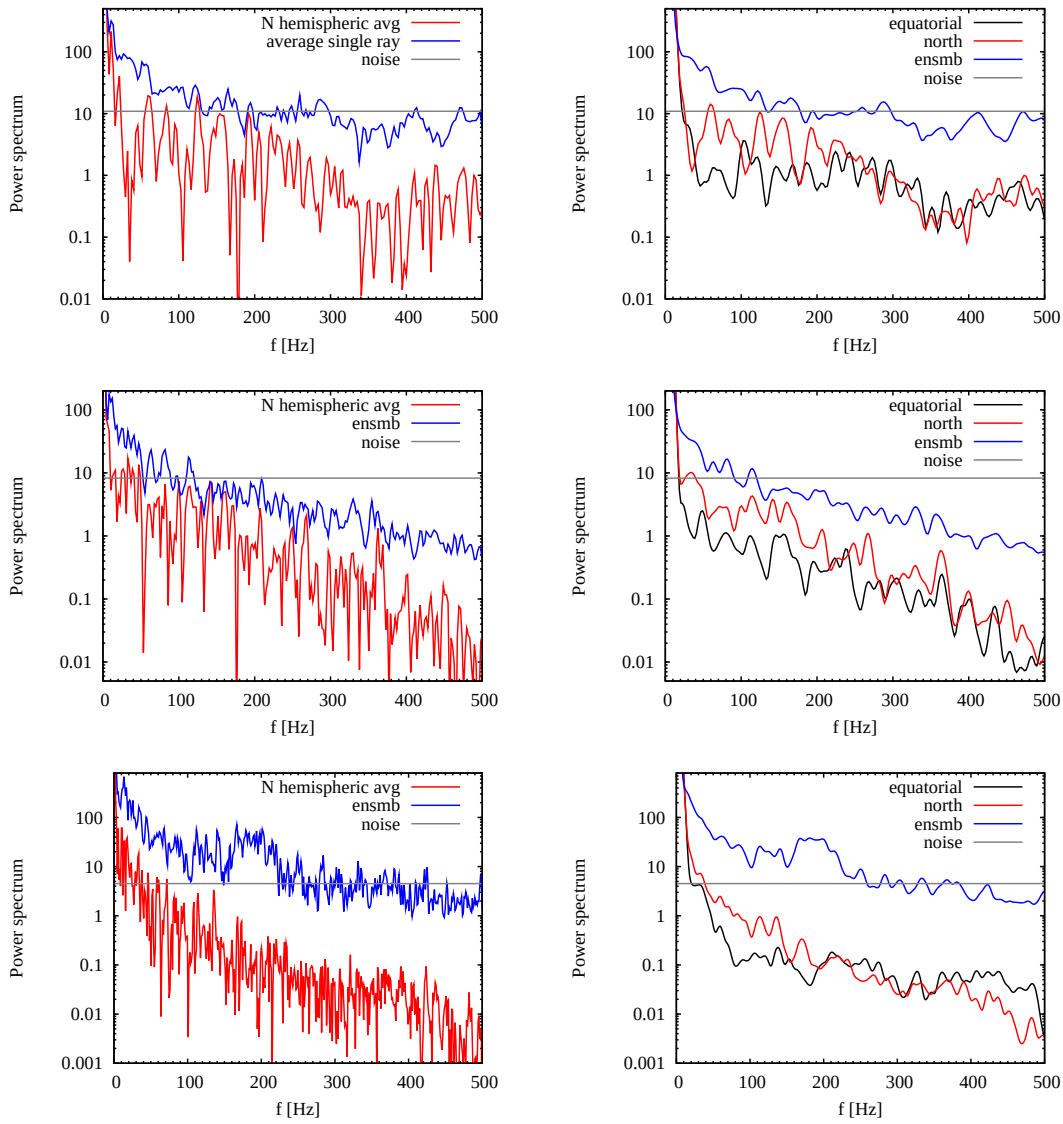

Figure 11.2: *Left:* Power spectra for a single average ray and for the north hemispheric average. *Right:* Smoothed power spectra for a single ray, and the north and equatorial hemispheric averages. *Top:* LS EoS. *Middle:* HW EoS.*Bottom:* Shen EoS. Analogous to figs. 9.2 and 9.4.

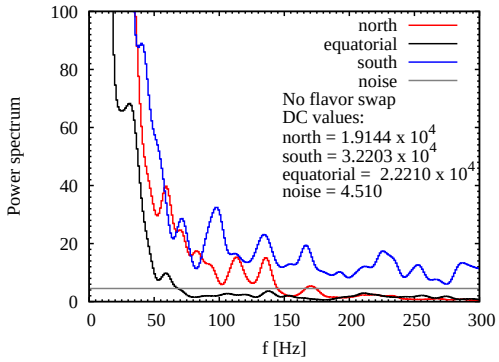

Figure 11.3: Power spectra for the three hemispheric averages of the Shen EoS event rate, but with the SN moved to a distance of 5 kpc.

increase the signal-to-noise ratio. Moving our fiducial SN from a distance of 10 kpc and to a distance of 5 kpc would increase the signal power by a factor 16, making most of the signals detectable or marginally detectable. In fig. 11.3 we show the resulting power spectrum for the Shen EoS for a SN at 5 kpc. The corresponding figures for the other EoSs are work in progress, and therefore we will show below the power spectra for all three EoSs for a SN at the original distance of 10 kpc.

We showed for the 15 $M_\odot$ model in fig. 10.3 that the power spectrum for a spherical symmetric model would be clearly different from the signal due to an axisymmetrical model with hydrodynamical instabilities. Here, we will therefore not show the corresponding plots for the 11.2 $M_\odot$ model, but merely state that the result is the same.

11.1.2.1 Lattimer & Swesty EoS

In fig. 11.4 we show the power spectra for the $\bar{\nu}_e$ on the right and on the left the corresponding power spectra for the ν_x, i.e. assuming a total flavor swap. In both figures we show the three hemispheric averages and the power level of the background shot noise. The tallest peaks in

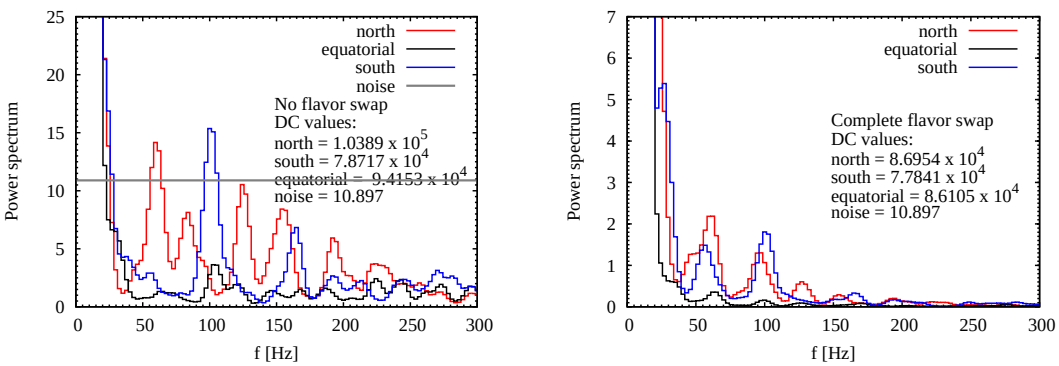

Figure 11.4: LS EoS. *Left:* $\bar{\nu}_e$ power spectrum. *Right:* ν_x power spectrum.

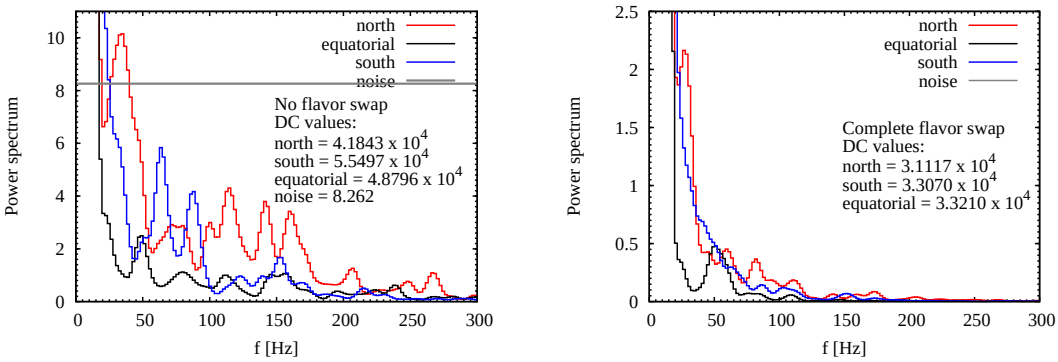

Figure 11.5: HW EoS. *Left:* $\bar{\nu}_e$ power spectrum. *Right:* ν_x power spectrum.

the $\bar{\nu}_e$ power spectrum for south and north reach roughly 15 on our scale. If we assume the SN would be at a distance of 5 kpc instead of 10 kpc, these peaks would reach 240 and be clear above the detector noise that would remain unchanged at the $\sim$ 10 unit level. We see some nicely coinciding peaks for the three hemispheric averages for the ν_x (moving the SN to 5 kpc would put these peaks at 32 instead of 2 and thus above the noise), but the same is not the case for the $\bar{\nu}_e$. The lowest frequency peaks (f $\sim$60 Hz) in the ν_x spectra can possibly be associated to the $\ell = 1$ SASI mode, whereas the next peaks at f $\sim$100 Hz, has a slightly higher frequency than the one usually associated with the $\ell = 2$ SASI mode. The relative weakness of the SASI in this model suggests that most of the power peaks are consequences of the less correlated convective overturns and turbulence in general.

11.1.2.2 Hillebrandt & Wolff EoS

The three hemispheric power spectra for the HW EoS are shown in fig. 11.5 for the $\bar{\nu}_e$ (left) and the ν_x (right). As was the case with the 15 $M_\odot$ model, here the power spectra have less power than the corresponding spectra for the LS EoS. The slightly chaotic distribution of peaks make a clear identification with any of the SASI modes difficult, except maybe for the $\bar{\nu}_e$ equatorial case where we see distinctive peaks at f $\sim$50 Hz and f $\sim$70–75 Hz, corresponding to the frequencies we have identified with the $\ell = 1$ and $\ell = 2$ SASI modes. Comparing this plot with the corresponding one for the 15 $M_\odot$ model (fig. 10.8), we furthermore see that the mismatch between hemispheres seem to be inherent to the HW EoS. For the ν_x spectra again only the equatorial hemispheric average show a significant peak at 50 Hz, although one with a little optimism can see peaks in the northern spectrum at 60 Hz and 80 Hz that might be identified with the SASI frequencies.

11.1.2.3 Shen EoS

Not much structure is visible in the three hemispheric power spectra for the Shen EoS shown in fig. 11.6, with the $\bar{\nu}_e$ spectra on the left and the ν_x on the right. The structure actually present in the $\bar{\nu}_e$ power spectra is more easily seen in fig. 11.3. However, an identification of peaks for frequencies corresponding to the SASI modes is not obvious. Considering the relative weakness of the SASI in this model, together with an early shock revival, this is not surprising. The accretion onto the PNS in the late part of the long time duration will have an

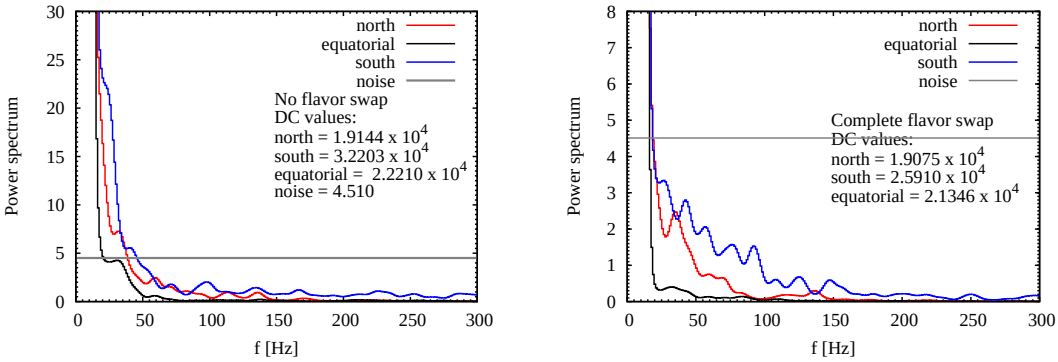

Figure 11.6: Shen EoS. *Left:* $\bar{\nu}_e$ power spectrum. *Right:* ν_x power spectrum.

impact on the neutrino emission, and may provide a part of the explanation for the observed power spectra. However, we also know numerical issues are present in this run, and we will therefore not attempt more conclusions.

11.1.3 Comparison with non-rotating 15 $M_\odot$ model

We conclude that the fast time variations of the neutrino signal from an 11.2 $M_\odot$ would be observable in IceCube, provided the SN was at a smaller distance than the 10 kpc assumed for the 15 $M_\odot$ model. The preliminary results for the 11.2 $M_\odot$ model gives power spectra that have detailed differences from the power spectra given in chapter 10 belonging to the 15 $M_\odot$ model. These differences are tentatively ascribed to the different strengths of the SASI in the two models. The relative weakness in the 11.2 $M_\odot$ model results in less characteristic peaks. We expect that an enhancement of the peaks relative to the noise level could be obtained by taking shorter subsamples of the time duration for the 11.2 $M_\odot$ too, as was seen in the thirds method for the heavier model. Likewise a further investigation of the time evolution of the frequencies might prove useful.

11.2 The rotating 15 $M_\odot$ model

The progenitor for the rotating model is the 15 $M_\odot$ s15s7b2 model of Woosley & Weaver [WW95] with a rotation period of 12 s (initially imposed on the core and from a radius of 1750 km falling off with $r^{-3/2}$ [Mar07]). The rotation rate is roughly a factor of 10 larger than predicted rotation rates for stellar cores, but too slow to allow an explosion by the magneto-rotational mechanism [MJ09]. The employed EoS was Lattimer & Swesty, and 128 rays were used to cover a hemisphere. The width of each ray was thus 1.406°. The starting time was 0.502050 ms and the run ended at 617.125 ms. Close to the end of run time (∼500–600 ms) a strong outward movement of the shock front had begun and explosion was expected to ensue. Further details on this 2D simulation can be found in the paper "Delayed neutrino-driven SN explosions aided by the standing accretion-shock instability" [MJ09] or in the thesis by A. Marek [Mar07].

As an effect of the rotation of the star, the shape of the core deviates from an exact sphere and becomes more oblate ("pancake-like"). And since the centrifugal effects opposes

the gravitational pull the advection time for matter is increased [Mar07]. The deviation from sphericity will make the neutrino emission anisotropic. The extended equatorial regions will emit fewer neutrinos, and with lower energies, which should be kept in mind when interpreting the impact of the SASI. Overall A. Marek finds slightly higher neutrino luminosities and energies in the rotating model than in the non-rotating model (cf. fig. 6.5 in [Mar07]) at early times ($t \lesssim$200 ms), but comparable magnitudes at later times. The rotational model develops convection throughout the layer between the PNS and the shock front, and a strong $\ell = 1$ SASI "sloshing" mode is also present. The detailed evolution of the SASI is different from the one observed in the non-rotating case, but the amplitudes of the shock instability are comparable (up to ∼500 ms) [Mar07].

In our resampling we started at $t = 1$ms and the total resampled time stretch was 616 ms. The resulting power level for the background noise will therefore be $P_{\text{shot}} = 6.545$, cf. eq. 8.7, and the frequency spacing became $\delta f = 1.62$ Hz. We kept the sampling rate at 1 ms, obtaining again a Nyquist frequency of 500 Hz. In the hemispheric averaging the number of rays for the polar averages became $N_{\text{rays}} = 64$, cf. section 9.1. Due to the small frequency spacing, the power level smoothing for this model was done with a slightly smaller sigma than we previously employed; This time taking $\sigma = 3$ Hz.

11.2.1 Time domain neutrino signals

In fig. 11.7 we show the north hemispheric averages of the luminosity, energy and event rate for the rotating 15 $M_\odot$ model (left) along with the corresponding smoothed versions. In the right column we show for comparison the same quantities for the non-rotating model. The higher neutrino luminosity for the rotating case at early times is evident, as well as the fluctuations for the two models being similar in magnitude. The fluctuations of the energy, on the other hand, are marginally smaller than in the corresponding non-rotating model. For the energy the fluctuations in the rotating model are more regular than for the non-rotating case. This regularity is reflected in the event rate. The overall event rate is lower in the rotating case than in the non-rotating case, and it seems like the fluctuations have an additional higher frequency component.

11.2.2 Results in the frequency domain

In fig. 11.8 we show the power spectra for an ensemble ray and the north (and equatorial) hemispheric average. We see, as was also the case in the non-rotating model, that the hemispheric averages fall off more quickly than the ensemble single ray. However, the north hemispheric average remain above the noise level until 150 Hz, and the equatorial average remains above the noise until roughly 100 Hz. When comparing with figs. 9.2 and 9.4 for the non-rotating model, we see that the ensemble ray in the rotating case "levels off" for high frequencies, indicating that stronger small scale turbulence is present. Generally the power for the hemispheric averages seem to be a factor of ∼2–4 smaller in the rotating case than in the non-rotating case. This is also why the power spectra in the rotating case falls below the noise level at a lower frequency than what is observed for the non-rotating case.

Part of the explanation for this seemingly lower power can be found in the fact that the overall event rate is smaller in the rotating model than in the non-rotating model. This leads to quite different DC values for the non-rotating and the rotating cases. (We remember that the

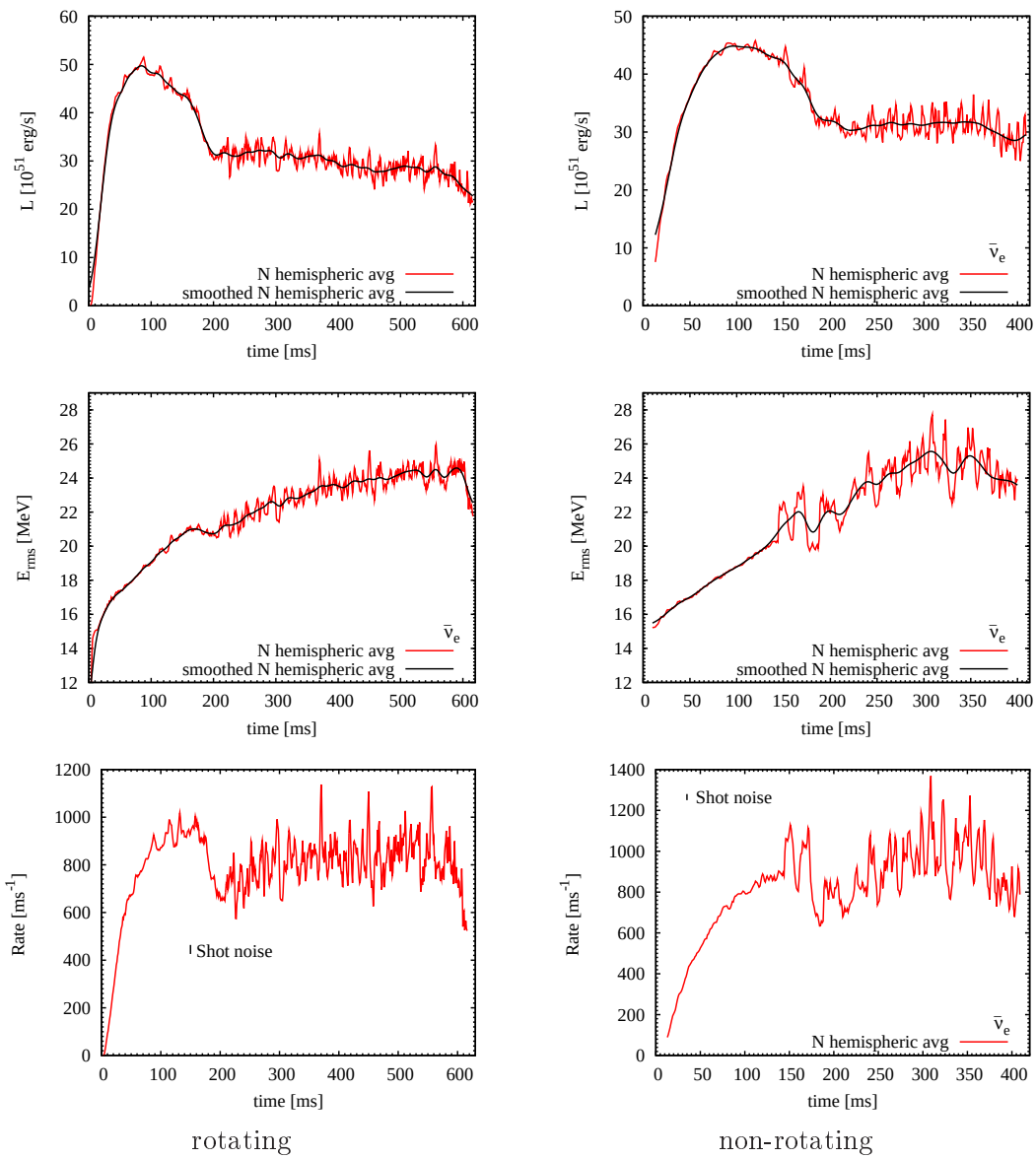

Figure 11.7: *Top:* $\bar{\nu}_e$ luminosity. *Middle:* rms energy. *Bottom:* event rate for a SN at a distance of 10 kpc. Red lines are the north hemispheric averages. Black lines are the smoothed versions. *Left:* rotating model (LS EoS). *Right:* non-rotating model (LS EoS). Note the different scales in the two columns.

DC component was equal to $N^2_{\text{events}}/N^2_{\text{bins}}$). For the $\bar{\nu}_e$ for the non-rotating model we have the following DC values: north = 3.787×10^5, equatorial = 4.149×10^5 and south = 4.173×10^5. For the rotating model the corresponding values are: north = 3.341×10^5, equatorial = 2.968×10^5 and south = 3.328×10^5. This means that the non-rotating values are larger than the rotating ones by 13%, 39.8% and 25% respectively. We already know the extreme difference in the equatorial values are due to a lower emission and lower energies for the neutrinos emitted from the rotationally extended equatorial regions.

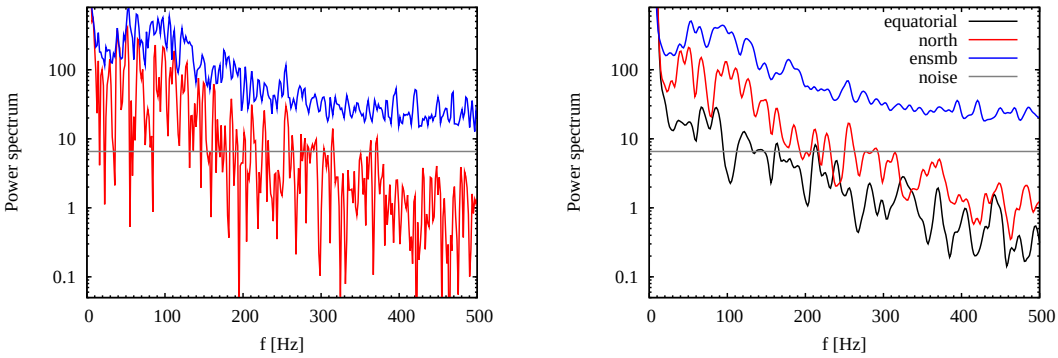

Figure 11.8: *Left:* Power spectra for the single ray (blue) and the north hemispheric average (red). *Right:* Smoothed versions. Black line is equatorial hemispheric average.

In fig. 11.9 we show on the left the power spectra for the three hemispheric averages for the $\bar{\nu}_e$ and for the ν_x on the right. Looking at the $\bar{\nu}_e$ spectra first, we see that the equatorial average is barely above the noise level but the north and south hemispheric averages are well above the noise level. A pronounced peak in the southern spectra is visible at 55 Hz and a strong double peak at 80-90 Hz. From fig. 6.9 in [Mar07] we find a frequency for the $\ell = 1$ mode of roughly 50 Hz, however it appears to be developing from a frequency slightly higher than 50 Hz at early times to one slightly lower than 50 Hz at later times. Therefore taking a value of 50 Hz seems like a conservative estimate. The perceived change in frequency suggest that a further investigation into the time evolution of the frequencies in the IceCube signal could be desirable. The first strong and fairly narrow peak in the $\bar{\nu}_e$ southern spectrum in fig. 11.9 is therefore easily identified with the $\ell = 1$ SASI mode, that was strong in this model. No equally clear peak corresponding to the $\ell = 1$ mode is visible in the northern average. Instead we see two peaks at 40 and 50 Hz, and one at ∼65 Hz, where the two first (or all 3) might be associated with the dipolar oscillation. In the northern average we furthermore see a "bump" of unresolved "peaks" reflecting power at a multitude of frequencies spanning roughly the range from 80 to 130 Hz. In the equatorial power spectrum we see a broad feature spanning from ∼35–55 Hz and two peaks at 70 and 90 Hz. A priori we know that rotational splitting can only be possible for the equatorial viewing direction, as we would be observing perpendicular to the rotational motion, when we look along the polar directions. However, to calculate the exact rotational splitting we would need a detailed velocity profile as a function of radius and time. This is not available. We will, therefore, defer this complex calculation to a future project.

Turning now our attention to the $\bar{\nu}_x$ spectrum we see a similarity in the peak distribution for both the north and the south hemispheric averages when comparing to the corresponding $\bar{\nu}_e$ spectra. The overall power levels of the spectra however is much lower relative to the $\bar{\nu}_e$ spectra than for the non-rotating case. We see a relatively clear peak at 55 Hz in both polar spectra, and for the northern case also a significant peak in at 70 Hz and the broad feature again ranges from ∼85–130 Hz. For the southern average the double peak in the $\bar{\nu}_e$ spectra has been replaced by a wider feature spanning from to 80 to 115 Hz, and a stronger peak at 130 Hz has appeared. The equatorial spectra falls below the noise level almost immediately but a few wiggles can with good will be seen at 55, 65, 85 and 130 Hz. Overall, more structures

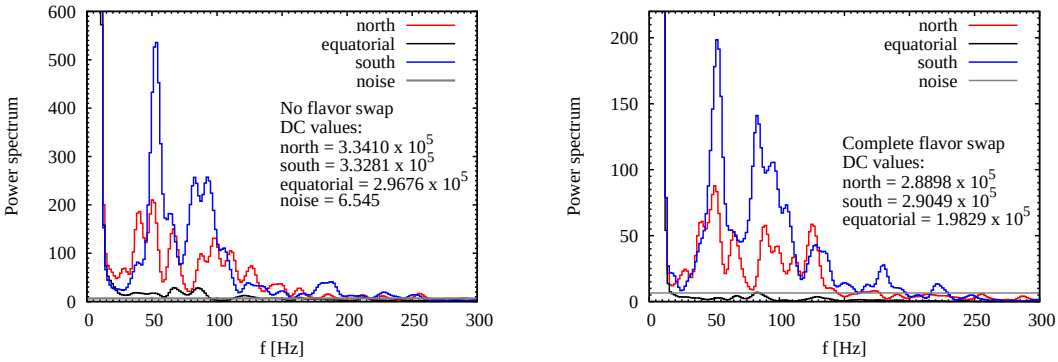

Figure 11.9: Power spectra for the three hemispheric averages for the rotating model. *Left:* for $\bar{\nu}_e$. *Right:* for ν_x. Note the different scales on the y-axes.

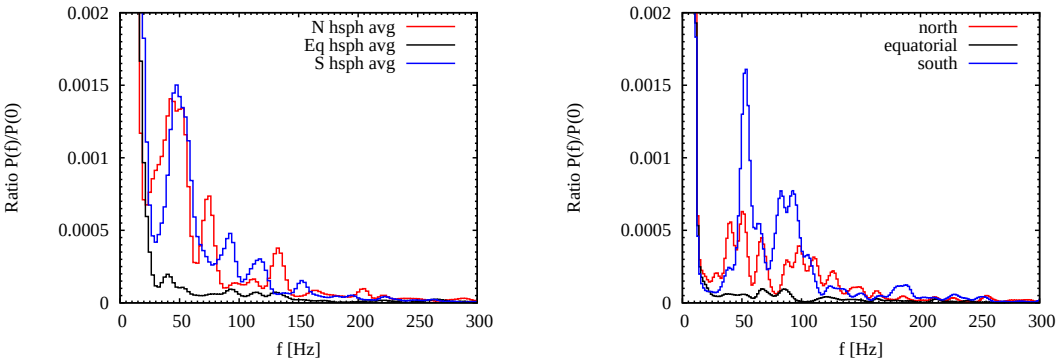

Figure 11.10: Power spectra for $\bar{\nu}_e$ normalized to their DC values. *Left:* non-rotating model. *Right:* rotating model.

are visible in the spectra for the rotating model than in the corresponding non-rotating case (right panel of fig. 10.4), like it was the case with the $\bar{\nu}_e$ spectra.

For a brief revisit to the discussion of generally lower power levels in the rotating case compared to the non-rotating case, we show in fig. 11.10 the power levels for both models, but normalized to the respective DC components. We observe that the relative power for the southern and equatorial averages are comparable in the two cases. The power in the northern case is a factor of almost three smaller. These results agree with the conclusion found in [Mar07] and [MJM08]: the SASI is equally strong in the non-rotating as well as the rotating model.

11.2.3 Comparison with 11.2 $M_\odot$ model

Only the spectra for the Lattimer & Swesty EoS can be used for a comparison between the rotating 15 $M_\odot$ model and the 11.2 $M_\odot$ model. Contrasting therefore fig. 11.9 and fig. 11.4 we find very few similarities, for both flavors. This is unsurprising since in the lower-mass model the SASI does not develop much before the explosion it taking off, where as a strong dipolar SASI motion develops in the rotating case.

11.3 Heavier progenitor: 20 $M_\odot$ model by Brandt et al.

In Brandt et al. [BBO10] they investigate an even heavier model with a mass of 20 $M_\odot$ both with rapid rotation and without. The mass of this progenitor matches the believed progenitor mass of the blue super-giant that exploded as SN1987A. In contrast to the investigation we have made, they choose their fiducial distance to the SN to be 5 kpc. They use the Shen EoS, a Newtonian set up and multi-group flux limited diffusion in the interior, but transitions to a Boltzmann solver for the outer parts. The imposed central rotation is 2 s initially and falls off with r^{-2}. Brandt et al. show that fluctuations in shock positions are correlated to the fluctuations of the (anti) neutrino luminosities, although with a phase lag determined at the decoupling radii. The ν_e leads the shock position by 120° and $\bar{\nu}_e$ leads it by 70° [BBO10]. They also find a stronger correlation between the shock oscillations and the electron neutrinos than with the anti-electron neutrinos, since $\bar{\nu}_e$ decouple further in and are thus less influenced by the hydrodynamics. The stronger correlation with neutrinos suggest that more interest could be focused towards and devoted to detectors capable of registering electron neutrinos[2].

In light of their proof of correlation between the two quantities, they agree with our conclusion that observing fluctuations in the (anti) neutrino signal here on Earth would give strong evidence of the SASI present in 2D simulations. Brandt et al. find a frequency of ∼50 Hz for the $\ell = 1$ SASI mode in the non-rotating model, but do not investigate higher modes. Their finding of a dipolar frequency of 50 Hz for a 20 $M_\odot$ model combined with our findings of similar frequencies in both the 11.2 and 15 $M_\odot$ model, indicate that this is a generic frequency independent of progenitor mass.

For their rotating model Brandt et al. find that the intrinsic shot noise of their secular signal overshadows fast any time fluctuations that might be present. They therefore do not expect any characteristic signatures of convective overturns or shock instabilities. In addition they find large variations in the observed neutrino luminosity depending on viewing angle. In the case of their non-rotating model, however they find that changes due to viewing direction are less than 10%. The orientation effects are therefore smaller than the fast time-varying fluctuations due to hydrodynamic effects. For the non-rotating model they therefore expect to observe clear signal characteristics of shock instabilities and convective overturn, however, they estimate only 10% fluctuations in the $\bar{\nu}_e$ and ν_e signals in IceCube, where we see ∼30–35% fluctuations. The weak dependence upon viewing direction is not too different from our findings. From fig. 11.11 we see a difference in our directional signals of at least 15%.

Using a different method than our Fourier approach to analyze the signal, Brandt et al. calculate via a modified version of the Rayleigh test the distance where *any* fast varying component may be detected. At the same time they point out that we would need a more complete spectrum (i.e. information on several frequencies) to get insight into the physics going on in the SN. They show that rapid variations of the neutrino signal from their non-rotating model would be detectable with IceCube if a full flavor swap occurs and the supernova is within 5 kpc. If no flavor swap is assumed they say a detailed spectrum may be obtained in IceCube for a SN out to ∼8 kpc.

This conclusion is slightly more pessimistic than our conclusions. We estimate that a

[2]For example the proposed scintillator detector LENA will have sensitivity also to electron neutrinos. And it is expected to observe 200-700 electron neutrino induced events for a 8 $M_\odot$ SN at 10 kpc. (Web-page: http://www.e15.physik.tu-muenchen.de/researchi_and_projects/lena/)

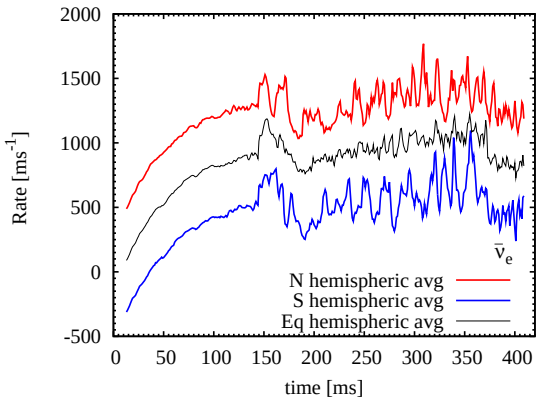

Figure 11.11: Event rates for the non-rotating 15 $M_\odot$ model. Northern hemispheric average (red) offset by +400 with respect to the equatorial hemispheric average (black). Southern hemispheric average (blue) offset by -400.

detailed spectrum for our non-rotating 15 $M_\odot$ model can be seen at a distance of 10 kpc. The highest frequency peak for the southern average of ~ 600 might be observed even at a distance of 20 kpc, where it would be reduced to 37. For an extreme case moving the SN to 25 kpc would give a peak height of 15, still marginally above the noise, and effectively making a SN anywhere in our galaxy borderline observable. For our rotating model the picture is similar, with a maximum peak in the southern spectrum of 535, and a slightly lower noise level. Less opportune is the northern average where observations would be limited to within 20 kpc.

11.4 Summary

In the extended studies we find a stronger dependence on viewing direction than was the case in the non-rotating 15 $M_\odot$. In our original model we found large differences between the power levels of the polar hemispheric averages and the equatorial average. The two polar averages, however, showed not only a comparable power level, but also similar structures. In the 11.2 $M_\odot$ model, this changed. Here we do not find similar structures for the two polar directions, and additionally the power levels differ, see e.g. the left panel of fig. 11.5. The equatorial averages remains consistently below the polar power for all three EoSs. For the rotating 15 $M_\odot$ model we likewise find larger differences between the power of the polar viewing directions.

For the non-rotating 15 $M_\odot$ we found a marked difference in the power spectra depending on the EoS employed. The same was the case for the 11.2 $M_\odot$ model. The differences were in both cases ascribed to the different strength the SASI develops to. For the EoSs where the SASI is weaker, the Shen and LS EoS, the power spectra for the 11.2 $M_\odot$ model do not primarily have well-defined peaks at the characteristic frequencies, but rather have power at several frequencies. In a few instances, e.g. the northern spectrum for the LS EoS, a peak is present close to the characteristic frequencies.

The rotating 15 $M_\odot$ have a strong peak in the southern spectrum corresponding to the $\ell = 1$ SASI mode. This mode was strong in both the non-rotating and the rotating model, which is reflected in both their power spectra. Comparing the overall spectra of the two, the

rotating 15 $M_\odot$ model have more structures in the power spectra than appear in the non-rotating case. We therefore conclude that for our 15 $M_\odot$ models, independent of rotation, a power peak at $f \sim$50 Hz appears to be a good marker for the $\ell = 1$ SASI mode. Furthermore the northern hemispheric averages for both the two 15 $M_\odot$ models show consistently a peak or feature around 130–135 Hz in both flavors that could call for further attention.

We come to the overall conclusion that the spectra for the investigated models show clear differences, and a few repeated features. However, I would be hesitant that we know well enough why the different peaks appear where they do, to be able to make definite distinctions. Knowing a priori the SASI frequencies and underlying convective motions of a model, it is simpler to identify the corresponding peaks in the calculated event rate. Observing a signal, and from that predicting the mass or EoS of the star where the signal originated is more difficult. A further note of caution is that all of the above calculations assume that 2D simulations of core-collapse supernova are a good representation of the actual physics. Only future studies in both 2D and 3D can determine if this is a just assumption.

Part III

Conclusions – Looking to the future

" Experience is a brutal teacher, but you learn.
My God, do you learn."

— C. S. Lewis

12
Conclusions

Throughout this thesis the main theme has been the interplay of neutrinos and the physics in core-collapse supernova. I have sought to add my own little drop of knowledge to the vast ocean of wisdom. This quest has lead me from analytical calculations of matrix elements to numerical programming.

I have investigated how a new strong interaction with a low-mass pseudo-scalar would influence the neutrino energy spectra. I found for our choice of coupling strength that the decoupling radii for processes involving this new interaction were comparable to the decoupling radii of the charged and the neutral current interactions. The resulting neutrino energy spectra were compared to model spectra that complies with observational bounds from SN1987A. I found discernible differences, but not so severe as to rule out this new interaction. Future investigations should be devoted to determine how much energy might be transferred to the post-shock layer, since this interaction effectively provides a back-door for flavor transformations.

Turning my attention from a proposed, but so far unobserved particle to cold, hard data I investigated a specific supernova neutrino signal in IceCube. This investigation was carried out in collaboration with Georg Raffelt, Thomas Janka, Andreas Marek and Cecilia Lunardini. We studied the signature that would be imposed on the neutrino signal from the Standing Accretion Shock Instability (SASI). The instability would imprint fast time variations on the neutrino signal, and we investigated if these variations would be observable in the IceCube Cherenkov detector. The investigation was based on luminosities and energies from recent axisymmetrical simulations. We calculated the expected event rate in IceCube, and performed a Fourier transformation of the signal to investigate the frequencies it contained. We found for our non-rotating 15 $M_\odot$ model strong imprints in the neutrino signal from the SASI sloshing modes as well as smaller-scale, short-period convective overturns. The frequencies of the SASI depend on time and the mode ($\ell = 1$ or 2), but generally have frequencies of 50–100 Hz.

The observed signal would be visible above the noise in IceCube up to 100–200 Hz and would not change much in case of a flavor swap. Since the SASI imprints change over time, we found that a Fourier transform on a shorter time window could provide a higher signal-to-noise ratio. We extended our analysis to a 15 $M_\odot$ model with rotation and a less massive progenitor, our 11.2 $M_\odot$ model. For all of our models we saw significant differences between the power of equatorial and polar viewing directions. In realistic 3D models, this strong directional dependence would likely be less pronounced, since 3D simulations does not confine the dipolar oscillation to follow a predefined axis. A few recent 3D simulations furthermore show the appearance of one or more spiral modes for the SASI [BS]. These modes would make the frequency spectrum more complex. Our analysis of the rotating 15 $M_\odot$ gave a spectrum comparable to the one for the non-rotating model, but with detailed differences. For both of the 15 $M_\odot$ models, the signals we calculate contains features that would be detectable for a SN throughout the Milky Way galaxy. Less opportune is the 11.2 $M_\odot$ model. The power in this case is so low, due to weak SASI activity, that a SN should happen within $\sim$5 kpc if we are to observe detailed power spectra. All the investigated models have a strong dependence on equation on state in common.

Through our calculations we showed that IceCube, despite its inability to resolve energies, would be uniquely qualified for these investigations owing to its large counting rate. However, we showed in one case that the rate fluctuations were primarily due to the fluctuations of energy. Therefore a strong case can be made for future megaton water Cherenkov detectors that will have event-by-event energy information as well as a high count rate. As an extension, a natural project to pursue would therefore be a further investigation into the signal we would expect in such a detector. An actual observation of this signature would provide a crucial test of our theoretical understanding of the core-collapse mechanism. It is uncertain if this method could contribute with more detailed conclusions. We would need to apply this analysis on many more models before we could hope with any confidence to match a given signal with a specific progenitor. Furthermore we would need to include models, that provides different mechanisms for the explosion, e.g. the core g-modes suggested by Burrows et al. [BLD$^+$07].

One thing above all still hampers all our efforts, the lack of data. This applies equally well to a proposed new particle as to a proposed signature in an observed neutrino signal. All of our speculations and hard work would be in vain unless it is proven either correct or incomplete. Because, although we have a vast ocean of wisdom, there is a Universe of questions.

A humble wish for the future would therefore be; to observe the exquisite event of a core-collapse supernova in the Milky Way galaxy.

Appendices

A

Matrix element calculation

In this appendix we calculate the matrix element for the neutrino-Majoron bremsstrahlung process. We start from the general expression for the matrix element.

$$F = \bar{u}(p')\, g\gamma_5\, u(p) \frac{\mathscr{C}}{(p-p')^2 - m_\phi^2} \bar{u}(k') g\, \gamma_5 \frac{i(\not{l} + m_\nu)}{l^2 - m_\nu^2} g\, \gamma_5 u(k)\phi(q) \tag{A.1}$$

where $\mathscr{C}$ is a (complex) constant.

$$\begin{aligned} |F|^2 = \frac{g^6\, |\mathscr{C}|^2}{|(p-p')^2 - m_\phi^2|^2} \bar{u}(p')\gamma_5 u(p) \bar{u}(k')\gamma_5 \frac{i(\not{l} + m_\nu)}{l^2 - m_\nu^2} \gamma_5 u(k)\phi(q)\phi^\dagger(q) \times \\ u^\dagger(k)\gamma_5 \left(\frac{i(\not{l} + m_\nu)}{l^2 - m_\nu^2} \right)^\dagger \gamma_5 \bar{u}^\dagger(k') u^\dagger(p)\gamma_5 \bar{u}^\dagger(p') \end{aligned} \tag{A.2}$$

Using the identities $\gamma^0\gamma^0 = 1$ and $\phi\,\phi^\dagger = 1$ together with the anti-commutation relation $\gamma_5\gamma^0 = -\gamma^0\gamma_5$, and remembering that $\bar{u} = u^\dagger\gamma^0$ and $\bar{u}^\dagger = \gamma^0 u$, leads to

$$\begin{aligned} |F|^2 = \frac{g^6\, |\mathscr{C}|^2}{|(p-p')^2 - m_\phi^2)|^2} \bar{u}(p')\gamma_5 u(p) \bar{u}(k')\gamma_5 \frac{i(\not{l} + m_\nu)}{l^2 - m_\nu^2} \gamma_5 u(k) \times \\ \bar{u}(k)\gamma^0\gamma_5 \left(\frac{i(\not{l} + m_\nu)}{l^2 - m_\nu^2} \right)^\dagger \gamma_5\gamma^0 u(k') \bar{u}(p)\gamma^0\gamma_5\gamma^0 u(p') \end{aligned} \tag{A.3}$$

$$\begin{aligned} |F|^2 = \frac{g^6\, |\mathscr{C}|^2}{|(p-p')^2 - m_\phi^2)|^2} \bar{u}(p')\gamma_5 u(p) \bar{u}(k')\gamma_5 \frac{i(\not{l} + m_\nu)}{l^2 - m_\nu^2} \gamma_5 \times \\ u(k)\bar{u}(k)(-\gamma_5\gamma^0) \left(\frac{i(\not{l} + m_\nu)}{l^2 - m_\nu^2} \right)^\dagger (-\gamma^0\gamma_5) u(k') \bar{u}(p)(-\gamma_5) u(p') \end{aligned} \tag{A.4}$$

Recalling the identities

$$\sum_s u(p,s)\bar{u}(p,s) = (\not{p} + m) \tag{A.5}$$

$$\sum_s v(p,s)\bar{v}(p,s) = (\not{p} - m) \tag{A.6}$$

leads to

$$\begin{aligned}\frac{1}{4}\sum_{s=1,2,3,4}|F|^2 = -\sum_{s=1,2,3}\frac{g^6\,|\mathscr{C}|^2}{|(p-p')^2-m_\phi^2)|^2}\bar{u}(p')\gamma_5 u(p)\bar{u}(k')\gamma_5\frac{i(\not{l}+m_\nu)}{l^2-m_\nu^2}\gamma_5 \times \\ (\not{k}+m)\gamma_5\gamma^0\left(\frac{i(\not{l}+m_\nu)}{l^2-m_\nu^2}\right)^\dagger\gamma^0\gamma_5 u(k')\bar{u}(p)\gamma_5 u(p')\end{aligned} \tag{A.7}$$

$$\begin{aligned}\frac{1}{4}\sum_{s=1,2,3,4}|F|^2 = -\sum_{s=1,2,3}\frac{g^6\,|\mathscr{C}|^2}{|(p-p')^2-m_\phi^2)|^2}\bar{u}(p')\gamma_5 u(p)\bar{u}(k')\gamma_5\frac{i(\not{l}+m_\nu)}{l^2-m_\nu^2}\gamma_5 \times \\ (\not{k}+m)\gamma_5\gamma^0\left(\frac{i(\not{l}+m_\nu)}{l^2-m_\nu^2}\right)^\dagger\gamma^0\gamma_5 u(k')\bar{u}(p)\gamma_5 u(p')\end{aligned} \tag{A.8}$$

$$\begin{aligned}\frac{1}{4}\sum_{s=1,2,3,4}|F|^2 = -\frac{g^6\,|\mathscr{C}|^2}{|(p-p')^2-m_\phi^2)|^2}\,\mathrm{Tr}[(\not{p}'+m)\gamma_5(\not{p}+m)\gamma_5] \times \\ \mathrm{Tr}\left[(\not{k}'+m)\gamma_5\frac{i(\not{l}+m)}{l^2-m^2}\gamma_5(\not{k}+m)\gamma_5\gamma^0\left(\frac{i(\not{l}+m)}{l^2-m^2}\right)^\dagger\gamma^0\gamma_5\right]\end{aligned} \tag{A.9}$$

We calculate the 2 traces

$$\mathrm{Tr}_1 = \mathrm{Tr}[(\not{p}'+m)\gamma_5(\not{p}+m)\gamma_5] = \mathrm{Tr}[\not{p}'\gamma_5\not{p}\gamma_5]+4m^2 = -\,\mathrm{Tr}[\not{p}'\not{p}]+4m^2 = -4p'\cdot p+4m^2 \tag{A.10}$$

Using $\overline{\gamma^\mu} \equiv \gamma^0\gamma^{\mu\dagger}\gamma^0 = \gamma^\mu$ and the fact that l is a real vector, we find the second trace

$$\begin{aligned}\mathrm{Tr}_2 = \mathrm{Tr}\left[(\not{k}'+m)\gamma_5\tfrac{i(\not{l}+m)}{l^2-m^2}\gamma_5(\not{k}+m)\gamma_5\gamma^0\left(\tfrac{i(\not{l}+m)}{l^2-m^2}\right)^\dagger\gamma^0\gamma_5\right] = \\ \mathrm{Tr}\left[(\not{k}'+m)\gamma_5\tfrac{i(\not{l}+m)}{l^2-m^2}\gamma_5(\not{k}+m)\gamma_5\gamma^0\left(\tfrac{-i(\not{l}^\dagger+m)}{l^2-m^2}\right)\gamma^0\gamma_5\right] = \\ \mathrm{Tr}\left[(\not{k}'+m)\gamma_5\tfrac{(\not{l}+m)}{l^2-m^2}\gamma_5(\not{k}+m)\gamma_5\left(\tfrac{\gamma^0\not{l}^\dagger\gamma^0+m}{l^2-m^2}\right)\gamma_5\right]\end{aligned}$$

Now we are allowed to cycle the last γ_5 in the trace to the front

$$\mathrm{Tr}\left[\gamma_5(\not{k}'+m)\gamma_5\frac{(\not{l}+m)}{l^2-m^2}\gamma_5(\not{k}+m)\gamma_5\left(\frac{\gamma^0\not{l}^\dagger\gamma^0+m}{l^2-m^2}\right)\right] \tag{A.11}$$

Since γ_5 anti-commutes with the individual γ^μ: $\{\gamma_5,\gamma^\mu\} = 0$ and k_μ is a vector, we can pass the γ_5 through $(\not{k}+m)$ at the expense of a minus sign that is canceled by a minus from the $(\not{k}'+m)$ term. This results in

$$\mathrm{Tr}\left[(\not{k}'+m)\frac{(\not{l}+m)}{l^2-m^2}(\not{k}+m)\left(\frac{\gamma^0\not{l}^\dagger\gamma^0+m}{l^2-m^2}\right)\right]=$$
$$\frac{1}{(l^2-m^2)^2}\,\mathrm{Tr}\left[(\not{k}'+m)(\not{l}+m)(\not{k}+m)(\gamma^0\not{l}^\dagger\gamma^0+m)\right]$$

Let us take a closer look at the term $\gamma^0\not{l}^\dagger\gamma^0$.

$$\gamma^0\not{l}^\dagger\gamma^0=\gamma^0(\gamma^\mu l_\mu)^\dagger\gamma^0=\gamma^0(\gamma^0 l_0-\gamma^1 l_1-\gamma^2 l_2-\gamma^3 l_3)^\dagger\gamma^0$$

Here $l_{0,1,2,3}$ are numbers, thus the Hermitian conjugation leaves them unaffected, and γ^0 is Hermitian whereas the γ^i are anti-hermitian and get a minus. This gives us

$$\gamma^0\not{l}^\dagger\gamma^0=\gamma^0(\gamma^0 l_0+\gamma^1 l_1+\gamma^2 l_2+\gamma^3 l_3)\gamma^0$$

Now taking the γ^0 inside the parenthesis, one gets terms like $\gamma^0\gamma^1 l_1\gamma^0$, where you can pull l_1 to one end since it is just a number, and since γ^0 and γ^i anti-commutes it gives us a minus sign, bringing us to

$$\gamma^0\not{l}^\dagger\gamma^0=\gamma^0 l_0-\gamma^1 l_1-\gamma^2 l_2-\gamma^3 l_3=\not{l}$$

Continuing we remember that the trace of an odd number of γ-matrices is zero, leaving us with the following terms

$$\frac{1}{(l^2-m^2)^2}\,\mathrm{Tr}\left[\not{k}'\not{l}\not{k}\not{l}+m^4+2m^2\not{k}'\not{l}+m^2\not{k}'\not{k}+m^2\not{l}\not{k}+m^2\not{l}\not{l}+m^2\not{k}\not{l}\right] \tag{A.12}$$

$$\mathrm{Tr}_2=\frac{1}{(l^2-m^2)^2}\Big(\mathrm{Tr}\left[\not{k}'\not{l}\not{k}\not{l}\right]+4m^4+8m^2k'\cdot l+4m^2k'\cdot k+4m^2 l\cdot l+4m^2 l\cdot k+4m^2 k\cdot l\Big) \tag{A.13}$$

$$\begin{aligned}=&\frac{1}{(l^2-m^2)^2}\Big(4\left[(k'\cdot l)(k\cdot l)+(k'\cdot l)(k\cdot l)-(k'\cdot k)(l\cdot l)\right]\\&+4m^4+8m^2k'\cdot l+4m^2k'\cdot k+4m^2 l\cdot l+8m^2k\cdot l\Big)\end{aligned} \tag{A.14}$$

$$\begin{aligned}=&\frac{4}{(l^2-m^2)^2}\Big[m^4+2(k'\cdot l)(k\cdot l)+2m^2(k'\cdot l)+2m^2(k\cdot l)\\&+m^2(k'\cdot k)+m^2(l\cdot l)-4(k'\cdot k)(l\cdot l)\Big]\end{aligned} \tag{A.15}$$

Combining the two traces to obtain the final matrix element

$$\begin{aligned}\frac{1}{4}\sum|F|^2=&-\frac{4g^6}{((p-p')^2-m_\phi^2)^2(l^2-m^2)^2}(-4p'\cdot p+4m^2)\Big[m^4+(k'\cdot l)(k\cdot l)\\&+m^2(k'\cdot l)+m^2(k\cdot l)+m^2(k'\cdot k)+m^2(l\cdot l)-(k'\cdot k)(l\cdot l)\Big]\end{aligned} \tag{A.16}$$

$$= \frac{16g^6}{(p-p')^4(l^2-m^2)^2}\Big[m^4(p'\cdot p - m^2) + (k'\cdot l)(k\cdot l)(p'\cdot p - m^2) + m^2(p'\cdot p - m^2)(k'\cdot l) \\ + m^2(p'\cdot p - m^2)(k\cdot l) + m^2(p'\cdot p - m^2)(k'\cdot k) \\ + m^2(p'\cdot p - m^2)(l\cdot l) - (p'\cdot p - m^2)(k'\cdot k)(l\cdot l)\Big] \tag{A.17}$$

Since we are working in the strongly relativistic regime, we will neglect all terms proportional to m^2 or higher, resulting in

$$\frac{1}{4}\sum |F|^2 = \frac{16g^6}{(p-p')^4 l^4}(k'\cdot l)(k\cdot l)(p'\cdot p) - (k'\cdot k)(l\cdot l)(p'\cdot p) \tag{A.18}$$

$$\frac{1}{4}\sum |F|^2 = \frac{4g^6}{(p\cdot p')^2 l^4}(k'\cdot l)(k\cdot l)(p'\cdot p) - (k'\cdot k)(l\cdot l)(p'\cdot p) \tag{A.19}$$

$$\frac{1}{4}\sum |F|^2 = \frac{4g^6}{(p\cdot p') l^4}(k'\cdot l)(k\cdot l) - (k'\cdot k)(l\cdot l) \tag{A.20}$$

B

Paper: Fast time variations of neutrino fluxes and their detectability

Fast time variations of supernova neutrino fluxes and their detectability

Tina Lund,[1] Andreas Marek,[2] Cecilia Lunardini,[3,4] Hans-Thomas Janka,[2] and Georg Raffelt[5]

[1]*Department of Physics and Astronomy, Aarhus University, Ny Munkegade 120, 8000 Aarhus C, Denmark*
[2]*Max-Planck-Institut für Astrophysik, Karl-Schwarzschild-Str. 1, 85748 Garching, Germany*
[3]*Arizona State University, Tempe, Arizona 85287-1504, USA*
[4]*RIKEN BNL Research Center, Brookhaven National Laboratory, Upton, New York 11973, USA*
[5]*Max-Planck-Institut für Physik (Werner-Heisenberg-Institut), Föhringer Ring 6, 80805 München, Germany*

(Received 10 June 2010; published 21 September 2010)

In the delayed explosion scenario of core-collapse supernovae, the accretion phase shows pronounced convective overturns and a low-multipole hydrodynamic instability, the standing accretion shock instability. These effects imprint detectable fast time variations on the emerging neutrino flux. Among existing detectors, IceCube is best suited to this task, providing an event rate of $\sim$1000 ms^{-1} during the accretion phase for a fiducial SN distance of 10 kpc, comparable to what could be achieved with a megaton water Cherenkov detector. If the standing accretion shock instability activity lasts for several hundred ms, a Fourier component with an amplitude of 1% of the average signal clearly sticks out from the shot noise. We analyze in detail the output of axially symmetric hydrodynamical simulations that predict much larger amplitudes up to frequencies of a few hundred Hz. If these models are roughly representative for realistic SNe, fast time variations of the neutrino signal are easily detectable in IceCube or future megaton-class instruments. We also discuss the information that could be deduced from such a measurement about the physics in the SN core and the explosion mechanism of the SN.

DOI: 10.1103/PhysRevD.82.063007 PACS numbers: 14.60.Pq, 97.60.Bw

I. INTRODUCTION

The delayed explosion scenario remains the standard paradigm for the core-collapse supernova (SN) mechanism. After core bounce a shock wave forms that stalls at a typical radius of 100–200 km while matter keeps falling in, forming a standing accretion shock that can last for several hundred ms before the shock is relaunched, presumably after sufficient neutrino-energy deposition in the region behind the shock. Two- and three-dimensional hydrodynamic simulations reveal convective instabilities that quickly develop into large-scale convective overturns and a strong dipole oscillation of the neutron star against the "cavity" formed by the standing shock, the standing accretion shock instability (SASI) [1–7].

During the accretion phase, neutrino emission is particularly large, being powered primarily by the gravitational energy of the in-falling material. In the SASI scenario the neutrino emission is strongly modulated. As an example we show in Fig. 1 the $\bar{\nu}_e$ luminosity as a function of time, averaged over one hemisphere, from the two-dimensional (2D) simulations of Marek, Janka, and Müller (2009) [6]. As noted by these authors, such large flux variations could well become detectable in the high-statistics neutrino signal of the next galactic SN, revealing direct evidence for the predicted SASI mode and convective overturns.

The detection of fast time variations, or equivalently, identifying high-frequency Fourier modes in the signal, is limited by the number of registered events: a significant signal must stick above the shot noise caused by the fluctuating event rate, so a large counting rate is crucial. Among the existing or near-future detectors, IceCube is the most promising because it detects a large number of Cherenkov photons triggered by neutrinos. At most one single Cherenkov photon is picked up from a given neutrino, so every photon tags the arrival time of a different neutrino. For our SN example of Fig. 1, assumed at a fiducial distance of 10 kpc, the maximum photon detection rate is roughly 1000 ms^{-1}, similar to the intrinsic background rate. On the other hand, for Super-Kamiokande (fiducial volume 22.5 kt) the corresponding neutrino detection rate is approximately 2 orders of magnitude smaller, although essentially background free. Based on this simple estimate, we use IceCube as our benchmark detector. On the other hand, a megaton-class water Cherenkov detector would achieve neutrino detection rates similar to IceCube and in addition would provide event-by-event energy information, a quantity also showing strong fluctuations. The potential of such a detector will be studied elsewhere.

A possible limiting factor to detecting fast signal variations is time-of-flight dispersion caused by neutrino masses. The delay of arrival times is

$$\Delta t = 0.57\ \mathrm{ms}\left(\frac{m}{\mathrm{eV}}\right)^2\left(\frac{30\ \mathrm{MeV}}{E}\right)^2\left(\frac{D}{10\ \mathrm{kpc}}\right)^2. \qquad (1)$$

We will see that signal variations may be detectable up to a few hundred Hz, corresponding to time scales of several ms. So even for eV neutrino masses, arrival time dispersion would be a marginal effect. Moreover, current cosmological limits on the overall neutrino mass scale are approximately 0.2 eV [8], very similar to the sensitivity of the

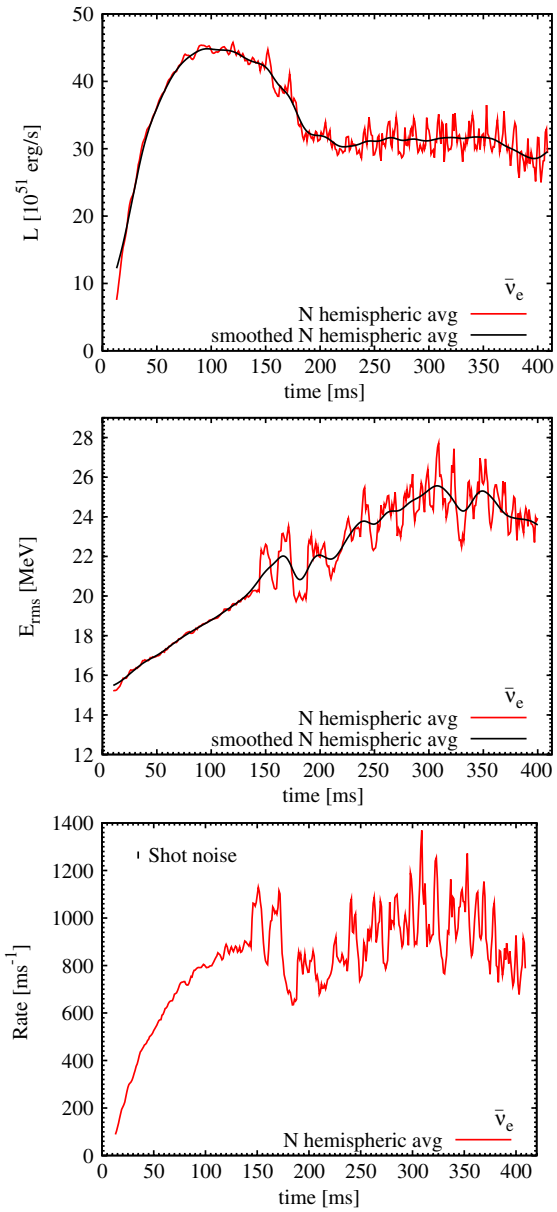

FIG. 1 (color online). *Top:* $\bar{\nu}_e$ luminosity of our baseline SN model sampled at 1 ms intervals. Red line: north hemispheric average. Black line: moving average with a Gaussian window function ($\sigma = 7$ ms). *Middle:* $\bar{\nu}_e$ rms energy. Red and black lines as the panel above. *Bottom:* detection rate in IceCube. Also shown is the 1σ range caused by shot noise, assuming a bin width of 1 ms.

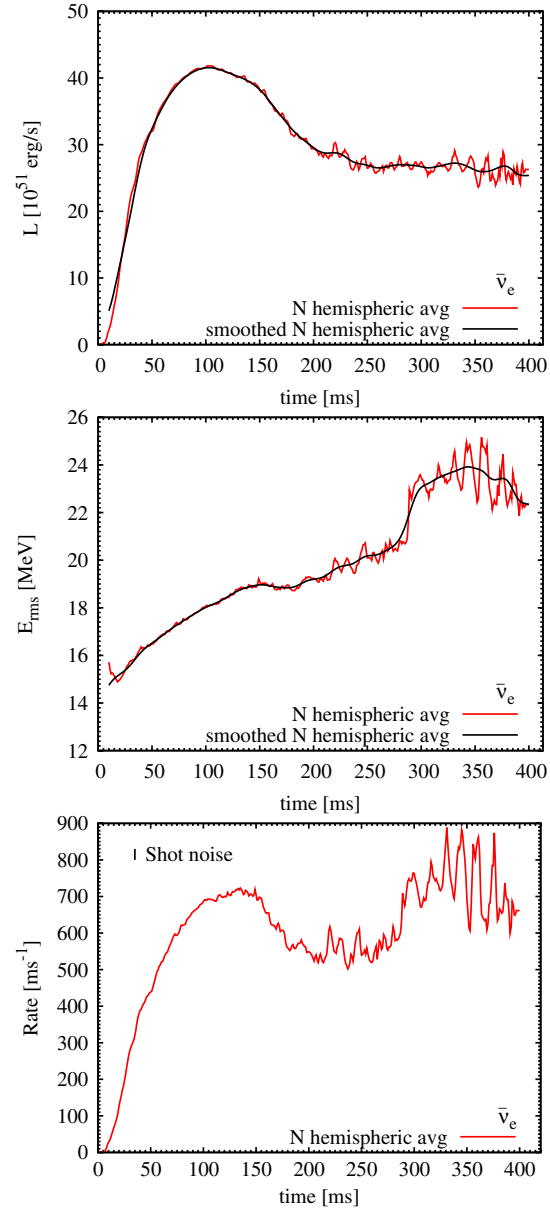

FIG. 2 (color online). Same as Fig. 1 using the EoS of Hillebrandt and Wolff. See Sec. V for more details.

ongoing Karlsruhe Tritium Neutrino Experiment (KATRIN) [9]. Assuming KATRIN will confirm this limit, arrival time dispersion of SN neutrinos will be completely irrelevant in our context. Should KATRIN discover eV-scale neutrino masses in violation of cosmological limits one could return to this study and include time-of-flight dispersion.

In Sec. II we review the detector response of IceCube to SN neutrinos. In Sec. III we use the output from the numerical models of Marek, Janka, and Müller (2009) [6] and study the signal power as a function of frequency relative to the detector shot noise. In Sec. IV we briefly discuss the fluctuations of neutrino energies relative to luminosity variations. In Sec. V we consider the modification caused by a stiffer nuclear equation of state. In Sec. VI we interpret the results of our analysis on the basis of present explosion models and our understanding of the physics relevant in the SN core. We also briefly address the question what could be learned if SASI and convective neutrino signal variations were detected. We discuss and summarize our findings in Sec. VII. In the Appendix we derive the detector shot noise and define the normalization of our Fourier transform of binned data.

II. DETECTOR MODEL

The IceCube detector, soon to be completed at the South Pole, currently provides by far the largest detection rate for the next nearby SN. For our sensitivity forecast we use a somewhat schematic model for its response to a SN neutrino signal. For the finished detector with 4800 optical modules, the latest efficiencies provide a detection rate of Cherenkov photons originating from the dominant inverse beta reaction $\bar{\nu}_e + p \to n + e^+$ of [10–12]

$$R_{\bar{\nu}_e} = 114\ \mathrm{ms}^{-1} \frac{L_{\bar{\nu}_e}}{10^{52}\ \mathrm{erg\,s}^{-1}} \left(\frac{10\ \mathrm{kpc}}{D}\right)^2 \left(\frac{E_{\mathrm{rms}}}{15\ \mathrm{MeV}}\right)^2. \quad (2)$$

Here we use the definition

$$E_{\mathrm{rms}}^2 = \frac{\langle E^3 \rangle}{\langle E \rangle}, \quad (3)$$

where the average is to be taken over the neutrino distribution function. This quantity plays the role of an rms energy relative to the energy spectrum, not the flux spectrum. Other authors use the definition $E_{\mathrm{rms}} = \sqrt{\langle E^2 \rangle}$, which is perhaps more appropriately called the rms energy, but our definition is what appears in the IceCube rate and thus will be used. In other words, because the Cherenkov light measures the neutrino-energy deposition in ice, $L_{\bar{\nu}_e}$ and E_{rms} are the most natural parameters to describe the instantaneous neutrino flux. Our estimate of the photon count rate Eq. (2) uses an approximate inverse beta cross section of $\sigma = 9.52 \times 10^{-44}\ \mathrm{cm}^2 (E_{\bar{\nu}_e}/\mathrm{MeV})^2$ to obtain a simple scaling behavior with energy.

For low-energy neutrino detection, IceCube is a very coarse detector, implying that from a given neutrino it picks up at most one Cherenkov photon. Assuming more closely spaced optical modules, the average photon detection rate remains unchanged, but the fluctuations increase in that several detected photons may have been triggered by the same neutrino. This increased shot noise reduces the capability to detect fast time variations. In the extreme case of a densely instrumented detector such as Super-Kamiokande, one measures so many photons from a given neutrino that one can reconstruct detailed energy and directional information, at the expense of relatively few neutrino events and therefore much larger shot noise. In this sense the apparent weakness of IceCube for low-energy neutrino detection is actually a virtue for diagnosing fast time variations. Since for IceCube a single photon detection is identical with detecting the arrival time of a neutrino (except for background), we use the term "event" interchangeably for "photon detection" or "neutrino detection."

For our SN models, a typical rate during the accretion phase is around $10^3\ \mathrm{ms}^{-1}$. This is to be compared with the estimated IceCube background rate of [11]

$$R_{\mathrm{bkgd}} = 1.34 \times 10^3\ \mathrm{ms}^{-1}. \quad (4)$$

This is the dark current of $280\ \mathrm{s}^{-1}$ per optical module, multiplied with 4800 optical modules of the final detector to be completed by the end of this year. Therefore, for a SN at the fiducial distance, the signal and background rates are comparable, but the background dominates. Therefore, it is essentially the shot noise of the background that limits the detectability of fast signal variations unless the SN is closer.

IceCube samples the data in 1.6384 ms bins, whereas low-energy water Cherenkov or scintillator detectors register the times t_j of every event with high precision. The bin width, or the absence of binning, only affects the sensitivity to frequencies that we will see are too high to be detected. Therefore, the details of signal binning do not enter our discussion. We have found it convenient to use 1 ms as a nominal bin width and also as a sampling rate of the numerical SN results.

The main obstacle to detecting fast time variations is shot noise (Poisson fluctuations of the limited number of events). In the lower panel of Fig. 1 we show as a vertical bar the 1σ fluctuation per 1 ms bin for an event rate of $900\ \mathrm{ms}^{-1}$. Therefore, it is evident that with IceCube one can follow the overall neutrino light curve with excellent precision.

To estimate the required amplitude for a fast periodic variation to be detectable, we model the signal as a sequence of arrival times t_j with $j = 1, \ldots, N$. The Fourier transform of this signal (frequency f) is

$$g(f) = \sum_{j=1}^{N} e^{-i2\pi f t_j} \quad (5)$$

with the spectral power $G(f) = |g(f)|^2$. The detection rate has units of inverse time, so the Fourier components are dimensionless. If the sequence of events is completely random, i.e., the times t_j sample a uniform distribution on a given time interval, one can show (see the Appendix) that

$$\frac{\langle G_{f\neq 0} \rangle}{G_{f=0}} = \frac{1}{N} \quad (6)$$

and we note that $G(0) = N^2$.

Next we assume the signal has a frequency f_a imprinted upon it; i.e., it is proportional to $[1 + a\cos(2\pi f_a t)]$. The power of this signal vanishes everywhere except at $f = 0$ and $f = \pm f_a$. The relative power is $G(\pm f_a)/G(0) = a^2/4$. Therefore, an imprinted cosine variation with the amplitude $a = 2/\sqrt{N}$ is equal to the shot noise. Assuming that the accretion phase lasts for 400 ms and using the background rate of Eq. (4) as the dominant source of shot noise, the number of events is $N = 5.4 \times 10^5$ and the shot-noise level corresponds to a cosine amplitude of $a = 3 \times 10^{-3}$. Of course, to stick reliably above background, a Fourier component would need to be somewhat larger. In other words, for a SN at 10 kpc one can expect to detect signal variations with an amplitude roughly on the 1% level

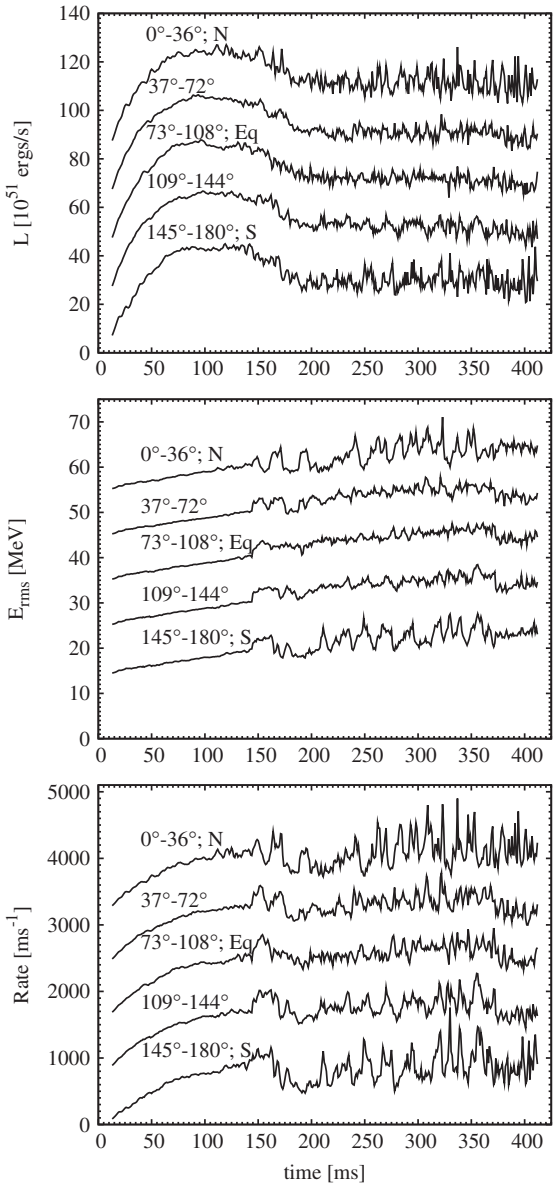

FIG. 3. Luminosity, rms energy, and IceCube event rate based on the $\bar{\nu}_e$ fluxes of our model with Lattimer and Swesty EoS. The 96 angular rays have been combined into five averages ranging from north (top curve) to south (bottom curve), where in each panel the curves are offset relative to each other by 20, 10, and 800 units of the vertical axes, respectively.

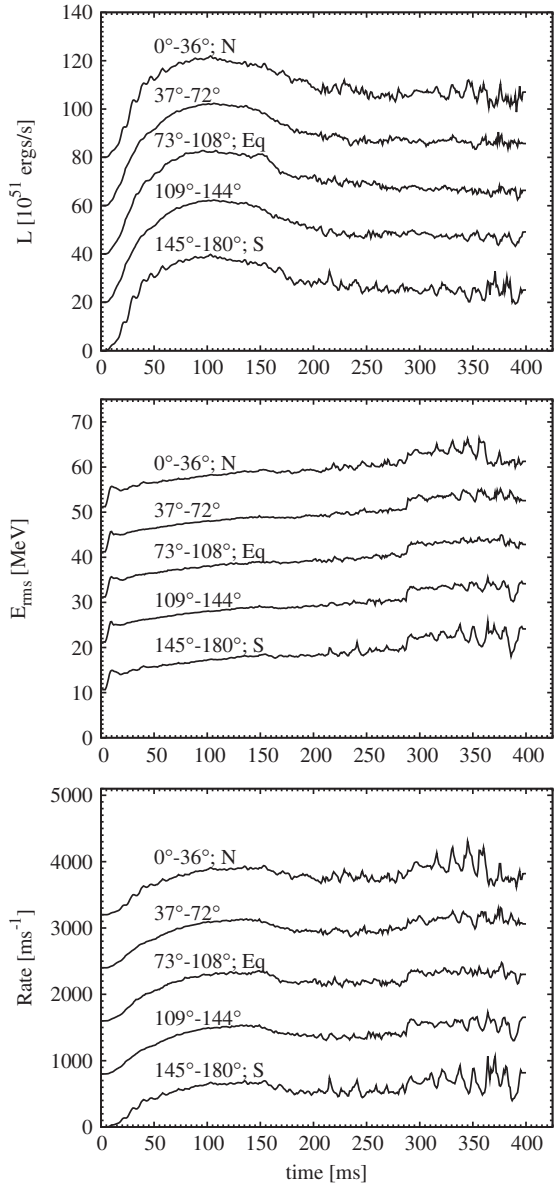

FIG. 4. Same as Fig. 3 for a run with the EoS of Hillebrandt and Wolff.

of the average rate. The signal variations shown in the lower panel of Fig. 1 would easily show up in IceCube.

III. NUMERICAL SUPERNOVA SIGNAL

A. Description of the model

To make this rough estimate more concrete, we next use a numerical simulation to compare the expected signal fluctuations with the sensitivity of IceCube. The two-dimensional (axially symmetric) simulations which this discussion is based on were performed with the PROMETHEUS-VERTEX code [13,14] and the simulations are discussed in detail in Ref. [6]. We therefore repeat only a few essential aspects of both the numerical treatment and the simulation runs and refer to Refs. [5,6] for more complete information.

The hydrodynamic part of the code is based on a conservative and explicit Eulerian implementation of a Godunov-type scheme with higher-order spatial and temporal accuracy. It solves the nonrelativistic conservation equations for the stellar fluid, whose self-gravity is described by an "effective relativistic potential" [15]. It provides a sufficiently accurate approximation of general relativistic corrections [16].

The neutrino transport solver, which is coupled to the hydrodynamics module via lepton number, energy, and

momentum source terms, is computed with a "ray-by-ray plus" scheme [14]. It accounts for the full neutrino-energy dependence in the transport but assumes the neutrino flux at every point to be radial (i.e., the neutrino phase space distribution function is assumed to be axially symmetric around the radial direction), which is numerically less demanding and more efficient than a full multidimensional version of the transport.

The simulations used here are based on the progenitor model s15s7b2 from Woosley and Weaver [17], and are representative for the collapse of stars with progenitor masses around $15M_\odot$. The dense proto-neutron star matter is described by the equation of state (EoS) of Lattimer and Swesty [18], which leads to a radius of 12 km for a cold neutron star with a gravitational mass of $1.4M_\odot$. We also consider briefly an example with the EoS of Hillebrandt and Wolff that is considerably stiffer [19]. Unless otherwise noted, our discussion always refers to the Lattimer and Swesty case as a benchmark.

The two-dimensional model was computed under the assumption of axial symmetry and covers the region between the north and south pole with 192 equally spaced angular grid points. The model was evolved in total for about 600 ms from the onset of the collapse to a time of about 450 ms after the formation of the SN shock front and shows in the postbounce evolution a strong SASI sloshing activity of the SN shock front.

The oscillations of the SN shock front due to SASI activity and convective overturn cause luminosity fluctuations by modulating the mass accretion on the proto-neutron star: a strong shock retraction leads to a transient increase of the gas flow towards the neutron star and to the compression and enhanced cooling of the matter (i.e., enhanced neutrino emission) near the neutron star surface [6]. On the other hand, a shock expansion has the opposite effect because it causes a deceleration of the infall or even outward acceleration of material that is accreted through the shock front. Thus shock expansion stretches the time this matter stays in the gain layer and less cooling by neutrino emission occurs.

From the 192 angular rays of the models, we used in the postprocessing the luminosity for all species ν_e, $\bar{\nu}_e$, and ν_x and the corresponding $\langle E\rangle_{\rm rms}$ on every second angular bin and extracted the information in steps of about 0.5 ms that were subsequently resampled in exact 1 ms steps. To illustrate the general appearance and directional differences of the fluctuations, we combined the angular rays into 5 directional averages: north polar, equatorial, south polar, and an intermediate wedge between each pole and equator, each of them covering a zenith-angle range of 36°. For $\bar{\nu}_e$, the luminosity, rms energy, and IceCube detection rate of the 5 wedges are shown in Fig. 3. Of course, these plots have no direct observational significance and merely serve to illustrate the angular variation of the SN output. We clearly see that fluctuations in the energy and luminosity are larger along the polar directions than at the equator. In Fig. 4 we show the same information for the run with the EoS of Hillebrandt and Wolff, on which we will comment later.

B. Fourier transform and spectral power

In order to assess the detectability of such fluctuations we calculate the Fourier transform of the detection rate, at first for the run with the Lattimer and Swesty EoS. To simplify this process we have resampled the data in exact 1 ms intervals over a range of 400 ms, discarding a few ms of data at the beginning and end of the original sequence that covered the interval 10.5 ms to 417 ms postbounce. We take the Fourier transform on the full 400 ms interval, however, applying a Hann window function to reduce edge effects (see the Appendix). From Fig. 3 it is apparent that fast time variations commence in earnest at about 150 ms postbounce and we could have left out the initial phase of the signal to reduce the number of background events within the signal region. On the other hand, the window function anyway suppresses the signal portion at the edges and so we have kept the full 400 ms range.

The power spectra are in absolute units, not relative to the average signal. In our normalization the Fourier amplitude at $f = 0$ is $N_{\rm events}/N_{\rm bins}$, i.e. the average rate per bin (see the Appendix). In this way the average power does not change if we consider subsamples of the data for a shorter duration, keeping the individual bin width fixed. The power at $f = 0$ is therefore $(N_{\rm events}/N_{\rm bins})^2$. Since a typical event rate is 1000 ms^{-1} and our bin width is 1 ms, the power spectrum at $f = 0$ is around 10^6 and much smaller at other frequencies. Using a 400 ms time interval implies that the natural frequency spacing is 2.5 Hz, and based on our 1 ms binning the largest frequency that can be resolved is 500 Hz (Nyquist frequency).

Based on the background rate of Eq. (4), a signal duration of $\tau = 400$ ms, and a Hann window function, the shot-noise power of the detector dark current is given in Eq. (A12) and is found to be 10.08 in the described units where the zero-frequency power is $(N_{\rm events}/N_{\rm bins})^2$. In the subsequent plots this power level is shown as a horizontal grey line.

The modification of our power spectra plots as a function of SN distance D is not entirely trivial. If the SN is farther away than 10 kpc, we lose event rate quadratically with distance. Since we are showing the power spectrum, another power of 2 arises. Therefore, relative to the fixed IceCube dark current (the horizontal line), the power spectra are lowered by a factor $(10\ {\rm kpc}/D)^4$. The distance distribution of galactic SNe is very broad, but declines quickly beyond about 20 kpc [20]. At this pessimistic distance, the signal power spectrum would be lowered by a factor of 16, whereas the shot-noise level would remain fixed.

On the other hand, if the SN is closer than 10 kpc, the IceCube dark current quickly becomes irrelevant. The shot noise is determined by the number of detected SN events which increases with decreasing distance as $(10\ \mathrm{kpc}/D)^2$ and therefore the shot-noise level increases with this factor. The signal power spectrum increases with the fourth power $(10\ \mathrm{kpc}/D)^4$ as before, so relative to the shot-noise level the signal power increases quadratically with decreasing distance as $(10\ \mathrm{kpc}/D)^2$.

C. Hemispheric averaging

As a first example we show in Fig. 5 as a blue line (upper curve) the power spectrum of the event rate based on a single ray. To this end we have taken an ensemble average of the power spectra of all 96 angular rays with equal weights, treating each one as if it were responsible for the full 4π neutrino emission and thus for the full detector signal. Taking a true single ray instead of an ensemble average shows the same trend with much greater noise and of course with directional differences. (Such a single-ray treatment would correspond to the assumption that all neutrinos are emitted strictly in the radial direction and the observer receives neutrinos just from one spot on the stellar surface.) Up to the Nyquist frequency of 500 Hz the single-ray power stays far above the background and thus would be clearly detectable.

The true signal is caused by the integrated emission over the hemisphere facing the detector. In principle, it could be reconstructed from the detailed angular information of the neutrino emission as provided by our numerical solution of the neutrino transport. However, in view of the approximative nature of 2D models and of the "ray-by-ray plus" transport treatment (see Sec. III A), we preferred to avoid processing the huge amount of corresponding data. As a simplification we assumed that each surface element radiates isotropically with an energy spectrum according to the local conditions. In other words, we added the computed local fluxes, weighted by the projected area of the surface elements as seen by the observer. Taking the northern hemispheric average in this sense leads to the red (lower) curve in Fig. 5.

The spectral power declines much faster with increasing frequency than in the single-ray case. This is expected because high-frequency luminosity variations are due to small spatial scales of the "boiling" medium, whereas the lowest frequencies are due to the largest-scale convective overturns and SASI activity. The variations on small spatial scales are not strongly correlated and therefore reduced when taking an average over the entire hemisphere, whereas the large-scale motions are correlated and not averaged away.

The hemispheric power spectrum is quite noisy and the overall trend is better seen in a smoothed version shown in Fig. 6. Here we show the same information based on a moving average with a Gaussian window function with $\sigma = 4$ Hz. In addition we show the equatorial average as a black curve. It is the lowest curve and has significantly less power than the northern case (which is similar to the southern one). In this simulation the large-scale motion is essentially along the symmetry axis of the simulation, explaining much larger luminosity variations in the polar directions than the equatorial one. Indeed, the luminosity and temperature variations in the north and south are anticorrelated because of the dipole nature of the SASI oscillation, so in the equatorial view the variations largely cancel. In a realistic 3D situation, the dipole direction is not necessarily fixed in space, so over several hundred ms the average view from different directions probably would not differ as dramatically as in this axisymmetric simulation.

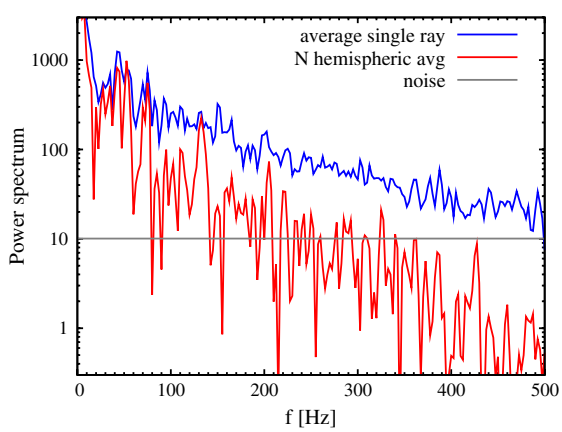

FIG. 5 (color online). Power spectrum of the IceCube event rate for our model (EoS of Lattimer and Swesty) in 2.5 Hz increments. Blue line (upper curve): average single-ray power spectrum. Red line (lower curve): northern hemispheric average. Horizontal line: shot noise from IceCube dark current.

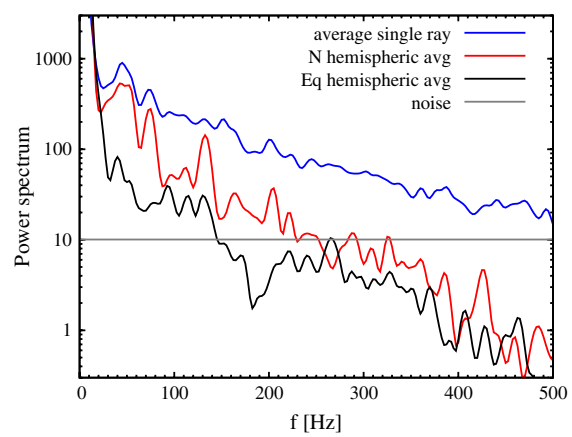

FIG. 6 (color online). Same as Fig. 5 with smoothing by a moving average with a Gaussian window function of width $\sigma = 4$ Hz. Average power of all 96 single rays (blue line), northern hemispheric average (red line), and equatorial hemispheric average (black line), from top to bottom.

D. Comparison with spherically symmetric case

An important issue is how well one can distinguish the signal from a spherically symmetric model from a convecting one. To this end we have produced an equivalent spherically symmetric model by smoothing the output from our model by a moving average. An example for the corresponding smooth luminosity is shown in Fig. 1. We compare the signal power spectrum for the equatorial hemispheric average in Fig. 7 with that from a smoothed version of this average. We see that the smooth signal plummets below the IceCube background noise level at around 20 Hz. In other words, for the case studied here the power spectrum roughly above 20 Hz is a clear indication for fast time fluctuations of the neutrino source.

E. Directional and flavor dependence

For a more detailed appreciation we next show in Fig. 8, upper panel, the smoothed power spectrum for the northern, southern, and equatorial average signals. We first observe that from ~20 Hz to ~175 Hz for $\bar{\nu}_e$ the power spectrum for all three hemispheric averages is comfortably above the noise level in IceCube. We furthermore see that the first peaks for both polar directions are roughly coinciding, and although the specific pattern differs at larger frequencies, the levels are comparable. The pronounced peak at 50 Hz corresponds to variations with a 20 ms period. This period is easily seen in Fig. 5 of Ref. [6] where the dipole motion of the shock-wave surface is plotted.

In the lower panel we show the same signal under the assumption that complete flavor transformations have taken place and what reaches IceCube are $\bar{\nu}_e$ that at the SN were born as $\bar{\nu}_x$. The qualitative features are similar as before. In other words, full or partial flavor transformations would not change the picture substantially. The overall power spectrum is now slightly lower. However, this effect is due to the reduced $\bar{\nu}_x$ luminosity during the accretion phase relative to the $\bar{\nu}_e$ luminosity. In the figure panels we give the DC ("direct current") values of the power spectrum, i.e., the power at zero frequency which is significantly larger in the $\bar{\nu}_e$ case (upper panel). In other words, the relative fluctuation amplitude is similar for both species.

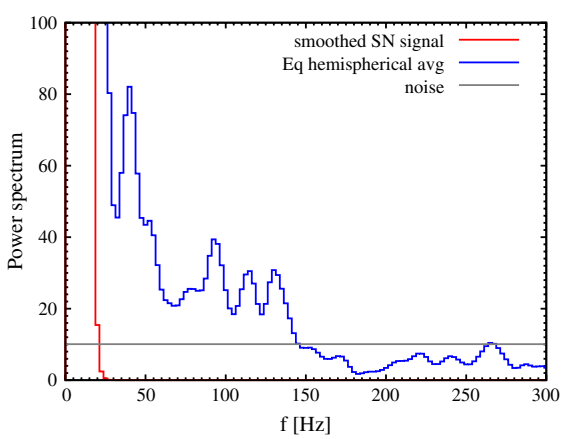

FIG. 7 (color online). Comparison between fluctuating and smooth signal for the model with Lattimer and Swesty EoS. Blue line: power spectrum of equatorial hemispheric average signal. Red line: same for smoothed SN signal.

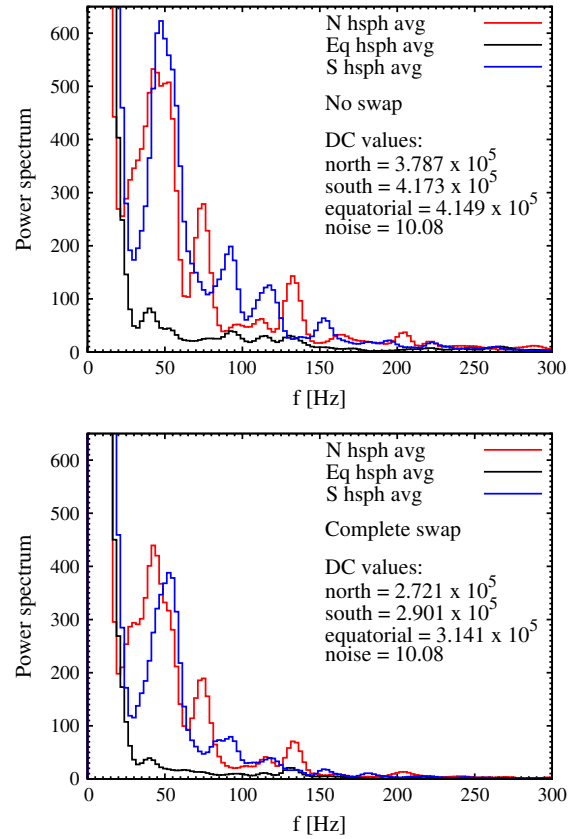

FIG. 8 (color online). Smoothed power spectrum of the event rate for the northern (red line), equatorial (black line), and southern (blue line) hemispheric averages (EoS of Lattimer and Swesty). The shot-noise level of the background is at 10.08. *Top:* no flavor oscillations. *Bottom:* complete swap $\bar{\nu}_e \leftrightarrow \bar{\nu}_x$. In the panels we also give the DC values, i.e., the power at zero frequency, corresponding to $(N_{\rm events}/N_{\rm bins})^2$.

The same information is given in Fig. 9 where we show the equatorial average (top panel) and northern average (bottom) and each time compare the $\bar{\nu}_e$ signal with the case of complete flavor swap. The northern case, especially (very similar to the southern one), shows that flavor transformations have little impact on the interpretation of fast signal variations.

IV. LUMINOSITY VS ENERGY FLUCTUATIONS

Thus far we have focused on the counting-rate fluctuations in IceCube because among existing detectors it provides by far the largest event rate. With a future megaton-class water Cherenkov detector the picture would change because the event rate would be comparable to IceCube and in addition one would obtain event-by-event

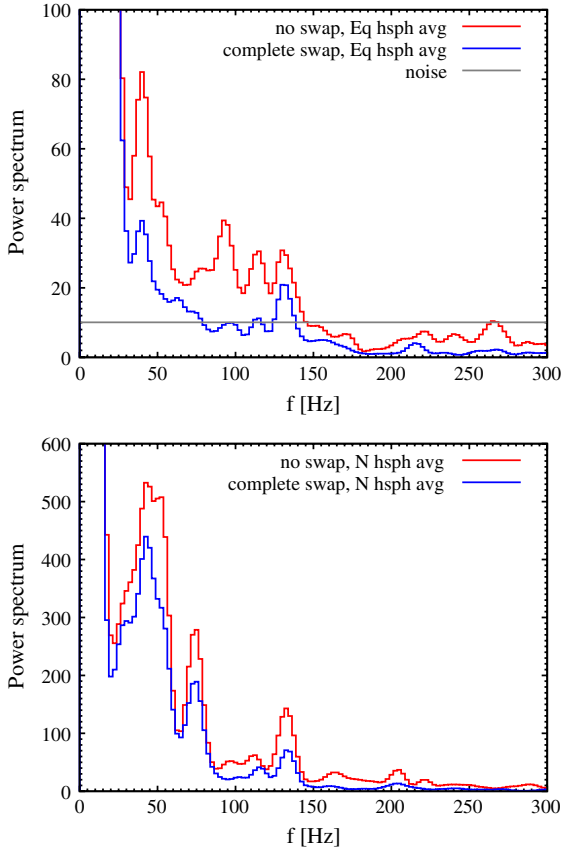

FIG. 9 (color online). Comparing no oscillations (red line) with complete flavor swap (blue line) for the model with Lattimer and Swesty EoS. *Top:* equatorial. *Bottom:* northern.

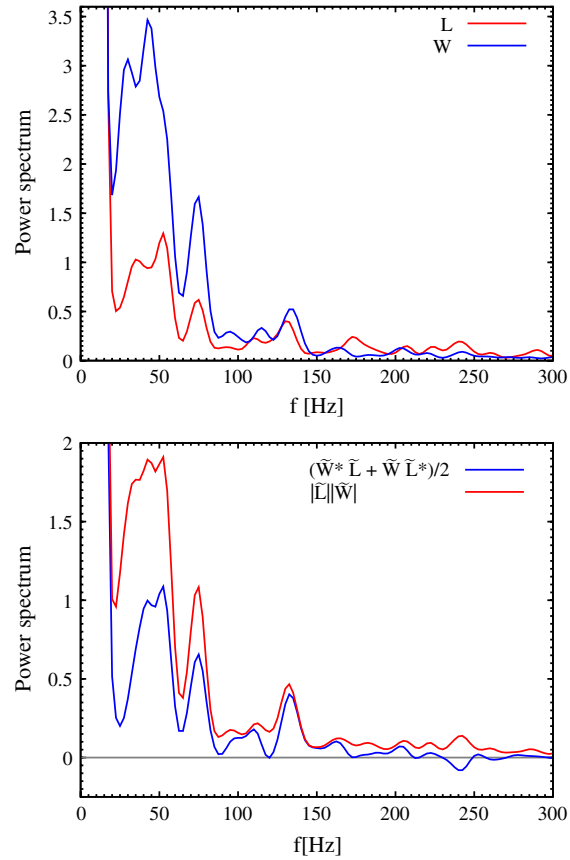

FIG. 10 (color online). Smoothed power spectrum of luminosity (L) and spectral energy ($W = E_{\rm rms}^2$) fluctuations for the model with Lattimer and Swesty EoS. L and W were normalized to their respective average values over the 274–400 ms interval. *Top:* power spectra of L (red, lower curve) and W (blue, higher curve). *Bottom:* $|\tilde{L}||\tilde{W}|$ as a red line and correlation function $\frac{1}{2}(\tilde{W}^*\tilde{L} + \tilde{W}\tilde{L}^*)$ as a blue line.

energy information. In this case spectral fluctuations would become important as well.

In Fig. 1 it is apparent that the IceCube signal variations are much larger than the luminosity variations. The fluctuations of $E_{\rm rms}$ must be responsible for the difference. Moreover, one expects that the spectral fluctuations are correlated with the luminosity fluctuations so that both effects interfere constructively.

To quantify these arguments we consider as a specific example the northern hemispheric average of the luminosity $L(t)$ and the rms energy $E_{\rm rms}(t)$ and their correlation. Since we are here concerned with the IceCube signal, which is proportional to $E_{\rm rms}^2$, we consider the two functions $L(t)$ and $W(t) = E_{\rm rms}^2(t)$. For convenience we normalize them somewhat arbitrarily to their average values over the 274–400 ms interval since now we are primarily interested in relative fluctuations. (Our conclusions do not change much if we normalize to the average values over the entire 400 ms interval.) We next calculate the Fourier transforms $\tilde{L}$ and $\tilde{W}$ of these dimensionless functions. In the upper panel of Fig. 10 we show the power spectra. The spectral power of W is significantly larger than that of L; i.e., the IceCube signal variations are dominated by $E_{\rm rms}^2$ variations.

To quantify correlations between spectral and luminosity variations we show in the lower panel of Fig. 10 the quantities $|\tilde{W}||\tilde{L}|$ and $\frac{1}{2}(\tilde{W}^*\tilde{L} + \tilde{W}\tilde{L}^*)$. The two quantities are similar and the correlation function is positive almost everywhere, so indeed $W(t)$ and $L(t)$ are strongly correlated.

These results suggest that energy- and event-rate fluctuations and their correlation, which could be measured in a megaton water Cherenkov detector, would provide additional signatures for convection and SASI activity.

V. STIFF EQUATION OF STATE

Finally we briefly address the dependence of our results on the EoS used in the SN simulation. To this end we consider the run of Ref. [6] with the EoS of Hillebrandt and Wolff [19]. The $\bar{\nu}_e$ luminosity, rms energy, and IceCube rate corresponding to our five angular wedges were shown in Fig. 4 in juxtaposition to the run with the Lattimer and

Swesty EoS. In Fig. 2 we showed the $\bar{\nu}_e$ luminosity, rms energy, and IceCube signal rate for the northern hemispheric average with the Hillebrandt and Wolff EoS in analogy to Fig. 1.

The figures reveal that strong fluctuations begin in earnest only at around 300 ms postbounce as already noted in Ref. [6]. Therefore, it makes little sense to compare the power spectrum over the first 400 ms of this run with the Lattimer and Swesty case. Instead we compare in Fig. 11 the power spectra of the IceCube rate for the northern hemispheric averages, taken over the 274–400 ms interval postbounce for the Lattimer and Swesty case (top panel) and the Hillebrandt and Wolff case (bottom). In other words, our signal duration is now $\tau = 126$ ms, implying a frequency spacing of 8 Hz and an increase of the shot-noise level by a factor $400/126 = 3.2$ (see the Appendix).

Both cases show strong power with a frequency of around 70 Hz which is also visible to the naked eye in the time evolution (lower panel of Fig. 2), although the power is larger in the Lattimer and Swesty case. The signal time variations for the stiffer EoS would be plainly visible with similar significance as for the softer one.

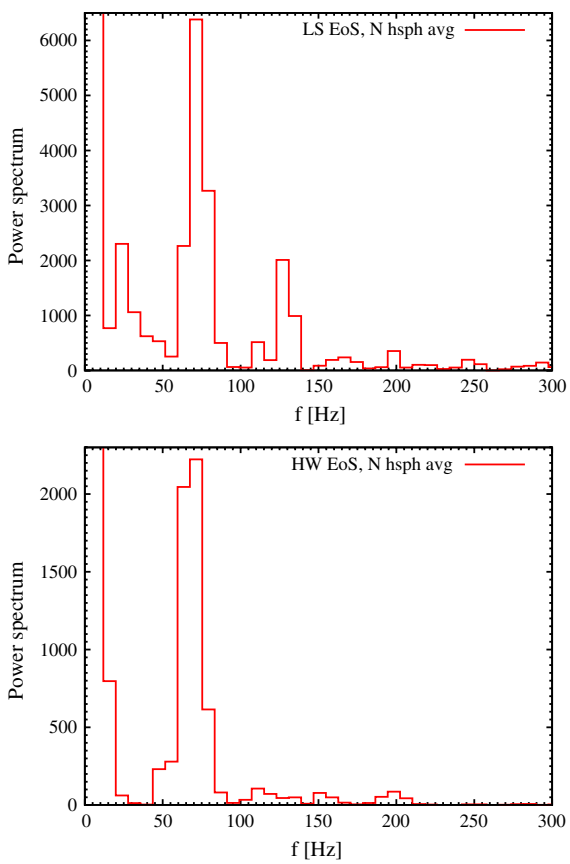

FIG. 11 (color online). Power spectra of the IceCube rate without flavor oscillations for the northern hemispheric averages, taken for the 274–400 ms postbounce interval. Because of the reduced integration time, the shot-noise level of the IceCube dark current is now at 30.26. *Top:* Lattimer and Swesty EoS in analogy to Fig. 8. *Bottom:* Hillebrandt and Wolff EoS.

We also note that the 70 Hz peak in the upper panel of Fig. 11 is much larger than in Fig. 8 (upper panel, red line). The difference between the two curves is only the analyzed signal interval. Here it is the final 126 ms of the run; in Fig. 8 the full 400 ms. If the signal was roughly stationary, the power of the peak would have to be the same. However, here we have a strong peak at 70 Hz with a much larger signal-to-noise than in Fig. 8, where in turn we have a much stronger peak at 50 Hz. In other words, the Fourier spectrum varies significantly as a function of time. The analysis of a realistic signal would involve studying subsets of the full-length signal where Fourier components can show up with much larger significance in spite of the increased shot noise relevant for a shorter integration time.

VI. IMPLICATIONS OF DETECTION

Hydrodynamical instabilities—in particular, convective and SASI activity—and multidimensional processes are thought to be crucial ingredients of the mechanism that causes the explosion of core-collapse SNe [21,22]. The nonradial asymmetries during the very early stages of the explosion can manifest themselves in large-scale asphericity and mixing of the SN blast (for recent 3D models see Ref. [23]). A measurement of neutrino signal modulations and gravitational waves would provide direct evidence for these theoretical ideas and could yield much deeper insight into the strength, evolution, and role of nonradial hydrodynamic flows on the path to successful explosions. While the main focus of this paper is the experimental detectability of SASI and convective variations of the neutrino emission—at least as predicted by 2D simulations—we briefly address possible interpretations of such a measurement.

A thorough discussion is hampered by the small number of SN models that are available for an analysis of the signal characteristics and dependence on the progenitor and core microphysics. Moreover, a conclusive theoretical assessment will require 3D models. The present 2D calculations can serve only for preliminary indications of what might be expected, provided 3D models roughly confirm the 2D results. The prominence of strong dipolar asymmetries as obtained by the lowest ($\ell = 1$ in terms of an expansion in spherical harmonics) SASI modes in 2D has indeed been questioned on the basis of recent 3D simulations [24]. However, these models do not include neutrino transport in a self-consistent way and only a small set of nonrotating models for special conditions was computed. Therefore, it is premature to judge the role of low-mode asymmetries in 3D.

The peaks of the power spectrum of the neutrino signal reflect the mode pattern of the SN core activity. They are connected with temporal changes of the mass accretion rate onto the neutron star, which are either caused by SASI or by convective modulations of the in-falling mass flow between shock and neutron star surface [5,6]. Since the

accretion downflows can be channeled more strongly to the northern or southern hemisphere, the hemispheric symmetry can easily be broken, and even long-lasting hemispheric asymmetries of the accretion structures and shock-expansion strength can emerge. Therefore there is no reason to expect exactly equal power spectra for both hemispheres. Even the dipolar SASI sloshing mode can develop different strengths in both hemispheres.

A causal connection of the peaks in the neutrino power spectra with global deformation modes of the shock surface and thus of the accretion flow between shock and proto-neutron star is supported by results presented in Ref. [6]. The Fourier spectra of the time-variable spherical harmonics dipole and quadrupole amplitudes of the shock position in that paper (Fig. 5, right column) exhibit maxima whose positions agree well with the lowest characteristic frequencies of the neutrino power spectra.

The corresponding 50 Hz peak of our model with Lattimer and Swesty EoS is actually a broad feature with high power (half-width) roughly between 30 Hz and 60 Hz. This feature is present in the northern, southern, and equatorial signals. In the equatorial case we identify it with the first two-hump maximum visible to the right of the low-frequency spike (Fig. 8, upper panel). This peak around 50 Hz is caused by the $\ell = 1$ SASI sloshing mode, which leads to quasiperiodic modulations of the mass accretion rate and associated neutrino emission in both hemispheres (see Ref. [6], p. 485). The peak width is explained by the time variations of the SASI frequency; its north-south differences by the lack of perfect hemispheric symmetry (cf. Fig. 3 in Ref. [6]).

The frequency of the $\ell = 1$ SASI mode depends on the sound-travel and mass-inflow times between neutron star surface and shock [see Eq. (32) in [2] and Eq. (18) in [4]] and thus mainly on the time-variable shock radius and to a lesser extent also on the continuously contracting neutron star radius. Roughly, when the average shock radius is large, the SASI frequency is lower; when the shock radius shrinks, the SASI frequency tends to be higher. Since the shock radius shows sizable time evolution (Fig. 4, left panel, in [6]), it is natural that the SASI peak of the time-integrated neutrino signal becomes fairly broad.

The peak with the next higher frequency of around 70 Hz is most easily explained by $\ell = 2$ (quadrupolar) SASI activity, although a strict discrimination of global shock oscillation modes from convective mass motions in the postshock layer is very difficult in the nonlinear phases of the two hydrodynamic instabilities. Both instabilities can trigger each other and therefore occur mostly simultaneously [4]. A possible connection of the ~70 Hz power maximum with the quadrupolar SASI mode is suggested by three facts: (1) Analytic analysis and numerical experiments in the linear regime show that the frequency of the $\ell = 2$ mode is slightly higher than that of the $\ell = 1$ mode (cf. Fig. 5 in [2], Fig. 13 in [4]), but the exact frequency ratio depends strongly on the size of the SASI region (see Fig. 4 in [25]). (2) The appearance of the ~70 Hz peak in the upper panel of Fig. 11 and relative weakness of power at lower frequencies at late times (274–400 ms) in our model with the Lattimer and Swesty EoS can be explained by the increasing power of the $\ell = 2$ shock oscillation mode, whose amplitude at these times becomes larger than that of the $\ell = 1$ mode (see the left panels of Fig. 5 in [6]). (3) The presence of the peak in the northern power spectrum but relative weakness or absence in the southern hemisphere may correspond to the hemispheric asymmetry of the quadrupolar shock deformation as visible in the panels of Fig. 4 in Ref. [6].

Local convective overturn motions in the accretion flow on smaller angular scales (corresponding to higher spherical harmonics modes) take place on shorter time scales than the global dipolar and quadrupolar mass shifts. Therefore they are the most probable explanation for the power peaks at frequencies above 90–100 Hz. In particular such short-wavelength structures may exhibit considerable differences in the two hemispheres and also in the equatorial region, where long-lasting, nonstationary downdrafts develop at later postbounce times. Differences between these directions in the neutrino power spectra at high frequencies are therefore not astonishing.

Moreover, the layer between shock and neutron star surface is generally more compact for the SN model with the Hillebrandt and Wolff EoS (cf. Fig. 4, left panel, of [6]). Therefore, the global shock-motion and accretion modes of this model have a lower amplitude and higher frequency than in the simulation with the Lattimer and Swesty EoS. It is possible that the very broad peak roughly between 60 Hz and 85 Hz in the former case (lower panel of Fig. 11) and simultaneous lack of a second strong peak at somewhat higher frequency is the result of a superposition of $\ell = 1$ and $\ell = 2$ activity. This interpretation is suggested by the presence of both modes with comparable amplitudes (Fig. 5 in [6]) and by the fact that for a compact postshock layer the characteristic frequencies of both modes become very similar as shown in Fig. 4 of Ref. [25].

SASI activity can therefore be reflected by different peaks in the neutrino power spectra, depending on the presence of different modes, the fastest growing ones and typically strongest in 2D being those of $\ell = 1$ and $\ell = 2$. The exact frequencies of the peaks depend on the time-evolving structure of the postshock layer. The strongest SASI activity and thus most easily measurable signal features must be expected to occur in a time window of some 100 ms just before the explosion sets in. The peaks in the power spectra of the integrated signal over this shorter period are significantly enhanced relative to the shot-noise level (compare upper panels of Figs. 8 and 11), favoring easier detection of these features.

The measurement of the neutrino luminosity modulations could thus confirm the existence of large nonradial

hydrodynamical instabilities (SASI and convective overturn) around the beginning of the explosion, which would have to be strong enough to affect the neutrino emission from the accreting neutron star. Such a measurement would reveal an important component of SN physics, whose potential relevance is presently suggested only by numerical models, theoretical analysis, and indirect arguments based on the presence of ejecta asymmetries at much later stages of the evolution.

A detection of the SASI would definitely exclude the prompt explosion mechanism (which already seems to be ruled out by simulations) as well as all other explosion mechanisms that work faster than the SASI can develop in the SN core. The growth of the SASI activity to the nonlinear regime takes typically 100–200 ms after bounce [2,4,25], so SASI signatures would require a significantly delayed explosion as expected for the neutrino-driven mechanism. Most probably, their measurement would also exclude the magnetohydrodynamic mechanism, which could take place in rapidly rotating stellar cores and according to 2D simulations could lead to relatively rapid explosions [26]. Conversely, a nondetection of strong SASI features in the neutrino signal is likely to disfavor the acoustic explosion mechanism [27,28], which might initiate the blast wave as late as 1 s or more after core bounce. In this case the onset of the explosion would be preceded by at least a transient phase of strong SASI and convective overturn activity around the newborn neutron star. Such a phase is probably important to excite the compact remnant to the required powerful, large-amplitude dipole oscillations that yield the acoustic energy flux for launching the explosion.

Exclusion arguments of this kind can become even more powerful in combination with gravitational-wave measurements as recently pointed out by Ott [29]. Thus gravitational waves and neutrino-emission variations could help to unravel the still heavily disputed processes that cause the explosions of massive stars.

VII. CONCLUSIONS

We have studied the signature of fast SN neutrino time variations in IceCube, a detector that would produce the largest event rate of any existing experiment. We have used the output of axially symmetric SN simulations recently produced by some of us. The SASI sloshing motion with time- and mode-dependent frequencies of about 50–100 Hz as well as smaller-scale, shorter-period convective overturns provide a strong imprint in the neutrino signal. Typically it would be visible even to the naked eye by simply inspecting the time sequence of registered Cherenkov photons. A Fourier analysis of the signal reveals a large signal-to-noise ratio that would be detectable for a SN throughout our galaxy.

The spectral power of the time-varying SN signal decreases with frequency and it depends on distance up to which frequency time variations can be detected. For a fiducial distance of 10 kpc the IceCube dark current is comparable to the SN signal. Based on our simulation, at this distance signal modulations typically could be seen up to 100–200 Hz. This conclusion is barely affected by possible flavor conversions.

The strongly dipolar nature of the SASI mode along the symmetry axis of the simulations implies that the observable signal variations strongly depend on the direction of viewing the SN. In particular, in the equatorial direction the signal variations caused by neutrinos emerging from the northern and southern hemispheres nearly cancel and in our most pessimistic example would be visible only to a distance of a few kpc. However, such directional cancellation effects likely would be smaller in a realistic 3D situation, although the overall SASI signal might also be smaller. Moreover, the signal-to-noise for a given Fourier mode depends on the time window used for the analysis because the power spectrum varies strongly with time. It is premature to study these issues in too much detail because the available 2D simulations as well as the approximations used in the neutrino transport provide only a first glance of what might be expected from a more realistic treatment.

The event-rate fluctuations in IceCube are caused by fluctuations of the luminosity and of the neutrino energies, the latter being the more important effect. Therefore, in a detector with spectral information such as a water Cherenkov detector additional information can be extracted. A future megaton-class detector will have a neutrino event rate comparable to IceCube's and thus would offer significant additional capabilities through its event-by-event spectral sensitivity.

Our main message is that IceCube and future large-scale detectors can measure intriguing time-dependent features of the neutrino signal of a future galactic SN, allowing one to observe the SASI activity with neutrinos *in situ*, if our 2D model is roughly representative for a more realistic treatment. Such signatures would provide a crucial test of our theoretical understanding of the core-collapse phenomenon. The secular evolution of the signal as well as its fast variations may hold information, for example, on the growth time of large-scale nonradial asymmetries in the SN core, the SN explosion mechanism, and the contraction behavior of the nascent neutron star and thus on the nuclear equation of state, but once more it is premature to forecast generic signatures on the basis of our 2D models. Moreover, the spectral range that can be probed strongly depends on the SN distance—a fiducial case at 10 kpc may not be representative if the SN is much closer or much farther away.

The excellent time resolution of IceCube can be used in other ways. For example, the signal onset and therefore bounce time can be pinned down very well, allowing for correlations with gravitational-wave detectors [12]. On the more exotic side, a possible QCD phase transition can produce a short $\bar{\nu}_e$ burst that could be detected with high significance [30].

In summary, among existing SN detectors IceCube has unique capabilities to measure fast signal variations. Identifying such features with additional spectral information is a powerful motivation to build a megaton water Cherenkov detector.

ACKNOWLEDGMENTS

We acknowledge partial support by the DFG (Germany) under Grant No. TR-27 "Neutrinos and Beyond," the Cluster of Excellence "Origin and Structure of the Universe," and the NSF under Grant No. PHY-0854827. We acknowledge computer time grants at the John von Neumann Institute for Computing (NIC) in Jülich, the Höchstleistungsrechenzentrum of the Stuttgart University (HLRS) under Grant No. SuperN/12758, the Leibniz-Rechenzentrum München, and the RZG in Garching. T. L. thanks the MPI Physics for hospitality while this work was begun. We thank the participants of the workshop JIGSAW 2010 (22–26 February 2010, Mumbai, India) for comments and discussions, in particular, Timo Griesel and Thomas Kowarik.

APPENDIX A: SHOT NOISE IN ICECUBE AND FOURIER TRANSFORM OF BINNED DATA

To estimate the shot noise of the IceCube signal we consider a signal consisting of a sequence t_j of N measured arrival times. They sample the rate $R(t)$ over the signal duration τ. The Fourier transform is

$$g(f) = \int_0^\tau dt R(t) e^{-i2\pi f t} = \sum_{j=1}^{N} e^{-i2\pi f t_j} \tag{A1}$$

with the spectral power $G(f) = |g(f)|^2$. The detection rate has units of inverse time, so the Fourier components are dimensionless and $g(0) = N$ and $G(0) = N^2$. The finite-time Fourier transform is limited to the discrete frequencies $f_k = k\Delta f = k/\tau$. It is understood that a frequency f stands for a member of this discrete set.

If the sequence of events samples a uniform distribution on the interval $0 \le t_j \le \tau$, the sum in Eq. (A1) represents a random walk in the complex plane with unit step size. One concludes that an ensemble average for $G(f)$ is independent of frequency for $f \neq 0$ and follows the normalized distribution $p(G) = N^{-1} e^{-G/N}$ [31]. The average is $\langle G \rangle = N$ so that

$$\frac{\langle G_{f\neq 0} \rangle}{G_{f=0}} = \frac{1}{N}. \tag{A2}$$

Usually we will include a window function $w(t)$ on the interval $0 \le t \le \tau$ to suppress edge effects on the Fourier transform. Therefore, we actually use

$$g(f) = \int_0^\tau dt w(t) R(t) e^{-i2\pi f t}. \tag{A3}$$

The average weight must be unity, implying

$$\int_0^\tau \frac{dt}{\tau} w(t) = 1. \tag{A4}$$

Fourier components that vary fast on the scale τ are returned with their original amplitude.

We determine the impact of a window function on the shot noise by extending the picture of a random walk in the complex plane to a variable step size. The different random walks must be combined in quadrature and the expectation value is modified as

$$\langle G \rangle = \langle w^2 \rangle N, \tag{A5}$$

where

$$\langle w^2 \rangle = \int_0^\tau \frac{dt}{\tau} w^2(t). \tag{A6}$$

We will specifically use the Hann window

$$w(t) = 1 - \cos(2\pi t/\tau), \tag{A7}$$

implying that the shot-noise power increases by a factor

$$\langle w^2 \rangle = \tfrac{3}{2}. \tag{A8}$$

Next we translate this result to the appropriate normalization for our Fourier transform. If we have $N_{\rm bins}$ bins of equal width $\Delta = \tau/N_{\rm bins}$, and the signal rate $R(t)$, the Fourier transform of this rate sampled at times $t_j = j\Delta$ with $j = 0, \ldots, N_{\rm bins} - 1$ is

$$h(f_k) = \Delta \sum_{j=0}^{N_{\rm bins}-1} R(t_j) e^{i2\pi t_j k \delta f}. \tag{A9}$$

The frequencies are $f_k = k/\tau = k\delta f$ with $k = 0, \ldots, N_f$ and $N_f = f_{\rm max}/\delta f$. Here $f_{\rm max} = 1/2\Delta$ is the Nyquist frequency. Since $\delta f = 1/\tau$ we have $N_f = N_{\rm bins}/2$.

In practice our data are provided for a duration $\tau = 400$ ms so that $\delta f = 2.5$ Hz. We use 1 ms sampling and thus consider $\Delta = 1$ ms bins, providing a Nyquist frequency of $f_{\rm max} = 500$ Hz as an upper cutoff. For $f = 0$ and $f_{\rm max}$ the spectral power is, respectively, defined as

$$P(0) = \frac{|h(0)|^2}{N_{\rm bins}^2} \quad \text{and} \quad P(f_{\rm max}) = \frac{|h(f_{\rm max})|^2}{N_{\rm bins}^2}. \tag{A10}$$

For all other frequencies we define

$$P(f_k) = \frac{|h(f_k)|^2 + |h(-f_k)|^2}{N_{\rm bins}^2} = 2\frac{|h(f_k)|^2}{N_{\rm bins}^2}. \tag{A11}$$

The second equality applies because the transformed function is real and therefore $|h(-f)|^2 = |h(f)|^2$.

Using a signal duration $\tau = 400$ ms and Eq. (4) for the background rate we find $N_{\rm bkgd} = 5.4 \times 10^5$ and $h(0) = N_{\rm bkgd}$. The ratio $|h(f_k)|^2/|h(0)|^2$ was earlier found to be $1/N_{\rm bkgd}$ times a factor $3/2$ if we use the Hann window. Our definition of power for binned data involves a factor $2/N_{\rm bins}^2$. Therefore, we find for the IceCube shot noise,

relevant for a signal duration of 400 ms and a Hann window,

$$P_{\rm shot} = \frac{3}{2}\frac{N_{\rm bkgd}^2}{N_{\rm bkgd}}\frac{2}{N_{\rm bins}^2} = \frac{3N_{\rm bkgd}}{N_{\rm bins}^2} = 10.08. \qquad \text{(A12)}$$

We have confirmed this result with a few numerical Monte Carlo realizations.

If we use a subset of the full data, i.e., a shorter signal duration τ with correspondingly fewer bins, the frequency spacing is increased, but the power at a given frequency remains the same except for detailed changes implied by the reduced data. Both $N_{\rm bkgd}$ and $N_{\rm bins}$ get reduced linearly with τ and therefore $P_{\rm shot} \propto \tau^{-1}$. The signal-to-noise of spectral power in a stationary signal increases linearly with integration time.

[1] J. M. Blondin, A. Mezzacappa, and C. DeMarino, Astrophys. J. **584**, 971 (2003).
[2] N. Ohnishi, K. Kotake, and S. Yamada, Astrophys. J. **641**, 1018 (2006).
[3] T. Foglizzo, P. Galletti, L. Scheck, and H.-T. Janka, Astrophys. J. **654**, 1006 (2007).
[4] L. Scheck, H.-T. Janka, T. Foglizzo, and K. Kifonidis, Astron. Astrophys. **477**, 931 (2008).
[5] A. Marek and H.-T. Janka, Astrophys. J. **694**, 664 (2009).
[6] A. Marek, H.-T. Janka, and E. Müller, Astron. Astrophys. **496**, 475 (2009).
[7] C. D. Ott, A. Burrows, L. Dessart, and E. Livne, Astrophys. J. **685**, 1069 (2008).
[8] S. Hannestad, A. Mirizzi, G. G. Raffelt, and Y. Y. Y. Wong, J. Cosmol. Astropart. Phys. 08 (2010) 001.
[9] G. Drexlin, J. Phys. Conf. Ser. **136**, 022 031 (2008).
[10] A. S. Dighe, M. T. Keil, and G. G. Raffelt, J. Cosmol. Astropart. Phys. 06 (2003) 005.
[11] T. Kowarik, T. Griesel, and A. Piegsa (IceCube Collaboration), in Proceedings of the 31st ICRC, Lodz, Poland, July 2009 (unpublished).
[12] F. Halzen and G. G. Raffelt, Phys. Rev. D **80**, 087301 (2009).
[13] M. Rampp and H.-T. Janka, Astron. Astrophys. **396**, 361 (2002).
[14] R. Buras, M. Rampp, H.-T. Janka, and K. Kifonidis, Astron. Astrophys. **447**, 1049 (2006).
[15] A. Marek, H. Dimmelmeier, H.-T. Janka, E. Müller, and R. Buras, Astron. Astrophys. **445**, 273 (2006).
[16] B. Müller, H.-T. Janka, and H. Dimmelmeier, Astrophys. J. Suppl. Ser. **189**, 104 (2010).
[17] S. E. Woosley and T. A. Weaver, Astrophys. J. Suppl. Ser. **101**, 181 (1995).
[18] J. M. Lattimer and F. D. Swesty, Nucl. Phys. **A535**, 331 (1991).
[19] W. Hillebrandt and R. G. Wolff, in *Nucleosynthesis: Challenges and New Developments*, edited by W. D. Arnett and J. W. Truran (University of Chicago Press, Chicago, 1985), p. 131.
[20] A. Mirizzi, G. G. Raffelt, and P. D. Serpico, J. Cosmol. Astropart. Phys. 05 (2006) 012.
[21] H.-T. Janka, K. Langanke, A. Marek, G. Martínez-Pinedo, and B. Müller, Phys. Rep. **442**, 38 (2007).
[22] A. Burrows, L. Dessart, C. D. Ott, and E. Livne, Phys. Rep. **442**, 23 (2007).
[23] N. J. Hammer, H.-T. Janka, and E. Müller, Astrophys. J. **714**, 1371 (2010).
[24] J. Nordhaus, A. Burrows, A. Almgren, and J. Bell, Astrophys. J. **720**, 694 (2010).
[25] J. M. Blondin and A. Mezzacappa, Astrophys. J. **642**, 401 (2006).
[26] A. Burrows, L. Dessart, E. Livne, C. D. Ott, and J. Murphy, Astrophys. J. **664**, 416 (2007).
[27] A. Burrows, E. Livne, L. Dessart, C. Ott, and J. Murphy, Astrophys. J. **640**, 878 (2006).
[28] A. Burrows, E. Livne, L. Dessart, C. D. Ott, and J. Murphy, Astrophys. J. **655**, 416 (2007).
[29] C. D. Ott, Classical Quantum Gravity **26**, 063 001 (2009).
[30] B. Dasgupta, T. Fischer, S. Horiuchi, M. Liebendörfer, A. Mirizzi, I. Sagert, and J. Schaffner-Bielich, Phys. Rev. D **81**, 103005 (2010).
[31] A. S. Dighe, M. T. Keil, and G. G. Raffelt, J. Cosmol. Astropart. Phys. 06 (2003) 006.

Bibliography

[ABKW89] W. D. Arnett, J. N. Bahcall, R. P. Kirshner, and S. E. Woosley, *Supernova 1987A*, Annual Review of Astronomy and Astrophysics **27** (1989), 629–700.

[BBO10] T. D. Brandt, A. Burrows, and C. D. Ott, *Results from core-collapse simulations with multi-dimensional, multi-angle neutrino transport*, [arXiv:1009.4654v1], 2010.

[BDL+07] Adam Burrows, Luc Dessart, Eli Livne, Christian D. Ott, and Jeremiah Murphy, *Simulations of magnetically-driven supernova and hypernova explosions in the context of rapid rotation*, Astrophys. J. **664** (2007), 416.

[BLD+06] Adam Burrows, Eli Livne, Luc Dessart, Christian Ott, and Jeremiah Murphy, *A new mechanism for core-collapse supernova explosions*, Astrophys.J.640:878-890, 2006.

[BLD+07] A. Burrows, E. Livne, L. Dessart, C. D. Ott, and J. Murphy, *Features of the acoustic mechanism of core-collapse supernova explosions*, Astrophys.J.655:416-433, 2007.

[BM06] John M. Blondin and Anthony Mezzacappa, *The spherical accretion shock instability in the linear regime*, Astrophys.J.642:401-409, 2006.

[BMD] John M. Blondin, Anthony Mezzacappa, and Christine DeMarino, *Stability of standing accretion shocks, with an eye toward core collapse supernovae*, Astrophys.J. 584 (2003) 971-980.

[BMH+10] S. W. Bruenn, A. Mezzacappa, W. R. Hix, J. M. Blondin, P. Marronetti, O. E. B. Messer, C. J. Dirk, and S. Yoshida, *2D and 3D core-collapse supernovae simulation results obtained with the CHIMERA code*, [arXiv:1002.4914v1].

[BRJK06] R. Buras, M. Rampp, H.-T. Janka, and K. Kifonidis, *Two-dimensional hydrodynamic core-collapse supernova simulations with spectral neutrino transport. i. numerical method and results for a* $15\,M_\odot$ *star*, Astron. Astrophys **447** (2006), 1049, [arXiv:astro-ph/0512189].

[Bru85] S. W. Bruenn, *Stellar Core Collapse: numerical model and infall epoch*, The Astrophysical Journal Supplement Series **58** (1985), 771–841, Only the apendices were used.

[BS] J. M. Blondin and S. Shaw, *Linear growth of spiral SASI modes in core-collapse supernovae*, Astrophys.J.656:366-371,2007, [arXiv:astro-ph/0611698v1].

[BZ34] W. Baade and F. Zwicky, *On super-novae*, Proc. Nat. Acad. Sci. **20** (1934), 254–259.

[CMP81] Y. Chikashige, R. N. Mohapatra, and R. D. Peccei, *Are there real Goldstone bosons associated with broken lepton number?*, Physics Letters **98B** (1981), 265–268.

[CO96] B. W. Carroll and D. A. Ostlie, *An Introduction to Modern Astrophysics*, Addison-Wesley, 1996.

[Col] IceCube Collaboration, webpage: http://www.icecube.wisc.edu/.

[CS90] K. Choi and A. Santamaria, *Majorons and supernova cooling*, Physical Review D **42** (1990), 293–302.

[CW66] S. A. Colgate and R. H. White, *The hydrodynamic behaviour of supernovae explosions*, Astrophys. J. **143** (1966), 626–681.

[DKR03a] A. S. Dighe, M. T. Keil, and G. G. Raffelt, *Detecting the neutrino mass hierarchy with a supernova at icecube*, JCAP **005** (2003), 0306, [arXiv:hep-ph/0303210].

[DKR03b] A. S. Dighe, M. T. Keil, and G. G. Raffelt, *Identifying earth matter effects on supernova neutrinos at a single detector*, JCAP **006** (2003), 03006, [hep-ph/0304150].

[DPRV97] A. D. Dolgov, S. Pastor, J. C. Romão, and J. W. F Valle, *Primordial Nucleosynthesis, Majorons and Heavy Tau Neutrinos*, Nucl. Phys. **B496** (1997), 24–40, [arXiv: hep-ph/9610507v2].

[DS00] A. S. Dighe and A. Y. Smirnov, *Identifying the neutrino mass spectrum from a supernova neutrino burst*, Physical Review D **62** (2000), [arXiv: hep-ph/9907423v2].

[eaPDG08] C. Amsler et al. (Particle Data Group), *Review of Particle Physics*, Physics Letters B **667** (2008).

[eaPDG10] K. Nakamura et al. (Particle Data Group), J. Phys. G **37** (2010), 075021, webpage:http://pdg.lbl.gov/index.html.

[FGSJ07] T. Foglizzo, P. Galletti, L. Scheck, and H. Th. Janka, *Instability of a stalled accretion shock: evidence for the advective-acoustic cycle*, Astrophys.J.654:1006-1021, 2007.

[FLMM07] G. Fogli, E. Lisi, A. Marrone, and A. Mirizzi, *Collective neutrino flavor transitions in supernovae and the role of trajectory averaging*, arXiv:hep-ph/0707.1998v1 (2007).

[Fog08] T. Foglizzo, *A simple toy model of the advective-acoustic instability i. pertubative approach.*, [arXiv:0809.2302v2].

[FWM+09] T. Fischer, S. C. Whitehouse, A. Mezzacappa, F.-K. Thielemann, and M. Liebendörfer, *Protoneutron star evolution and the neutrino driven wind in general relativistic neutrino radiation hydrodynamics simulations*, [arXiv:0908.1871v2], 2009.

[FY03] M. Fukugita and T. Yanagida, *Physics of Neutrinos and Applications to Astrophysics*, Springer, 2003.

[HMJ+] L. Hüdepohl, B. Müller, H.-Th. Janka, A. Marek, and G.G. Raffelt, *Neutrino signal of electron-capture supernova from core collapse to cooling*, Phys.Rev.Lett.104:251101,2010, [arXiv:0912.0260v1].

[HMRW10] S. Hannestad, A. Mirizzi, G. G. Raffelt, and Y. Y. Y. Wong, *Neutrino and axion hot dark matter bounds after wmap-7*, JCAP08(2010)001, 2010.

[HR05] S. Hannestad and G. G. Raffelt, *Constraining invisible neutrino decays with the cosmic microwave background*, Physical Review D **72** (2005), 103514, arXiv.org: hep-ph/0509278v1.

[HR09] Francis Halzen and Georg G. Raffelt, *Reconstructing the supernova bounce time with neutrinos in icecube*, Phys.Rev.D80:087301,2009, 2009.

[HRSW06] S. Hannestad, G. G. Raffelt, G. Sigl, and Y. Y. Y. Wong, *Self-induced conversions in dense neutrino gases: Pendulum in flavor space*, Physical Review D **74** (2006), 105010–21, [arXiv.org: astro-ph/0608695].

[HW85] W. Hillebrandt and R. G. Wolff, in Nucleosynthesis: Challenges and New Developments, ed. W. D. Arnett and J. W. Truran (Univ. Chicago Press, 1985), p. 131, 1985.

[JLM+07] H.-Th. Janka, K. Langanke, A. Marek, G. Martínez-Pinedo, and B. Müller, *Theory of core-collapse supernovae*, Physics Reports **442** (2007), 38–74.

[JM10] H.-Th. Janka and A. Marek, *personal communication*, 2010.

[KGftIC09] Thomas Kowarik, Timo Griesel, and Alexander Piégsa (for the Icecube Collaboration), *Supernova Search with the AMANDA / IceCube Detectors*, 2009.

[Kin07] S. F. King, *Neutrino mass*, Contemporary Physics **4** (2007), 195–211.

[KP93] C. W. Kim and A. Pevsner, *Neutrinos in Physics and Astrophysics*, Harwood Academic Publishers, 1993.

[KRJ03] M. Th. Keil, G. G. Raffelt, and H.-Th. Janka, *Monte Carlo Study of Supernova Neutrino Spectra Formation*, The Astrophysical Journal **590** (2003), 971–991, [arXiv: astro-ph/0208035v2].

[KTV00] M. Kachelriess, R. Tomàs, and J. W. F. Valle, *Supernova bounds on Majoron-emitting decays of light neutrinos*, Physical Review D **62** (2000), 023004, arXiv:hep-ph/0001039v1.

[LML+10] T. Lund, A. Marek, C. Lunardini, H.-Th. Janka, and G. G. Raffelt, *Fast time variations of supernova neutrino fluxes and their detectability*, Physical Review D **82** (2010), [arXiv:1006.1889v2].

[LS91] J. M. Lattimer and F. D. Swesty, *A generalised equation of state for hot, dense matter*, Nucl.Phys.A,535,331,1991, 1991.

[Mar07] A. Marek, *Multi-dimensional simulations of core collapse supernovae with different equations of state for hot proto-neutron stars*, Ph.D. thesis, Technische Universität Münich, Germany, 2007.

[MDJ+06] A. Marek, H. Dimmelmeier, H.-T. Janka, E. Müller, and R. Buras, *Exploring the relativistic regime with newtonian hydrodynamics: an improved effective gravitational potential for supernova simulations*, Astron.Astrophys.445:273,2006, 2006.

[MJ09] A. Marek and H. Th. Janka, *Delayed neutrino-driven supernova explosions aided by the standing accretion-shock instability*, Astrophys.J.694:664-696, 2009.

[MJD10] B. Mueller, H. Th. Janka, and H. Dimmelmeier, *A new multi-dimensional general relativistic neutrino hydrodynamics code for core-collapse supernovae. i. method and code tests in spherical symmetry*, 2010.

[MJM08] A. Marek, H. Th. Janka, and E. Mueller, *Equation-of-state dependent features in shock-oscillation modulated neutrino and gravitational-wave signals from supernovae*, 2008.

[NBAB10] J. Nordhaus, A. Burrows, A. Almgren, and J. Bell, *Dimension as a key to the neutrino mechanism of core-collapse supernova explosions*, 2010.

[ODMA09] M. Obergaulinger, P. Cerdá Durán, E. Müller, and M. A. Aloy, *Simulations of the Magneto-Rotational Instablities in Core-Collapse Supernovae*, [arXiv:0911.3222v1].

[OKY05] Naofumi Ohnishi, Kei Kotake, and Shoichi Yamada, *Numerical analysis on standing accretion shock instability with neutrino heating in the supernova cores*, Astrophys.J. 641 (2006) 1018-1028, 2005.

[Ott08] Christian D. Ott, *The gravitational wave signature of core-collapse supernovae*, Class.Quant.Grav.26:063001,2009, 2008.

[PFTV86] W. H. Press, B. P. Flannery, S. A. Teukolsky, and W. T. Vetterling, *Numerical Recipes. the Art of Scientific Computing*, Cambridge University Press, 1986.

[PS95] M. E. Peskin and D. V. Schroeder, *An Introduction to Quantum Field Theory*, Westview Press, 1995.

[Raf96] G. G. Raffelt, *Stars as Laboratories for Fundamental Physics*, University of Chicago Press, 1996.

[Raf01] ———, *Mu- and Tau-neutrino spectra formation in supernovae*, The Astrophysical Journal **561** (2001), 890–914.

[Raf07] ———, *Foredrag fra konferencen "Twenty Years After SN1987A"*, 2007, hjemmeside: http://sn1987a-20th.physics.uci.edu/.

[RJ02] Markus Rampp and H. Thomas Janka, *Radiation hydrodynamics with neutrinos: Variable eddington factor method for core-collapse supernova simulations*, Astron.Astrophys.396:361,2002, 2002.

[RS07] G. G. Raffelt and A. Y. Smirnov, *Self-induced spectral splits in supernovae neutrino fluxes*, [arXiv.org: hep-ph/0705.1830v2] (2007).

[SJFK07] L. Scheck, H. Th. Janka, T. Foglizzo, and K. Kifonidis, *Multidimensional supernova simulations with approximative neutrino transport. ii. convection and the advective-acoustic cycle in the supernova core*, Astron.Astrophys.477:931,2008, 2007.

[Smi97] S. W. Smith, *The Scientist and Engineer's Guide to Digital Signal Processing*, California Technical Publishing, 1997.

[STOS98] H. Shen, H. Toki, K. Oyamatsu, and K. Sumiyoshi, *Relativistic equation of state of nuclear matter for supernova explosion*, Prog. Theor. Phys **100** (1998), 1013–1031, [arXiv:nucl-th/9805035v1].

[TKDW98] T. Totani, K.Sato, H. E. Dalhed, and J. R. Wilson, *Future Detection of Supernova Neutrino Burst and Explosion Mechanism*, The Astrophysical Journal **496** (1998), 216–225.

[VB] P. Vogel and J. F. Beacom, *Angular distribution of neutron inverse beta decay* $\bar{\nu}_{+}p \rightarrow e^{+} + n$, Phys.Rev. D60 (1999) 053003, [arXiv:hep-ph/9903554v1].

[WHW02] S. E. Woosley, A. Heger, and T. A. Weaver, *The evolution and explosion of massive stars*, Reviews of Modern Physics **74** (2002), 1015–1071.

[WJ05] S. Woosley and H.-Th. Janka, *The physics of core-collapse supernovae*, Nature **1** (2005), 147–154.

[WW95] S. E. Woosley and T. A. Weaver, *The evolution and explosion of massive stars. ii. explosive hydrodynamics and nucleosynthesis*, Astrophys.J.Suppl.101,181,1995, 1995.